論文 / 著書情報
Article / Book Information

題目(和文)	下部マントル構成鉱物の高温高圧力下輸送特性測定から推定されるコア-マントル境界熱流量
Title(English)	Core-mantle boundary heat flow inferred from high-P,T transport property measurements on lower mantle minerals
著者(和文)	奥田善之
Author(English)	Yoshiyuki Okuda
出典(和文)	学位:博士(理学), 学位授与機関:東京工業大学, 報告番号:甲第11884号, 授与年月日:2021年3月26日, 学位の種別:課程博士, 審査員:太田 健二,中本 泰史,石川 晃,神田 径,玄田 英典
Citation(English)	Degree:Doctor (Science), Conferring organization: Tokyo Institute of Technology, Report number:甲第11884号, Conferred date:2021/3/26, Degree Type:Course doctor, Examiner:,,,,
学位種別(和文)	博士論文
Category(English)	Doctoral Thesis
種別(和文)	要約
Type(English)	Outline

Doctoral Dissertation

博士論文

Core-mantle boundary heat flow inferred from high-*P,T* transport property measurements on lower mantle minerals

（下部マントル構成鉱物の高温高圧力下輸送特性測定から推定されるコア−マントル境界熱流量）

Yoshiyuki Okuda

奥田善之

Tokyo Institute of Technology

Department of Earth and Planetary Sciences, Ohta laboratory

東京工業大学 理学院地球惑星科学系 太田研究室

Abstract

The thermal evolution of the earth is the history of its cooling by releasing massive heat from the surface to the outer space — currently estimated as 46±3 TW — as a consequence of the net heat transportation from the Earth's interior mainly via the mantle cooling, radiogenic heating, and the heat transfer from the core to the mantle across the core-mantle boundary (CMB), with other minor contribution such as tidal heating. The CMB heat flux is given by the product of the thermal conductivity of the lowermost mantle and the temperature gradient at the CMB, hence the knowledge of the lowermost mantle thermal conductivity and the temperature profile at the CMB is a key for better understanding the Earth's thermal evolution. The most abundant mineral in the Earth's lowermost mantle is $MgSiO_3$ bridgmanite and post-perovskite, containing a certain amount of iron and aluminum, and possibly hydrogen, as impurities. This dissertation is focused on the thermal conductivity measurements of lower mantle constituent minerals under high pressure (P) and temperature (T) conditions to estimate that of the Earth's lowermost mantle and the amount of CMB heat flow. The present experimental study consists of the following four experimental developments and investigations: the effect of iron and aluminum incorporation on the thermal conductivity of bridgmanite (Chapters 2, 5) and post-perovskite (Chapter 6); the spin state of iron in the lower mantle bridgmanite (Chapters 3, 4); the development of a new heating technique in a diamond anvil cell (Chapter 7); and the effect of hydration on the electrical conductivity of bridgmanite (Chapter 8).

In Chapter 1, I summarize the current understanding of the Earth's total energy budget, and the heat generation and transportation in its interior. I also review the previous studies on the estimation of the thermal conductivity of lower mantle minerals.

In Chapters 2, 5, and 6, the effect of impurity incorporation on the thermal conductivities of bridgmanite and post-perovskite was investigated by a combination of the pulse-light heating thermoreflectance technique and a diamond-anvil cell as a high-pressure generator. The thermal conductivity of bridgmanite showed minimal reduction due to impurity, while that of post-perovskite decreased by ~50% compared to pure $MgSiO_3$ composition by adding 10 mol.% iron to its crystal.

In Chapters 3 and 4, the spin state of Fe in the Earth's lower mantle bridgmanite was revealed by X-ray diffraction measurements and Mössbauer spectroscopy measurements at high-*P*, which has been an unsolved issue for decades. Lower mantle bridgmanite was found to contain a certain amount of low-spin iron, which questions the general view and has profound implications for mantle dynamics, and the evolution of the early magma ocean.

A new externally heated diamond anvil cell technique capable of performing a relatively temperature-accurate high-*P,T* experiments up to 1500 K was developed in Chapter 7. Using this heating technique, the water concentration in the Earth's lower mantle was estimated from high-*P,T* electrical conductivity measurements on water-bearing bridgmanite. Water abundance in the lower mantle bridgmanite was estimated to be lower than 10 ppm wt. H_2O, implying a significantly dry lower mantle.

In the final chapter, I summarize the results and significance of each chapter. The CMB heat flow and the geotherm are estimated based on the present results and added constraints to the core cooling rate. Our estimation shows a coincident match with the conventionally believed CMB heat flow value. A back transformation of post-perovskite to bridgmanite above the CMB referred to as the “double-crossing model”, is not likely to take place at the base of the Earth. A huge lateral CMB heat flux variation was inferred from the present estimation, having profound implications for thermo-physical structures of the core and the mantle.

Contents

Chapter 1. General Introduction

1.1. Overview of the Earth's energy budget and the CMB heat flow

The Earth is cooling by releasing massive energy to outer space. Direct temperature gradient measurements in boreholes of both land and ocean floor with the information of the thermal conductivity of constituting rocks indicate a uniform terrestrial heat flux of 69 mW/m^2, corresponding to a global heat flow of 35 TW. By adding the contribution of the volcanic activities and hydrothermal circulations (Pollack et al., 1993), the current total heat flow from the Earth's surface to outer space is estimated as 46 ± 3 TW (for review, see Lay et al., 2008), which is not only supplied from the core and mantle cooling but is also contributed by the heat from radioactive elements and other minor contribution such as tidal heating. The global radiogenic heat of ~20 TW is inferred from the chondritic bulk silicate Earth model (Arevalo et al., 2009; Jaupart et al., 2015), which approximately matches with the geoneutrino observation of ~16 TW (Araki et al., 2005). Therefore, determining the heat flow of mantle or core cooling gives a strong constrain to the rest of the component. The amount of mantle cooling has been estimated by numerical convection modeling reproducing the plume heat flux observed in seismic tomography (Davies, 1993; Sleep, 1990), but the estimated lower mantle cooling ranges from 5 to 30 TW mainly due to the uncertainty in the use of the poorly known temperature dependence of mantle viscosity, and in the effect of chemical buoyancy.

The heat flux across the core-mantle boundary (CMB) represents the amount of the core cooling. Since heat is passed from the liquid metallic outer core to the solid rocky lowermost mantle fully via thermal conduction, the CMB heat flow (Q_{CMB}) can be given by the following equation called Fourier's law:

$$Q_{\mathrm{CMB}} = -\kappa \left(\frac{\partial T}{\partial z}\right) A, \qquad (1\text{-}1)$$

where A is the CMB surface area, and κ and $\partial T/\partial z$ are the thermal conductivity of the lowermost mantle and the temperature gradient in the thermal boundary layer at the CMB, respectively. Eq. (1-1) indicates that the determination of the Q_{CMB} requires the information of the lowermost mantle thermal conductivity and the temperature profile at the CMB.

The temperature profile at the CMB has been estimated from the combination of seismic wave velocity profile obtained from seismic observations and its temperature dependence. However, the temperature dependence is strongly reliant on the theoretical study (Wentzcovitch et al., 2009, 2006), which currently lacks the check of the consistency by experimental studies. Another way to estimate the CMB temperature profile from seismic data is by attributing the observed S-wave velocity increase and the subsequent rapid decrease to the bridgmanite to post-perovskite to bridgmanite transition at the D" discontinuity, which provides two temperature tie-points in the lowermost mantle (Lay et al., 2006), referred as a double-crossing model (Hernlund et al., 2005). However, Kawai and Tsuchiya (2009) argued that such double-crossing requires significantly steep Clapeyron slope of the bridgmanite to post-perovskite transition of

~16 MPa/K, while both experiment and theory show good agreement with the value of ~8 MPa/K (Ohta et al., 2008a; Tsuchiya et al., 2004). Seismology provides not only the one-dimensional seismic discontinuities but also the evidence of lateral seismic wave variation at the CMB. Based on the assumption that such seismic wave variation is merely caused by the lateral temperature difference, theoretical calculations and numerical global circulation model simulations have suggested a huge lateral variation of heat flow at the CMB (Nakagawa and Tackley, 2008; Stackhouse et al., 2015). This is an intriguing issue having implications for the size and stability of the mantle plumes (Tosi et al., 2013), geomagnetic intensities and reversals (Glatzmaier et al., 1999; Takahashi et al., 2008), the inner core structure and age (Gubbins et al., 2011; Olson, 2016), and even for the origin of the Earth's magnetic field (Olson and Christensen, 2002), if present. However, as previously mentioned, their estimated temperature profile at the CMB relies on the theoretical study on temperature dependence of seismic wave velocity. Also, seismological studies (Lay et al., 2006; van der Hilst et al., 2007) have derived the Q_{CMB} from a typically used 10 W/m/K (Stacey, 1992) for the thermal conductivity of the lowermost mantle due to the lack of the reliable thermal conductivity data, which results in an obscure view of this topic. A typical value of ~10 W/m/K was first suggested by Stacey (1992), which was calculated from the thermal conductivity of 60 vol.% MgO periclase +40 vol.% rutile-type SiO_2 (stishovite) aggregate based on the assumption that post-spinel transition forms a periclase and stishovite mixture because bridgmanite has not been discovered at this time (Tschauner et al., 2014). Moreover, the thermal conductivity data of periclase (Clark, 1966) and stishovite (Soga et al., 1972) used in his

calculation were both from the measurements at ambient conditions, where Soga et al. (1972) estimated the thermal conductivity of stishovite from that of SiO_2 quartz and a rutile-type crystal structure analog of GeO_2. Direct high-*P,T* thermal conductivity measurements on lower mantle minerals would hence significantly improve the understanding of the thermal conduction phenomenon at the Earth's lowermost mantle.

The thermal conductivity of a material is the sum of lattice, radiative, and electronic terms. The radiative thermal conductivity of lower mantle minerals is estimated based on optical absorption measurement (e.g., Hofmeister, 1999; Lobanov et al., 2017; Goncharov et al., 2008; Hofmeister, 2014b; Kavner and Rainey, 2016; Keppler et al., 2008). The radiative thermal conductivity of pyrolite was found to be very small due to the strong light absorption of ferropericlase enhanced by temperature (Lobanov et al., 2020). Also, negligibly weak heat conduction by electrons in the lower mantle is anticipated from high-*P,T* electrical conductivity measurements on bridgmanite, ferropericlase, and post-perovskite (Ohta et al., 2008b, 2010, 2017; Sinmyo et al., 2014). Therefore, among all conduction mechanisms, the lattice thermal conductivity of lower mantle mineral controls the lower mantle thermal conductivity, so its determination is essential for estimating the CMB heat flow.

1.2. Previous estimates of the lattice thermal conductivity of lower mantle minerals

Fe,Al-bearing $MgSiO_3$-rich polymorph of bridgmanite is thought to be the most abundant mineral in the Earth's lower mantle (Hirose, 2009). Due to its importance, the thermal conductivity of bridgmanite has extensively been studied (Ammann et al., 2014; Dekura et al., 2013; Ghaderi et al., 2017; Goncharov et al., 2010; Haigis et al., 2012; Hsieh et al., 2017; Manthilake et al., 2011; Ohta et al., 2012, 2014; Okuda et al., 2017, 2019; Osako and Ito, 1991; Stackhouse et al., 2015; Tang et al., 2014; Zhang et al., 2017). Bridgmanite in the lower mantle contains impurities (Al, Fe^{2+}, and Fe^{3+}, Sinmyo et al., 2011), which show complex site occupancies and iron spin state (Lin et al., 2013). Theoretical calculation of the lattice conductivity of Fe,Al-bearing bridgmanite is still challenging, which is limited to Mg-pure composition (Dekura et al., 2013; Ghaderi et al., 2017; Stackhouse et al., 2015; Tang et al., 2014; Zhang et al., 2017). Measurements on the high-*P,T* lattice thermal conductivity of Fe,Al-bearing bridgmanite was performed using the Ångstrom method with a large volume press as a pressure generator (Manthilake et al., 2011), but the applied pressure was limited to 26 GPa, which is equivalent to the very top of the lower mantle due to the instrumental limitation. Diamond anvil cell measurements have succeeded in expanding the pressure to the entire lower mantle pressure condition (Ohta et al., 2012; Okuda et al., 2017, 2019; Hsieh et al., 2017). A flash heating method (Goncharov et al., 2010) and a time-domain thermoreflectance (TR)

method (Hsieh et al., 2017; Ohta et al., 2012; Okuda et al., 2017, 2019) have developed for the lattice thermal conductivity measurement in a DAC.

A flash heating method in a DAC has succeeded in measuring high-*P,T* thermal conductivity of minerals up to ~10,000 K (Beck et al., 2007), but this method involves a huge temperature difference in the DAC sample in the thermal conduction direction of more than a few hundred kelvins, which leads to large uncertainty in the measured thermal conductivity. Goncharov et al. (2010) reported the lattice thermal conductivity of bridgmanite using this method up to 125 GPa and at high-*T*, but the uncertainty was extremely large of more than 300%.

A time-domain TR method overcomes the limitations of the flash heating method. The experimental setup is similar to the flash heating method but uses a temperature dependence of the reflectivity of metals to detect the sample temperature. Since the temperature coefficient of the reflectivity of metals is typically ~10^{-4} to 10^{-5} K^{-1} (Yagi et al., 2011; Hasegawa et al., 2019), this method is capable of measuring the thermal conductivity with producing much less temperature gradient in the DAC sample than that in a flash heating. Hsieh et al. (2009) developed a room-temperature TR measurement in a DAC in a front heating/ front detection (FF) configuration, i.e., the heating laser and the detector are on the same side. The front side of the sample is heated by a pump laser, and the applied heat escapes to the sample. The thermal conductivity is calculated by monitoring the decrease of the sample surface temperature. This was applied to thermal conductivity measurement on bridgmanite up to 120 GPa (Hsieh et al., 2017). However,

the heat applied to the sample surface conducts not only to the sample but also to the pressure medium. The heat loss to the pressure medium has to be assumed by its thermal conductivity and its thickness, which is critical to the yielded conductivity data of the sample. Also, in their configuration the sample is directly in contact with a diamond anvil, so laser heating of the rear side is impossible. Alternatively, a room-temperature TR measurement in a rear heating/ front detection (RF) configuration in a DAC was developed by Yagi et al. (2011). The applied heat at the rear side of the sample surface transfers through it and reaches the front side. In this configuration, the heat loss to the pressure medium has a negligible effect on the sample thermal conductivity but requires the information of the sample thickness instead. Hasegawa et al. (2019) improved this technique to a high-*P,T* conditions up to 60 GPa and 2000 K combining with a laser-heated DAC. TR method in an RF configuration has succeeded in measuring $MgSiO_3$ bridgmanite up to lowermost mantle pressure (Ohta et al., 2012), but the measurement on Fe,Al-bearing one has not been reported until 2017 (Okuda et al., 2017).

The post-perovskite phase is thought to be a dominant phase at the base of the mantle (Murakami et al., 2004), which is thought to contain impurities as well as bridgmanite (Al, Fe^{2+}, and Fe^{3+}, Sinmyo et al., 2011). In spite of its importance, the reports on its lattice thermal conductivity are scarce (Ammann et al., 2014; Dekura and Tsuchiya, 2019; Haigis et al., 2012; Ohta et al., 2012; Okuda et al., 2020). There was only one experimental report on the lattice thermal conductivity of post-perovskite with an Mg-pure sample until 2020 (Ohta et al., 2012). Theoretical calculation suggested that the

incorporation of Fe may halve the thermal conductivity of post-perovskite (Ammann et al., 2014), which requires experimental verification. The impurity effect of Fe, Al on mineralogy and physical properties of $MgSiO_3$ polymorph bridgmanite and post-perovskite need detailed investigations for a better understanding of the thermal conductivity of the lowermost mantle and hence of the CMB heat flow.

1.3. Aim of this dissertation

Here we experimentally determined the impurity effect on the thermal conductivity of bridgmanite and post-perovskite at high-*P,T* conditions using the thermoreflectance measurements in a DAC (Yagi et al., 2011; Hasegawa et al., 2019), to estimate the CMB heat flow. We summarize the novelties and significances of studies in each chapter as follows.

- **Chapter 2**

The effect of impurity incorporation on the thermal conductivity of bridgmanite has only been investigated with the simple composition of Fe-only (Manthilake et al., 2011) and Al-only (Manthilake et al., 2011; Ohta et al., 2014). However, it is well known that the presence of Al significantly changes the cation configuration and valence state of Fe

(Sinmyo et al., 2011). Moreover, the reported pressures were limited up to 26 GPa, which was by far the pressure equivalent to that at the CMB. Therefore, thermal conductivity measurement on (Fe,Al)-bearing bridgmanite up to CMB pressure is required to assess that in the actual lower mantle. We report the first experimental data providing the effect of both Fe and Al incorporations on the thermal conductivity of bridgmanite up to 142 GPa.

- **Chapters 3−5**

The spin state of Fe in the lower mantle bridgmanite has been a matter of debate since the discovery of high-spin to low-spin transition of Fe in bridgmanite by the high-pressure experiment (Badro et al., 2004). The spin transition of Fe has been reported to affect various physical properties including thermal conductivity, but the essential comprehension of whether Fe contained in the lower mantle bridgmanite experiences the spin transition has not been accomplished since some other studies have denied such transition in their experiments and calculations (Glazyrin et al., 2014; Hsu et al., 2012; Mao et al., 2017). From the systematic studies on X-ray diffraction measurements (*Chapter 3*) and *in-situ* Mössbauer spectroscopy measurements (*Chapter 4*), we determined the cause of the spin transition of Fe in experimental studies and clarified the spin state of Fe in bridgmanite in the Earth's lower mantle, which has been an unsolved problem for decades (*Chapters 3, 4*). We also investigated the effect of the spin state of Fe on the thermal conductivity of bridgmanite (*Chapter 5*).

- **Chapter 6**

Post-perovskite is the high-pressure polymorph of bridgmanite formed at a pressure of >~120 GPa. Such a high necessitated pressure is hindering the number of experimental studies. The thermal conductivity measurement of post-perovskite is so far limited to that by Ohta et al. (2012) with Mg-pure composition. Theoretical studies have contributed to the better understanding of the thermal conductivity of post-perovskite (Ammann et al., 2014; Dekura and Tsuchiya, 2019; Haigis et al., 2012), but its impurity effect has examined only in Ammann et al. (2014). However, their calculation was based on the potentials provided in experimental studies, which inevitably would become arbitrary. Dekura and Tsuchiya (2019) has provided the very first first-principle calculation but without impurities. In this chapter, we show the first thermal conductivity measurements on Fe-bearing post-perovskite with two different Fe contents at high-*P,T* conditions.

- **Chapter 7**

Application of heating technique is required for high-*P,T* DAC experiments. The external resistive heating method produces stable and homogeneous heating superior to other heating techniques such as laser heating. However, the conventional heater assemblies have the potential disadvantage of lower achievable temperature or poor temperature accuracy. We developed a new externally heated diamond anvil cell technique capable of performing a temperature-accurate stable high-*P,T* experiments up to 1,500 K at low cost. Improvement of both attainable temperature and its accuracy in this heating method allows us to obtain more reliable data that can be applied to various

transport property measurements such as thermal conductivity, electrical conductivity, and seismic wave velocity.

- **Chapter 8**

Water concentration and its distribution in the Earth's interior are one of the most important fundamental information affecting various physical and chemical properties. Those at the upper mantle and the mantle transition zone have been estimated by the comparison between the laboratory electrical conductivity measurements on constituent minerals in these layers such as olivine, wadsleyite, and ringwoodite, and the electrical conductivity depth profile inferred from electromagnetic observations. However, the amount of water in the lower mantle —which accounts for more than a half of the Earth's total volume hence easily affects the total amount of the water in the Earth— is fully unknown since water content dependence on the electrical conductivity of lower mantle minerals has never been investigated. By utilizing the developed heating method introduced in *Chapter 7*, we determined the water abundance in the Earth's lower mantle from high-*P,T* electrical conductivity measurements on water-bearing bridgmanite.

In the final chapter, we calculate the temperature profile at the lowermost mantle, from our collected thermal conductivity data, and lastly estimate the CMB heat flow.

1.4. References

Ammann, M.W., Walker, A.M., Stackhouse, S., Wookey, J., Forte, A.M., Brodholt, J.P., Dobson, D.P., 2014. Variation of thermal conductivity and heat flux at the Earth's core mantle boundary. Earth Planet. Sci. Lett. 390, 175–185. https://doi.org/10.1016/j.epsl.2014.01.009

Araki, T., Enomoto, S., Furuno, K., Gando, Y., Ichimura, K., Ikeda, H., Inoue, K., Kishimoto, Y., Koga, M., Koseki, Y., Maeda, T., Mitsui, T., Motoki, M., Nakajima, K., Ogawa, H., Ogawa, M., Owada, K., Ricol, J.S., Shimizu, I., Shirai, J., Suekane, F., Suzuki, A., Tada, K., Takeuchi, S., Tamae, K., Tsuda, Y., Watanabe, H., Busenitz, J., Classen, T., Djurcic, Z., Keefer, G., Leonard, D., Piepke, A., Yakushev, E., Berger, B.E., Chan, Y.D., Decowski, M.P., Dwyer, D.A., Freedman, S.J., Fujikawa, B.K., Goldman, J., Gray, F., Heeger, K.M., Hsu, L., Lesko, K.T., Luk, K.B., Murayama, H., O'Donnell, T., Poon, A.W.P., Steiner, H.M., Winslow, L.A., Mauger, C., McKeown, R.D., Vogel, P., Lane, C.E., Miletic, T., Guillian, G., Learned, J.G., Maricic, J., Matsuno, S., Pakvasa, S., Horton-Smith, G.A., Dazeley, S., Hatakeyama, S., Rojas, A., Svoboda, R., Dieterle, B.D., Detwiler, J., Gratta, G., Ishii, K., Tolich, N., Uchida, Y., Batygov, M., Bugg, W., Efremenko, Y., Kamyshkov, Y., Kozlov, A., Nakamura, Y., Karwowski, H.J., Markoff, D.M., Nakamura, K., Rohm, R.M., Tornow, W., Wendell, R., Chen, M.J., Wang, Y.F., Piquemal, F., 2005. Experimental investigation of geologically produced antineutrinos with KamLAND. Nature 436, 499–503. https://doi.org/10.1038/nature03980

Arevalo, R., McDonough, W.F., Luong, M., 2009. The K/U ratio of the silicate Earth: Insights into mantle composition, structure and thermal evolution. Earth Planet. Sci. Lett. 278, 361–369. https://doi.org/10.1016/j.epsl.2008.12.02

Badro, J., Rueff, J.P., Vankó, G., Monaco, G., Fiquet, G., Guyot, F., 2004. Electronic transitions in perovskite: Possible nonconvecting layers in the lower mantle. Science 305, 383–386. https://doi.org/10.1126/science.1098840

Beck, P., Goncharov, A.F., Struzhkin, V. V., Militzer, B., Mao, H.K., Hemley, R.J., 2007. Measurement of thermal diffusivity at high pressure using a transient heating technique. Appl. Phys. Lett. 91, 10–13. https://doi.org/10.1063/1.2799243

Davies, G.F., 1993. Cooling the core and mantle by plume and plate flows. Geophys. J. Int. 115, 132–146. https://doi.org/10.1111/j.1365-246X.1993.tb05593.x

Dekura, H., Tsuchiya, T., Tsuchiya, J., 2013. Ab initio lattice thermal conductivity of $MgSiO_3$ perovskite as found in earth's lower mantle. Phys. Rev. Lett. 110, 1–5. https://doi.org/10.1103/PhysRevLett.110.025904

Dekura, H., Tsuchiya, T., 2019. Lattice Thermal Conductivity of $MgSiO_3$ Postperovskite Under the Lowermost Mantle Conditions From Ab Initio Anharmonic Lattice Dynamics. Geophys. Res. Lett. 1–8. https://doi.org/10.1029/2019GL085273

Ghaderi, N., Zhang, D.B., Zhang, H., Xian, J., Wentzcovitch, R.M., Sun, T., 2017. Lattice Thermal Conductivity of $MgSiO_3$ Perovskite from First Principles. Sci. Rep. 7, 1–9. https://doi.org/10.1038/s41598-017-05523-6

Glatzmaier, G.A., Coe, R.S., Hongre, L., Roberts, P.H., 1999. The role of the Earth's mantle in controlling the frequency of geomagnetic reversals. Nature 401, 885–890. https://doi.org/10.1038/44776

Glazyrin, K., Boffa Ballaran, T., Frost, D.J., McCammon, C., Kantor, A., Merlini, M., Hanfland, M., Dubrovinsky, L., 2014. Magnesium silicate perovskite and effect of iron oxidation state on its bulk sound velocity at the conditions of the lower mantle. Earth Planet. Sci. Lett. 393, 182–186. https://doi.org/10.1016/j.epsl.2014.01.056

Goncharov, A.F., Haugen, B.D., Struzhkin, V. V., Beck, P., Jacobsen, S.D., 2008. Radiative conductivity in the Earth's lower mantle. Nature 456, 231–234. https://doi.org/10.1038/nature07412

Goncharov, A.F., Struzhkin, V. V., Montoya, J.A., Kharlamova, S., Kundargi, R., Siebert, J., Badro, J., Antonangeli, D., Ryerson, F.J., Mao, W., 2010. Effect of composition, structure, and spin state on the thermal conductivity of the Earth's lower mantle. Phys. Earth Planet. Inter. 180, 148–153. https://doi.org/10.1016/j.pepi.2010.02.002

Gubbins, D., Sreenivasan, B., Mound, J., Rost, S., 2011. Melting of the Earths inner core. Nature 473, 361–364. https://doi.org/10.1038/nature10068

Haigis, V., Salanne, M., Jahn, S., 2012. Thermal conductivity of MgO, $MgSiO_3$ perovskite and post-perovskite in the Earth's deep mantle. Earth Planet. Sci. Lett. 355–356, 102–108. https://doi.org/10.1016/j.epsl.2012.09.002

Hasegawa, A., Yagi, T., Ohta, K., 2019. Combination of pulsed light heating thermoreflectance and laser-heated diamond anvil cell for in-situ high pressure-temperature thermal diffusivity measurements. Rev. Sci. Instrum. 90. https://doi.org/10.1063/1.5093343

Hernlund, J.W., Thomas, C., Tackley, P.J., 2005. A doubling of the post-perovskite phase boundary and structure of the Earth's lowermost mantle. Nature 434, 882–886. https://doi.org/10.1038/nature03472

Hofmeister, A.M., 1999. Mantle values of thermal conductivity and the geotherm from phonon lifetimes. Science. 283, 1699–1706. https://doi.org/10.1126/science.283.5408.1699

Hsieh, W.P., Chen, B., Li, J., Keblinski, P., Cahill, D.G., 2009. Pressure tuning of the thermal conductivity of the layered muscovite crystal. Phys. Rev. B - Condens. Matter Mater. Phys. 80, 1–4. https://doi.org/10.1103/PhysRevB.80.180302

Hsieh, W.P., Deschamps, F., Okuchi, T., Lin, J.F., 2017. Reduced lattice thermal conductivity of Fe-bearing bridgmanite in Earth's deep mantle. J. Geophys. Res. Solid Earth 122, 4900–4917. https://doi.org/10.1002/2017JB014339

Hsu, H., Yu, Y.G., Wentzcovitch, R.M., 2012. Spin crossover of iron in aluminous $MgSiO_3$ perovskite and post-perovskite. Earth Planet. Sci. Lett. 359–360, 34–39. https://doi.org/10.1016/j.epsl.2012.09.029

Jaupart, C., Labrosse, S., Lucazeau, F., Mareschal, J.C., 2015. Temperatures, Heat, and Energy in the Mantle of the Earth, Treatise on Geophysics: Second Edition. Elsevier B.V. https://doi.org/10.1016/B978-0-444-53802-4.00126-3

Kavner, A., Rainey, E.S.G., 2016. Heat Transfer in the Core and Mantle. Deep Earth Phys. Chem. Low. Mantle Core 31–42. https://doi.org/10.1002/9781118992487.ch3

Kawai, K., Tsuchiya, T., 2009. Temperature profile in the lowermost mantle from seismological and mineral physics joint modeling. Proc. Natl. Acad. Sci. U. S. A. 106, 22119–22123. https://doi.org/10.1073/pnas.0905920106

Keppler, H., Dubrovinsky, L.S., Narygina, O., Kantor, I., 2008. Optical Absorption and Radiative Thermal Conductivity of Silicate Perovskite to 125 Gigapascals. Science 322, 1529–1532. https://doi.org/10.1126/science.1164609

Lay, T., Hernlund, J., Buffett, B.A., 2008. Core-mantle boundary heat flow. Nat. Geosci. 1, 25–32. https://doi.org/10.1038/ngeo.2007.44

Lay, T., Hernlund, J., Garnero, E.J., Thorne, M.S., 2006. A post-perovskite lens and D″ heat flux beneath the central Pacific. Science 314, 1272–1276. https://doi.org/10.1126/science.1133280

Lin, J.F., Speziale, S., Mao, Z., Marquardt, H., 2013. Effects of the electronic spin transitions of iron in lower mantle minerals: Implications for deep mantle geophysics and geochemistry. Rev. Geophys. 51, 244–275. https://doi.org/10.1002/rog.20010

Lobanov, S.S., Holtgrewe, N., Ito, G., Badro, J., Piet, H., Nabiei, F., Lin, J.F., Bayarjargal, L., Wirth, R., Schreiber, A., Goncharov, A.F., 2020. Blocked radiative heat transport in the hot pyrolitic lower mantle. Earth Planet. Sci. Lett. 537, 116176. https://doi.org/10.1016/j.epsl.2020.116176

Lobanov, S.S., Holtgrewe, N., Lin, J.F., Goncharov, A.F., 2017. Radiative conductivity and abundance of post-perovskite in the lowermost mantle. Earth Planet. Sci. Lett. 479, 43–49. https://doi.org/10.1016/j.epsl.2017.09.016

Manthilake, M.A.G.M., De Koker, N., Frost, D.J., 2011. Thermal conductivity of $CaGeO_3$ perovskite at high pressure. Geophys. Res. Lett. 38, 3–6. https://doi.org/10.1029/2011GL046882

Mao, Z., Wang, F., Lin, J.F., Fu, S., Yang, J., Wu, X., Okuchi, T., Tomioka, N., Prakapenka, V.B., Xiao, Y., Chow, P., 2017. Equation of state and hyperfine parameters of high-spin bridgmanite in the Earth's lower mantle by synchrotron X-ray diffraction and Mössbauer spectroscopy. Am. Mineral. 102, 357–368. https://doi.org/10.2138/am-2017-5770

Murakami, M., 2004. Post-Perovskite Phase Transition in $MgSiO_3$. Science 304, 855–858. https://doi.org/10.1126/science.1095932

Nakagawa, T., Tackley, P.J., 2008. Lateral variations in CMB heat flux and deep mantle seismic velocity caused by a thermal-chemical-phase boundary layer in 3D spherical convection. Earth Planet. Sci. Lett. 271, 348–358. https://doi.org/10.1016/j.epsl.2008.04.013

Ohta, K., Hirose, K., Lay, T., Sata, N., Ohishi, Y., 2008a. Phase transitions in pyrolite and MORB at lowermost mantle conditions: Implications for a MORB-rich pile above the core-mantle boundary. Earth Planet. Sci. Lett. 267, 107–117. https://doi.org/10.1016/j.epsl.2007.11.037

Ohta, K., Onoda, S., Hirose, K., Sinmyo, R., Shimizu, K., Sata, N., Ohishi, Y., Yasuhara, A., 2008b. The Electrical Conductivity of Post-Perovskite in Earth's D'' Layer. Science 320, 89–91. https://doi.org/10.1126/science.1155148

Ohta, K., Hirose, K., Ichiki, M., Shimizu, K., Sata, N., Ohishi, Y., 2010. Electrical conductivities of pyrolitic mantle and MORB materials up to the lowermost mantle conditions. Earth Planet. Sci. Lett. 289, 497–502. https://doi.org/10.1016/j.epsl.2009.11.042

Ohta, K., Yagi, T., Taketoshi, N., Hirose, K., Komabayashi, T., Baba, T., Ohishi, Y., Hernlund, J., 2012. Lattice thermal conductivity of $MgSiO_3$ perovskite and post-perovskite at the core-mantle boundary. Earth Planet. Sci. Lett. 349–350, 109–115. https://doi.org/10.1016/j.epsl.2012.06.043

Ohta, K., Yagi, T., Hirose, K., 2014. Thermal diffusivities of $MgSiO_3$ and Al-bearing $MgSiO_3$ perovskites. Am. Mineral. 99, 94–97. https://doi.org/10.2138/am.2014.4598

Ohta, K., Yagi, T., Hirose, K., Ohishi, Y., 2017. Thermal conductivity of ferropericlase in the Earth's lower mantle. Earth Planet. Sci. Lett. 465, 29–37. https://doi.org/10.1016/j.epsl.2017.02.030

Okuda, Y., Ohta, K., Hasegawa, A., Yagi, T., Hirose, K., Kawaguchi, S.I., Ohishi, Y., 2020. Thermal conductivity of Fe-bearing post-perovskite in the Earth's lowermost mantle. Earth Planet. Sci. Lett. 547, 116466. https://doi.org/10.1016/j.epsl.2020.116466

Okuda, Y., Ohta, K., Sinmyo, R., Hirose, K., Yagi, T., Ohishi, Y., 2019. Effect of spin transition of iron on the thermal conductivity of (Fe, Al)-bearing bridgmanite. Earth Planet. Sci. Lett. 520, 188–198. https://doi.org/10.1016/j.epsl.2019.05.042

Okuda, Y., Ohta, K., Yagi, T., Sinmyo, R., Wakamatsu, T., Hirose, K., Ohishi, Y., 2017. The effect of iron and aluminum incorporation on lattice thermal conductivity of

bridgmanite at the Earth's lower mantle. Earth Planet. Sci. Lett. 474, 25–31. https://doi.org/10.1016/j.epsl.2017.06.022

Olson, P., 2016. Mantle control of the geodynamo: Consequences of top-down regulation. Geochemistry, Geophys. Geosystems 17, 1935–1956. https://doi.org/10.1002/2016GC006334

Olson, P., Christensen, U.R., 2002. The time-averaged magnetic field in numerical dynamos with non-uniform boundary heat flow. Geophys. J. Int. 151, 809–823. https://doi.org/10.1046/j.1365-246X.2002.01818.x

Osako, M., Ito, E., 1991. Thermal diffusivity of $MgSiO_3$ perovskite. Geophys. Res. Lett. 18, 239–242. https://doi.org/10.1029/91GL00212

Peslier, A.H., Schönbächler, M., Busemann, H., Karato, S.I., 2017. Water in the Earth's Interior: Distribution and Origin. Space Sci. Rev. 212, 1–68. https://doi.org/10.1007/s11214-017-0387-z

Pollack, H.N., Hurter, S.J., Johnson, J.R., 1993. Heat flow from the Earth's interior: Analysis of the global data set. Rev. Geophys. 31, 267–280. https://doi.org/10.1029/93RG01249

Sinmyo, R., Hirose, K., Muto, S., Ohishi, Y., Yasuhara, A., 2011. The valence state and partitioning of iron in the Earth's lowermost mantle. J. Geophys. Res. Solid Earth 116, 1–9. https://doi.org/10.1029/2010JB008179

Sleep, N.H., 1990. Hotspots and mantle plumes: Some phenomenology. J. Geophys. Res. 95, 6715. https://doi.org/10.1029/JB095iB05p06715

Soga, N., Klemas, G.H., Horai, K., 1972. Thermal-conductivity-density relationship for high- and low-pressure polymorphs of silicates and germanates. J. Geophys. Res. 77, 2610–2612. https://doi.org/10.1029/JB077i014p02610

Stacey, F., 1992. Physics of the Earth. Brookfield, Brisbane, Australia, ed. 1.

Stackhouse, S., Stixrude, L., Karki, B.B., 2015. First-principles calculations of the lattice thermal conductivity of the lower mantle. Earth Planet. Sci. Lett. 427, 11–17. https://doi.org/10.1016/j.epsl.2015.06.050

Takahashi, F., Tsunakawa, H., Matsushima, M., Mochizuki, N., Honkura, Y., 2008. Effects of thermally heterogeneous structure in the lowermost mantle on the geomagnetic field strength. Earth Planet. Sci. Lett. 272, 738–746. https://doi.org/10.1016/j.epsl.2008.06.017

Tang, X., Ntam, M.C., Dong, J., Rainey, E.S.G., Kavner, A., 2014. The thermal conductivity of Earth's lower mantle. Geophys. Res. Lett. 41, 2746–2752. https://doi.org/10.1002/2014GL059385

Tosi, N., Yuen, D.A., de Koker, N., Wentzcovitch, R.M., 2013. Mantle dynamics with pressure- and temperature-dependent thermal expansivity and conductivity. Phys. Earth Planet. Inter. 217, 48–58. https://doi.org/10.1016/j.pepi.2013.02.004

Tschauner, O., Chi, M., Beckett, J.R., Prescher, C., Prakapenka, V.B., Rossman, G.R., 2014. Discovery of bridgmanite, the most abundant mineral in Earth, in a shocked meteorite. Science 346, 1100–1102. https://doi.org/10.1126/science.1259369

Tsuchiya, T., Tsuchiya, J., Umemoto, K., Wentzcovitch, R.M., 2004. Phase transition in $MgSiO_3$ perovskite in the earth's lower mantle. Earth Planet. Sci. Lett. 224, 241–248. https://doi.org/10.1016/j.epsl.2004.05.017

van der Hilst, R.D., de Hoop, M. V., Wang, P., Shim, S.-H., Ma, P., Tenorio, L., 2007. Seismostratigraphy and Thermal Structure of Earth's Core-Mantle Boundary Region. Science 315, 1813–1817. https://doi.org/10.1126/science.1137867

Wentzcovitch, R.M., Justo, J.F., Wu, Z., da Silva, C.R.S., Yuen, D.A., Kohlstedt, D., 2009. Anomalous compressibility of ferropericlase throughout the iron spin cross-over. Proc. Natl. Acad. Sci. 106, 8447–8452. https://doi.org/10.1073/pnas.0812150106

Wentzcovitch, R.M., Tsuchiya, T., Tsuchiya, J., 2006. $MgSiO_3$ postperovskite at D″ conditions. Proc. Natl. Acad. Sci. U. S. A. 103, 543–546. https://doi.org/10.1073/pnas.0506879103

Yagi, T., Ohta, K., Kobayashi, K., Taketoshi, N., Hirose, K., Baba, T., 2011. Thermal diffusivity measurement in a diamond anvil cell using a light pulse thermoreflectance technique. Meas. Sci. Technol. 22. https://doi.org/10.1088/0957-0233/22/2/024011

Zhang, D.B., Allen, P.B., Sun, T., Wentzcovitch, R.M., 2017. Thermal conductivity from phonon quasiparticles with subminimal mean free path in the $MgSiO_3$ perovskite. Phys. Rev. B 96, 1–5. https://doi.org/10.1103/PhysRevB.96.100302

Chapter 2. The effect of iron and aluminum incorporation on lattice thermal conductivity of bridgmanite

This chapter was updated from the published article as *"The effect of iron and aluminum incorporation on lattice thermal conductivity of bridgmanite at the Earth's lower mantle"* by **Yoshiyuki Okuda**, Kenji Ohta, Takashi Yagi, Ryosuke Sinmyo, Tatsuya Wakamatsu, Kei Hirose, Yasuo Ohishi (2017) Earth and Planetary Science Letters, 474, 25-31. https://doi.org/10.1016/j.epsl.2017.06.022

Abstract

Bridgmanite (bdg), iron (Fe)- and aluminum (Al)-bearing magnesium silicate perovskite is the most abundant mineral in the Earth's lower mantle. Thus, its thermal conductivity governs the lower mantle thermal conductivity that critically controls the thermo-chemical evolution of both the core and the lower mantle. While there is extensive research for the lattice thermal conductivity of $MgSiO_3$ bdg, the effects of Fe and Al incorporation on its lattice thermal conduction are still controversial. Here we report the lattice thermal conductivity of $Mg_{0.832}Fe_{0.209}Al_{0.060}Si_{0.916}O_3$ bdg measured up to 142 GPa at 300 K using the pulsed light heating thermoreflectance technique in a diamond anvil cell. The results show that the lattice thermal conductivity of bdg is 25.5 ± 2.2 W/m/K at 135 GPa and 300 K, which is 19% lower than that of Fe and Al-free bdg at identical conditions. Considering the temperature effect on the lattice conductivity and the contribution of radiative thermal conductivity, the total thermal conductivity of Fe and Al-bearing bdg shows a weak temperature dependence at 135 GPa.

2.1. Introduction

The lower mantle is the largest region of the Earth and verges the outer core, creating an extreme thermal boundary layer (TBL) just above the core–mantle boundary (CMB) (Lay et al., 2008). The structure of the TBL is controlled by the temperature contrast between the core and the mantle and thermal conductivity of the lowermost mantle, and it strongly influences the size and stability of the mantle plume generated at the CMB (Tosi et al., 2013) and the frequency of geomagnetic reversal (Olson, 2016). In addition, regional variations in temperature and chemical composition may occur at the lowermost mantle, which induces the CMB heat flux heterogeneity in a lateral direction. This lateral CMB heat flux variation has interesting geodynamical implications for the evolution of geomagnetic field intensity (Takahashi et al., 2008), inner core growth (Aubert et al., 2008) and the flow pattern of mantle convection (Ammann et al., 2014), as introduced in Chapter 1.

The most abundant mineral in the Earth's lower mantle is $MgSiO_3$ bridgmanite (bdg hereafter) containing a certain amount of iron (Fe) and aluminum (Al). Therefore, determination of the thermal conductivity of Fe and Al-bearing bdg is of great importance to assess the thermal conductivity of the lower mantle. Lattice thermal conduction due to phonon-phonon interaction would be the primary heat conduction mechanism in bdg, while radiative thermal conduction (i.e., radiation and absorption of photons) could be important at very high-temperature conditions, such as at the CMB. A number of experimental and theoretical studies reported the lattice thermal

conductivity of bdg with $MgSiO_3$ composition (Osako and Ito, 1991; Manthilake et al., 2011; Ohta et al., 2012, 2014; Haigis et al., 2012; Dekura et al., 2013; Ammann et al., 2014; Tang et al., 2014; Stackhouse et al., 2015). However, the Fe and Al impurity effects on lattice thermal conductivity of bdg at high pressures and high temperatures remain in question. Manthilake et al. (2011) reported that even a small amount of Fe or Al into $MgSiO_3$ bdg decreased its thermal conductivity to about 50% at the CMB conditions. On the other hand, another measurement showed the negligible effect of Al incorporation on the thermal conductivity of bdg (Ohta et al., 2014). Theoretical calculations predicted, on the basis of scaling relations, that the 10 mol% Fe impurity is to reduce only 10% of the lattice thermal conductivity of bdg (Ammann et al., 2014; Stackhouse et al., 2015).

In this study, we measured the lattice thermal conductivity of $Mg_{0.832}Fe_{0.209}Al_{0.060}Si_{0.916}O_3$ bdg up to 142 GPa at room temperature by means of the pulsed light heating thermoreflectance technique with a diamond anvil cell (DAC) (Yagi et al., 2011; Ohta et al., 2012, 2017). We found about 19% lower lattice thermal conductivity of our bdg sample than (Fe,Al)-free one at 135 GPa and 300 K (Ohta et al., 2012). The lattice thermal conductivity of the Fe and Al-bearing bdg corresponding to the pressure and temperature of CMB (135 GPa and 3700 K) is estimated to be 7.7–10.5 W/m/K, which is 15% lower or less than that of $MgSiO_3$ bdg. Compositional variation in bdg is unlikely to induce significant heterogeneity of thermal conductivity in the Earth's lower mantle.

2.2. Experiments

2.2.1. Sample preparation

Bridgmanite sample we used in this study was synthesized at BGI, Bayreuth. A mixture of MgO, SiO_2, Al_2O_3, 90% enriched $^{57}Fe_2O_3$, the starting material, in a rhenium capsule was heated at 973 K for 1 day in a H_2–CO_2 gas-mixing furnace. During this time, oxygen fugacity was controlled at $\log fO_2 = -21$ to reduce Fe^{3+} to Fe^{2+}. The starting material was then kept in the multi anvil apparatus at 26 GPa and 1800 ℃ for 30 min. Thereafter, the sample recovered from the apparatus was analyzed at ambient conditions using the electron microprobe (JEOL, JXA-8200, under the operating conditions 15 kV and 15 nA), which showed the chemical composition to be $Mg_{0.832(21)}Fe_{0.209(22)}Al_{0.060(2)}Si_{0.916(24)}O_3$. To identify the crystal structure of the synthesized sample, powder X-ray diffraction (XRD) measurement was conducted using a FR-D high-brilliance Rigaku X-ray diffractometer with Mo-Kα radiation operated at 55 kV and 60 mA. From the XRD pattern, the sample was identified to be single phase of perovskite structure with the unit cell volume at ambient conditions (V_0) of 164.68 $Å^3$. $Fe^{3+}/(Fe^{2+}+Fe^{3+})$ was determined by Mössbauer spectroscopy (Prescher et al., 2012), which showed the ratio of $Fe^{3+}/(Fe^{2+}+Fe^{3+})$ to be 0.36 ± 0.05 (Sinmyo et al., 2014). The grain size of the obtained single-crystal bdg sample is about 20–30 μm.

Compressibility of the bdg sample was investigated up to 142 GPa at 300 K by the synchrotron XRD measurements at BL10XU, SPring-8. The bdg sample was loaded

into the sample chamber of the DAC with a pressure transmitting medium of KCl, NaCl or Al_2O_3, and a gold pressure marker. Thermal annealing was carried out in order to release deviatoric stress in the sample chamber. Pressure was calibrated from the unit cell volume of gold based on an equation of state (EoS) of gold (Tsuchiya, 2003). The obtained pressure versus unit cell volume relation was analyzed on the basis of the third-order Birch-Murnaghan EOS. As a result, the isothermal bulk modulus (K_T) and pressure derivative of K_T (K') of the bdg sample was determined to be 252 ± 7 GPa and 3.78 ± 0.22 with a fixed unit cell volume at ambient conditions (V_0) of 164.68 Å^3 (Fig. 2-1).

2.2.2. High-pressure thermal conductivity measurement

Thermal conductivity (κ) can be obtained from density (ρ), thermal diffusivity (D) and isobaric specific heat (C_P):

$$\kappa = \rho D C_P. \qquad (2\text{-}1)$$

Density of our bdg sample (ρ_{bdg}) at high pressures was calculated from the EOS that we obtained in this study (Fig. 2-1). We employed the pulsed light heating thermoreflectance technique to determine the thermal diffusivity of bdg (D_{bdg}) at high pressures. Details of the thermoreflectance method may be found in the literature (Yagi et al., 2011; Ohta et al., 2012, 2017). In this study, all of the thermoreflectance measurements were conducted at Tokyo Institute of Technology. The single-crystal bdg sample was pressed to make it into a thin disc shape. Then, we sputtered gold (Au) on

both sides of the sample's surface for the thermoreflectance measurements. The bdg sample covered with Au film was then loaded together with the pressure medium into the sample chamber in a DAC. Pressure was calibrated from the Raman shift of the diamond anvil (Akahama and Kawamura, 2006) or ruby fluorescence method (Mao et al., 1986).

The pulsed light heating thermoreflectance method yields transient temperature curves of bdg at each pressure (Fig. 2-2). In order to determine heat diffusion time (τ) through the sample, the obtained curves were fitted by a theoretical curve based on the one-dimensional thermal conduction equation for the film thickness direction by pulse heating:

$$T(t) = \bar{T}\sqrt{\frac{\tau}{\pi t}}\sum_{n=0}^{\infty}\gamma^{2n}exp\left[-\frac{(2n+1)^2}{4}\frac{\tau}{t}\right], \qquad (2\text{-}2)$$

where $T(t)$ is temperature, $\bar{T}$ is a constant, t is time, and γ is fitting parameter describing heat effusion to the pressure medium. The obtained thermal diffusion time τ using Eq. (2-2) was analyzed as a three-layer heat diffusion model to obtain D_{bdg} using the equations below:

$$D_{\mathrm{bdg}} = \frac{\frac{\Gamma}{6}+1+\frac{1}{\Gamma}}{(\Gamma+2)\frac{\tau}{6}-(\Gamma+\frac{4}{3})\frac{d_{\mathrm{Au}}^2}{D_{\mathrm{Au}}}}d_{\mathrm{bdg}}^2, \qquad (2\text{-}3)$$

$$\Gamma = \frac{C_{\mathrm{bdg}}d_{\mathrm{bdg}}}{C_{\mathrm{Au}}d_{\mathrm{Au}}}, \qquad (2\text{-}4)$$

where D_{Au} is thermal diffusivity of Au, d_{bdg}, d_{Au} are thickness of bdg and Au respectively, and C_{bdg}, C_{Au} are heat capacity per unit volume ($C = \rho C_{\mathrm{P}}$) of bdg and Au,

respectively. D_{Au} at ambient conditions is 127 mm^2/s (Ho et al., 1972). We use the pressure derivative of D_{Au} of 4%/GPa obtained by thermal conductivity measurements only up to a few GPa (Ross et al., 1984) because of no other available data. Thermodynamic parameters of bdg and Au used to obtain its thermal diffusivity and conductivity were estimated in the following manner for each temperature and pressure condition (Table 2-1): C_{Au} at high pressures was taken from Tsuchiya (2003). We calculated C_P of bdg at high pressures on the basis of the Debye model and thermodynamic functions with its thermoelastic parameters. Thermoelastic parameters of bdg were inferred from that of Fe 13% -bearing bdg (Wolf et al., 2015), which was the sample most similar in chemical composition to our bdg that we could find so far.

After the thermoreflectance measurements, we recovered the bdg sample with gold film. A cross section of the pump and probe lasers-focused portion of a sample was obtained parallel to a compression axis by milling with a focused Ga ion beam (FIB), and we measured the thickness of the recovered sample under a scanning electron microscope (SEM) (Fig. 2-3). d_{bdg} and d_{Au} were determined from the measured sample thickness with pressure correction, assuming elastic deformation during decompression based on the EOSs of gold (Tsuchiya, 2003) and bdg (this study) (Table 2-1).

2.3. Results and discussion

2.3.1. High-pressure lattice thermal conductivity of $Mg_{0.832}Fe_{0.209}Al_{0.060}Si_{0.916}O_3$ bdg

We performed eight separate measurements of the lattice thermal conductivity (κ_{latt}) of $Mg_{0.832}Fe_{0.209}Al_{0.060}Si_{0.916}O_3$ bdg from 1 bar to 142 GPa at room temperature, indicating that pressure range we examined the κ_{latt} covers the entire area of the Earth's mantle. All measurements were carried out upon decompression from the highest pressure in each run. At ambient conditions, the value of κ_{latt} of our bdg sample was obtained as 7.4 ± 0.5 W/m/K. Pressure enhances the κ_{latt} of bdg to 36.5 ± 9.2 W/m/K at 142 GPa (Fig. 2-4).

Chemical impurity reduces the κ_{latt} of minerals due to additional phonon scattering, mass disorder, and weaker chemical bonds. For instance, the impurity effect on olivine and orthopyroxene shows about 8% reduction in their thermal conductivities in the presence of 10 mol% Fe (Horai, 1971). Similarly, we found that the κ_{latt} of $Mg_{0.832}Fe_{0.209}Al_{0.060}Si_{0.916}O_3$ bdg at ambient conditions was 9% lower than that of Fe and Al-free bdg (Ohta et al., 2014) (Fig. 2-4). Even at 142 GPa, the present κ_{latt} is slightly lower than the κ_{latt} of $MgSiO_3$ bridgmanite. Our results are contradictory to the report by Manthilake et al. (2011) that showed a significant decrease of conductivity due to the small amount of Fe and Al incorporation into bdg, but they are in good agreement with recent theoretical predictions (Ammann et al., 2014; Stackhouse et al., 2015).

The electronic spin transition of Fe in bdg occurs in the Earth's lower mantle conditions, although the spin crossover behavior of Fe in bdg is complicated due to the

existence of different valence states and crystallographic site occupancies (Lin et al., 2013). Kupenko et al. (2015) investigated electronic configurations of Fe in the bdg sample synthesized by same run to ours using the energy domain Synchrotron Mössbauer Source technique up to 78 GPa. They showed that, in a large distorted 8- to 12- coordinated site (A site), Fe^{3+} remained in the high-spin state, while in an undistorted octahedral site (B site), it underwent a low spin state at 40 GPa. Fe^{2+} occupying the A site transitioned from high- to intermediate-spin state at 40 GPa, although *ab initio* computations predicted that Fe^{2+} would remain in a high-spin state at all mantle pressures (Zhang and Oganov, 2006; Umemoto et al., 2010). The abundance of Fe^{3+} in the B site in our bdg sample is less than 5% of the total iron content (Kupenko et al., 2015), and the effect of high- to intermediate-spin transition in Fe^{2+} on elastic properties was found to be negligible (Boffa-Ballaran et al., 2012). Therefore, we conclude that the effect of the Fe spin transition in bdg on its κ_{latt} is too small to observe in our experimental results (Fig. 2-4). On the other hand, the κ_{latt} of (Mg,Fe)O ferropericlase, the second most abundant mineral in the lower mantle, obviously changes in spin transition pressures because Fe in ferropericlase exists entirely in the magnesium site and as Fe^{2+} (Ohta et al., 2017).

2.3.2. Extrapolation to CMB pressure-temperature conditions

In order to extrapolate our present data to pressure-temperature conditions relevant to the Earth's CMB, we employed the pressure (density)-temperature model of κ proposed by Manthilake et al. (2011):

$$\kappa_{\mathrm{bdg}} = \kappa_{\mathrm{ref}} \left(\frac{\rho}{\rho_{\mathrm{ref}}}\right)^{g} \left(\frac{T_{\mathrm{ref}}}{T}\right)^{a}, \qquad (2\text{-}5)$$

where κ_{ref} and ρ_{ref} are thermal conductivity and density at reference pressure (P_{ref}) and temperature (T_{ref}), g and a are pressure and temperature dependence coefficients, respectively (Klemens, 1960; Ross et al., 1984). For P_{ref}, T_{ref} and κ_{ref}, we used 0 GPa, 300 K and 7.5 W/m/K obtained in Run #5 (Table 2-1), in which case ρ_{ref} is 4.31 g/cm^3.

Lattice thermal conduction of a material occurs by its phonon-phonon scattering, and its κ_{latt} can be illustrated simply as the following equation:

$$\kappa_{latt} = \frac{1}{3} C_V v^2 \tau, \qquad (2\text{-}6)$$

where C_V is specific heat capacity per volume, v is average phonon velocity, τ is mean phonon lifetime. Based on this kinetic phonon gas theory, density (pressure) dependence coefficient g can be approximated as follows.

$$g = (\partial \ln \kappa_{latt} / \partial \ln \rho)_T \qquad (2\text{-}7)$$

By using Eq. (2-7), we determined the g value of $Mg_{0.832}Fe_{0.209}Al_{0.060}Si_{0.916}O_3$ bdg, which was calculated to be 4.06 ± 0.30. This value is quite a lot lower than the g value of Fe and Al-free bdg reported by Ohta et al. (2012), which is 5.6. With the value of g =

4.06 ± 0.30, we obtained the relation of pressure and κ_{latt} of $Mg_{0.832}Fe_{0.209}Al_{0.060}Si_{0.916}O_3$ bdg at room temperature (Fig. 2-4). As a result, the κ_{latt} of the bdg is 25.5 ± 2.2 W/m/K at 135 GPa and 300 K, which is 19% lower than that of Fe and Al-free bdg at identical conditions (Ohta et al., 2012).

It is known that silicates and complex compounds show a gentler temperature response in κ_{latt} than simple pure oxide such as MgO that obeys the T^{-1} relation (Hofmeister, 1999). Chemical impurity, point defect, mass disorder, and other imperfections in the crystal also make the temperature dependence weaker. Manthilake et al. (2011) reported that temperature dependence coefficient a in the T^{-a} form for pure $MgSiO_3$ bdg was 0.43 that is similar to that for forsterite (Hofmeister, 1999). It was reported that the a value decreased to 0.20 due to the incorporation of 3 mol% Fe or 2 mol% Al into bdg (Manthilake et al., 2011). However, if we employed these a values to calculate high-temperature κ_{latt} both of (Fe,Al)-free and -bearing bdg at 135 GPa, the conductivity of (Fe,Al)-bearing bdg turns out to be higher than that of the experimentally determined $MgSiO_3$ (Ohta et al., 2012) above 950 K, and also theoretically determined one (Ammann et al., 2014) (Fig. 2-5a). In principle, the κ_{latt} of minerals with some impurity should always be lower than that of a pure mineral at any pressure and temperature. Thus, the a value for our bdg sample should be higher than 0.20, but should not exceed 0.43. When the a value has a range between 0.37 and 0.43, the high-temperature κ_{latt} of (Fe,Al)-bearing bdg shows lower values than that in $MgSiO_3$ composition at least up to 4300 K, corresponding to the solidus temperature of

the peridotite mantle at 135 GPa (Fiquet et al., 2010), which constrains the range of the κ_{latt} of $Mg_{0.832}Fe_{0.209}Al_{0.060}Si_{0.916}O_3$ bdg as being 7.7−10.5 W/m/K at 135 GPa and 3700 K (Fig. 2-5b).

Note that Fe and Al content in bdg in the pyrolitic composition may be 12 and 10 mol% at the lowermost mantle, respectively (e.g., Sinmyo et al., 2011), which is a slightly lower Fe content than our bdg sample. However, Ammann et al. (2014) reported that the κ_{latt} of bdg rapidly saturates with increasing Fe content. Based on this theoretical prediction, we can assume that the value of κ_{latt} of our bdg sample (Fe 20 mol% and Al 6 mol%) represents the actual value of the κ_{latt} of bdg in the Earth's lower mantle.

2.4. Geophysical implications

In order to assess the thermal conductivity of the lowermost mantle, we first calculated the κ_{latt} of 80 vol% bdg + 20 vol% ferropericlase (fp) aggregate, which is similar to the composition of the pyrolitic lower mantle. The Hashin–Shtrikman averaging was used here (Hashin and Shtrikman, 1962). For the calculation, we used the value of κ_{latt} of bdg estimated from the present study using the temperature coefficient a = 0.37−0.43, and $(Mg_{0.81}Fe_{0.19})O$ fp reported by Ohta et al. (2017). The κ_{latt} of bdg (this study) and fp (Ohta et al., 2017) at the CMB conditions are 7.7−10.5 W/m/K and 7.4 ± 1.2 W/m/K, respectively, which exhibit similar values. Thus, the κ_{latt} of the pyrolitic

lower mantle is calculated to be 7.7−9.9 W/m/K at 135 GPa and 3700 K, relevant to the *P-T* condition of the CMB. The present estimate of 7.7−9.9 W/m/K is about 20% lower than the previous estimate for the Fe,Al-free pyrolitic mantle (Ohta et al., 2012).

The total thermal conductivity of bdg (κ_{bdg}) is the summation of its κ_{latt}, radiative thermal conductivity (κ_{rad}), and electronic thermal conductivity (κ_{el}). Since the dominant electrical conduction mechanism in bdg is small-polaron or ionic conduction, the κ_{el} of bdg should be negligible (Ohta et al., 2008; Sinmyo et al., 2014; Yoshino et al., 2016). At the lowermost mantle, κ_{rad} may be a significant additional heat transport mechanism due to the very high temperature there. Optical absorption measurements on $(Mg_{0.892}Fe^{2+}_{0.059}Fe^{3+}_{0.042})(Si_{0.972}Al_{0.028})O_3$ bdg at high pressures by Keppler et al. (2008) suggested κ_{rad} is approaching ~5 W/m/K at the CMB conditions, and similar optical measurements on $(Mg_{0.94}Fe_{0.06})SiO_3$ bdg ($Fe^{3+}/\sum Fe = 0.45$) showed a similar κ_{rad} (Goncharov et al., 2015). On the other hand, $(Mg_{0.9}Fe_{0.1})SiO_3$ bdg with $Fe^{3+}/\sum Fe = 0.11$ exhibited a smaller κ_{rad} of about 2.2 W/m/K at the CMB (Goncharov et al., 2008). Since the iron contents in the bdg samples of Keppler et al. (2008) and Goncharov et al. (2008) are same but the $Fe^{3+}/\sum Fe$ ratios are different, it is conceivable that Fe^{3+} promotes radiative thermal conduction in bdg. However, Fe^{3+} enhances the Fe^{2+}-Fe^{3+} charge transfer absorption band in the middle of the visible range, results in the reduction of the radiative thermal conductivity. Thus, the discrepancy of the results between Keppler et al. (2008) and Goncharov et al. (2008) may be attributed to the uncertainty in sample thickness used in the measurements of Keppler et al. (2008). The

difference between Goncharov et al. (2008) and Goncharov et al. (2015) may be due to both the Fe content and $Fe^{3+}/\sum Fe$ ratio. Fe and Al-bearing bdg in the Earth's lower mantle is likely to have a $Fe^{3+}/(Fe^{3+}+Fe^{2+})$ ratio of about 0.5, which is independent of the oxygen fugacity (Frost et al., 2004; Sinmyo et al., 2011). Here we use the data of Goncharov et al. (2015) for the κ_{rad}($Fe^{3+}/\sum Fe$ ratio = 0.45) instead of Goncharov et al. (2008) ($Fe^{3+}/\sum Fe$ ratio = 0.11).

Fig. 2-6 shows the calculated κ_{bdg} as a function of temperature at 135 GPa. The κ_{latt} of bdg decreases with increasing temperature as expressed by Eq. (2-5), while the κ_{rad} of bdg shows the opposite behavior, which leads to a poor temperature variation of total thermal conductivity of bdg, κ_{bdg}. This variation in temperature is at most ~16% in the range of 2500 K to 4300 K, though the variation of κ_{latt} of bdg in the range of same temperature range is ~23%. Since the κ_{rad} of bdg contributes to supplementing the loss of its κ_{latt} due to Fe and Al impurity, variation in the chemistry of bdg would have little effect on the thermal conductivity of the lowermost mantle. The κ_{rad} of fp at CMB conditions is reported to be weak, exhibiting only <0.5 W/m/K (Lobanov et al., 2016; Kavner and Rainey, 2016). As a result, the total thermal conductivity of the pyrolitic lower mantle κ_{LM} (80 vol% bdg + 20 vol% fp) is calculated to be about 12.2−14.2 W/m/K at 135 GPa and 3700 K, which is insensitive to temperature variation due to the balance between κ_{bdg} and κ_{fp} (Fig. 2-7). Therefore, the regional variations in temperature and chemical composition would not induce strong CMB heat flux heterogeneity in the lateral direction. The κ_{LM} at CMB conditions that was calculated to be 12.2−14.2

W/m/K is in the middle of the 4−21 W/m/K range estimated from previous studies (see Kavner and Rainey, 2016 for review), and is reasonably consistent with the recently favored value of ~10 W/m/K estimated in the composition of the Fe,Al-free pyrolitic mantle (Ohta et al., 2012). We found that the absolute value of κ_{LM} does not differ from recently believed values even if the impurity effect was taken into consideration, on the grounds that the effect of radiative thermal conduction counterbalances the effect of impurities on κ_{LM}.

Post-perovskite (ppv), a high-pressure polymorph of bdg, shows 50~70% higher κ_{latt} than bdg in $MgSiO_3$ composition (Ohta et al., 2012; Ammann et al., 2014), but *ab initio* computations showed that Fe substitution in ppv induces a stronger reduction in κ_{latt} than bdg (Ammann et al., 2014). This implies that iron-bearing ppv has a similar κ_{latt} to that of bdg. In addition, ppv may have a much smaller κ_{rad} of 1.2 W/m/K relative to bdg according to recent absorption coefficient measurements *in-situ* at high pressures and high temperatures (Lobanov et al., 2016). From these studies, one can predict that ppv has a lower total thermal conductivity than bdg at the lowermost mantle, contradictory to the case of the Fe and Al-free system (Ohta et al., 2012; Ammann et al., 2014). To test this hypothesis, it is obviously required to investigate the effect of iron and aluminum incorporation into ppv on its thermal conductivity at the lowermost mantle conditions, which would be examined in Chapter 6.

2.5. References

Akahama, Y., Kawamura, H., 2006. Pressure calibration of diamond anvil Raman gauge to 310 GPa. J. Appl. Phys. 100, 043516.

Ammann, M., Walker, A., Stackhouse, S., Wookey, J., Forte, A., Brodholt, J., Dobson, D., 2014. Variation of thermal conductivity and heat flux at the Earth's core mantle boundary. Earth Planet. Sci. Lett. 390, 175–185.

Aubert, J., Amit, H., Hulot, G., Olson, P., 2008. Thermochemical flows couple the Earth's inner core growth to mantle heterogeneity. Nature 454, 758–761.

Boffa-Ballaran, T., Kurnosov, A., Glazyrin, K., Frost, D. J., Merlini, M., Hanfland, M., Caracas, R., 2012. Effect of chemistry on the compressibility of silicate perovskite in the lower mantle. Earth Planet. Sci. Lett. 333-334, 181–190.

Dekura, H., Tsuchiya, T., Tsuchiya, J., 2013. *Ab initio* lattice thermal conductivity of MgSiO3 perovskite as found in Earth's lower mantle. Phys. Rev. Lett. 110, 025904.

Fiquet, G., Auzende, A. L., Siebert, J., Corgne, A., Bureau, H., Ozawa, H., Garbarino, G., 2010. Melting of Peridotite to 140 Gigapascals. Science 329, 1516–1518.

Frost, D.J., Liebske, C., Langenhorst, F., McCammon, C.A., Trønnes, R.G., Rubie, D.C., 2004. Experimental evidence for the existence of iron-rich metal in the Earth's lower mantle. Nature 428, 409–412.

Goncharov, A.F., Haugen, B.D., Struzhkin, V.V., Beck, P., Jacobsen, S.D., 2008. Radiative conductivity in the Earth's lower mantle. Nature 456, 231–234.

Goncharov, A., Lobanov, S., Tan, X., Hohensee, G., Cahill, D., Lin, J.-F., Thomas, S.-M., Okuchi, T., Tomioka, N., 2015. Experimental study of thermal conductivity at high pressures: Implications for the deep Earth's interior. Phys. Earth Planet. Inter. 247, 11–16.

Haigis, V., Salanne, M., Jahn, S., 2012. Thermal conductivity of MgO, $MgSiO_3$ perovskite and post-perovskite in the Earth's deep mantle. Earth Planet. Sci. Lett. 355-356, 102–108.

Hashin, Z., Shtrikman, S., 1962. A variational approach to the theory of the effective magnetic permeability of multiphase materials. J Appl Phys 33, 3125–3131.

Ho, C., Powell, R., Liley, P., 1972. Thermal Conductivity of the Elements. J. Phys. Chem. Ref. Data 1, 279–421.

Hofmeister, A.M., 1999. Mantle Values of Thermal Conductivity and the Geotherm from Phonon Lifetimes. Science 283, 1699–1706.

Horai, K.-I., 1971. Thermal conductivity of rock-forming minerals. J. Geophys. Res. 76, 1278–1308.

Kavner, A., Rainey, E., 2016. In: Deep Earth: Physics and Chemistry of the Lower Mantle and Core, pp. 31-42.

Keppler, H., Dubrovinsky, L. S., Narygina, O., Kantor, I., 2008. Optical absorption and radiative thermal conductivity of silicate perovskite to 125 gigapascals. Science 322, 1529–1532.

Klemens, P. G., 1960. Thermal resistance due to point defects at high temperatures. Phys. Rev. 119, 507–509.

Kupenko, I., McCammon, C., Sinmyo, R., Cerantola, V., Potapkin, V., Chumakov, A.I., Kantor, A., Rüffer, R., Dubrovinsky, L., 2015. Oxidation state of the lower mantle: In situ observations of the iron electronic configuration in bridgmanite at extreme conditions. Earth Planet. Sci. Lett. 423, 78–86.

Lay, T., Hernlund, J., Buffett, B., 2008. Core-mantle boundary heat flow. Nature Geosci. 1, 25–32.

Lin, J.-F., Speziale, S., Mao, Z., Marquardt, H., 2013. Effects of the electronic spin transitions of iron in lower mantle minerals: Implications for deep mantle geophysics and geochemistry. Rev. Geophys. 51, 244–275.

Lobanov, S.S., Holtgrewe, N., Lin, J., Goncharov, F.A., 2016. Radiative conductivity and abundance of post-perovskite in the lowermost mantle. arXiv:1609.06996 [physics.geo-ph]

Manthilake, G.M., de Koker, N., Frost, D.J., McCammon, C.A., 2011. Lattice thermal conductivity of lower mantle minerals and heat flux from Earth's core. Proc. Natl. Acad. Sci. U.S.A. 108, 17901–17904.

Mao, H.K., Xu, J., Bell, P. M., 1986. Calibration of the Ruby Pressure Gauge to 800 kbar Under Quasi-Hydrostatic Conditions. J. Geophys. Res. 91, 4673–4676.

Matsui, M., 2010. High temperature and high pressure equation of state of gold. J. Phys.: Conf. Ser. 215, 012197.

Ohta, K., Onoda, S., Hirose, K., Sinmyo, R., Shimizu, K., Sata, N., Ohishi, Y., Yasuhara, A., 2008. The electrical conductivity of post-perovskite in Earth's D" layer. Science 320, 89–91.

Ohta, K., Yagi, T., Taketoshi, N., Hirose, K., Komabayashi, T. Baba, T., Ohishi, Y., Hernlund, J., 2012. Lattice thermal conductivity of $MgSiO_3$ perovskite and post-perovskite at the core–mantle boundary. Earth Planet. Sci. Lett. 349-350, 109–115.

Ohta, K., Yagi, T. Hirose, K., 2014. Thermal diffusivities of $MgSiO_3$ and Al-bearing MgSiO3 perovskites. Am. Mineral. 99, 94–97.

Ohta, K., Yagi, T., Hirose, K., Ohishi, Y., 2017. Thermal conductivity of ferropericlase in the Earth's lower mantle. Earth Planet. Sci. Lett. 465, 29–37.

Osako, M., Ito, E., 1991. Thermal diffusivity of $MgSiO_3$ perovskite. Geophys. Res. Lett. 18, 239–242.

Olson, P., 2016. Mantle control of the geodynamo: Consequences of top‐down regulation. Geochem. Geophys. Geosystems. 17, 1935–1956.

Prescher, C., McCammon, C., Dubrovinsky, L., 2012. MossA: a program for analyzing energy-domain Mössbauer spectra from conventional and synchrotron sources. J. Appl. Cryst. 45, 329–331.

Ross, R.G., Andersson, P., Sundqvist, B., Bäckström, G., 1984. Thermal conductivity of solids and liquids under pressure. Rep. Prog. Phys. 47, 1347–1402.

Sinmyo, R., Hirose, K., Muto, S., Ohishi, Y., Yasuhara, A., 2011. The valence state and partitioning of iron in the Earth's lowermost mantle. J. Geophys. Res. 116, B07205.

Sinmyo, R., Pesce, G., Greenberg, E., McCammon, C., Dubrovinsky, L., 2014. Lower mantle electrical conductivity based on measurements of Al, Fe-bearing perovskite under lower mantle conditions. Earth Planet. Sci. Lett. 393, 165–172.

Stackhouse, S., Stixrude, L., Karki, B., 2015. First-principles calculations of the lattice thermal conductivity of the lower mantle. Earth Planet. Sci. Lett. 427, 11–17.

Takahashi, F., Tsunakawa, H., Matsushima, M., Mochizuki, N., Honkura, Y., 2008. Effects of thermally heterogeneous structure in the lowermost mantle on the geomagnetic field strength. Earth Planet. Sci. Lett. 272, 738–746.

Tang, X., Ntam, M., Dong, J., Rainey, E., Kavner, A., 2014. The thermal conductivity of Earth's lower mantle. Geophys. Res. Lett. 41, 2746–2752.

Tateno, S., Hirose, K., Sata, N., Ohishi, Y., 2009. Determination of post-perovskite phase transition boundary up to 4400 K and implications for thermal structure in D″ layer. Earth Planet. Sci. Lett. 277, 130–136.

Tosi, N., Yuen, D., de Koker, N., Wentzcovitch, R., 2013. Mantle dynamics with pressure- and temperature-dependent thermal expansivity and conductivity. Phys. Earth Planet. Inter. 217, 48–58.

Tsuchiya, T., 2003. First-principles prediction of the *P-V-T* equation of state of gold and the 660-km discontinuity in Earth's mantle. J. Geophys. Res. 108, B10,2462.

Umemoto, K., Hsu, H., Wentzcovitch, R.M., 2010. Effect of site degeneracies on the spin crossovers in (Mg,Fe)SiO_3 perovskite. Phys. Earth Planet. Inter. 180, 209–214.

Wolf, S.A., Jackson, M.J., Dera, P., Prakapenka, B.V., 2015. The thermal equation of state of (Mg,Fe)SiO_3 bridgmanite (perovskite) and implications for lower mantle structures. J. Geophys. Res. 120, 11, 7460–7489.

Yagi, T., Ohta, K. Kobayashi, K., Taketoshi, N., Hirose, K., Baba, T., 2011. Thermal diffusivity measurement in a diamond anvil cell using a light pulse thermoreflectance technique. Meas. Sci. Technol. 22, 024011.

Yoshino, T., Kamada, S., Zhao, C., Ohtani, E., Hirao, N., 2016. Electrical conductivity model of Al-bearing bridgmanite with implications for the electrical structure of the Earth's lower mantle. Earth Planet Sc Lett 434, 208–219.

Zhang, F., Oganov, A.R., 2006. Valence state and spin transitions of iron in Earth's mantle silicates. Earth Planet. Sci. Lett., 249, 436–443.

2.6. Table and Figures

Table 2-1. Thermal conductivity of bridgmanite at high pressures and 300 K along with the values used for calculation

Run #	Pressure (GPa)	Pressure medium	ρ_{bdg} (kg/m^3)	C_p of bdg (J/kg/K)	ρ_{Au} (kg/m^3)	C_p of gold (J/kg/K)	D_{Au} (mm^2/s)	d_{Au} (nm)*	τ of sample (μs)	d_{bdg} (μm)*	D_{bdg} (mm^2/s)	κ_{bdg} (W/m/K)
1	18	KCl	4593.5	661.5	23574.0	127.8	260.9	284.4(149)	11.46(33)	4.76(3)	2.44(8)	7.40(24)
	39		4875.6	611.1	25187.1	125.9	604.4	278.7(149)	8.34(44)	4.67(3)	3.27(18)	9.73(53)
2	9	NaCl	4458.4	686.3	22714.2	128.7	182.0	333.8(173)	15.62(10)	5.73(4)	2.56(4)	7.82(11)
	15		4549.6	669.5	23302.6	128.1	231.4	331(173)	14.11(19)	5.69(4)	2.80(5)	8.54(16)
	19		4607.9	658.9	23661.7	127.7	271.6	329.4(173)	13.22(23)	5.67(4)	2.97(6)	9.03(19)
	27		4719.4	638.8	24318.3	126.9	374.0	326.6(173)	11.02(30)	5.62(4)	3.53(11)	10.65(32)
3	60	Al_2O_3	5127.9	567.7	26496.9	124.4	278.9	406.5(787)	5.54(14)	4.12(59)	4.38(119)	12.74(345)
4	0	KCl	4311.5	713.4	21674.0	129.9	25.0	225.5(173)	37.36(6)	9.04(34)	2.39(18)	7.35(54)
5	107	Al_2O_3	5604.7	492.0	28765.4	121.7	1806.0	116.8(406)	2.10(2)	3.33(17)	6.21(81)	17.13(224)
6	74	Al_2O_3	5273.4	543.6	27213.7	123.5	476.1	81.5(497)	1.60(2)	2.73(28)	5.29(100)	15.16(287)
	82		5356.5	530.2	27612.3	123.0	655.2	81.1(497)	1.16(2)	2.69(27)	7.11(134)	20.19(382)
7	63	Al_2O_3	5158.1	562.6	26536.2	124.2	310.9	107.6(317)	1.73(5)	3.08(58)	6.35(225)	18.42(653)
8	142	KCl	5916.2	449.9	30147.8	120.0	7323.7	193.8(327)	0.42(2)	1.95(26)	13.70(343)	36.48(923)

* After correction for pressure effect using the equation of state of Au (Matsui et al., 2010) and bridgmanite (this study)

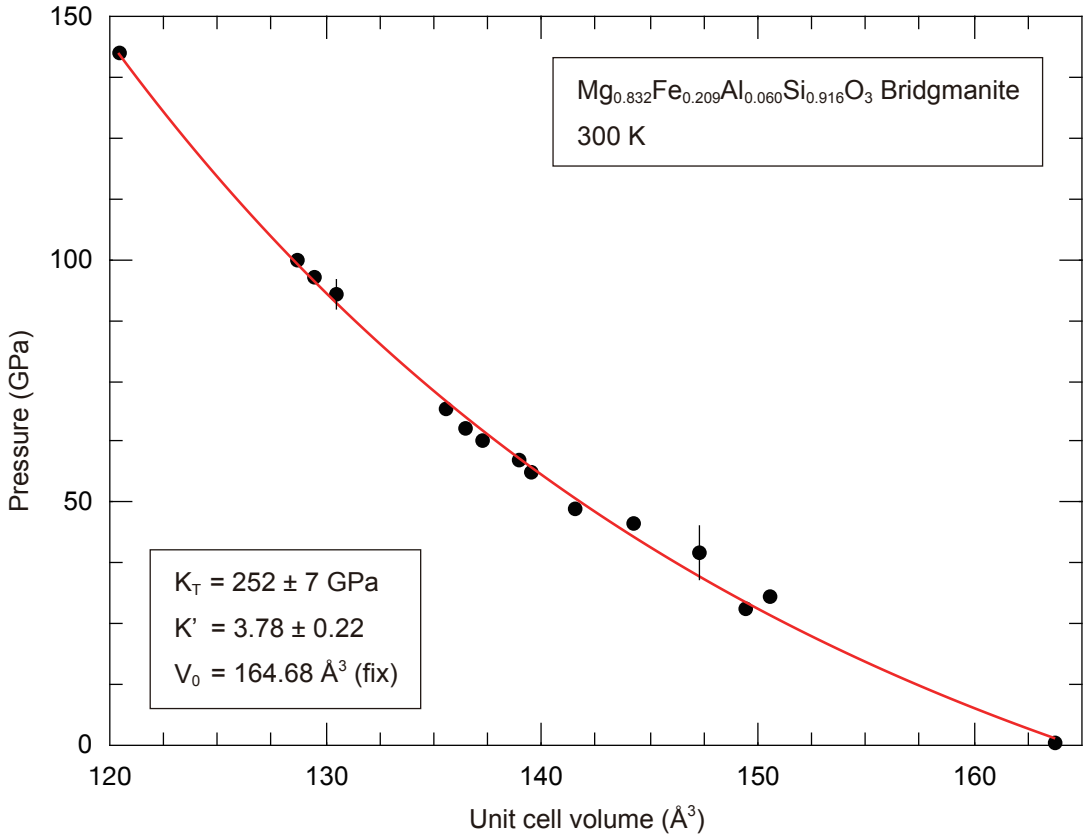

Fig. 2-1. Compression curve of the $Mg_{0.832}Fe_{0.209}Al_{0.060}Si_{0.916}O_3$ bdg sample up to 142 GPa and 300 K. Parameters for the third-order Birch-Murnaghan EoS was obtained as the legend in this figure.

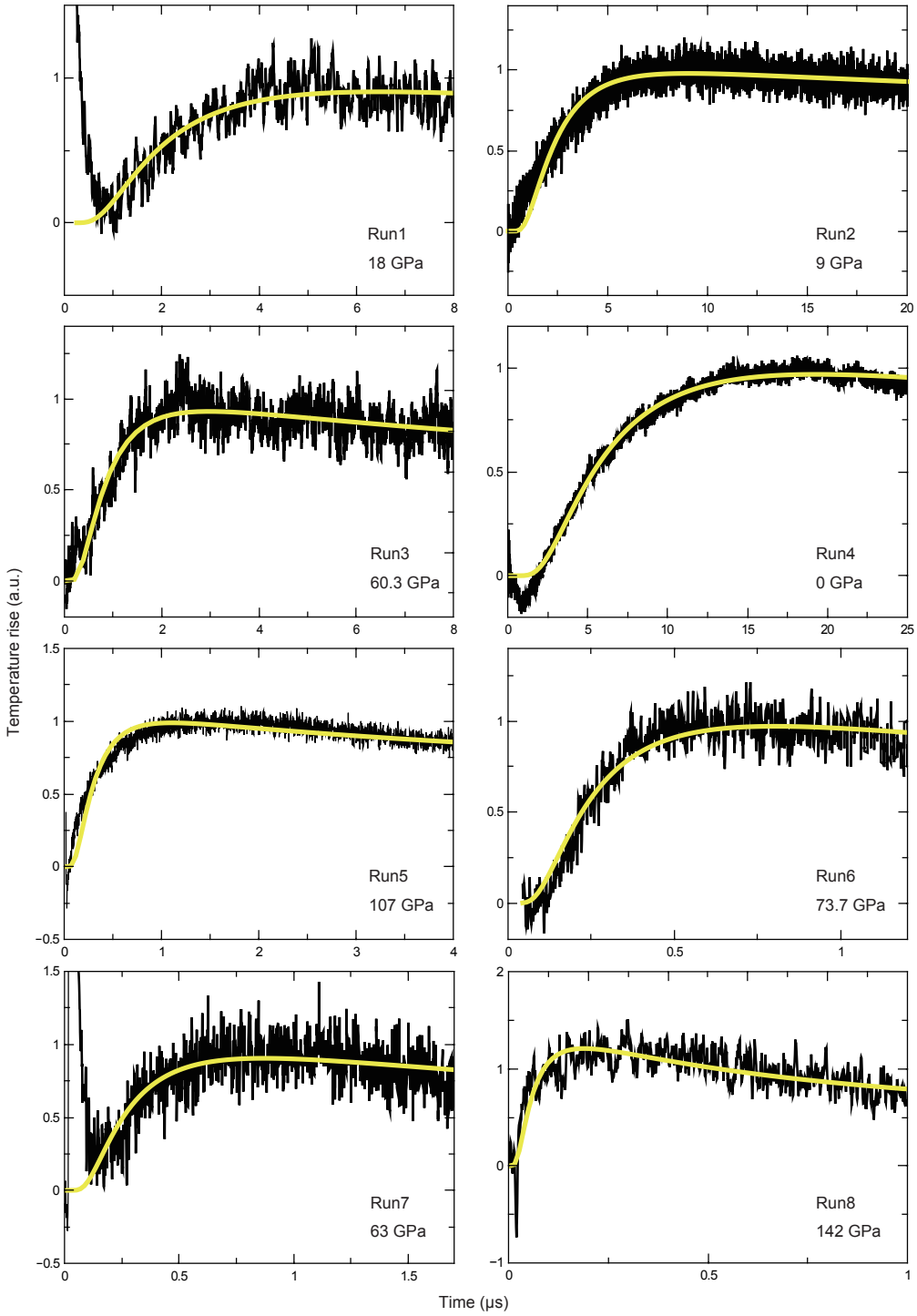

Fig. 2-2. Eight temperature history curves obtained in each run in this study. Yellow lines indicate fitting curves (Eq. 2-2) to obtain the heat diffusion time (τ) of sample.

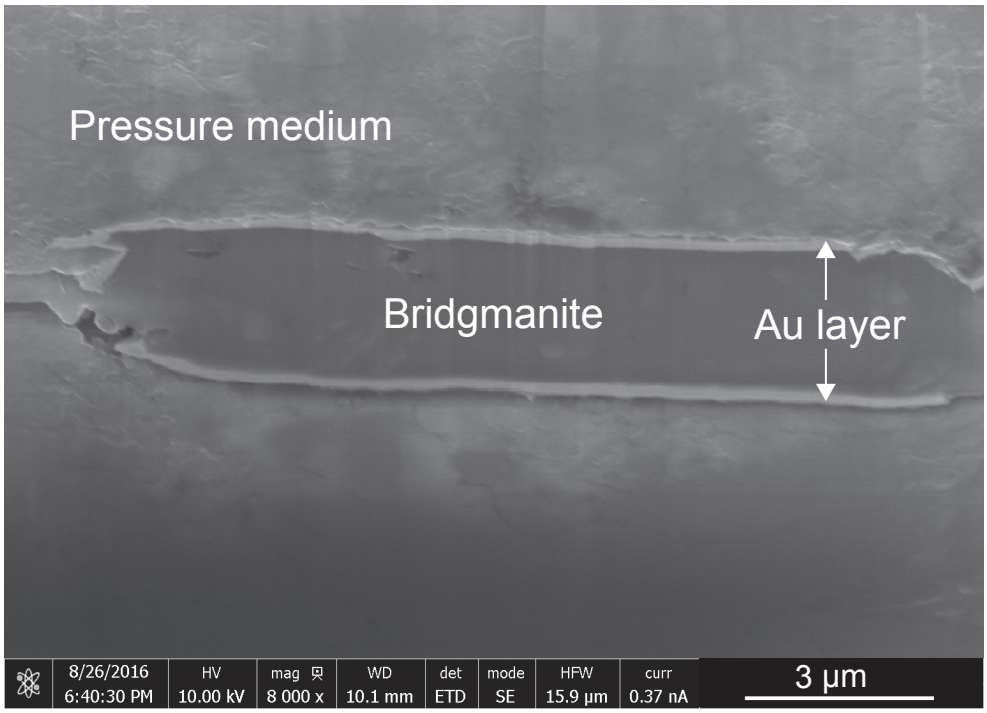

Fig. 2-3. SEM image of a cross section of the recovered sample from 39 GPa prepared by the FIB apparatus. Note that this image has been acquired from an oblique direction to sample stage, and thus the apparent thickness shown in this figure is different from the actual sample thickness (Table 2-1).

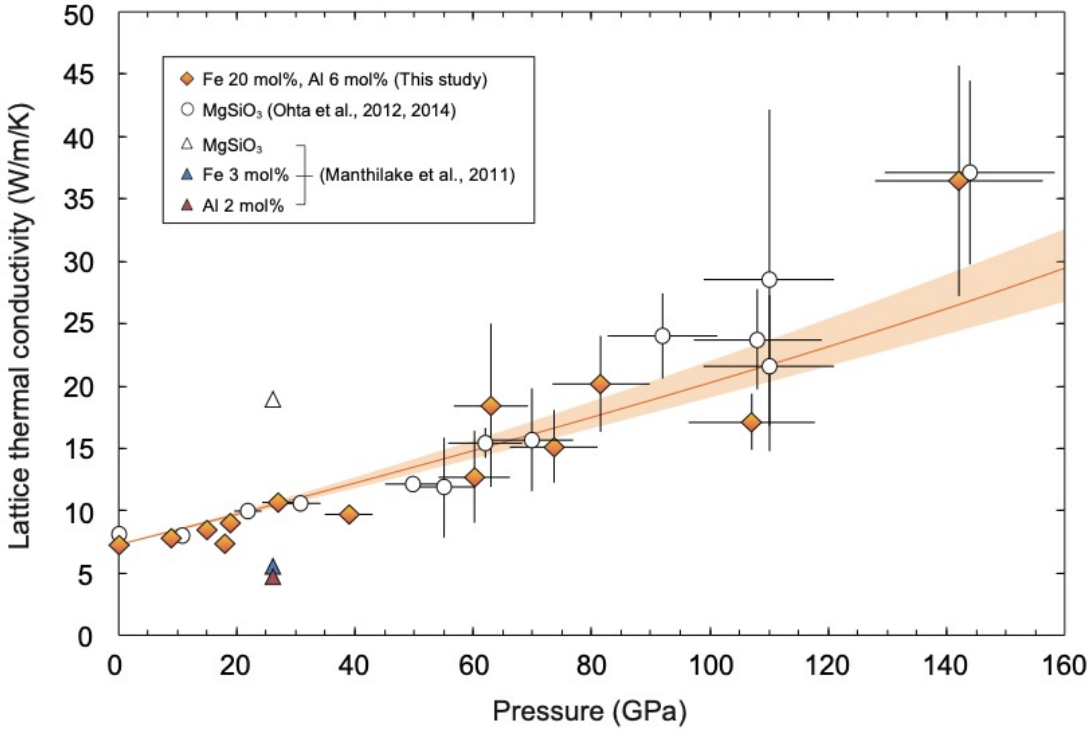

Fig. 2-4. Lattice thermal conductivity (κ_{latt}) of bdg at 300 K as a function of pressure. Orange diamonds, $Mg_{0.832}Fe_{0.209}Al_{0.060}Si_{0.916}O_3$ bdg (this study); open circles, $MgSiO_3$ bdg (Ohta et al., 2012, 2014); white, blue, and red triangles, $MgSiO_3$ bdg, $MgSiO_3$ + 3 mol% $FeSiO_3$ bdg, and $MgSiO_3$ + 2 mol% Al_2O_3 bdg, respectively (Manthilake et al., 2011). The orange curve indicates the pressure dependence of the κ_{latt} of our sample determined from Eq. (2-7), and orange band indicates the error of κ_{latt} estimated from the error of density dependence coefficient g.

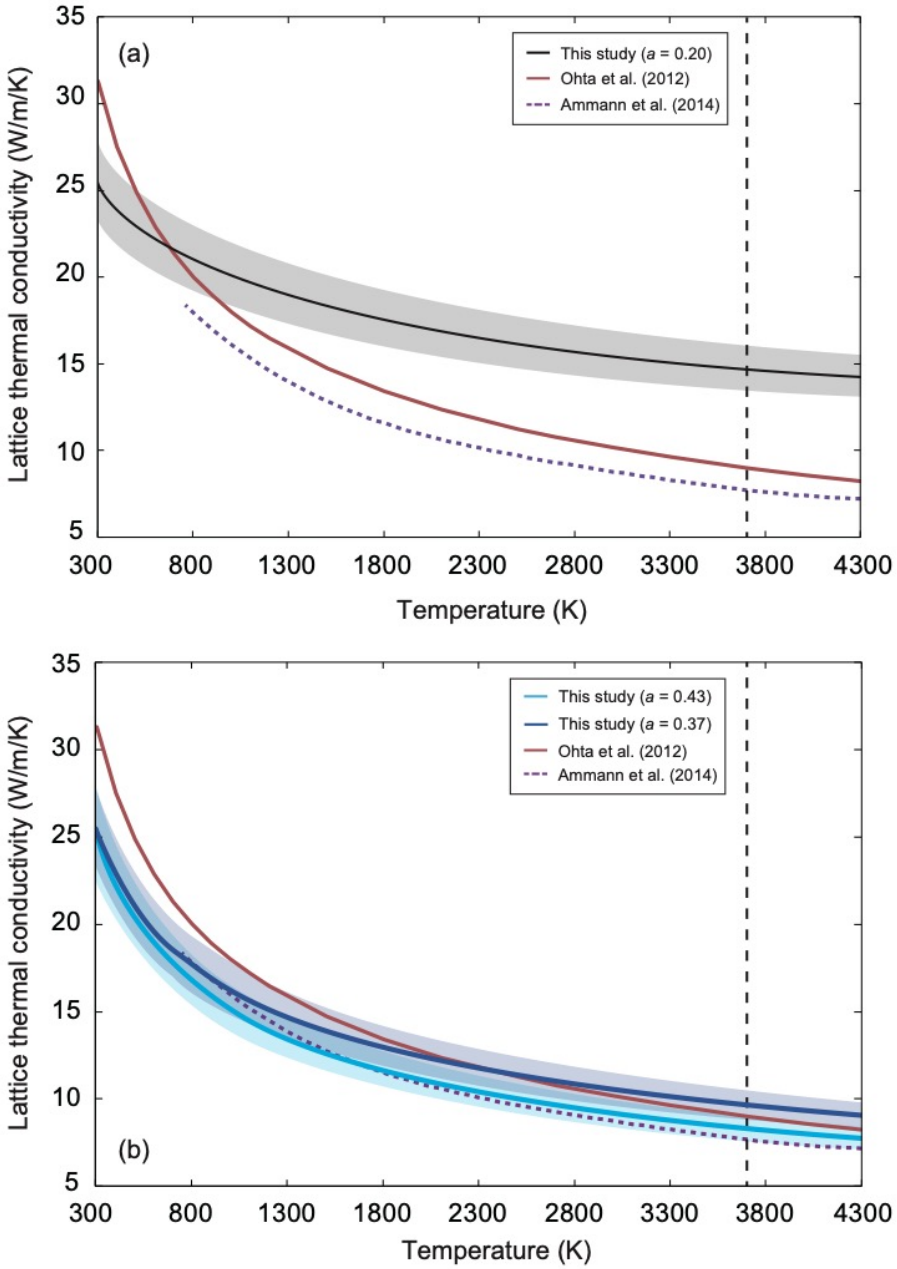

Fig. 2-5. (a) Temperature dependence of κ_{latt} of bdg using a = 0.20 (black line) and **(b)** a = 0.37, 0.43 in this study (dark blue and light blue lines). Red curves are the temperature dependence of the κ_{latt} of $MgSiO_3$ bdg estimated by Ohta et al. (2012). Purple broken line is the κ_{latt} of $MgSiO_3$ bdg estimated by calculation (Ammann et al., 2014). Black broken lines show a suggested CMB temperature of 3700 K from high-pressure experiments (Tateno et al., 2009).

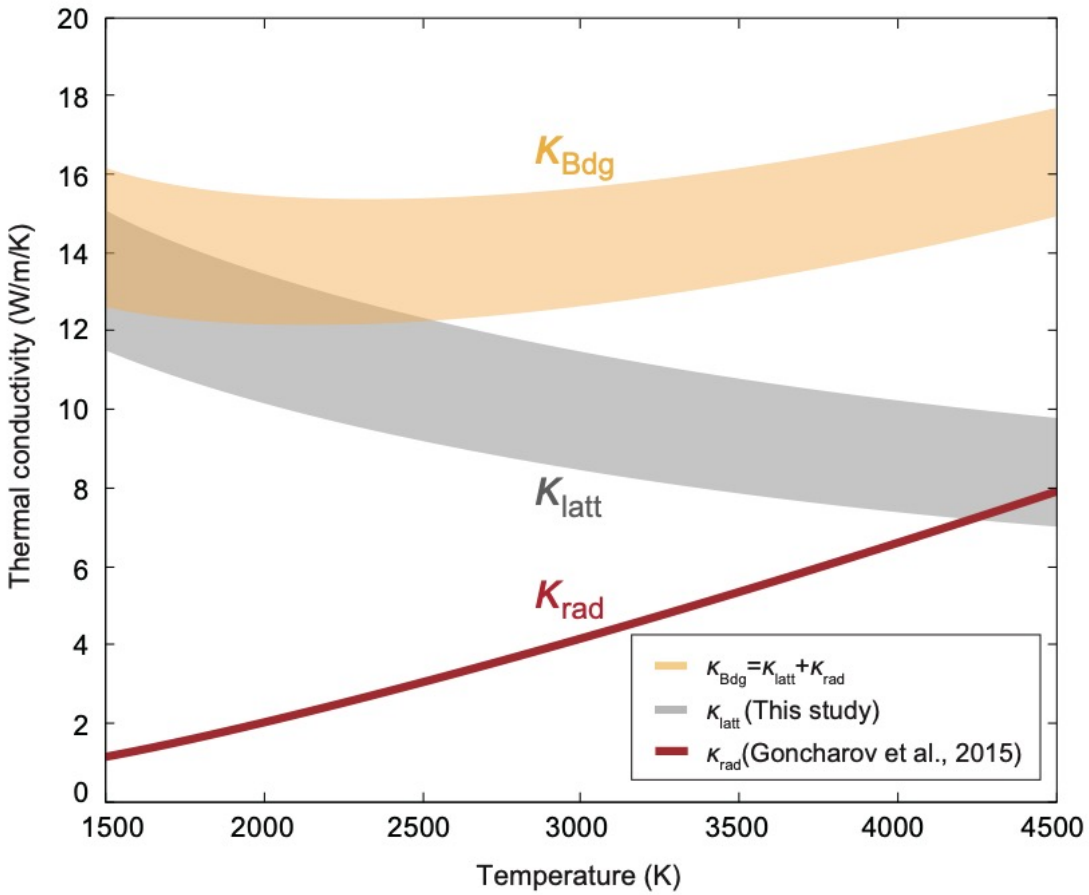

Fig. 2-6. Thermal conductivity of Fe and Al-bearing bdg at CMB pressure as a function of temperature. Gray band is the lattice thermal conductivity of $Mg_{0.832}Fe_{0.209}Al_{0.060}Si_{0.916}O_3$ bdg obtained from this study. Red line indicates the radiative thermal conductivity of $Mg_{0.94}Fe_{0.06}SiO_3$ at 46 GPa (Goncharov et al., 2015). Orange band shows total thermal conductivity of bdg (the sum of gray and red curves).

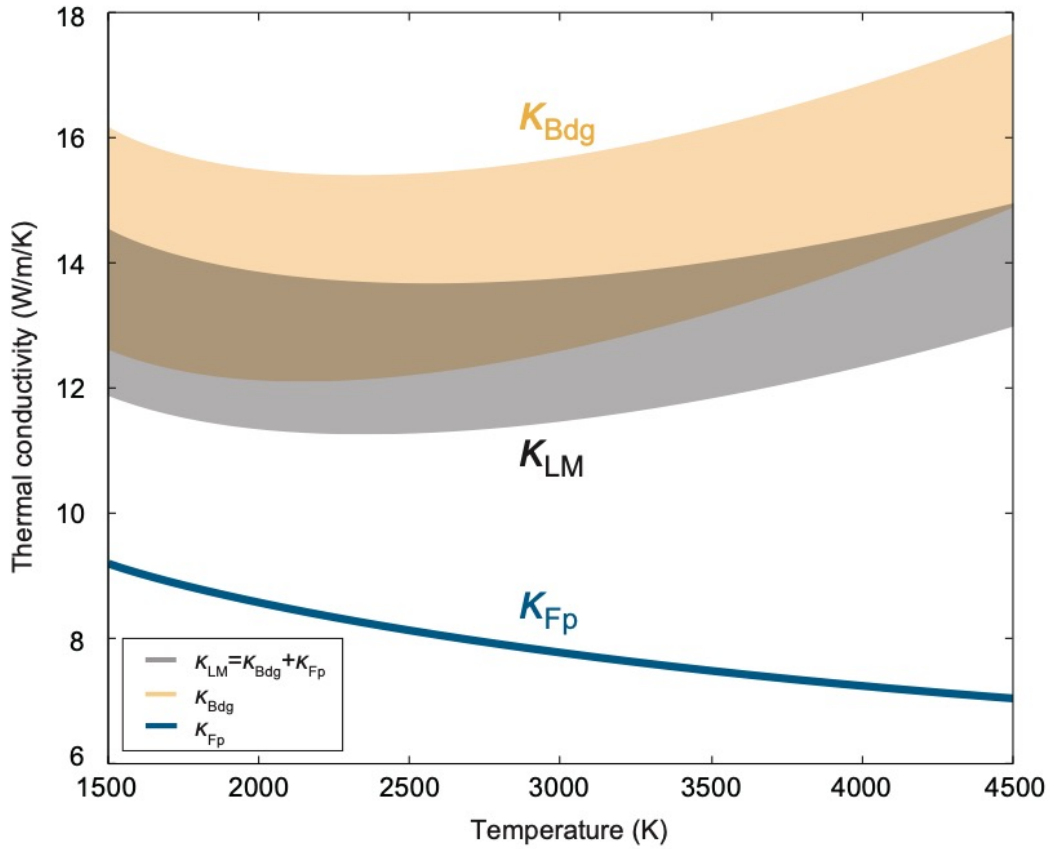

Fig. 2-7. Thermal conductivity of pyrolitic mantle at CMB pressure as a function of temperature. Orange band and blue curve are total thermal conductivity of bdg and fp respectively, gray curve is the total thermal conductivity of pyrolitic mantle. We used the value of total thermal conductivity of fp as the value of lattice thermal conductivity (Ohta et al., 2017), in which radiative thermal conductivity is thought to be negligibly small (Lobanov et al., 2016; Kavner and Rainey, 2016).

Chapter 3. Experimental evidence of the low-spin state Fe in lower mantle bridgmanite: I. compressibility of (Fe,Al)-bearing bridgmanite

This chapter was updated from the published article as *"Anomalous compressibility in (Fe,Al)-bearing bridgmanite: implications for the spin state of iron"* by **Yoshiyuki Okuda**, Kenji Ohta, Ryosuke Sinmyo, Kei Hirose, Saori I. Kawaguchi, Yasuo Ohishi (2020) Physics and Chemistry of Minerals, 47, 40. https://doi.org/10.1007/s00269-020-01109-3

Abstract

The valence and spin states of Fe in (Fe,Al)-bearing bridgmanite (bdg) affect its physical properties, which is important for the interpretation of geophysical observations. Currently, tens of studies on the compressibility and spin states of Fe-bearing bdg have been reported. A consensus is that Fe-bearing bdg shows spin transition, which affects its elastic parameters. However, there is a conflict between reports on the compressibility and spin states of (Fe,Al)-bearing bdg in experiments using samples pre-synthesized in a multi-anvil apparatus (MA), and samples directly synthesized in a diamond anvil cell (DAC). There are no reports showing evidence of spin transition of Fe in compression experiments using (Fe,Al)-bearing bdg samples pre-synthesized in a MA, while those synthesized at relatively high pressure (at least above 45 GPa) in a DAC all exhibited the spin transition. Here we performed synchrotron X-ray diffraction measurements on $Mg_{0.85}Fe_{0.09}Al_{0.21}Si_{0.86}O_3$ and $Mg_{0.85}Fe_{0.14}Al_{0.05}Si_{0.96}O_3$ bdg synthesized at relatively high pressure in a laser-heated DAC from amorphous starting material up to 47 and 56 GPa respectively at room temperature. The obtained pressure (*P*)-lattice volume *(V)* relations show noticeable softening at 22−30 GPa and 35−45 GPa respectively, which is probably due to the spin transition of Fe. Combining our results and previous reports, we suggest that the lower mantle bdg is capable of containing low-spin Fe^{3+}, which questions the general view. Such a transition changes density and may affect the physical properties of bridgmanite

such as thermal conductivity and iron partitioning coefficient, thus having profound implications for mantle dynamics, and the chemical composition of the Earth.

3.1. Introduction

Bridgmanite (bdg), (Fe,Al)-bearing $MgSiO_3$ perovskite, is accepted to be the most abundant mineral in the Earth's lower mantle. Bdg in the pyrolitic lower mantle is likely to contain ~10 mol% for both Fe and Al (e.g., Irifune et al. 2010; Sinmyo et al. 2011), while bdg in the subducted MORB is suggested to contain larger amounts of Fe and Al such as 30.6 mol% and 29.4 mol% at 60 GPa, respectively (Hirose et al. 2005). Previous experimental and theoretical results show that the valence and spin state of Fe are affected by iron distribution to different crystallographic sites in bdg (for review, see Lin et al. 2013). A shared view of the distribution of Fe in bdg is that both Fe^{2+} and Fe^{3+} can be incorporated, in which Fe^{2+} only exists in the large pseudo-dodecahedral Mg^{2+} site (A-site), while Fe^{3+} mainly enters the A-site, but can also occupy the relatively small octahedral Si^{4+} site (B-site). Speciation of Fe is the key factor when discussing the spin transition of bdg; it has been shown that only the Fe^{3+} in the octahedral B-site would undergo spin transition from high spin (HS) to low spin (LS) state at the lower mantle *P-T* conditions. Note that there is a discrepancy in the onset pressure and pressure range of the transition, which is often attributed to the difference in chemical composition of bdg or the difference in experimental protocols in each study (e.g., Badro et al. 2004; Li et al. 2004; Jackson et al. 2005; Stackhouse et al. 2007; Catalli et al. 2010; Hsu et al. 2011; Hummer and Fei, 2012; Lin et al. 2012; Sinmyo et al. 2017).

Fe^{3+} content and its speciation in bdg are strongly affected by Al content due to the charge-coupled substitution, $Mg^{2+}_A + Si^{4+}_B \Leftrightarrow Fe^{3+}_A + Al^{3+}_B$ (Miyajima et al. 2004;

Vanpeteghem et al. 2006; Glazyrin et al. 2014). Therefore, study of the spin state of Fe in (Fe,Al)-bearing bdg is very important for determining the speciation and spin state of Fe in the actual lower mantle bdg, though previous reports are scarce compared to that on Fe-bearing bdg. The previously reported SMS results on a compressed single crystal sample pre-synthesized in a multi-anvil press (MA) never show evidence of LS-Fe^{3+} (Ballaran et al. 2012; Potapkin et al. 2013; Glazyrin et al. 2014; Ismailova et al. 2016; Lin et al. 2016; Mao et al. 2017)—which is also supported by theoretical studies (Hsu et al. 2012; Mohn & Trønnes, 2016)—implying that bdg in the Earth's lower mantle should predominantly contain Fe^{3+} in the A-site (i.e., absence of spin transition of Fe in lower mantle bdg). In contrast, the other (Fe,Al)-bearing bdg samples all showed the spin transition of octahedral Fe^{3+} (Catalli et al. 2011; Fujino et al. 2012; Zhu et al. 2020) (see Tables 3-1, 3-3). Note that Al-bearing hiroseite, a Fe endmember of perovskite, was reported to show no evidence of spin transition (Dorfman et al. 2020), though the $Fe^{3+}/\Sigma Fe$ ratio of the sample was lower than 10%. The LS-fraction of Fe^{3+} confirmed by SMS studies on multigrain bridgmanite samples pre-synthesized in a MA show relatively low ratio of ~5−20% (Kupenko et al. 2015; Zhu et al. 2020), where those synthesized in a DAC were reported to be ~40% (Catalli et al. 2011). Fujino et al. (2012) attributed these inconsistent results to a redistribution of Fe3+ from the A site to the B site by thermal annealing:

$$Fe^{3+}_{A,HS}+Al^{3+}_{B} \Leftrightarrow Al^{3+}_{A}+Fe^{3+}_{B,LS}. \quad (3\text{-}1)$$

However, the later experimental studies (Potapkin et al. 2013; Glazyrin et al. 2014) and theoretical studies (Hsu et al. 2012; Mohn & Trønnes, 2016) denied this hypothesis. The very recent study by Zhu et al. (2020) proposed that the kinetic barrier of the cation exchange Eq. (3-1) is large, which can explain the invisible LS-Fe^{3+} in the previous studies (Ballaran et al. 2012; Potapkin et al. 2013; Glazyrin et al. 2014; Ismailova et al. 2016; Lin et al. 2016; Mao et al. 2017).

X-ray diffraction (XRD) measurement is an indirect but convenient way to investigate the occurrence of spin transition of Fe in bdg. Experimental and theoretical studies have shown that the spin transition of Fe^{3+} in bdg accompanied a gradual reduction in unit cell volume (V), yielding "softening"; in other words, reduction in bulk modulus (K) (Hsu et al. 2011; Tsuchiya and Wang 2013; Mao et al. 2015; Liu et al. 2018). The XRD measurements using (Fe,Al)-bearing bdg samples synthesized in a MA, i.e., those synthesized at relatively low pressure, have never shown such P-V relation anomalies (Fujino et al. 2012; Boffa Ballaran et al. 2012; Glazyrin et al. 2014; Mao et al. 2017; Ismailova et al. 2016; Okuda et al. 2017; Zhu et al. 2020) (see Table 3-2 for summary). Zhu et al. (2020) showed that relatively sensitive probes of SMS and XES were able to detect the LS-Fe^{3+}, but the relatively poor XRD could not. The authors attributed their probe-dependent SMS+XES and XRD results to the gradual occurrence of Eq. (3-1) along compression and thermal annealing. In contrast, XRD measurements using bdg samples synthesized in a DAC, i.e., those synthesized at relatively high pressure, show anomalous compressibility (Nishio-Hamane et al. 2008; Catalli et al. 2011; Okuda et al. 2019). A two-dimensional compilation of previous

studies visualizes the above (Table 3-3). The kinetic barrier of studies located in the 1st quadrant in Table 3-3 should be different from those in the 2nd and 3rd quadrants since a direct synthesis of bdg at high-P from the amorphous phase does not require Eq. (3-1) to accommodate LS-Fe^{3+} in B-site, which may explain the observed high LS-Fe^{3+} fraction in Catalli et al. (2011). However, so far there are relatively few reports on studies located in the 1st quadrant, calling for additional examination. Here we report the compressibility of (Fe,Al)-bearing bdg synthesized directly from the amorphous phase at relatively high pressure in a DAC. Our obtained compressibility of bdg experienced noticeable softening, which indicates the presence of the pressure-induced spin transition of Fe. Our results are consistent with the trend that bdg synthesized at high-P directly in a DAC shows a spin transition (Nishio-Hamane et al. 2008; Catalli et al. 2011; Okuda et al. 2019). This supports the suggested large kinetic barrier hypothesis (Zhu et al. 2020), which can explain the conflicting results among experiments using (Fe,Al)-bearing bdg samples synthesized in a MA and in a DAC.

3.2. Experimental Methods

We performed *in-situ* XRD measurements of (Fe,Al)-bearing bdg with two chemical compositions: $Mg_{0.85}Fe_{0.09}Al_{0.21}Si_{0.86}O_3$ (gF9A21), the same composition as was used in Okuda et al. (2019), and $Mg_{0.85}Fe_{0.14}Al_{0.05}Si_{0.96}O_3$ (gF14A5), up to 47 and 56 GPa respectively, and 300 K using a laser-heated DAC (Table 3-4).

Synthesis of gel-state starting material gF9A21 is described in detail in Okuda et al. (2019). Gel-state starting material of gF14A5 was dehydrated at 1000 K in a H_2-CO_2 gas-mixing furnace. Oxygen fugacity was controlled slightly above the iron-wüstite buffer. The chemical composition of the starting gel sample was determined by means of Electron Dispersive Spectroscopy (EDS) as $Mg_{0.85(7)}Fe^{2+}_{0.11(1)}Fe^{3+}_{0.03(1)}Al_{0.05(1)}Si_{0.96(8)}O_3$, of which the valence state was determined according to charge balance (Table S3-1). Note the Al excess composition compared to Fe^{3+} content. Gold was sputtered on both sides of the sample to act as a pressure marker and laser absorber to heat the sample homogeneously and thus to avoid chemical segregation of the starting material during laser heating (Sinmyo and Hirose 2010).

Synchrotron XRD measurements were carried out at BL10XU, SPring-8 (Hirao et al. 2020). We used an imaging plate to obtain the XRD pattern. The gel materials covered with gold were loaded into the sample chamber of the DAC with a pressure transmitting medium of NaCl or Al_2O_3. In each run, rhenium was used as a gasket, and 300 μm culet-size diamond anvils were used. Gel samples were then compressed to the pressure where bdg phase is stable. Subsequently, double-sided laser heating was conducted to synthesize bdg with a couple of fiber lasers. We used beam shapers to reduce radial temperature gradients in the sample. These convert a beam with a Gaussian intensity distribution to the one with a flat-top distribution. At each synthesis, the gel sample was heated to ~2000 K for an hour. All the compressibility data were obtained under decompression. Pressure was calibrated from the unit cell volume of gold based on an equation of state (EoS) of gold (Tsuchiya 2003).

3.3. Results

We collected the XRD patterns of gF9A21 and gF14A5 bdg synthesized in a DAC from the amorphous gel starting material. We confirmed the synthesis of bdg and the minor amount of stishovite in each run (Fig. 3-1). The amount of stishovite did not exceed 10% in volume (see supplemental material S3-1). Chemical compositions of the recovered gF9A21 sample in run #1 using EDS was obtained as $Mg_{0.82(7)}Fe_{0.07(1)}Al_{0.22(2)}Si_{0.89(7)}O_3$, which is consistent with the composition of the starting gel material. Thus, we observe that the composition of the synthesized bdg samples do not differ from that of the starting gel sample. Also, we could not find any Fe segregation, indicating that the Soret effect was minimal in our experiments (Fig. 3-2).

Interestingly, both collected *P*-*V* relations on gF9A21 and gF14A5 exhibited noticeable softening at the pressure intervals of 22 to 30 GPa and 35 to 42 GPa respectively, which are similar trends to that of $Mg_{0.85}Fe_{0.09}Al_{0.21}Si_{0.86}O_3$ bdg (Okuda et al. 2019) and $(Mg_{0.46}Fe^{3+}_{0.53})(Si_{0.49}Fe^{3+}_{0.51})O_3$ (Liu et al. 2018) (Fig. 3-3). Fig. 3-4 shows the pressure dependences of the obtained lattice constants *a*, *b* and *c* with the previous reports for $Mg_{0.88}Fe_{0.13}Al_{0.11}Si_{0.88}O_3$ (Catalli et al. 2011), $(Mg_{0.46}Fe^{3+}_{0.53})(Si_{0.49}Fe^{3+}_{0.51})O_3$ (Liu et al. 2018) and $MgSiO_3$ bdg (Boffa Ballaran et al. 2012). Compressional behavior of *b* and *c*-axes in both of our bdg samples shows a

similar trend to those reported in Liu et al. (2018); both axes of gF9A21 and gF14A5 bdg experienced noticeable softening at the pressure ranges of 22 GPa to 30 GPa and 35 to 42 GPa, respectively. In contrast, *a*-axis in both gF9A21 and gF14A5 bdg showed a clear softening, while *a*-axis reported in Liu et al. (2018) showed a minimal softening (Fig. 3-4). Note that all our lattice constants were higher than the values for $MgSiO_3$ (Boffa Ballaran et al. 2012), which is a natural result because of the incorporation of an Fe atom larger than Mg and Si; the substitution of larger Al with Si should also expand the *V* of bdg. As above, each obtained axis showed a discontinuous change in identical pressure ranges of 22 to 30 GPa and 35 to 45 GPa respectively, yielding the anomalous softening of *V* (Fig. 3-3).

3.4. Discussion

3.4.1. The effect of uniaxial compression

Based on the lattice theory, uniaxial stress on a mineral causes a relative shift among its different diffraction lines. Since a solid pressure medium was used in this study, we offer quantitative analyses of the effect of uniaxial compression on our compressibility results. In order to estimate the uniaxial stress in our bdg sample, we calculated the *St* value, a product of the elastic anisotropy *S* and the uniaxial stress component *t*, can be used as an indicator of the magnitude of such uniaxial stress (e.g., Shim et al. 2000; Sata et al. 2002), of Au sputtered on both sides of the sample from the

diffraction of Au (Fig. 3-5). The measured lattice constant a_m can be written as the following (Singh and Takemura 2001):

$$a_m(hkl) = M_0 + M_1\{3(1 - 3\sin^2\theta)\Gamma(hkl)\}, \quad (3\text{-}2)$$

$$M_0 = a_p\left\{1 + \left(\frac{\alpha t}{3}\right)(1 - 3\sin^2\theta)[S_{11} - S_{12} - (2G_V)^{-1}(1 - \alpha^{-1})]\right\}, \quad (3\text{-}3)$$

$$M_1 = -a_p\alpha t S/3, \quad (3\text{-}4)$$

$$\Gamma(hkl) = (h^2k^2 + k^2l^2 + l^2h^2)/(h^2 + k^2 + l^2)^2, \quad (3\text{-}5)$$

$$S = S_{11} - S_{12} - S_{44}/2, \quad (3\text{-}6)$$

where a_p is the lattice parameter under hydrostatic pressure, S_{ij} is the single-crystal elastic compliance, G_V is the shear modulus of the polycrystalline aggregate under the assumption of strain continuity across the grain boundaries, α is the ratio of uniform stress model and uniform strain model ($0.5<\alpha<1$). By assuming $M_0 \sim a_p$, we can obtain the *St* value from Eq. (3-4):

$$St \sim -3M_1/(\alpha M_0), \quad (3\text{-}7)$$

where M_0 and M_1 were obtained from fitting the slope of a Γ plot, a plot $a_m(hkl)$ versus $3(1\text{-}3\sin^2\theta)\Gamma(hkl)$. We used (111), (200), (220) and (311) reflections to obtain each of the four plots (Fig. 3-6). Note that we excluded a certain reflection which overlapped with peaks of samples or the pressure medium. Also, by using α=1 (uniform stress model), we estimated the *St* values. Compression at high-*P* using a solid pressure medium without annealing tends to enhance the uniaxial stress, which *St* value can be greater than 0.1 (e.g., KCl before annealing at 200 GPa in Tateno et al. 2019). Shim et

al. (2000) proposed a criterion: an *St* value less than ~0.005 can be treated as a quasihydrostatic condition. Our obtained *St* value did not greatly deviate from 0.005, indicating that the effect of uniaxial stress on obtained compressibility is small. Here, we could choose the distance between the imaging plate and the sample of 350 mm and 450 mm in the system in BL10XU, SPring-8. In run #1 on gF9A21, the XRD patterns were collected with the distance of 450 mm. This increased distance enables us to obtain XRD peaks from a wider 2-theta range. On the other hand, in run #1 on gF14A5 bdg, the distance between the imaging plate and the sample was 350 mm. With this closer distance, we can get a clearer XRD pattern than the 450 mm. However, since the collectible 2-theta range was narrower, we could not obtain the Au peaks from 220 and 311. As a result, unfortunately, we could not calculate the *St* value of Au used in gF14A5 bdg. Still, since the pressure medium we used in run #1 on gF14A5 bdg was NaCl, which is accepted to be softer than the Al_2O_3 powder used in run #1 on gF9A21, we believe that the effect of uniaxial stress on the obtained compressibility of gF14A5 bdg is also small. Given the reproducibility of the anomalous volume reduction observed in Okuda et al. (2019) and in our study though using different pressure media, it is difficult to explain the anomalous *P*-*V* relation only by the effect of uniaxial stress. Moreover, the pressure interval of softening seen in gF14A5 was way above the akimotoite-bridgmanite transition pressure, indicating that the observed softening in *V* is not a volumetric expansion due to metastable bdg in the akimotoite stability zone.

3.4.2. Obtained anomalous P-V relations

Assuming that the octahedron is rigid, the bond length of the octahedron [*B*-*X*] can be expressed with lattice constants as follows (e.g., O'Keeffe and Hyde 1977):

$$[B - X] = bc/4a. \quad (3\text{-}8)$$

Spin transition of Fe^{3+} in the octahedral B-site should affect the *P*-*V* relations and [*B*-*X*] because of the changing ionic radius of Fe^{3+} across the spin transition. Our bdg samples show abnormal changes in [*B*-*X*], which is similar to the trend seen in Liu et al. (2018) (Fig. 3-4). Although the direct observation of the spin state of Fe from SMS data on our bdg samples is impossible because the Fe in our samples was not ^{57}Fe-enriched, together with the observed softening in *V* of our bdg sample—which is similar to the previous reports on compressibility of Fe^{3+}-bearing bdg (Hsu et al. 2011; Tsuchiya and Wang 2013; Mao et al. 2015; Liu et al. 2018)—it is appropriate to attribute the anomalous reduction in *V* in our (Fe,Al)-bearing bdg sample to the spin transition of Fe.

When the spin transition occurs under decompression and at room-*T*, LS-Fe^{3+} changes to HS-Fe^{3+} in the B-site, which is suggested to be energetically less preferable (Hsu et al. 2012) due to the increase of ionic radius of Fe^{3+} as much as 12% (Shannon 1976). The full width at half maximum (FWHM) of the obtained XRD peaks of bdg samples showed a sudden increase at the pressure range where softening in *V* was observed (Fig. 3-7). The FWHM of the XRD peaks reflects not only the sample size, but also distortion (and/or structural defects) and crystallinity, so we attributed the broadening of XRD peaks from our bdg samples to the distortion of bdg crystal due to the HS-Fe^{3+} in B-site; the HS-Fe^{3+} in the B-site having a much larger ionic radii should

excessively expand the site and thus lead to the over-expanded unit-cell volume of bridgmanite. We believe that the observed larger volume of gF9A21 compared to gF14A5 at low-pressure regime, which contradicts itself based on the Fe content, is due to the above.

The pressure of the anomalous decompression behavior and the broadening in FWHM of bdg peaks in our gF14A5 sample was from 43 GPa, while that of gF9A21 was from 30 GPa (this study; Okuda et al. 2019). This indicates a compositional dependence on the spin transition pressure of Fe in bdg, which was suggested in previous studies (e.g., Sinmyo et al. 2017).

3.4.3. Explaining compelling reports on the spin transition of Fe in bdg

It is important to reiterate that the spin transition of the B-site Fe^{3+} and/or anomalous *P*-*V* relation in (Fe,Al)-bearing bdg has not been sufficiently observed in experiments using a bdg sample synthesized at relatively low-*P* (Boffa Ballaran et al. 2012; Potapkin et al. 2013; Glazyrin et al. 2014; Lin et al. 2016; Mao et al. 2017; Okuda et al. 2017), but has observed in bdg samples synthesized at relatively high-*P* (Nishio-Hamane et al. 2008; Catalli et al. 2011; Okuda et al. 2019). Note that, although Kupenko et al. (2015) showed that B-site Fe^{3+} in $(Mg_{0.832}Fe^{2+}_{0.136}Fe^{3+}_{0.073})(Al_{0.060}Si_{0.916})O_3$ above 40 GPa with annealing exhibits spin transition, the amount of LS Fe^{3+} still did not exceed ~5% in all of their experiments. The interesting exceptions are Fujino et al. (2012) and Zhu et al. (2020), both of which detected LS-Fe^{3+} using bdg samples synthesized at relatively low-*P*. If spin transition of

Fe occurs in bdg pre-synthesized at 24−26 GPa along further compression and annealing, Fe^{3+} in the A-site requires relocation to the B-site. The enhanced cation exchange between Al^{3+} and Fe^{3+} (Eq. 3-1) at high-*T* was suggested by Fujino et al. (2012), which was first denied by both experimental studies (Potapkin et al. 2013; Glazyrin et al. 2014) and theoretical calculations (Hsu et al. 2012; Mohn & Trønnes, 2016). Very recently, Zhu et al. (2020) showed that the kinetic barrier of the cation exchange Eq. (3-1) can be large, which indicates the difficulty in achieving an equilibrium of the site distribution of Fe^{3+} even with performing thermal annealing within the experimental time scale. The absence of LS-Fe^{3+} in the previous studies located in the 3rd quadrants in Table 3-3 (Boffa Ballaran et al. 2012; Potapkin et al. 2013; Glazyrin et al. 2014; Lin et al. 2016; Mao et al. 2017; Okuda et al. 2017) can be explained by the large kinetic barrier of Eq. (3-1) or merely the lack of thermal annealing (see Tables 3-1, 3-2). Our results suggest that (Fe,Al)-bearing bdg synthesized at relatively high-*P* can contain LS-Fe^{3+} in B-site, which is consistent with the previous studies located in the 1st quadrant in Table 3-3 (Nishio-Hamane et al. 2008; Catalli et al. 2011; Okuda et al. 2019). The bdg samples in the present study and the previous studies located in the 1st quadrant in Table 3-3 were all directly synthesized from gel- or glass-state amorphous starting material, which do not require cation exchange Eq. (3-1) when accommodating LS-Fe^{3+}, of which the kinetic barrier is suggested to be large (Zhu et al. 2020). The compelling results between bdg synthesized in a MA and a DAC can be sufficiently explained by the difference in kinetic barrier starting from amorphous and crystalline phases. We note that a spin transition in

amorphous starting material may have also contributed to the accommodation of LS-Fe^{3+} and the detectable anomalous decompression behavior. Nomura et al. (2011), Murakami et al. (2014) and Dorfman et al. (2016) demonstrated that Fe-bearing amorphous silicate glass undergoes a spin transition, although note that there are studies providing conflicting results (Mao et al. 2014; Prescher et al. 2014; Solomatova et al. 2017; Maeda et al. 2017). Taking into account that all the previous studies reporting spin transition of Fe or anomalous compressibility of (Fe,Al)-bearing bdg were synthesized from amorphous starting materials (Nishio-Hamane et al. 2008; Catalli et al. 2011; Okuda et al. 2019; see Tables 3-1, 3-2), spin transition of Fe in the amorphous starting materials, which makes the ionic radii of Fe smaller, may have driven a certain amount of Fe into entering the B-site during the timescale of the synthesis of the bdg sample.

Our results indicate that a difference in chemical composition could be one of the main factors for changing the pressure range of the spin transition of Fe in bdg. Also, in experimental studies, we accentuate the importance of synthesizing (Fe,Al)-bearing bdg samples at *high-P* to observe low-spin Fe. Still, the present result is based on XRD measurements, which is an indirect probe for spin state of Fe. In order to better understand the spin state of Fe in lower mantle bdg, a relatively direct probe such as synchrotron Mössbauer spectroscopy on (Fe,Al)-bearing bdg samples synthesized at *high-P* can further clarify this controversial issue, which would be given in the next Chapter.

3.5. Conclusions

We report the compressibility of $Mg_{0.85}Fe_{0.09}Al_{0.21}Si_{0.86}O_3$ and $Mg_{0.85}Fe_{0.14}Al_{0.05}Si_{0.96}O_3$ bdg synthesized in a laser-heated DAC up to 47 and 56 GPa, respectively. The obtained compressibility showed obvious softening, which we attributed to the effect of spin transition of Fe. Such reduction in V was previously reported in experiments on Fe^{3+}-bearing bdg (Mao et al. 2015; Liu et al. 2018) and also predicted in theoretical calculations (Hsu et al. 2011; Tsuchiya and Wang 2013), but has not been reported in (Fe,Al)-bearing bdg samples synthesized in a MA (Boffa Ballaran et al. 2012; Glazyrin et al. 2014; Ismailova et al. 2016; Mao et al. 2017; Okuda et al. 2017; Zhu et al. 2020). Our finding questions the recent consensus that bdg in the lower mantle would not undergo spin transition and suggests that the Fe in bdg in the deep lower mantle is in the LS state. Our results support that the spin transition pressure of Fe in bdg depends on its chemical composition. Since the onset pressure of the spin transition of (Fe,Al)-bearing bdg is still highly under debate, with many arguing a pressure that falls in the range of ~15−50 GPa, a further systematical investigation focused on chemical composition using a more direct probe for spin state is required for a better understanding of that of Fe in the Earth's lower mantle.

3.6. References

Badro J, Rueff J-P, Vankó G, Monaco G, Fiquet G, Guyot F (2004) Electronic transitions in perovskite: possible nonconvecting layers in the lower mantle. Science 305: 383–386.

Ballmer MD, Houser C, Hernlund JW, Wentzcovitch RM, Hirose K (2017) Persistence of strong silica-enriched domains in the Earth's lower mantle. Nat Geosci 10: 236–240.

Boffa-Ballaran T, Kurnosov A, Glazyrin K, Frost DJ, Merlini M, Hanfland M, Caracas R (2012) Effect of chemistry on the compressibility of silicate perovskite in the lower mantle. Earth Planet Sci Lett 333–334: 181–190.

Catalli K, Shim SH, Prakapenka VB, Zhao JY, Sturhahn W, Chow P, Xiao YM, Liu HZ, Cynn H, Evans WJ (2010) Spin state of ferric iron in $MgSiO_3$ perovskite and its effect on elastic properties. Earth Planet Sci Lett 289: 68–75.

Catalli K, Shim SH, Dera P, Prakapenka VB, Zhao JY, Sturhahn W, Chow P, Xiao YM, Cynn H, Evans WJ (2011) Effects of the Fe^{3+} spin transition on the properties of aluminous perovskite-New insights for lower-mantle seismic heterogeneities. Earth Planet Sci Lett 310: 293–302.

Dorfman SM, Dutton SE, Potapkin V, Chumakov AI, Rueff J-P, Chow P, Xiao Y, Cava RJ, Duffy TS, McCammon C, Gillet P (2016) Electronic transitions of iron in almandine-composition glass to 91 GPa. Am Mineral 101: 1659–1667.

Dorfman SM, Potapkin V, Lv M, et al (2020) Effects of composition and pressure on electronic states of iron in bridgmanite. Am Mineral 105:1030–1039.

Fujino K, Nishio-Hamane D, Seto Y, Sata N, Nagai T, Shinmei T, Irifune T, Ishii H, Hiraoka N, Cai YQ, Tsuei KD (2012) Spin transition of ferric iron in Al-bearing Mg-perovskite up to 200 GPa and its implication for the lower mantle. Earth Planet Sci Lett 317: 407–412.

Glazyrin K, Boffa Ballaran TB, Frost DJ, McCammon C, Kantor A, Merlini M, Hanfland M, Dubrovinsky L (2014) Magnesium silicate perovskite and effect of iron oxidation state on its bulk sound velocity at the conditions of the lower mantle. Earth Planet Sci Lett 393: 182–186.

Hirao N, Kawaguchi SI, Hirose K, Shimizu K, Ohtani E, Ohishi Y (2020) New developments in high-pressure X-ray diffraction beamline for diamond anvil cell at SPring-8. Matter Radiat Extremes 5: 018403.

Hirose K, Takafuji N, Sata N, Ohishi Y (2005) Phase transition and density of subducted MORB crust in the lower mantle. Earth Planet Sci Lett 237: 239–251.

Hsu H, Blaha P, Cococcioni M, Wentzcovitch RM (2011) Spin-state crossover and hyperfine interactions of ferric iron in $MgSiO_3$ perovskite. Phys Rev Lett 106: 118501.

Hsu H, Yu YG, Wentzcovitch RM (2012) Spin crossover of iron in aluminous $MgSiO_3$ perovskite and post-perovskite. Earth Planet Sci Lett 359–360: 34–39.

Hummer DR, Fei Y (2012) Synthesis and crystal chemistry of Fe^{3+}-bearing $(Mg,Fe^{3+})(Si,Fe^{3+})O_3$ perovskite. Am Mineral 97: 1915–1921.

Irifune T, Shinmei T, McCammon CA, Miyajima N, Rubie DC, Frost DJ (2010) Iron partitioning and density changes of pyrolite in Earth's lower mantle. Science 327: 193–195.

Ismailova L, Bykova E, Bykov M, Cerantola V, McCammon C, Ballaran TB, Bobrov A, Sinmyo R, Dubrovinskaia N, Glazyrin K, Liermann HP, Kupenko I, Hanfland M, Prescher C, Prakapenka V, Svitlyk V, Dubrovinsky L (2016) Stability of Fe, Al-bearing bridgmanite in the lower mantle and synthesis of pure Fe-bridgmanite. Sci Adv 2: e1600427.

Jackson JM, Sturhahn W, Shen GY, Zhao JY, Hu MY, Errandonea D, Bass JD, Fei YW (2005) A synchrotron Mössbauer spectroscopy study of $(Mg,Fe)SiO_3$ perovskite up to 120 GPa. Am Mineral 90: 199–205.

Kudoh Y, Prewitt CT, Finger LW, Darovskikh A, Ito E (1990) Effect of iron on the crystal structure of $(Mg,Fe)SiO_3$ perovskite. Geophys Res Lett 17: 1481–1484.

Kupenko I, McCammon C, Sinmyo R, Cerantola V, Potapkin V, Chumakov AI, Kantor A, Rüffer R, Dubrovinsky L (2015) Oxidation state of the lower mantle: in situ observations of the iron electronic configuration in bridgmanite at extreme conditions. Earth Planet Sci Lett 423: 78–86.

Li J, Struzhkin VV, Mao H-K, Shu J, Hemley RJ, Fei Y, Mysen B, Dera P, Prakapenka VB, Shen G (2004) Electronic spin state of iron in lower mantle perovskite. Proc Natl Acad Sci USA 101(39): 14027–14030.

Lin JF, Alp EE, Mao Z, Inoue T, McCammon C, Xia YM, Chow P, Zhao JY (2012) Electronic spin states of ferric and ferrous iron in the lower mantle silicate perovskite Am Mineral 97: 592–597.

Lin JF, Speziale S, Mao Z, Marquardt H (2013) Effects of the electronic spin transitions of iron in lower mantle minerals: Implications for deep mantle geophysics and geochemistry. Rev Geophys 51: 244–275.

Lin JF, Mao Z, Yang J, Liu J, Xiao Y, Chow P, Okuchi T (2016) High-spin Fe^{2+} and Fe^{3+} in single-crystal aluminous bridgmanite in the lower mantle. Geophys Res Lett 43: 6952–6959.

Liu J, Dorfman SM, Zhu F, Li J, Wang Y, Zhang D, Xiao Y, Bi W, Ercan Alp E (2018) Valence and spin states of iron are invisible in Earth's lower mantle. Nat Commun 9: 1284.

Mao Z, Lin JF, Yang J, Inoue T, Prakapenka VB (2015) Effects of the Fe^{3+} spin transition on the equation of state of bridgmanite. Geophys Res Lett 42: 4335–4342.

Mao Z, Wang F, Lin JF, Fu S, Yang J, Wu X, Okuchi T, Tomioka N, Prakapenka VB, Xiao Y, Chow P (2017) Equation of state and hyperfine parameters of high-spin bridgmanite in the Earth's lower mantle by synchrotron X-ray diffraction and Mössbauer spectroscopy. Am Mineral 102: 357–368.

Miyajima N, Langenhorst F, Frost DJ, Yagi T (2004) Electron channeling spectroscopy of iron in majoritic garnet and silicate perovskite using a transmission electron microscopy. Phys Earth Planet Inter 143: 601–609.

Mohn CE, Trønnes RG (2016) Iron spin state and site distribution in $FeAlO_3$-bearing bridgmanite. Earth Planet Sci Lett 440: 178–186.

Murakami M., Goncharov AF, Hirao N, Masuda R, Mitsui T, Thomas T-M, Bina CR (2014) High-pressure radiative conductivity of dense silicate glasses with potential implications for dark magmas. Nat Commun 5: 5428.

Nishio-Hamane D, Seto Y, Fujino K, Nagai T (2008) Effect of $FeAlO_3$ incorporation into $MgSiO_3$ on the bulk modulus of perovskite. Phys Earth Planet Inter 166: 219–225.

Nomura R, Ozawa H, Tateno S, Hirose K, Hernlund J, Muto S, Ishii H, Hiraoka N (2011) Spin crossover and iron-rich silicate melt in the Earth's deep mantle. Nature 473: 199–202.

O'Keeffe M, Hyde BG (1977) Some structures topologically related to cubic perovskite (*E*21) ReO3 (*D*09) and Cu3Au (*L*12). Acta Cryst B33: 3802–3813.

Okuda Y, Ohta K, Yagi T, Sinmyo R, Wakamatsu T, Hirose K, Ohishi Y (2017) The effect of iron and aluminum incorporation on lattice thermal conductivity of bridgmanite at the Earth's lower mantle. Earth Planet Sci Lett 474: 25–31.

Okuda Y, Ohta K, Sinmyo R, Hirose K, Yagi T, Ohishi Y (2019) Effect of spin transition of iron on the thermal conductivity of (Fe, Al)-bearing bridgmanite. Earth Planet Sci Lett 520: 188–198.

Piet H, Badro J, Nabiei F, Dennenwaldt T, Shim S-H, Cantoni M, Hébert C, Gillet P (2016) Spin and valence dependence of iron partitioning in Earth's deep mantle. Proc Natl Acad Sci USA 113: 11127–11130.

Potapkin V, McCammon C, Glazyrin K, Kantor A, Kupenko I, Prescher C, Sinmyo R, Smirnov GV, Chumakov AI, Ruffer R, Dubrovinsky L (2013) Effect of iron oxidation state on the electrical conductivity of the Earth's lower mantle. Nat Commun 4: 1427. doi: 101038/Ncomms2436.

Prescher C, Weigel C, McCammon C, Narygina O, Potapkin V, Kupenko I, Sinmyo R, Chumakov AI, Dubrovinsky D (2014) Iron spin state in silicate glass at high pressure: Implications for melts in the Earth's lower mantle. Earth Planet Sci Lett 385: 130–136.

Sata N, Shen G, Rivers ML, Sutton SR (2002) Pressure–volume equation of state of the high-pressure B2 phase of NaCl. Phys Rev B 65: 104114.

Shannon RD (1976) Revised effective ionic radii and systematic studies of interatomic distances in halides and chalcogenides. Acta Crystallogr Sect A 32: 751–767.

Shim S-H, Duffy TS, Shen G (2000) The stability and P-V-T equation of state for $CaSiO_3$ perovskite in the earth's lower mantle. J Geophys Res 105: 25955–25968.

Shim S-H, Grocholski B, Ye Y, Alp EE, Xu S, Morgan D, Meng Y, Prakapenka VB (2017) Stability of ferrous-iron-rich bridgmanite under reducing midmantle conditions. Proc Natl Acad Sci USA 114: 6468–6473.

Shukla G, Wentzcovitch RM (2016) Spin crossover in $(Mg,Fe^{3+})(Si,Fe^{3+})O_3$ bridgmanite: Effects of disorder, iron concentration, and temperature. Phys Earth Planet Inter 260: 53–61.

Singh AK, Takemura K (2001) Measurement and analysis of nonhydrostatic lattice strain component in niobium to 145 GPa under various fluid pressure-transmitting media. J Appl Phys 90: 3269–3275.

Sinmyo R, Hirose K (2010) The Soret diffusion in laser-heated diamond-anvil cell. Phys Earth Planet Inter 180: 172–178.

Sinmyo R, Hirose K, Muto S, Ohishi Y, Yasuhara A (2011) The valence state and partitioning of iron in the Earth's lowermost mantle. J Geophys Res 116: B07205.

Sinmyo R, McCammon C, Dubrovinsky L (2017) The spin state of Fe^{3+} in lower mantle bridgmanite. Am Mineral 102: 1263–1269.

Solomatova NV, Jackson J M, Sturhahn W, Rossman GR, Roskosz M (2017) Electronic environments of ferrous iron in rhyolitic and basaltic glasses at high pressure. J Geophys Res Solid Earth 122: 6306–6322.

Stackhouse S, Brodholt JP, Price GD (2007) Electronic spin transitions in iron-bearing $MgSiO_3$ perovskite. Earth Planet Sci Lett 253: 282–290.

Tsuchiya T (2003) First-principles prediction of the *P–V–T* equation of state of gold and the 660-km discontinuity in Earth's mantle. J Geophys Res 108(B10): 2462.

Tsuchiya T, Wang X (2013) Ab initio investigation on the high-temperature thermodynamic properties of Fe^{3+}-bearing $MgSiO_3$ perovskite. J Geophys Res Solid Earth 118: 83–91.

Vanpeteghem CB, Angel RJ, Ross NL, Jacobsen SD, Dobson D, Litasov KD, Ohtani E (2006) Al, Fe substitution in the $MgSiO_3$ perovskite structure: A single crystal X-ray diffraction study. Phys Earth Planet Inter 155: 96–103.

Zhu F, Liu J, Lai X, et al (2020) Synthesis, elasticity and spin state of an intermediate $MgSiO_3$ -$FeAlO_3$ bridgmanite: Implications for iron in Earth's lower mantle. J Geophys Res Solid Earth. https://doi.org/10.1029/2020JB019964.

3.7. Tables and References

Table 3-1. Previous studies on spin state of Fe in (Fe,Al)-bearing bdg using SMS and/or XES measurements.

Chemical composition	Synthesis	Sample	Method	$Fe^{3+}/\sum Fe$	Experiment Pressure (GPa)	Starting material	Synthesis Temperature (K)	Synthesis Pressure (GPa)	Spin transition of Fe^{2+} in B-site	Annealed or not	Annealed temperature (K)	Annealed time (min)	Reference
$Mg_{0.88}Fe_{0.13}Al_{0.11}Si_{0.88}O_3$	in DAC	PC	SMS	1.0	0-95	glass	2000	above 45	present	annealed (above 45 GPa)	1800-2100	7-15	Catalli et al. (2011)
$Mg_{0.85}Fe_{0.15}Al_{0.15}Si_{0.85}O_3$	MA	PC	XES	1.0	0-121	gel	1600	117	present★	annealed	1200-1400	60	Fujino et al. (2012)
*1$Mg_{0.83}Fe_{0.20}Al_{0.09}Si_{0.91}O_3$	MA	SC	SMS	0.50	0-122	OM	2073	26	-	annealed*	2000-2400	?	Potapkin et al. (2013)
*1$Mg_{0.83}Fe_{0.21}Al_{0.08}Si_{0.92}O_3$	MA	PC	SMS	0.36(5)	12-77	OM	2073	26	present#	annealed (above 39 GPa)	2000	?	Kupenko et al. (2015)
*2$Mg_{0.89}Fe_{0.12}Al_{0.11}Si_{0.89}O_3$	MA	SC	SMS+XES	0.80	0-115	OM	2023	24	-	annealed*	1800	10	Lin et al. (2016)
*2$Mg_{0.89}Fe_{0.12}Al_{0.11}Si_{0.89}O_3$	MA	SC	SMS+XES	0.80	0-110	OM	2023	24	-	-	-	-	Mao et al. (2017)
$Fe_{0.67}Al_{0.54}Si_{0.73}O_3$	in DAC	PC	SMS	0.09(9)$^{\$}$	0-76	glass	2000-2500	76	-	-	-	-	Dorfman et al. (2020)
$Mg_{0.50}Fe_{0.50}Al_{0.50}Si_{0.50}O_3$	MA	PC	SMS+XES	1.0	27-102	OM	1873	24	present★	annealed*	1300-2100	15-35	Zhu et al. (2020)

OM: Oxide mixture, MA: Multi anvil press, PC: polycrystalline, SC: single crystal, $^{\$}$: at 76 GPa, *1,*2: same bdg samples are used, ★: suggested gradual spin transition at high P-T, #: suggested HS to IS crossover in A site Fe^{2+}, *: annealed at certain data points.

Table 3-2. Previous studies on *P-V* data of (Fe,Al)-bearing bdg.

Chemical composition	Synthesis	sample	$Fe^{3+}/\sum Fe$	Experiment Pressure (GPa)	Starting material	Synthesis Temperature (K)	Synthesis Pressure (GPa)	Anomalous change in *V*	Annealed or not	Annealed temperature (K)	Annealed time (min)	Reference
$Mg_{0.85}Fe_{0.15}Al_{0.15}Si_{0.85}O_3$	in DAC	PC	1.0	0-121	gel	1600	117	present*	annealed	1600	60	Nishio-Hamane et al. (2008)
$Mg_{0.88}Fe_{0.13}Al_{0.11}Si_{0.88}O_3$	in DAC	PC	1.0	0-95	glass	2000	above 45	present	annealed (above 45 GPa)	1800-2100	7-15	Fujino et al. (2012)
$Mg_{0.85}Fe_{0.15}Al_{0.15}Si_{0.85}O_3$	MA	PC	1.0	0-200	gel	2000	25	-	annealed	1200-1400	30	Catalli et al. (2011)
☆$Mg_{0.60}Fe_{0.41}Si_{0.62}Al_{0.36}O_3$	MA	SC	0.93(3)	0-74	OM	1573	25	-	-	-	-	Boffa Ballaran et al. (2012)
☆$Mg_{0.60}Fe_{0.40}Si_{0.63}Al_{0.37}O_3$	MA	SC	0.93(3)	0-70	OM	1573	25	-	annealed	1100-1300	10-15	Glazyrin et al. (2014)
$Mg_{0.86}Fe_{0.14}Si_{0.96}Al_{0.04}O_3$	MA	SC	0.20(3)	92-105	OM	1573	25	-	annealed*	2700-3100	30-40	Ismailova et al. (2016)
$Mg_{0.89}Fe_{0.12}Al_{0.11}Si_{0.89}O_3$	MA	SC	0.80	0-110	OM	2023	24	-	-	-	-	Mao et al. (2017)
$Mg_{0.83}Fe_{0.21}Al_{0.06}Si_{0.92}O_3$	MA	PC	0.36(5)	0-142	OM	2073	26	-	annealed (above 40 GPa)	1800-2000	10-15	Okuda et al. (2017)
$Mg_{0.79}Fe_{0.08}Al_{0.22}Si_{0.91}O_3$	in DAC	PC	<0.80※	0-55	gel	2000	37-55	present	annealed*	2000	15-30	Okuda et al. (2019)
$Mg_{0.50}Fe_{0.50}Al_{0.50}Si_{0.50}O_3$	MA	PC	1.0	27-102	OM	1873	24	-	annealed*	1600-1800	10	Zhu et al. (2020)

OM: Oxide mixture, MA: Multi anvil press, PC: polycrystalline, SC: single crystal, *: see Fujino and Nishio-Hamane et al. (2008), *: annealed at certain data points, ☆: same bdg samples are used, ※: estimated by Potapkin et al. (2013).

Table 3-3. Reported DAC experiments on spin transition of Fe in (Fe,Al)-bearing $MgSiO_3$ perovskite compiled in a two-dimensional diagram with x-axis as synthesis pressure of sample, and y-axis as its grain size

Polycrystalline

Reference	LS-Fe	Method
Fujino et al. (2012)	P	XES
Kupenko et al. (2015)	P	SMS
Zhu et al. (2020)	P	SMS+XES
Fujino et al. (2012)	N	XRD
Okuda et al. (2017)	N	XRD
Zhu et al. (2020)	N	XRD

Reference	LS-Fe	Method
Nishio-Hamane et al. (2008)	P	XRD*
Catalli et al. (2011)	P	SMS+XRD
Okuda et al. (2019)	P	XRD

Synthesis pressure

Reference	LS-Fe	Method
Boffa Ballaran et al. (2012)	N	XRD
Potapkin et al. (2013)	N	SMS
Glazyrin et al. (2014)	N	XRD
Ismaiova et al. (2016)	N	XRD
Lin et al. (2016)	N	SMS+XES
Mao et al. (2017)	N	SMS+XRD

Do not exist

Single crystal

1st and 2nd quadrants, studies used a multigrain sample, 3rd and 4th quadrants, studies used a single crystal sample.
1st and 4th quadrants, synthesized sample in a DAC, 2nd and 3rd quadrants, used a sample pre-synthesized in a MA.
*: discussed in Fujino et al. (2012). P: present; N: No evidence. Note the probe dependent results in the 2nd quadrant.

Table 3-4. Unit cell lattice parameters and experimental conditions of XRD measurements

Reference	Composition	Run #	Pressure (GPa)	Pressure medium	V_{Au} (Å^3)	a_{bdg} (Å)	b_{bdg} (Å)	c_{bdg} (Å)	V_{bdg} (Å^3)
This study	$Mg_{0.85}Fe_{0.09}Al_{0.21}Si_{0.86}O_3$ [#]	1	46.89[*s]	Al_2O_3	57.26(28)	4.551(1)	4.753(2)	6.601(2)	142.79(16)
	(gF9A21)		42.92		57.91(19)	4.568(1)	4.771(1)	6.626(1)	144.39(8)
			33.18[*]		59.46(16)	4.609(2)	4.799(2)	6.684(4)	147.84(24)
			29.69		60.07(25)	4.650(2)	4.838(2)	6.734(3)	151.49(20)
			26.70		60.63(25)	4.678(2)	4.871(2)	6.776(4)	154.40(28)
			21.92		61.60(20)	4.704(10)	4.901(7)	6.835(22)	157.56(125)
	$Mg_{0.85}Fe_{0.14}Al_{0.05}Si_{0.96}O_3$	1	56.176[*s]	NaCl	56.21(21)	4.528(1)	4.725(1)	6.552(1)	140.17(6)
	(gF14A5)		55.19		56.34(23)	4.532(1)	4.729(1)	6.558(1)	140.57(7)
			53.84		56.53(30)	4.538(1)	4.736(1)	6.565(1)	141.10(9)
			52.08		56.78(29)	4.546(1)	4.744(1)	6.577(2)	141.82(10)
			50.02		57.17(36)	4.555(2)	4.756(2)	6.590(4)	142.78(23)
			47.98		57.40(36)	4.566(1)	4.762(1)	6.604(2)	143.59(12)
			46.13		57.70(40)	4.577(1)	4.771(1)	6.619(2)	144.53(12)
			45.63		57.85(50)	4.583(1)	4.777(1)	6.627(2)	145.11(13)
			42.57		58.42(70)	4.605(1)	4.793(1)	6.655(2)	146.88(13)
			42.30		58.57(84)	4.611(1)	4.801(2)	6.667(2)	147.59(16)
			39.52		59.00(84)	4.623(2)	4.819(2)	6.678(5)	148.79(29)
			35.14		59.07(10)	4.661(3)	4.847(4)	6.722(4)	151.88(32)
			34.65		59.11(10)	4.666(2)	4.856(3)	6.730(3)	152.47(27)
			30.26		59.88(17)	4.686(2)	4.873(2)	6.761(3)	154.39(21)
			16.05		62.83(77)	4.739(2)	4.918(1)	6.818(4)	158.88(25)
			11.96		63.89(23)	4.756(1)	4.934(1)	6.845(7)	160.61(54)
Okuda et al. (2019)	$Mg_{0.85}Fe_{0.09}Al_{0.21}Si_{0.86}O_3$ [#]	1	36.57[*s]	KCl	58.80(5)	4.601(4)	4.799(4)	6.646(5)	146.72(41)
	(gF9A21)		37.24		58.69(6)	4.598(3)	4.791(4)	6.655(5)	146.57(36)
			38.68		58.46(10)	4.592(4)	4.790(3)	6.639(5)	146.06(38)
			42.09		57.94(13)	4.580(4)	4.778(4)	6.636(6)	145.22(43)
			39.52		58.33(13)	4.589(5)	4.790(4)	6.634(6)	145.80(45)
			36.61		58.79(10)	4.602(7)	4.811(9)	6.661(13)	147.53(87)
			32.84[*]		59.42(13)	4.611(6)	4.816(8)	6.667(12)	148.07(79)
			32.79		59.43(11)	4.617(6)	4.821(7)	6.674(11)	148.57(73)
			26.72		60.53(6)	4.680(1)	4.874(1)	6.783(1)	154.70(9)
			21.03		61.69(6)	4.725(1)	4.919(1)	6.844(1)	159.06(7)
			12.09		63.72(31)	4.753(4)	4.935(6)	6.879(4)	161.38(45)
		2	55.16[*s]	KCl	56.18(15)	4.522(7)	4.743(7)	6.548(10)	140.45(73)
			52.82		56.47(10)	4.530(3)	4.738(3)	6.560(4)	140.80(27)
			45.76[*]		57.41(6)	4.557(2)	4.757(2)	6.595(4)	142.94(25)
			37.58[*]		58.64(11)	4.590(1)	4.788(1)	6.661(1)	146.39(4)
			29.06		60.09(10)	4.635(1)	4.825(1)	6.722(1)	150.31(8)
			24.17		61.04(10)	4.696(1)	4.882(2)	6.807(3)	156.03(21)
			24.51		60.97(6)	4.717(1)	4.895(1)	6.823(1)	157.52(13)
			21.74		61.54(4)	4.736(1)	4.917(2)	6.855(2)	159.67(17)
			12.64		63.70(11)	4.755(3)	4.941(4)	6.891(9)	161.91(49)
		3	29.98[*]	Silicone oil	59.93(15)	4.630(2)	4.819(2)	6.725(4)	150.06(26)
			28.55	+KCl	60.19(18)	4.653(4)	4.840(5)	6.754(6)	152.10(48)
			26.35		60.61(12)	4.671(3)	4.856(4)	6.781(5)	153.80(40)
			24.66		60.94(11)	4.693(3)	4.869(4)	6.802(4)	155.43(33)
			22.94		61.31(7)	4.698(5)	4.905(7)	6.811(7)	156.97(59)
			11.69		63.96(20)	4.750(8)	4.930(10)	6.895(12)	161.47(96)

V_{Au}, a_{bdg}, b_{bdg}, c_{bdg} and V_{bdg}: lattice volume of gold, lattice constants a, b and c and lattice volume of bdg, respectively. #: same samples are used.

Pressure calibration was based on the EOS of gold (Tsuchiya, 2003). We used typical value of 5% for pressure errors.

[*] Data obtained after thermal annealing. [s] Synthesized pressure. Bdg sample in run #3 in Okuda et al. (2019) was synthesized at 55 GPa.

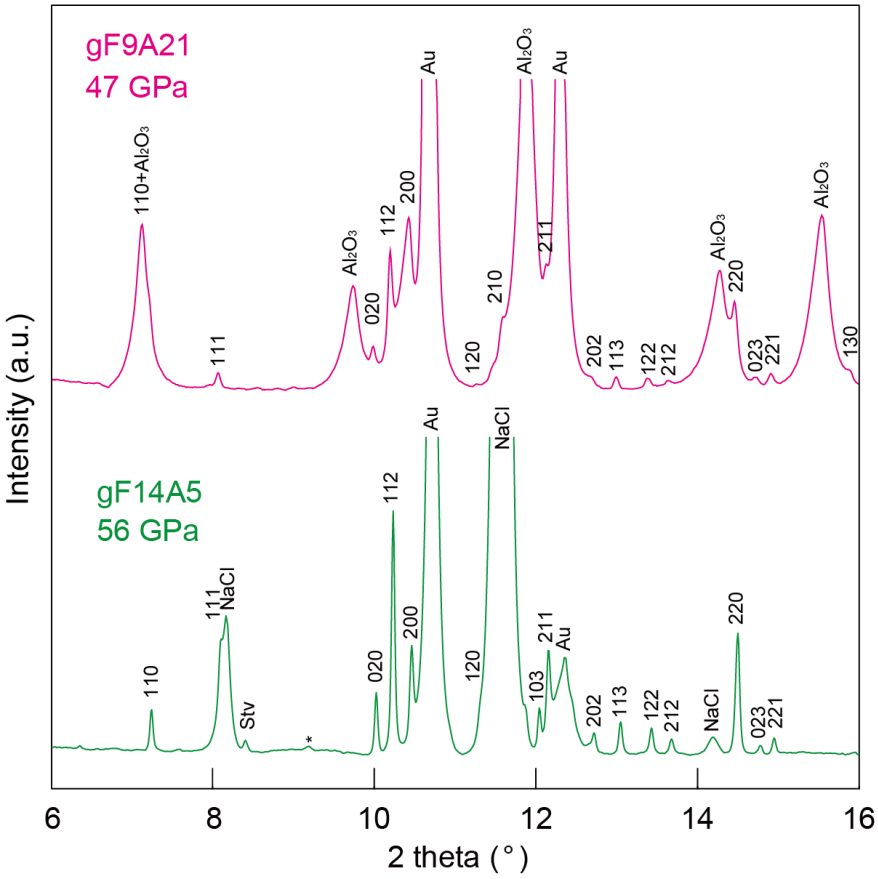

Fig. 3-1. XRD patterns of bridgmanite samples after the synthesis. The numbers in the figure indicate Miller indices of bdg. The notations of Stv, Au, Al_2O_3 and NaCl in the figure denote diffraction peaks from stishovite, gold as a pressure marker, Al_2O_3 and NaCl as pressure medium, respectively. *: unknown peak. This unknown peak may be derived from the instrument itself since we observed similar peaks at the exact same position with different pressure data.

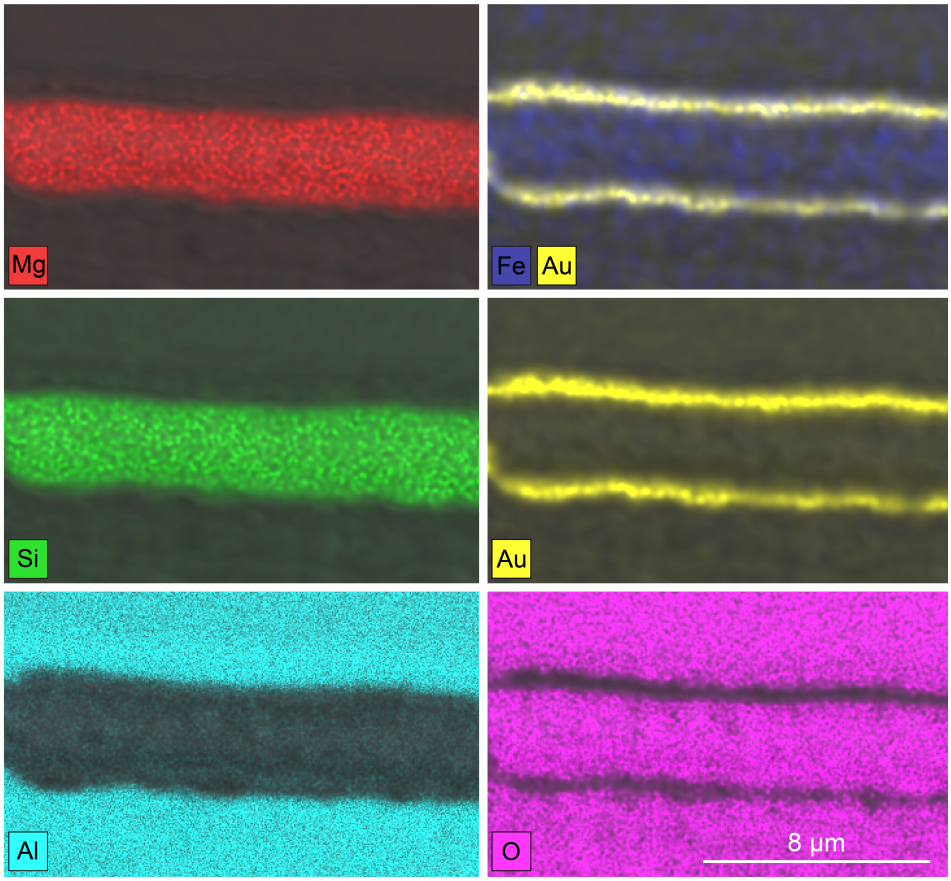

Fig. 3-2. EDS map of the recovered bdg sample after our compression experiment in run #1 on gF9A21. Red, green, blue, light blue, yellow, and pink regions illustrate mapping results of Mg, Si, Fe, Al, Au, and O, respectively.

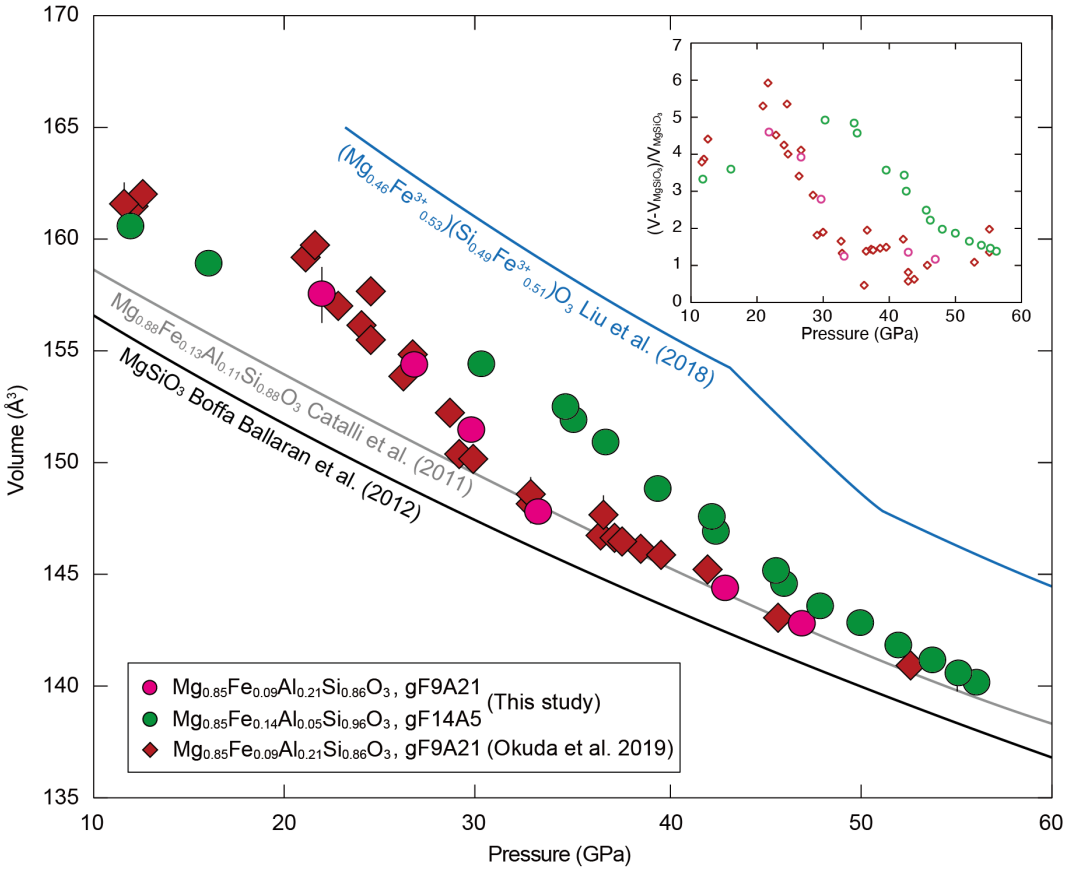

Fig. 3-3. Compression curve of bridgmanite. Pink circles, green circles and red diamonds show compressibility data of $Mg_{0.85}Fe_{0.09}Al_{0.21}Si_{0.86}O_3$ (this study), $Mg_{0.85}Fe_{0.14}Al_{0.05}Si_{0.96}O_3$ (this study) and $Mg_{0.85}Fe_{0.09}Al_{0.21}Si_{0.86}O_3$ (Okuda et al. 2019), respectively. Black, gray and blue curves indicate the EoSs of $MgSiO_3$ (Boffa Ballaran et al. 2012), $Mg_{0.88}Fe_{0.13}Al_{0.11}Si_{0.88}O_3$ (Catalli et al. 2011) and $(Mg_{0.46}Fe^{3+}_{0.53})(Si_{0.49}Fe^{3+}_{0.51})O_3$ (Liu et al. 2018), respectively. The pink and green open circles, and red open diamonds in the insert figure show the volume difference between (Fe,Al)-bearing bdg ($Mg_{0.85}Fe_{0.09}Al_{0.21}Si_{0.86}O_3$ (this study), $Mg_{0.85}Fe_{0.14}Al_{0.05}Si_{0.96}O_3$ (this

study), $Mg_{0.85}Fe_{0.09}Al_{0.21}Si_{0.86}O_3$ (Okuda et al. 2019) and $MgSiO_3$ bdg (Boffa Ballaran et al. 2012), respectively.

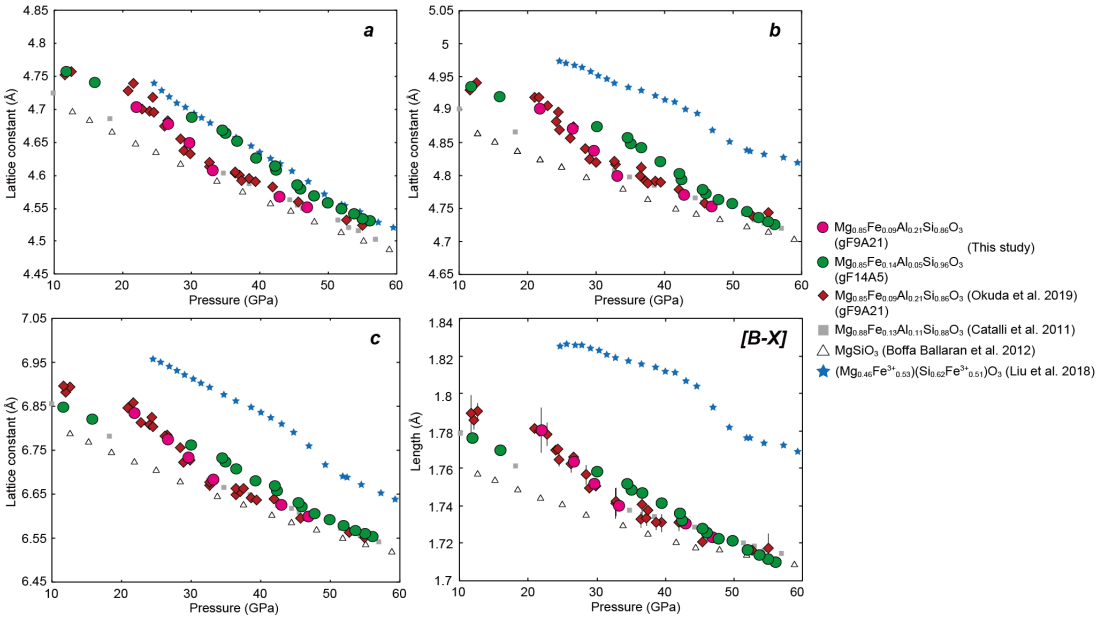

Fig. 3-4. Pressure dependence of lattice constants *a*, *b* and *c*, and octahedral bond length [*B*-*X*] of bridgmanite. Pink and green circles, $Mg_{0.85}Fe_{0.09}Al_{0.21}Si_{0.86}O_3$ and $Mg_{0.85}Fe_{0.14}Al_{0.05}Si_{0.96}O_3$, respectively (this study); red diamonds, open triangles, gray squares and blue stars, $Mg_{0.85}Fe_{0.09}Al_{0.21}Si_{0.86}O_3$ (Okuda et al. 2019), $MgSiO_3$ (Boffa Ballaran et al. 2012), $Mg_{0.88}Fe_{0.13}Al_{0.11}Si_{0.88}O_3$ (Catalli et al. 2011) and $(Mg_{0.46}Fe^{3+}_{0.53})(Si_{0.49}Fe^{3+}_{0.51})O_3$ (Liu et al. 2018), respectively.

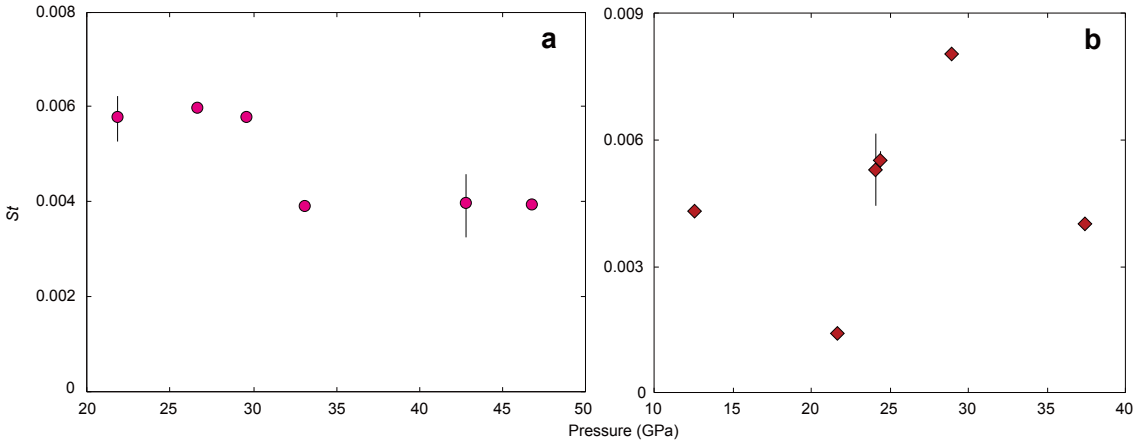

Fig. 3-5. *St* value of Au in (a) this study in run #1 on gF9A21, and (b) run #2 in Okuda et al. (2019).

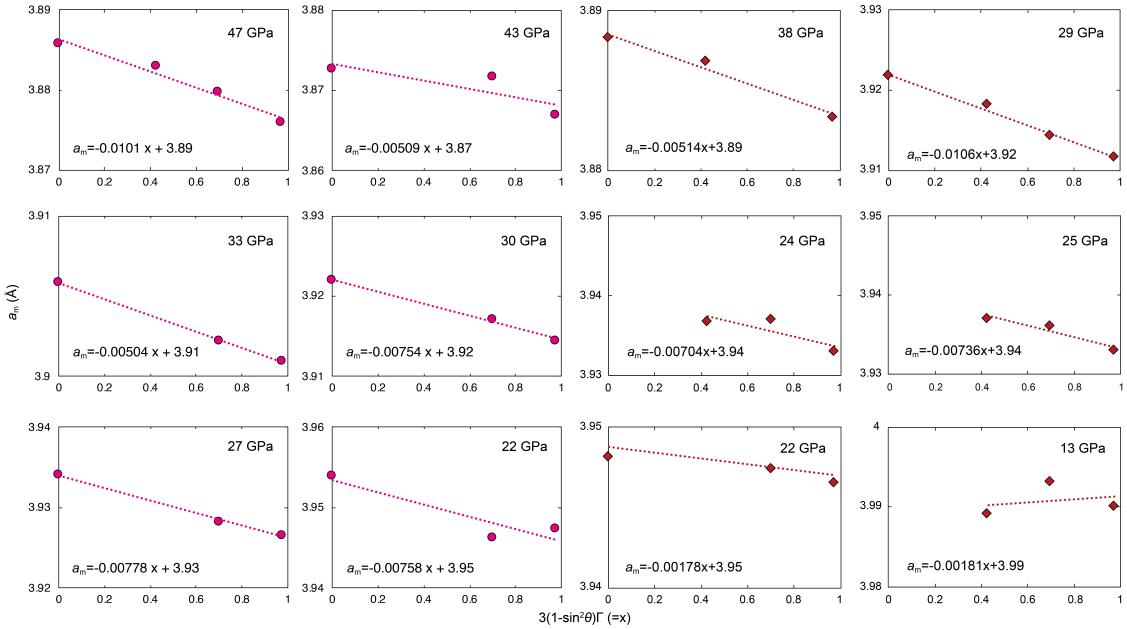

Fig. 3-6. Γ plot of Au. Pink circles and red diamonds indicate the Γ plot of Au obtained in this study in run #1 on gF9A21, and run #2 in Okuda et al. (2019), respectively. Dotted line and function in each figure indicate the fitting line of each plot and its function, respectively. All the Γ plot data where at least three different diffraction peaks of Au were available are plotted.

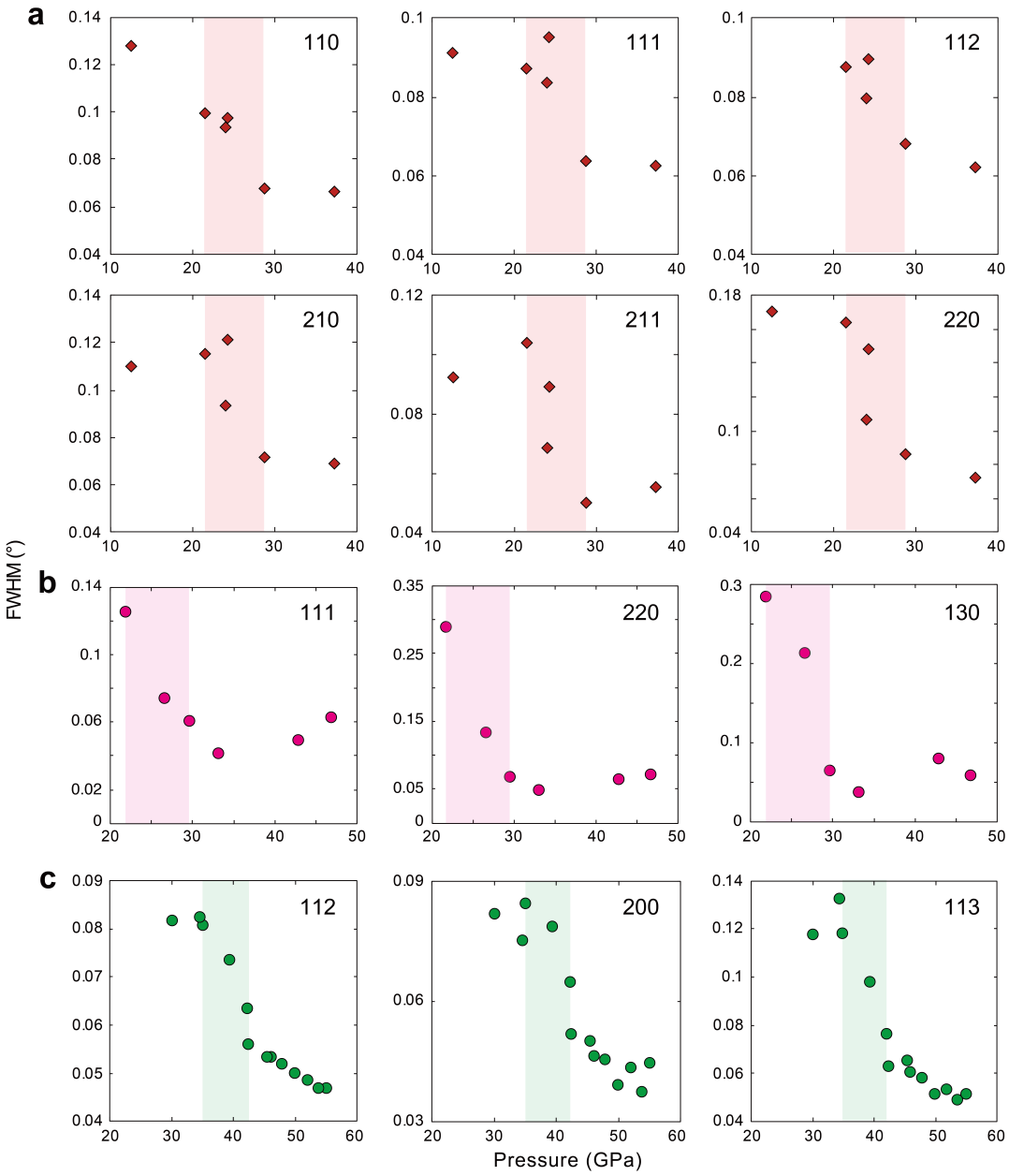

Fig. 3-7. FWHM of the XRD peaks from bdg sample in (a) run #2 in Okuda et al. (2019), (b) $Mg_{0.85}Fe_{0.09}Al_{0.21}Si_{0.86}O_3$ (gF9A21, this study), and (c) $Mg_{0.85}Fe_{0.14}Al_{0.05}Si_{0.96}O_3$ (gF14A5, this study). Numbers in the upper right of each figure indicate Miller indices of bdg. Red, pink and green bands show the pressure range where increase in FWHM of bdg peaks was observed in run #2 in Okuda et al. (2019), gF9A21, and gF14A5, respectively.

3.8. Supplemental material

Table S3-1. EDS analyses of gel starting material of gF14A5

Elements	wt%	error (wt%)	atm%
Mg	21.72	1.89	19.34
Fe	8.29	0.70	3.21
Al	1.49	0.20	1.20
Si	28.20	2.33	21.73

The composition of the gel is $Mg_{0.85(7)}Fe^{2+}_{0.11(1)}Fe^{3+}_{0.03(1)}Al_{0.05(1)}Si_{0.96(8)}O_3$, where valence state was determined according to charge balance, and O was normalized to 3 atoms.

Chapter 5. Effect of spin transition of iron on the thermal conductivity of (Fe, Al)-bearing bridgmanite

This chapter was updated from the published article as *"Effect of spin transition of iron on the thermal conductivity of (Fe, Al)-bearing bridgmanite"* by **Yoshiyuki Okuda**, Kenji Ohta, Ryosuke Sinmyo, Kei Hirose, Takashi Yagi, Yasuo Ohishi (2019) Earth and Planetary Science Letters, **520**, 188-198.
https://doi.org/10.1016/j.epsl.2019.05.042

Abstract

Thermal conductivity of bridgmanite (bdg) is the important physical property controlling the heat transfer inside the Earth. Here we report room temperature lattice thermal conductivity of (Fe,Al)-bearing bdg with chemical compositions of $Mg_{0.848}Fe_{0.090}Al_{0.206}Si_{0.856}O_3$ and $Mg_{0.718}Fe_{0.123}Al_{0.281}Si_{0.878}O_3$ measured up to 125 GPa and 74 GPa, respectively, using the pulsed light heating thermoreflectance technique in a diamond anvil cell. We found that the lattice thermal conductivity of these bdg samples show abnormal reduction in the pressure range of 20−40 GPa at 300 K, which is probably due to the spin transition of Fe^{3+} in octahedral Si-site (B-site). We propose that the lattice thermal conductivity of bdg is reduced by 46 ± 16% when Fe is in the mixed spin state, which may form a thermal insulating layer in the Earth's mid lower mantle. In addition, we provide a thermal conductivity model of bdg, taking into account the effect of compositional difference and the spin transition of Fe. Our conductivity model indicates that the thermal conductivity of bdg in the pyrolitic lower mantle is more than twice as high as that in the descending MORB, which is likely to create heterogeneity of lateral heat flux through the Earth's core-mantle boundary.

5.1. Introduction

The thermal conductivity (κ) of the lowermost mantle is one of the most important physical properties that can help us to understand lower mantle dynamics (e.g., Li et al., 2018) and thus the thermal evolution of the Earth (for review, see Lay et al., 2008). The chemical composition of bridgmanite (bdg) in mid-oceanic ridge basalt (MORB) rock in the lower mantle is different from that in the surroundings. Fe and Al contents of bdg in the pyrolitic lower mantle are considered to be both ~10 mol% (e.g., Sinmyo et al., 2011). On the other hand, bdg in the subducted MORB is thought to contain a large amount of Fe and Al, such as 31 mol% and 29 mol% (i.e., 0.31 and 0.29 in per formula unit), respectively (Hirose et al., 2005). These impurities necessarily change the κ of bdg from that of Mg endmember, thus we need to know how these impurities affect its κ. In addition, for Fe-bearing minerals, we also need to consider the effect of the spin transition of Fe. A number of experimental and theoretical studies suggested that the mechanism of the incorporation of Fe in bdg is complicated compared to other lower mantle minerals; Fe in bdg can exist in two different valence states of Fe^{2+} and Fe^{3+}, and these can be distributed to two cation sites such as the large pseudo-dodecahedral Mg^{2+} site (A-site) and the relatively small octahedral Si^{4+} site (B-site) (for review, see Lin et al., 2013). Previous studies provided a common view of iron spin transition in bdg: only the Fe^{3+} in the octahedral B-site would undergo a spin transition from high spin (HS) to low spin (LS) state via mixed spin (MS) state at the *P-T* conditions in the lower mantle. The systematical studies (e.g., Jackson et al., 2005; Catalli et al., 2011; Hsu et al., 2011;

Kupenko et al., 2015; Sinmyo et al., 2017; Zhu et al., 2020; Okuda et al., 2020) and experimental results in chapters 3 and 4 have shown the presence of the Fe spin transition in lower mantle bridgmanite, hence requires investigation of this effect on the κ of bdg.

There are a number of experimental and theoretical studies about the lattice thermal conductivity (κ_{latt}) of bdg, but the chemical compositions of bdg are almost entirely limited to Fe- and Al-free systems (Osako and Ito, 1991; Manthilake et al., 2011; Ohta et al., 2012, 2014; Haigis et al., 2012; Dekura et al., 2013; Ammann et al., 2014; Tang et al., 2014; Stackhouse et al., 2015; Zhang et al., 2017; Ghaderi et al., 2017). There are two reports on the κ_{latt} of bdg containing Fe *or* Al (Manthilake et al., 2011; Ohta et al., 2014), and until recently there was no report on that including both Fe *and* Al. But even so, two recent studies on the κ_{latt} of (Fe,Al)-bearing bdg were reported (Okuda et al., 2017, Chapter 2; Hsieh et al., 2017). However, interestingly they provided conflicting results. Okuda et al. (2017) suggested that the incorporation of Fe and Al to bdg has a minor effect on the κ_{latt} of bdg at whole lower mantle pressure. On the other hand, Hsieh et al. (2017) reported that the pressure derivative of the κ_{latt} of (Fe, Al)-bearing bdg shows a sudden change at 45 GPa, which could be attributed to the enhanced pressure-induced lattice distortion in the high-spin state Fe^{2+} in the A-site (Mao et al., 2017). Moreover, they both showed the absence of the spin transition in their samples, which is likely to be due to the use of the bdg samples synthesized in a

multi-anvil press, so the effect of spin transition on the κ of bdg is currently fully unknown.

Here we report the κ_{latt} of (Fe,Al)-bearing bdg samples with compositions of $Mg_{0.848}Fe_{0.090}Al_{0.206}Si_{0.856}O_3$ (gF9A21) and $Mg_{0.718}Fe_{0.123}Al_{0.281}Si_{0.878}O_3$ (gF12A28) up to 125 GPa and 74 GPa respectively, measured by means of the pulsed light heating thermoreflectance technique in a DAC (Yagi et al., 2011; Ohta et al., 2012, 2017; Okuda et al., 2017). The obtained κ_{latt} for both gF9A21 and gF12A28 exhibited anomalously low conductivities at the pressure range of 20−40 GPa. However, above 40 GPa, those conductivities eventually showed good agreement with the result of $MgSiO_3$ bdg (Ohta et al., 2012; Hsieh et al., 2017) and reported (Fe,Al)-bearing bdg (Okuda et al., 2017). We suggest that the discontinuous reduction in the present result is due to the spin transition of octahedral Fe^{3+}. Such a reduction in the κ_{latt} of bdg could create a thermal insulating layer in the mid lower mantle, which has important implications for mantle dynamics. In this chapter, we also provide a κ model considering the effect of the difference in chemical composition and the spin transition of Fe. Our estimated total κ of bdg in the pyrolitic lower mantle is more than twice as high as that in subducted MORB at the core-mantle boundary (CMB) conditions, which contributes to the lateral heat flux heterogeneity in the Earth's lowermost mantle.

5.2. Experimental procedure

5.2.1. Sample preparation

We prepared two gel starting materials with different chemical compositions. A gel-state starting material of gF9A21, which is the same sample used in Chapter 3, was dehydrated at 1000 K in a H_2-CO_2 gas-mixing furnace, in which oxygen fugacity was controlled slightly above the iron-wüstite buffer. The collected starting material of gF9A21 had a low $Fe^{3+}/\sum Fe$ ratio of 0.22(6) (Sinmyo et al., 2011). The starting material of gF12A28 in a rhenium capsule was heated at 1000 K for 1 day in a H_2-CO_2 gas-mixing furnace, in which the volume ratio H_2:CO_2 was maintained at 3:2. Both starting materials were synthesized at Tokyo Institute of Technology. The chemical homogeneity of both gel samples was confirmed by microprobe analyses (Supplemental material S5-1). In order to determine the chemical composition of the starting materials, Energy Dispersive Spectroscopy (EDS) analysis was conducted for each gel sample at the University of Tokyo. As a result, we obtained chemical compositions of starting gel sample gF9A21 and gF12A28 as $Mg_{0.848}Fe_{0.090}Al_{0.206}Si_{0.856}O_3$ and $Mg_{0.718}Fe_{0.123}Al_{0.281}Si_{0.878}O_3$, respectively.

For κ measurements, the obtained gel samples were shaped into the form of a disk, then gold was sputtered onto both sides of the samples, and they were loaded into the sample chamber of the DAC with a pressure transmitting medium of KCl, SiO_2 glass or Al_2O_3. The purpose of the sputtered gold was to act as a pressure marker, laser absorber and for κ measurements. Double sided laser heating was conducted at

BL10XU, SPring-8, which simultaneously conducted *in-situ* X-ray diffraction (XRD) measurement, for synthesis of the bdg sample and identification of the crystalline phase, respectively. In each synthesis, the gel sample was heated at ~2000 K for an hour. As a result, we obtained an almost single phase of bdg in each run (Fig. 5-1). In this manner, bdg samples gF9A21 and gF12A28 were synthesized inside a DAC in each run prior to high-pressure κ measurements.

5.2.2. High-pressure thermal conductivity measurement

We used the pulsed light heating thermoreflectance technique for the measurement of the thermal diffusivity of bdg (D_{bdg}) at high pressures (in details, see Yagi et al., 2011; Ohta et al., 2012, 2017; Okuda et al., 2017). κ can be obtained from the following equation:

$$\kappa = \rho D C_{\mathrm{P}} \qquad (5\text{-}1)$$

where ρ is density, D is thermal diffusivity and C_{p} is isobaric specific heat. We used the density of our bdg sample (ρ_{bdg}) at high pressures estimated from the obtained EoS using the same bdg sample with gF9A21 obtained in Chapter 3 (Fig. 3-3). The detailed information of used ρ_{bdg} and sample thickness correction for the calculation of κ is summarized in Supplemental material S5-2. The C_{P} of bdg at high pressures was calculated from the Debye model and thermodynamic functions, with its thermoelastic parameters for thermal EoS (Sun et al., 2018). All of the thermoreflectance measurements were conducted at Tokyo Institute of Technology. Pressure was calibrated from the lattice

volume of Au (Tsuchiya, 2003), Raman shift of the diamond anvil (Akahama and Kawamura, 2006) or ruby fluorescence method (Mao et al., 1986), which is summarized in Table 5-1.

The pulsed light heating thermoreflectance method yields transient temperature curves of bdg at each pressure (Fig. 5-2; see Supplemental material S5-3 for obtained temperature history curves in each run). The obtained curves were fitted by a theoretical curve based on the one-dimensional thermal conduction equation for the filmed sample thickness direction by pulse heating, for the estimation of the thermal diffusion time (τ) through the sample:

$$T(t) = \bar{T}\sqrt{\frac{\tau}{\pi t}}\sum_{n=0}^{\infty}\gamma^{2n} exp\left[-\frac{(2n+1)^2}{4}\frac{\tau}{t}\right], \quad (5\text{-}2)$$

where $T(t)$ is temperature, $\bar{T}$ is a constant, t is time, and γ is fitting parameter describing heat effusion to the pressure medium. This τ was then analyzed as a three-layer heat diffusion model to obtain D_{bdg} using the following equations:

$$D_{\mathrm{bdg}} = \frac{\frac{\Gamma}{6}+1+\frac{1}{\Gamma}}{(\Gamma+2)\frac{\tau}{6}-(\Gamma+\frac{4}{3})\frac{d_{\mathrm{Au}}^2}{D_{\mathrm{Au}}}} d_{\mathrm{bdg}}^2, \quad (5\text{-}3)$$

$$\Gamma = \frac{C_{\mathrm{bdg}} d_{\mathrm{bdg}}}{C_{\mathrm{Au}} d_{\mathrm{Au}}}, \quad (5\text{-}4)$$

where D_{Au} is thermal diffusivity of Au, d_{bdg}, d_{Au} are thickness of bdg and Au respectively, and C_{bdg}, C_{Au} are heat capacity per unit volume ($C = \rho C_{\mathrm{P}}$) of bdg and Au, respectively. We used 127 mm^2/s for D_{Au} at ambient conditions (Ho et al., 1972), and 4%/GPa for the pressure derivative of D_{Au} obtained by thermal conductivity

measurements (Ross et al., 1984). Note that Ross et al. (1984) was measured only up to a few GPa, however, so far there are no available data. We used the value of C_{Au} at high pressure from Tsuchiya (2003). Thermodynamic parameters of bdg and Au used to obtain its thermal diffusivities and conductivities are all summarized in Table 5-1.

For the measurement of the thickness of the sample, first we took the bdg sample with surrounding pressure medium and gasket out entirely after the thermoreflectance measurements. Then we cut out a cross section of the sample by using a Ga ion focused ion beam (FIB), and we observed the thickness of the sample with a scanning electron microscope (SEM). d_{bdg} and d_{Au} under high pressure were corrected by estimating the change in the lattice volume of bdg and Au, based on the EoSs of bdg (see Supplemental material S5-2 for detail) and gold (Tsuchiya, 2003), respectively.

5.3. Results

We performed three separate measurements on the κ_{latt} of gF9A21 up to 125 GPa, and three separate measurements on gF12A28 up to 74 GPa (Table 5-1). The κ_{latt} of gF9A21 and gF12A28 at ambient conditions was 4.8 ± 1.1 W/m/K and 4.6 ± 2.0 W/m/K, respectively (Fig. 5-3), which is considerably lower than those reported in Okuda et al. (2017) and Hsieh et al. (2017) at ambient pressure. The peak position of transient temperature curve obtained in thermoreflectance measurement is related to the thermal

diffusion time τ, which is inversely proportional to κ (Eqs. 5-3 and 5-4). Essentially, pressure enhances κ, thus increasing pressure should shift the peak position to the left side, when time is taken on the horizontal axis. However, with pressurization from around 20 GPa to 40 GPa the peak position of our yielded temperature history curves shifted to the right side (Fig. 5-2). Consequently, κ_{latt} of gF9A21 up to 42 GPa showed a smaller conductivity than that at ambient pressure, which is, at the minimum, less than 30% of the κ_{latt} of $Mg_{0.832}Fe_{0.209}Al_{0.060}Si_{0.916}O_3$ bdg reported in Okuda et al. (2017). However, κ_{latt} of gF9A21 at pressures above 50 GPa revived and showed a κ_{latt} value that was nearly consistent with that reported in Okuda et al. (2017). κ_{latt} of gF12A28 also behaves similarly to that of gF9A21: at a pressure range up to 33 GPa, κ_{latt} of gF12A28 showed a smaller value than that at ambient pressure, however κ_{latt} at higher pressure is also in good agreement with the reported κ_{latt} in Okuda et al. (2017). In short, κ_{latt} of gF9A21 and gF12A28 was strongly reduced at the pressure range until around 40 GPa, though at higher pressure those κ_{latt} showed values consistent with the reported κ_{latt} of $Mg_{0.832}Fe_{0.209}Al_{0.060}Si_{0.916}O_3$ bdg (Okuda et al., 2017) (Fig. 5-3). Such reduction of κ_{latt} as found in the present results has not been reported previously.

5.4. Discussion

5.4.1. Spin transition of Fe

Previous studies about the spin transition of Fe in bdg have provided a common view that only the Fe^{3+} in the B-site would undergo spin transition at the lower mantle pressure (for review, see Lin et al., 2013). The bdg samples in this study are expected to show the spin transition of Fe since these were synthesized in a DAC at relatively high pressure (Chapters 3, 4). Although the $Fe^{3+}/\sum Fe$ of our bdg samples gF9A21 and gF12A28 are not determined, the $Fe^{3+}/\sum Fe$ of $Mg_{0.79}Fe_{0.11}Al_{0.16}Si_{0.94}O_3$ bdg, which has a similar chemical composition to gF9A21, was determined in Sinmyo et al. (2011) using the Fe $L_{2,3}$-edge electron energy-loss near-edge structure (ELNES) spectroscopy measurement. The $Fe^{3+}/\sum Fe$ of $Mg_{0.79}Fe_{0.11}Al_{0.16}Si_{0.94}O_3$ bdg was found to have a high $Fe^{3+}/\sum Fe$ value of 0.80(15). Considering that the Al^{3+} content in both of our bdg samples is higher than that of $Mg_{0.79}Fe_{0.11}Al_{0.16}Si_{0.94}O_3$ bdg (Sinmyo et al., 2011), and also taking into account that the Al^{3+} content in bdg enhances the amount of Fe^{3+} (e.g., Frost et al., 2004; Sinmyo et al., 2011), it can be inferred that both gF9A21 and gF12A28 have very high $Fe^{3+}/\sum Fe$ content, which would be assumed to be higher than 0.80. Moreover, gF9A21 exhibited abnormal reduction in unit cell volume at the pressure range of 21−30 GPa (Chapter 3, Fig. 3-3), which sufficiently matches that of the reduction of κ_{latt} found in this study. Spin transition of Fe in Fe-bearing mineral yields reduction in the unit cell volume (V), due to the reduction of the ionic radius of Fe. Such V-reduction in bdg was predicted in theoretical studies (Hsu et al., 2011; Tsuchiya and Wang, 2013), and was also observed in experimental studies (Mao et al.,

2015; Liu et al., 2018). Thus, the observed softening of gF9A21 at the identical pressure range of the reduced κ_{latt} of gF9A21 in the present study supports the existence of the spin transition of Fe in our bdg samples. We thus conclude that the suppressed κ_{latt} at the pressure range of 20−40 GPa observed in gF9A21 and gF12A28 is due to the spin transition of octahedral Fe^{3+}.

The pressure range where a suppressed κ_{latt} was observed in this study matches with the pressure range in the MS (mixture of HS and LS) state of Fe^{3+} reported in previous studies (Lin et al., 2013). Our results indicate that κ_{latt} of bdg would be remarkably reduced only when the spin state of Fe is in the MS state. The effect of spin transition of Fe on the κ_{latt} of lower mantle minerals was first reported in Ohta et al. (2017) for ferropericlase (fp), the second most abundant mineral in the lower mantle. They showed that the κ_{latt} of (Mg,Fe)O fp greatly decreases in the pressure range of the MS state of Fe. This is consistent with the most recent measurements of the κ_{latt} of fp (Hsieh et al., 2018). In the MS state, Fe having different ionic radii are randomly arranged in the crystal lattice (Fig. S5-4); According to Shannon, 1976, the ionic radius of six-coordinated Fe^{3+} changes from 0.785 to 0.690 Å by its spin transition, where the difference in radius is as much as 12%. Such disorder in ionic radii should scatter phonons, yielding the reduction of its κ_{latt}. We presume that such reduction of κ_{latt} in the MS state may occur not only in bdg and fp but also in other Fe-bearing mantle minerals (further discussed in *section* (5.*5.2*)).

5.4.2. Comparison and interpretation of previously reported conductivities on (Fe,Al)-bearing bdg

There are currently two reports on the κ_{latt} measurements for (Fe,Al)-bearing bdg (Okuda et al., 2017; Hsieh et al., 2017). Hsieh et al. (2017) reported that both Fe-bearing bdg ($Mg_{0.96}Fe_{0.07}Si_{0.98}O_3$) and (Fe,Al)-bearing bdg ($Mg_{0.89}Fe_{0.12}Al_{0.11}Si_{0.89}O_3$) experience a sudden change in pressure derivative of κ_{latt} at 45 GPa, attributed to the enhanced pressure-induced lattice distortion of Fe^{2+} in the A-site (Mao et al., 2017). In contrast, Okuda et al. (2017) showed that the κ_{latt} of (Fe,Al)-bearing bdg ($Mg_{0.832}Fe_{0.209}Al_{0.060}Si_{0.916}O_3$) increased monotonously with increasing pressure, without any sudden change in its pressure derivative. Mao et al. (2017) suggested that, when in the presence of pressure-induced lattice distortion, there is a strong correlation between QS value in Mössbauer spectroscopy measurement and the tilting angle of the octahedral Φ, which can be expressed with lattice constants a, b and c as follows (e.g., O'Keeffe et al., 1977):

$$\Phi = \cos^{-1}\left(\frac{\sqrt{2}a^2}{bc}\right). \qquad (5\text{-}5)$$

They showed that $Mg_{0.94}Fe_{0.06}Al_{0.01}Si_{0.99}O_3$ bdg exhibits anomalous P-Φ behavior (Chapter 3, Fig. 3-4). On the other hand, they also showed that $Mg_{0.89}Fe_{0.12}Al_{0.11}Si_{0.89}O_3$ bdg, which sample was also used in Hsieh et al. (2017), did not exhibit such anomaly. Mao et al. (2017) explained this difference that the presence of Al in bdg reduces the occurrence of enhanced lattice distortion of (A site)-Fe^{2+}. Our calculated Φ of gF9A21 did not show any discontinuous change (Chapter 3, Fig. 3-4), implying the absence of

enhanced pressure-induced lattice distortion of (A site)-Fe^{2+} in gF9A21. This absence can also be explained from the large amount of Al content in gF9A21 compared with its Fe content, which is consistent with Mao et al. (2017). We also calculated the Φ in $Mg_{0.832}Fe_{0.209}Al_{0.060}Si_{0.916}O_3$ bdg used in Okuda et al. (2017) from their XRD measurement data, but their Φ did not show any anomalous change (Supplemental information S5-5). Also, the obtained SMS measurement data for bdg sample used in Okuda et al. (2017) did not show any anomalous behavior in QS with increasing pressure (Kupenko et al., 2015), which supports the absence of enhanced pressure-induced lattice distortion of (A site)-Fe^{2+} in their bdg sample. This absence matches with the observed monotonical increase of κ_{latt} in Okuda et al. (2017) (Chapter 2). From the above, we suggest that there may be other reasons for a sudden change in pressure derivative of κ_{latt} of $Mg_{0.89}Fe_{0.12}Al_{0.11}Si_{0.89}O_3$ bdg at 45 GPa from the pressure-induced lattice distortion reported in Hsieh et al. (2017). One possible explanation could be made with the presence/absence of thermal annealing. Both Mao et al. (2017) and Hsieh et al. (2017) conducted experiments along cold compression/decompression (i.e., without thermal annealing). It is true that thermal annealing may change the speciation of Fe at high pressure, making the interpretation of the obtained results complex. On the other hand, cold compression/decompression can keep the speciation of Fe in bdg from the pre-synthesized starting material, which enables clear and easier discussion for the effect of Fe on physical properties. However, we should also state that we have to be very careful whether anomalous behavior observed under cold compression also take place in the actual mantle's *P*-*T* conditions. Under cold compression, the number of dislocations

increase, so the deviatoric stress and defects in the sample also increases. These defects, dislocation and stress in the sample should affect its κ_{latt}. Here, annealing can minimize the deviatoric stress and dislocation caused by shear deformation in the sample. Therefore, thermal annealing is an essential task to measure physical properties at room temperature, high pressure. Kupenko et al. (2015) and Okuda et al. (2017) conducted thermal annealing before collecting SMS and κ_{latt} data, respectively. Since Okuda et al. (2017) conducted thermal annealing before collecting each XRD data above 45 GPa, this annealing may have suppressed the occurrence of lattice distortion in their bdg sample. We suggest that such enhanced lattice distortion may occur only under cold compression. Overall, the presence/absence of thermal annealing can explain the discrepancy between Hsieh et al. (2017) and Okuda et al. (2017).

5.4.3. Pressure-temperature dependence of κ_{latt} of bdg

It is known that silicates and complex compounds show weaker temperature response on κ_{latt} than simple pure oxide that obeys T^{-1} relation (Hofmeister, 1999). Chemical impurity, point defect, mass disorder, and other imperfections in the crystal also make the temperature dependence weaker. Hofmeister (1999) showed that κ_{latt} for oxides at high *P-T* conditions can be written with the temperature dependence coefficient a in the T^{-a} form as follows:

$$\kappa_{latt}(P,T) = \kappa_{latt}(298)\left(\frac{298}{T}\right)^{a} \times \exp\left[-\left(4\gamma + \frac{1}{3}\right)\int \alpha(\theta)d\theta\right] \times (1 + K_0'P/K_0), \quad (5\text{-}6)$$

where γ, α and K_0 are grüneisen parameter, thermal expansivity and bulk modulus, respectively. Manthilake et al. (2011) expanded this model, and introduced the following density-temperature dependent κ model:

$$\kappa_{\mathrm{bdg}}(P,T) = \kappa_{\mathrm{ref}}\left(\frac{\rho}{\rho_{\mathrm{ref}}}\right)^{g}\left(\frac{300\ \mathrm{K}}{T}\right)^{a}, \qquad (5\text{-}7)$$

where κ_{ref} and ρ_{ref} are thermal conductivity and density at reference pressure and temperature, g and a are pressure and temperature dependence coefficients, respectively. Here, g can be written as follows based on the kinetic phonon gas theory:

$$g = (\partial\kappa_{\mathrm{latt}}/\partial\ln\rho)_T. \qquad (5\text{-}8)$$

We have discussed in *section 5.4.1* that the MS state of Fe may scatter phonon, so we separately evaluated our κ_{latt} data obtained at 20−40 GPa (discuss in *section 5.4.5*) and those at other pressure ranges (discuss in the next section).

5.4.4. Impurity effect of Fe and Al on the κ_{latt} of bdg at high-P and 300 K

In chapter 2, we showed that κ_{latt} of $Mg_{0.832}Fe_{0.209}Al_{0.060}Si_{0.916}O_3$ is 19% lower than that of $MgSiO_3$ (Ohta et al., 2012) at 135 GPa and 300 K. Here we extended the evaluation of the impurity effect of Fe and Al on the κ_{latt} of bdg. The g values of gF9A12 and gF12A28 were obtained by using Eq. (5-8), which of those were calculated to be 4.96 ± 0.51 and 5.12 ± 0.78, respectively (Fig. 5-4). With these g values, we estimated the κ_{latt} of gF9A12 and gF12A28 at 135 GPa and 300 K by using Eq. (5-7). We set the reference *P, T* to be ambient conditions, in which case the κ_{ref} is 4.8 ± 1.1

W/m/K and 4.6 ± 2.0 W/m/K for gF9A12 and gF12A28, respectively. Fig. 5-5 shows the summarized κ_{latt} of the present study, Ohta et al. (2012), Okuda et al. (2017) (Chapter 2) and Hsieh et al. (2017) at 135 GPa and 300 K, with Fe+Al content in bdg on the horizontal axis. It can be seen that the κ_{latt} at 135 GPa and 300 K of the present study, Ohta et al. (2012) and Okuda et al. (2017) decreases linearly as Fe+Al content increases, while the estimated conductivity in Hsieh et al. (2017) is relatively lower than the other estimations due to the presence of pressure-induced lattice distortion. Since we consider that such pressure-induced lattice distortion occurs only when the bdg with small Al content compared with Fe is compressed/decompressed without thermal annealing, we conducted a linear approximation for data of the present study, Ohta et al. (2012) and Okuda et al. (2017). The linear approximation line of the κ_{latt} of (Fe,Al)-bearing bdg at 135 GPa, 300 K was obtained as the following equation:

$$\kappa_{\mathrm{bdg},x}(135\ \mathrm{GPa}, 300\ \mathrm{K}) = -24x + 31.3\ , \qquad (5\text{-}9)$$

where x is the summation of Fe and Al content in per formula unit, $\kappa_{\mathrm{bdg},x}$ is the κ_{latt} of bdg with Fe+Al=x (pfu), respectively. In the same manner, we calculated the $\kappa_{\mathrm{bdg},x}(P, 300\ \mathrm{K})$ at pressure from 20 to 135 GPa in 5 GPa steps (supplied in Supplemental material S5-6), which was used for the estimation of the κ_{latt} of bdg along the geotherm (further discuss in *section 5.4.6*).

5.4.5. Effect of the spin transition of Fe on the κ_{latt} of bdg

In the previous section, we estimated the high-pressure κ_{latt} of gF9A12 and gF12A28 by using our obtained κ_{latt} data except at 20−40 GPa. We regard these estimated κ_{latt} as those when Fe is in the HS or LS state ($\kappa_{\mathrm{HS,\,LS}}$), while κ_{latt} data at 20−40 GPa is treated as the conductivity when Fe is in the MS state (κ_{MS}). The contribution of phonon scattering by MS state Fe ions to the κ_{latt} of gF9A12 and gF12A28 were estimated by rationing the $\kappa_{\mathrm{HS,\,LS}}$ and κ_{MS}. The κ_{MS} /$\kappa_{\mathrm{HS,\,LS}}$ was 46 ± 16% in average, i.e., the κ for both bdg samples in the MS state were reduced by 46 ± 16% as those in the HS and LS state (see Supplemental material S5-7 for detail).

5.4.6. Estimation of the κ_{latt} of bdg along mantle geotherm

With a combination of the compositional effect of Fe and Al (provided in *section* (*5.4.4*)), and the effect of spin transition of Fe (provided in *section* (*5.4.5*)), we used the following models for the estimation of the κ_{latt} of (Fe,Al)-bearing bdg at high *P-T* conditions where Fe is in the HS or LS state ($\kappa_{\mathrm{bdg\_}x\mathrm{\_HS,\,LS}}$) and in the MS state ($\kappa_{\mathrm{bdg\_}x\mathrm{\_MS}}$), respectively:

$$\kappa_{\mathrm{bdg}\_x\_HS,LS}(P,T) = \kappa_{\mathrm{bdg},x}(P, 300\ \mathrm{K})\left(\frac{300\ \mathrm{K}}{T}\right)^{a}, \qquad (5\text{-}10)$$

$$\kappa_{\mathrm{bdg}\_x\_MS}(P,T) = f \times \kappa_{\mathrm{bdg},x}(P, 300\ \mathrm{K})\left(\frac{300\ \mathrm{K}}{T}\right)^{a}, \qquad (5\text{-}11)$$

where x is the summation of Fe and Al content in per formula unit, $\kappa_{\mathrm{bdg},x}$ (P, 300 K) is the κ_{latt} of bdg with Fe+Al=x (pfu) at certain pressure and ambient temperature, f is the κ_{MS}

/$\kappa_{HS,\,LS}$ value of 46 ± 16% and a is temperature dependence coefficient, respectively. We used the temperature dependence coefficient a of 0.37−0.43, which is the a value of (Fe,Al)-bearing bdg constrained in Okuda et al. (2017) for further discussion.

5.5. Geophysical implications

5.5.1. κ of bdg in the Earth's lower mantle

Onset pressure of the spin transition of Fe in bdg is extremely important for constraining the thermodynamic properties in the lower mantle, however there is a huge discrepancy in the reported transition pressure, and currently lacks the *in situ* high-*P,T* experimental reports (e.g., Jackson et al., 2005; Catalli et al., 2011; Hsu et al., 2011; Kupenko et al., 2015; Sinmyo et al., 2017; Zhu et al., 2020; Okuda et al., 2020). We used the reported transition pressure in Tsuchiya and Wang (2013), which provided the temperature effect on the onset pressure. These authors suggested that temperature enhances the onset pressure of the spin transition of Fe in bdg, and they showed that the HS to LS transition of Fe would occur at the pressure range of 84−89 GPa along the geotherm (Brown and Shankland, 1981). By using Eqs. (5-10, 5-11), the suggested geotherm (Brown and Shankland, 1981) and the onset pressure of 84−89 GPa for the spin transition of Fe in bdg (Tsuchiya and Wang, 2013), we estimated the κ_{latt} of bdg in the pyrolitic lower mantle and in the descending MORB. We used the typical Fe and Al

contents of both 10 mol% (Sinmyo et al., 2011), and 30.6 and 29.4 mol% (Hirose et al., 2005), respectively. For the model on bdg in MORB, since MORB in the subducting slab is colder than the surrounding mantle, we applied a typical value of 560 K (Chang et al., 2017) for the temperature difference between such MORB and the surrounding lower mantle (discussed further later). Figure 5-6 shows the detailed κ_{latt} profile of bdg in the pyrolitic lower mantle and in subducted MORB, extended from Okuda et al. (2017) with respect to the addition of the effect of compositional difference and spin transition of Fe. The κ_{latt} of bdg in the pyrolitic lower mantle is slightly higher than that in MORB at the Earth's uppermost mantle, which possess κ_{latt} of 4.1 ± 0.2 and 3.8 ± 0.2 W/m/K respectively when using a geotherm with temperature of 1400℃ at 660 km (Fig. 5-6a), and κ_{latt} of 3.6 ± 0.2 and 3.2 ± 0.2 W/m/K respectively, when using a geotherm with temperature of 2000℃ at 660 km (Fig. 5-6b). Both κ_{latt} increases with depth, however the κ_{latt} of bdg in the pyrolitic lower mantle is reduced at 1950−2050 km due to the effect of the spin transition of Fe, which has a conductivity of 3.8 ± 1.3 W/m/K. This 3.8 ± 1.3 W/m/K is a significantly small amount of conductivity, which is even a consistent value as the radiative thermal conductivity (κ_{rad}) in such *P*-*T* conditions (Goncharov et al., 2015), when using the geotherm with temperature of 2000 ℃ at 660 km (Brown and Shankland, 1981). At further depth, both conductivities increase up to the thermal boundary layer (TBL) above the CMB and drops at the CMB to 9.4 ± 0.7 and 6.4 ± 0.5 W/m/K respectively due to the high temperature in this region. Here, we assumed the CMB temperature to be 3700 K (Tateno et al., 2009). As mentioned above, we used a typical value of 560 K (Chang et al., 2017) for the temperature difference between the subducted

MORB and the surrounding lower mantle. Even so, we further investigated the effect of temperature contrast between them on the κ_{latt} of bdg in MORB. We found that a temperature difference of 200−800 K only changes the κ_{latt} of bdg in subducted MORB from 6.4 ± 0.5 W/m/K to 6.9 ± 0.5 W/m/K (Supplemental material S5-8), indicating that the effect of the temperature contrast between the subducted MORB and the surrounding lower mantle on the κ_{latt} of bdg is minimal. Thus, we emphasize that our estimated κ_{latt} of bdg with temperature contrast of 560 K for subducted MORB and the surrounding lower mantle is a reliable κ profile.

Total thermal conductivity of bdg is the summation of κ_{latt} and κ_{rad}. There are three previous reports on the κ_{rad} measurement of bdg (Keppler et al., 2008; Goncharov et al., 2008; Goncharov et al., 2015), revealing a common trend that the amount of Fe^{3+} enhances the κ_{rad} of bdg (also discussed in Okuda et al., 2017). (Fe,Al)-bearing bdg in the Earth's lower mantle is thought to have a $Fe^{3+}/\sum Fe$ ratio of ~0.5 (e.g., Frost et al., 2004; Sinmyo et al., 2011). The $Fe^{3+}/\sum Fe$ ratio of bdg sample used in Goncharov et al. (2015) is ~0.5, which is therefore suitable for estimating the κ_{rad} of bdg in the pyrolitic lower mantle. The pressure dependence of κ_{rad} of bdg was investigated by previous studies (Keppler et al., 2008; Goncharov et al., 2008; Goncharov et al., 2015), which seems to be slightly reduced (within 10%) with increasing pressure, at the temperature range in the Earth's lower mantle (Keppler et al., 2008; Goncharov et al., 2008; Goncharov et al., 2015). However, the quantification of the pressure dependence of κ_{rad} of bdg is still difficult, because Goncharov et al. (2015) only measured the κ_{rad} at 0 and 46 GPa. Thus,

we simply used the temperature-dependence of κ_{rad} obtained at 46 GPa in Goncharov et al. (2015), to estimate the κ_{rad} in pyrolitic lower mantle along the geotherm. Taking into account that an increase in Fe content decreases the κ_{rad}, the radiative conduction of bdg in MORB is negligible due to a much larger amount of Fe. As a result, the total κ ($=\kappa_{latt}+\kappa_{rad}$) of bdg at the CMB conditions is constrained to be 15.3 ± 0.7 W/m/K for those in the pyrolitic lower mantle, and 6.4 ± 0.5 W/m/K for those in the subducted MORB (Fig. 5-6). Such a difference in the κ would generate heterogeneity in lateral heat flow across the CMB, which was also suggested in Stackhouse et al. (2015). Still, note that we cannot estimate the actual conductivity of the subducted MORB because of the lack of information about both κ_{latt} and κ_{rad} in other minerals such as SiO_2 phase, $CaSiO_3$ perovskite (Ca-Pv) and Al-rich phase.

The reduced κ of bdg at the mid lower mantle due to the spin transition of Fe lowers the total κ of the lower mantle in this region (Fig. 5-6). This should create a thermal insulating layer in the mid lower mantle, which has profound implications for mantle dynamics.

5.5.2. Effect of spin transition on κ of other minerals in the Earth's mantle

We suggested that the κ_{latt} of major minerals in the Earth's lower mantle, such as bdg and fp, would decrease under their spin transition of Fe due to the disordered lattice in the MS state (Supplemental material S5-4). In this nature, such a reduction in κ_{latt} may also exist in other Fe-bearing minerals. For instance, MORB in the lower mantle consists

of 31% of (Fe,Al)-rich bdg, 23% of Ca-Pv, 23% of SiO_2 phase (stishovite, $CaCl_2$-type or α-PbO_2-type SiO_2 (seifertite)) and 23% of NAL (new aluminous phase) phase and CF (calcium ferrite-type aluminous phase) phase (Hirose et al., 2005), and all of these minerals except for SiO_2 phase are thought to contain Fe (Hirose et al., 2005). Recent experiments and calculation found that both Fe-bearing NAL and CF undergo spin transition (Wu et al., 2016; Hsu, 2017; Wu et al., 2017). For NAL, experimental research based on the combination of synchrotron nuclear forward scattering (NFS) and XRD showed that the octahedral Fe^{3+} in the Fe-bearing NAL ($Na_{0.71}Mg_{2.05}Al_{4.62}Si_{1.16}Fe^{2+}_{0.09}Fe^{3+}_{0.17}O_{12}$) underwent spin transition at 33−47 GPa (Wu et al., 2016). Recent calculation results also supported that only the Fe^{3+} in the octahedral site undergoes a spin transition at ~40 GPa (Hsu, 2017). With respect to CF, the octahedral Fe^{3+} in the Fe-bearing CF phase ($Na_{0.88}Al_{0.99}Fe_{0.13}Si_{0.94}O_4$) was found to undergo a spin transition at 25−35 GPa (Wu et al., 2017), based on the same methodology of Wu et al. (2016). Thus, it can be assumed that NAL and CF, as well as fp and bdg, may also show significantly low κ_{latt} at a certain pressure range (Wu et al., 2016; Wu et al., 2017). Since the heat inside the descending slab and MORB is predominantly transported by lattice conduction, the κ of MORB-constituting minerals directly determines the temperature structure inside the MORB. If the κ_{latt} of NAL and CF phase would be reduced due to the disordered lattice, the temperature of MORB would be lower than the previous estimation, which should have important implications for mantle dynamics and water transportation.

5.6. Conclusions

We measured the κ_{latt} of (Fe,Al)-bearing bdg of $Mg_{0.848}Fe_{0.090}Al_{0.206}Si_{0.856}O_3$ (gF9A21) and $Mg_{0.718}Fe_{0.123}Al_{0.281}Si_{0.878}O_3$ (gF12A28) under high pressure and 300 K in a DAC. The present results showed abnormally low κ_{latt} at the pressure range of 20−40 GPa, which may be due to the spin transition of octahedral Fe^{3+}. We further analyzed the present results and previous studies, and we suggest the following for the κ_{latt} of (Fe,Al)-bearing bdg:

・ When Fe is in the MS state, κ_{latt} of bdg is reduced by 46 ± 16% compared to HS or LS state, due to the disordered lattice (Supplemental material S5-4).

・ The compositional effect on the κ_{latt} of (Fe,Al)-bearing bdg (κ_x) is linearly proportional to the Fe+Al (=x, in pfu) content (Fig. 5-5; Supplemental material S5-6).

By using the obtained κ_{latt} model of bdg, we calculated the κ_{latt} profile of bdg in the Earth's lower mantle. As a result, we found that the κ of bdg in the pyrolitic lower mantle and in the MORB may alter by more than a factor of two, mainly due to the compositional effect and the κ_{rad} effect. This κ difference should create heterogeneity of lateral heat flux across the CMB. Here we note that further investigations into the κ of Ca-Pv and the other MORB-constituting minerals are required for the better constraint of the κ difference between the subducted MORB and the surrounding lower mantle. In addition, our κ measurements has so far remained at ambient temperature conditions. Considering that

the temperature may enhance the spin transition pressure (Tsuchiya and Wang., 2013), future work should focus on κ measurements at high temperature as well as high pressure.

5.7. References

Akahama, Y., Kawamura, H., 2006. Pressure calibration of diamond anvil Raman gauge to 310 GPa. J. Appl. Phys. 100, 043516.

Ammann, M., Walker, A., Stackhouse, S., Wookey, J., Forte, A., Brodholt, J., Dobson, D., 2014. Variation of thermal conductivity and heat flux at the Earth's core mantle boundary. Earth Planet. Sci. Lett. 390, 175–185.

Boffa-Ballaran, T., Kurnosov, A., Glazyrin, K., Frost, D.J., Merlini, M., Hanfland, M., Caracas, R., 2012. Effect of chemistry on the compressibility of silicate perovskite in the lower mantle. Earth Planet. Sci. Lett. 333–334, 181–190.

Brown, J. M., Shankland, T. J., 1981. Thermodynamic parameters in the Earth as determined from seismic profiles. Geophys. J. R. astr. Soc. 66, 579–596.

Catalli, K., Shim, S.H., Dera, P., Prakapenka, V.B., Zhao, J.Y., Sturhahn, W., Chow, P., Xiao, Y.M., Cynn, H., Evans, W.J., 2011. Effects of the Fe^{3+} spin transition on the properties of aluminous perovskite-New insights for lower-mantle seismic heterogeneities. Earth Planet. Sci. Lett. 310, 293–302.

Chang, Y. Y., Hsieh, W. P., Tan, E., Chen, J., 2017. Hydration-reduced lattice thermal conductivity of olivine in Earth's upper mantle. Proc. Natl. Acad. Sci. 114, 4078–4081.

Dekura, H., Tsuchiya, T., Tsuchiya, J., 2013. *Ab initio* lattice thermal conductivity of $MgSiO_3$ perovskite as found in Earth's lower mantle. Phys. Rev. Lett. 110, 025904.

Frost, D.J., Liebske, C., Langenhorst, F., McCammon, C.A., Trønnes, R.G., Rubie, D.C., 2004. Experimental evidence for the existence of iron-rich metal in the Earth's lower mantle. Nature 428, 409–412.

Ghaderi, N., Zhang, D-B., Zhang, H., Xian, J., Wentzcovitch, R.M., Sun, T., 2017. Lattice Thermal Conductivity of $MgSiO_3$ Perovskite from First Principles. Sci. Rep. 7, 5417.

Goncharov, A.F., Haugen, B.D., Struzhkin, V.V., Beck, P., Jacobsen, S.D., 2008. Radiative conductivity in the Earth's lower mantle. Nature 456, 231–234.

Goncharov, A.F., Lobanov, S., Tan, X., Hohensee, G., Cahill, D., Lin, J. F., Thomas, S. M., Okuchi, T., Tomioka, N., 2015. Experimental study of thermal conductivity at

high pressures: Implications for the deep Earth's interior. Phys. Earth Planet. Inter. 247, 11–16.

Haigis, V., Salanne, M., Jahn, S., 2012. Thermal conductivity of MgO, $MgSiO_3$ perovskite and post-perovskite in the Earth's deep mantle. Earth Planet. Sci. Lett. 355-356, 102–108.

Hirose, K., Takafuji, N., Sata, N., Ohishi, Y., 2005. Phase transition and density of subducted MORB crust in the lower mantle. Earth Planet. Sci. Lett. 237, 239–251.

Ho, C., Powell, R., Liley, P., 1972. Thermal Conductivity of the Elements. J. Phys. Chem. Ref. Data 1, 279–421.

Hofmeister, A. M., 1999. Mantle Values of Thermal Conductivity and the Geotherm from Phonon Lifetimes. Science 283 (5408), 1699–1706.

Hsieh, W. P., Deschamps, F., Okuchi, T., Lin, J. F., 2017. Reduced lattice thermal conductivity of Fe-bearing bridgmanite in Earth's deep mantle. J. Geophys. Res. Sol. Earth 122, 7, 4900–4917.

Hsieh, W.P., Deschamps, F., Okuchi, T., Lin, J.F., 2018. Effects of iron on the lattice thermal conductivity of Earth's deep mantle and implications for mantle dynamics. Proc. Natl. Acad. Sci. U.S.A. https://doi.org/10.1073/pnas.1718557115

Hsu, H., Blaha, P., Cococcioni, M., Wentzcovitch, R.M., 2011. Spin-state crossover and hyperfine interactions of ferric iron in $MgSiO_3$ perovskite. Phys. Rev. Lett. 106, doi: 10.1103/Physrevlett.106.118501.

Hsu, H., 2017. First-principles study of iron spin crossover in the new hexagonal aluminous phase. Phys. Rev. B, 95, 020406.

Jackson, J.M., Sturhahn, W., Shen, G.Y., Zhao, J.Y., Hu, M.Y., Errandonea, D., Bass, J.D., Fei, Y.W., 2005. A synchrotron Mössbauer spectroscopy study of $(Mg,Fe)SiO_3$ perovskite up to 120 GPa. Am. Mineral. 90, 199–205.

Keppler, H., Dubrovinsky, L.S., Narygina, O., Kantor, I., 2008. Optical absorption and radiative thermal conductivity of silicate perovskite to 125 gigapascals. Science 322, 1529–1532.

Kupenko, I., McCammon, C., Sinmyo, R., Cerantola, V., Potapkin, V., Chumakov, A.I., Kantor, A., Rüffer, R., Dubrovinsky, L., 2015. Oxidation state of the lower mantle: in situ observations of the iron electronic configuration in bridgmanite at extreme conditions. Earth Planet. Sci. Lett. 423, 78–86.

Lay, T., Hernlund, J., Buffett, B., 2008. Core–mantle boundary heat flow. Nat. Geosci. 1, 25–32.

Li, Y., Viella, K., Deschamps, F., Zhao, L., Tackley, P.J., 2018. Effects of iron spin transition on the structure and stability of large primordial reservoirs in Earth's lower mantle. Geophys. Res. Lett. 45, 5918–5928.

Lin, J.F., Speziale, S., Mao, Z., Marquardt, H., 2013. Effects of the electronic spin transitions of iron in lower mantle minerals: Implications for deep mantle geophysics and geochemistry. Rev. Geophys. 61, 244–275.

Liu, J., Dorfman, S.M., Zhu, F., Li, J., Wang, Y., Zhang, D., Xiao, Y., Bi, W., Ercan Alp, E., 2018. Valence and spin states of iron are invisible in Earth's lower mantle. Nat. Commun. 9, 1284. doi:10.1038/S51467-018-03671-5.

Manthilake, G.M., de Koker, N., Frost, D.J., McCammon, C.A., 2011. Lattice thermal conductivity of lower mantle minerals and heat flux from Earth's core. Proc. Natl. Acad. Sci. U.S.A. 108, 17901–17904.

Mao, H.K., Xu, J., Bell, P. M., 1986. Calibration of the Ruby Pressure Gauge to 800 kbar Under Quasi-Hydrostatic Conditions. J. Geophys. Res. 41, 4673–4676.

Mao, Z., Lin, J.F., Yang, J., Inoue, T., Prakapenka, V.B., 2015. Effects of the Fe^{3+} spin transition on the equation of state of bridgmanite. Geophys. Res. Lett. 42, 4335–4342.

Mao, Z., Wang, F., Lin, J.F., Fu, S., Yang, J., Wu, X., Okuchi, T., Tomioka, N., Prakapenka, V. B., Xiao, Y., Chow, P., 2017. Equation of state and hyperfine parameters of high-spin bridgmanite in the Earth's lower mantle by synchrotron X-ray diffraction and Mössbauer spectroscopy. Am. Mineral. 102, 357–368.

Ohta, K., Yagi, T., Taketoshi, N., Hirose, K., Komabayashi, T. Baba, T., Ohishi, Y., Hernlund, J., 2012. Lattice thermal conductivity of $MgSiO_3$ perovskite and post-perovskite at the core-mantle boundary. Earth Planet. Sci. Lett. 349-350, 109–115.

Ohta, K., Yagi, T. Hirose, K., 2014. Thermal diffusivities of $MgSiO_3$ and Al-bearing $MgSiO_3$ perovskites. Am. Mineral. 99, 94–97.

Ohta, K., Yagi, T., Hirose, K., Ohishi, Y., 2017. Thermal conductivity of ferropericlase in the Earth's lower mantle. Earth Planet. Sci. Lett. 465, 29–37.

O'Keeffe, M., Hyde, B.G., 1977. Some structures topologically related to cubic perovskite (*E*21), ReO3 (*D*09) and Cu3Au (*L*12). Acta Cryst. B33, 3802–3813.

Okuda, Y., Ohta, K., Yagi, T., Sinmyo, R., Wakamatsu, T., Hirose, K., Ohishi, Y., 2017. The effect of iron and aluminum incorporation on lattice thermal conductivity of bridgmanite at the Earth's lower mantle. Earth Planet. Sci. Lett. 474, 25–31.

Okuda, Y., Ohta, K., Sinmyo, R., Hirose, K., Ohishi, Y., 2020. Anomalous compressibility in (Fe,Al)-bearing bridgmanite: implications for the spin state of iron. Phys. Chem. Miner. 47, 40. https://doi.org/10.1007/s00269-020-01109-3

Osako, M., Ito, E., 1991. Thermal diffusivity of $MgSiO_3$ perovskite. Geophys. Res. Lett. 18, 239–242.

Ross, R.G., Andersson, P., Sundqvist, B., Bäckström, G., 1984. Thermal conductivity of solids and liquids under pressure. Rep. Prog. PhyS57, 1347–1402.

Shannon, R. D., 1976. Revised effective ionic radii and systematic studies of interatomic distances in halides and chalcogenides. Acta Crystallogr. A 32, 751–767.

Sinmyo, R., Hirose, K., Muto, S., Ohishi, Y., Yasuhara, A., 2011. The valence state and partitioning of iron in the Earth's lowermost mantle. J. Geophys. Res. 116, B07205.

Sinmyo, R., McCammon, C., Dubrovinsky, L., 2017. The spin state of Fe^{3+} in lower mantle bridgmanite. Am. Mineral. 102, 1263–1269.

Stackhouse, S., Stixrude, L., Karki, B., 2015. First-principles calculations of the lattice thermal conductivity of the lower mantle. Earth Planet. Sci. Lett. 427, 11–17.

Sun, N., Wei, W., Han, S., Song, J., Li, X., Duan, Y., Prakapenka, V.B., Mao, Z., 2018. Phase transition and thermal equations of state of (Fe,Al)-bridgmanite and post-perovskite: Implication for the chemical heterogeneity at the lowermost mantle. Earth Planet. Sci. Lett. 490, 161–169.

Tang, X., Ntam, M., Dong, J., Rainey, E., Kavner, A., 2014. The thermal conductivity of Earth's lower mantle. Geophys. Res. Lett. 41, 2746–2752.

Tateno, S., Hirose, K., Sata, N., Ohishi, Y., 2009. Determination of post-perovskite phase transition boundary up to 4400 K and implications for thermal structure in D″ layer. Earth Planet. Sci. Lett. 277, 130–136.

Tsuchiya, T., 2003. First-principles prediction of the *P-V-T* equation of state of gold and the 660-km discontinuity in Earth's mantle. J. Geophys. Res. 108, 2462.

Tsuchiya, T., and X. Wang (2013), Ab initio investigation on the high-temperature thermodynamic properties of Fe^{3+}-bearing $MgSiO_3$ perovskite, J. Geophys. Res. Solid Earth, 118, 83–91.

Wu, Y., Wu, X., Lin, J. F., McCammon, C. A., Xiao, Y., Chow, P., Prakapenka, V. B., Yoshino, T., Zhai, S., Qin, S., 2016. Spin transition of ferric iron in the NAL phase: Implications for the seismic heterogeneities of subducted slabs in the lower mantle. Earth Planet. Sci. Lett. 434, 91–100.

Wu, Y., Qin, F., Wu, X., Huang, H., McCammon, C. A., Yoshino, T., Zhai, S., Xiao, Y., Prakapenka, V. B., 2017. Spin transition of ferric iron in the calcium-ferrite type aluminous phase. J. Geophys. Res. Solid Earth 122, 5935–5944.

Yagi, T., Ohta, K. Kobayashi, K., Taketoshi, N., Hirose, K., Baba, T., 2011. Thermal diffusivity measurement in a diamond anvil cell using a light pulse thermoreflectance technique. Meas. Sci. Technol. 22, 024011.

Zhang, D., Allen, B. P., Sun, T., Wentzcovitch, M. R., 2017. Thermal conductivity from phonon quasiparticles with subminimal mean free path in the $MgSiO_3$ perovskite. Phys. Rev. B. 96, 100302.

Zhu, F., Liu, J., Lai, X., Xiao, Y., Prakapenka, V., Bi, W., Alp, E.E., Dera, P., Chen, B., Li, J., 2020. Synthesis, Elasticity, and Spin State of an Intermediate $MgSiO_3$ - $FeAlO_3$ Bridgmanite: Implications for Iron in Earth's Lower Mantle. J. Geophys. Res. Solid Earth 125. https://doi.org/10.1029/2020JB019964

Table 5-1. Thermodynamic properties used in the evaluation of the lattice thermal conductivity, experimental conditions, thermal diffusivity and conductivity of $Mg_{0.848}Fe_{0.090}Al_{0.206}Si_{0.856}O_3$ (gF9A21) and $Mg_{0.718}Fe_{0.123}Al_{0.281}Si_{0.878}O_3$ (gF12A28)

gF9A21 ($Mg_{0.848}Fe_{0.090}Al_{0.206}Si_{0.856}O_3$)

Run#	Synthesized Pressure (GPa)	Pressure (GPa)	Pressure medium	raw τ_{total} (μs)	raw d (μm)	Reduction rate of d at high P(%)	d after correction (μm)	d_{Au} ($\times10^2$ nm)	d_{Au} after correction ($\times10^2$ nm)	V/V_0 of bdg	$C_{bdg}\times10^{-6}$ (J/m^{3}K)	V/V_0 of Au	ρ_{Au} (kg/m^3)	C_p of Au (J/kg/K)	$C_{Au}\times10^{-6}$ (J/m^{3}K)	Γ	α_{Au} (P) ($\times10^3$ m^2/s)	τ_{bdg} (μs)	D_{bdg} (mm^2/s)	ρ_{bdg} (kg/m^3)	C_p of bdg (J/kg/K)	κ_{bdg} (W/(m*K))	Pressure error (GPa)
1	125	125	KCl	1.27(4)	2.97(28)	91.3	2.71	1.73(6)	1.58	0.74	1.50	0.73	29502	121	3.56	7.2	3.71	0.84(3)	8.8(17)	5561	449	21.9(43)	6.25*
2	52	52	SiO_2 glass	6.23(6)	4.30(64)	94.9	4.09	2.36(94)	2.22	0.85	1.66	0.83	26015	125	3.25	9.4	0.20	4.43(4)	3.8(11)	4851	571	10.4(31)	2.6*
		50	SiO_2 glass	5.44(12)		95.1	4.09		2.22	0.85	1.67	0.84	25894	125	3.24	9.5	0.18	3.87(8)	4.3(13)	4828	576	12.0(36)	5
		42	SiO_2 glass	21.56(4)		95.6	4.12		2.24	0.87	1.69	0.85	25387	126	3.19	9.7	0.13	15.48(3)	1.1(3)	4732	596	3.1(9)	4.2
		24	SiO_2 glass	15.90(11)		97.2	4.18		2.28	0.92	1.75	0.90	24081	127	3.06	10.5	0.07	11.6(1)	1.5(4)	4495	649	4.4(13)	2.4
3	78	78	KCl	0.80(3)	1.89(22)	93.4	1.76	1.92(95)	1.78	0.80	1.59	0.79	27432	123	3.38	4.6	0.57	0.45(2)	7.0(17)	5132	516	18.5(44)	3.9*
		57	KCl	1.00(3)		94.6	1.79		1.81	0.84	2.74	0.82	26309	125	3.28	8.3	0.24	0.68(2)	4.7(11)	4908	559	12.8(30)	5.7
		42	KCl	2.94(10)		95.6	1.81		1.83	0.87	2.82	0.85	25387	126	3.19	8.8	0.13	2.05(7)	1.6(4)	4732	596	4.5(11)	4.2
		24	KCl	5.40(5)		97.4	1.84		1.85	0.92	3.02	0.90	24081	127	3.06	9.8	0.07	3.88(3)	0.9(2)	4495	671	2.6(6)	2.4
		0	KCl	3.11(7)		100	1.89		1.92	1.00	3.04	1.00	21674	130	2.82	10.6	0.03	2.29(5)	1.6(4)	4114	741	4.8(11)	0

gF12A28 ($Mg_{0.718}Fe_{0.123}Al_{0.281}Si_{0.878}O_3$)

Run#	Synthesized Pressure (GPa)	Pressure (GPa)	Pressure medium	raw τ_{total} (μs)	raw d (μm)	Reduction rate of d at high P(%)	d after correction (μm)	d_{Au} ($\times10^2$ nm)	d_{Au} after correction ($\times10^2$ nm)	V/V_0 of bdg	$C_{bdg}\times10^{-6}$ (J/m^{3}K)	V/V_0 of Au	ρ_{Au} (kg/m^3)	C_p of Au (J/kg/K)	$C_{Au}\times10^{-6}$ (J/m^{3}K)	Γ	α_{Au} (P) ($\times10^3$ m^2/s)	τ_{bdg} (μs)	D_{bdg} (mm^2/s)	ρ_{bdg} (kg/m^3)	C_p of bdg (J/kg/K)	κ_{bdg} (W/(m*K))	Pressure error (GPa)
1	43	43	KCl	5.16(3)	3.28(19)	95.6	3.14	3.09(23)	2.93	0.87	2.82	0.85	25440	126	3.2	9.4	0.14	3.67(2)	2.7(3)	4789	588	7.6(9)	2.14*
2	122	74	SiO_2 glass	0.94(4)	1.95(42)	93.6	1.83	1.92(95)	1.79	0.81	2.66	0.80	27231	123	3.36	8.1	0.48	0.64(2)	5.2(23)	5142	518	13.9(60)	7.4
		47	SiO_2 glass	1.50(4)		95.3	1.86		1.82	0.86	2.79	0.84	25708	125	3.22	8.9	0.16	1.05(3)	3.3(14)	4841	577	9.2(40)	4.7
		33	SiO_2 glass	3.44(5)		96.4	1.88		1.84	0.89	2.87	0.88	24768	126	3.13	9.4	0.09	2.45(4)	1.4(6)	4664	615	4.2(18)	3.3
		0	SiO_2 glass	3.44(5)		100	1.95		1.92	1.00	3.04	1.00	21674	130	2.82	11.0	0.03	2.54(4)	1.5(6)	4155	733	4.6(20)	0
3	71	46	KCl	9.56(11)	4.98(46)	95.3	4.74	2.27(72)	2.16	0.86	2.80	0.85	25645	125	3.21	19.2	0.16	7.94(9)	2.8(5)	4829	580	7.9(15)	4.6
		38	KCl	10.87(18)		96.0	4.78		2.17	0.88	2.84	0.86	25119	126	3.16	19.8	0.11	9.07(15)	2.5(5)	4729	601	7.1(13)	3.8
		26	KCl	21.30(26)		97.0	4.83		2.19	0.91	2.91	0.89	24240	127	3.08	20.8	0.07	17.92(21)	1.3(2)	4568	636	3.8(7)	2.6

*data obtained after thermal annealing, and pressure calibration based on the EOS of gold (Tsuchiya, 2003)

We used typical values of 10% and 5% for pressure errors with pressure calibration using Raman spectroscopy of diamond and EOS of gold, respectively.

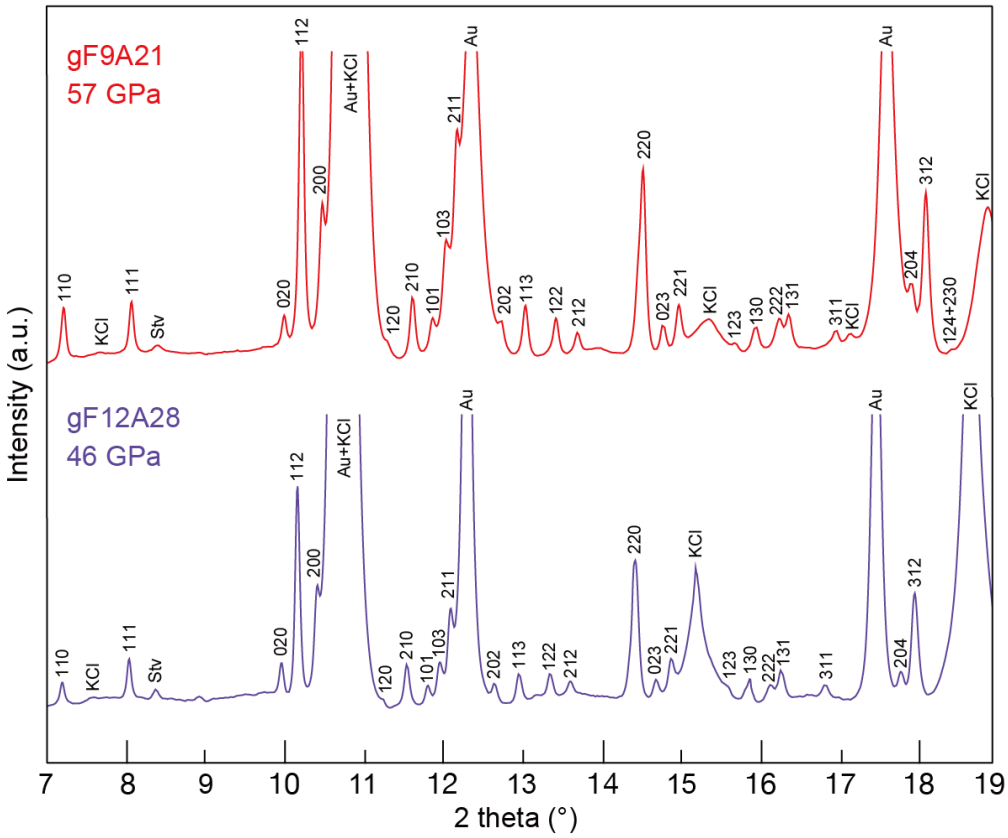

Fig. 5-1. XRD patterns of synthesized bdg sample gF9A21 and gF12A28. XRD pattern of gF9A21 (red) and gF12A28 (purple) synthesized both in run #3 (Table 5-1). The numbers in the figure indicate Miller indices of bdg. The notations Stv, Au and KCl in the figure denote diffraction peaks from stishovite, gold for pressure marker and KCl for pressure medium, respectively.

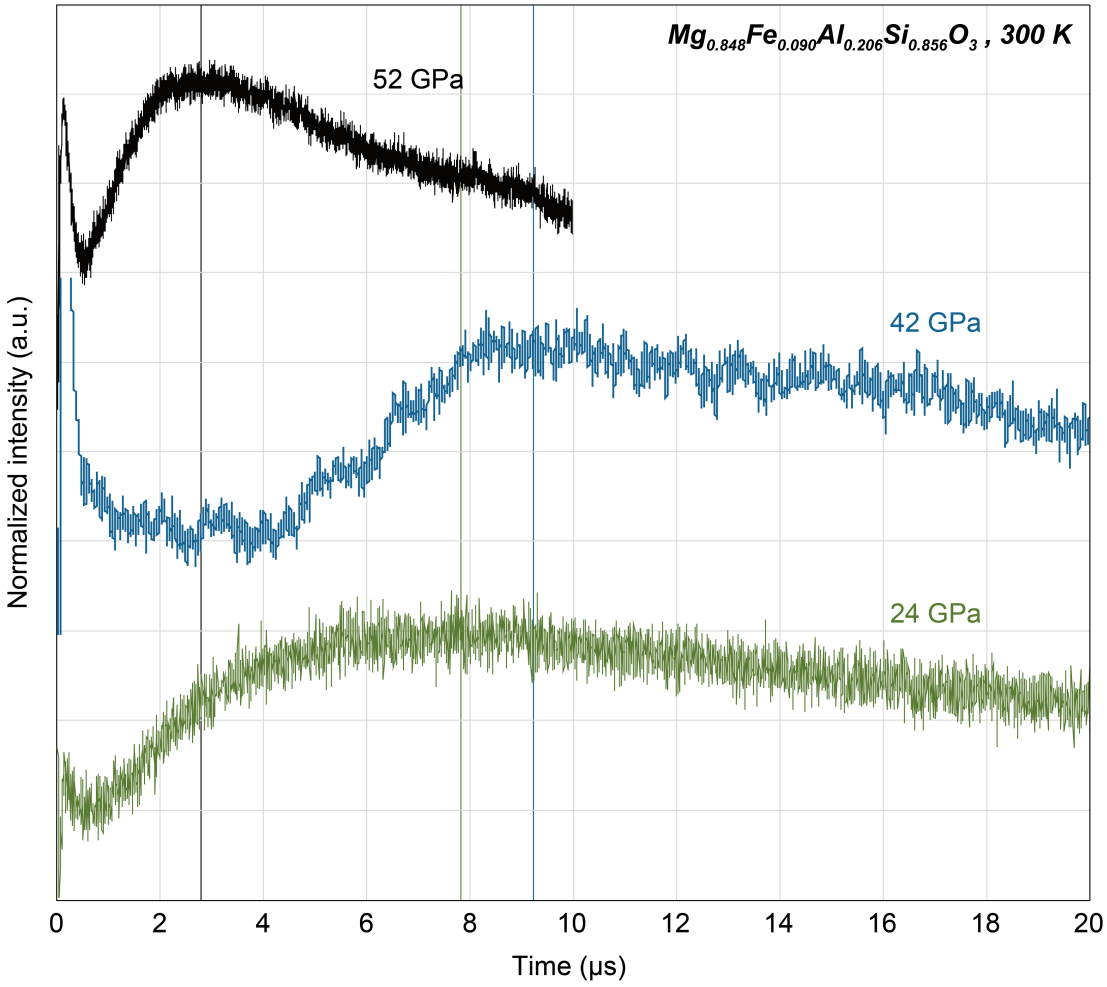

Fig. 5-2. Obtained transient temperature curves at high pressure and at ambient temperature. Black, blue and green curves indicate temperature history curves of gF9A21 obtained at 52 GPa, 42 GPa and 24 GPa in run #2, respectively. Black, blue and green lines indicate the position of peak maximum in the temperature history curve.

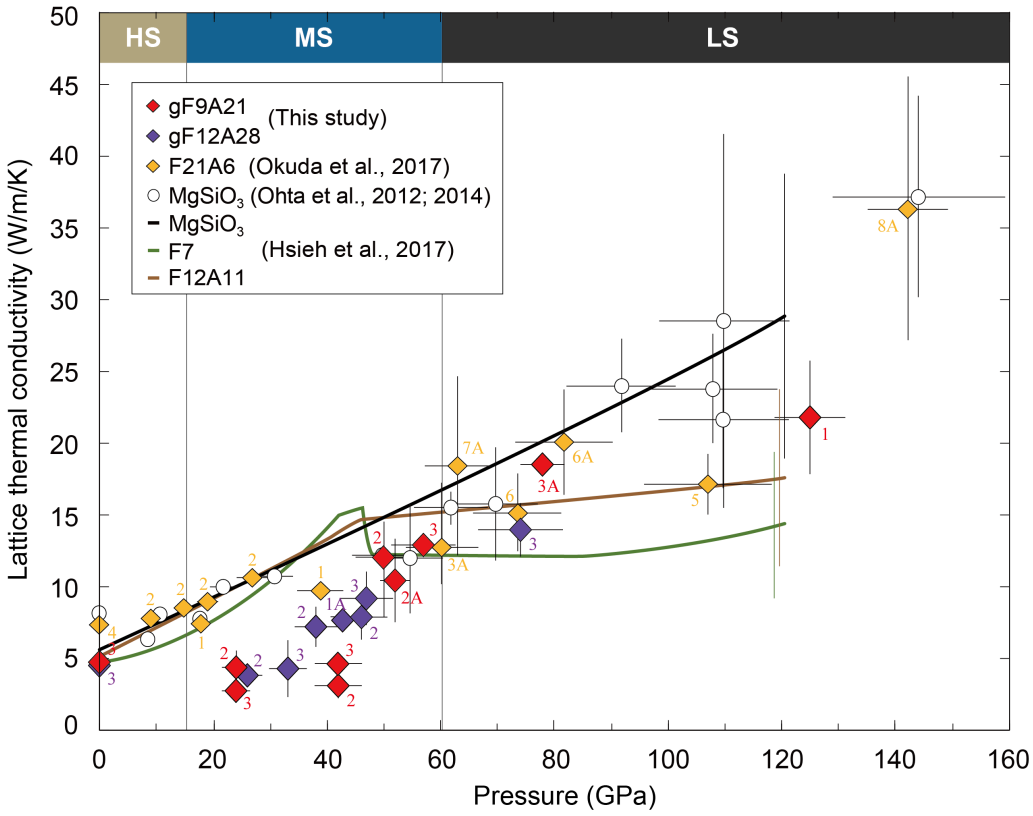

Fig. 5-3. Lattice thermal conductivity of $Mg_{0.848}Fe_{0.090}Al_{0.206}Si_{0.856}O_3$ bdg (gF9A21) and $Mg_{0.718}Fe_{0.123}Al_{0.281}Si_{0.878}O_3$ bdg (gF12A28) at 300 K. Red diamonds, gF9A21: $Mg_{0.848}Fe_{0.090}Al_{0.206}Si_{0.856}O_3$ bdg (this study); purple diamonds, gF12A28: $Mg_{0.718}Fe_{0.123}Al_{0.281}Si_{0.878}O_3$ bdg (this study); orange diamonds, $Mg_{0.832}Fe_{0.209}Al_{0.060}Si_{0.916}O_3$ bdg (Okuda et al., 2017); open circles, $MgSiO_3$ bdg (Ohta et al., 2012, 2014); black, green and brown curves, $MgSiO_3$, $Mg_{0.96}Fe_{0.07}Si_{0.98}O_3$ and $Mg_{0.89}Fe_{0.12}Al_{0.11}Si_{0.89}O_3$ bdg (Hsieh et al., 2017). The rightmost vertical line in black, green and brown curves indicate the measurement uncertainties reported in Hsieh et al. (2017). "A" in the figure indicates annealed data, and numbers indicate run numbers. HS, MS and LS in the top of the figure indicate the suggested pressure range of the spin state of high-spin, mixed-spin and low-spin of Fe, respectively (Lin et al., 2013).

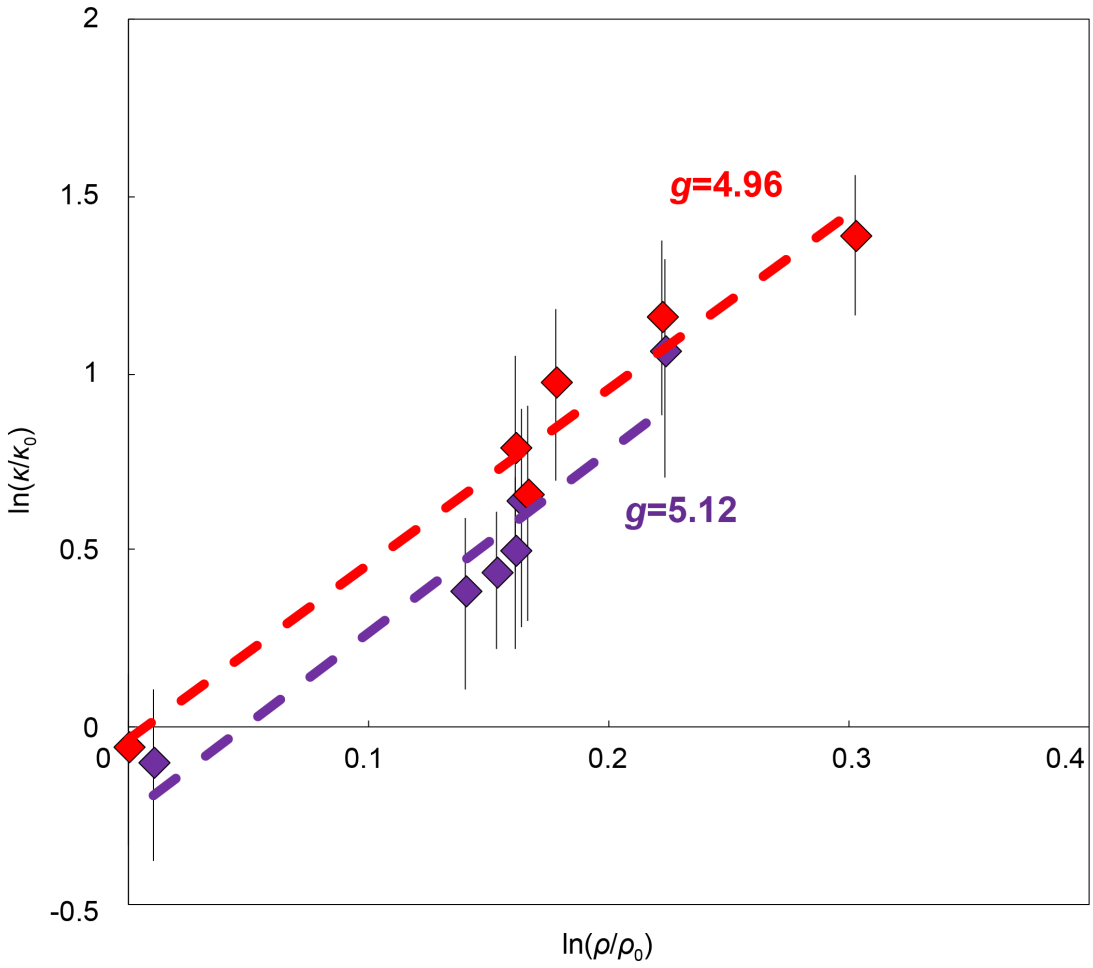

Fig. 5-4. Thermal conductivity (κ) of bdg at 300 K as a function of density (ρ). Red diamonds, gF9A21: $Mg_{0.848}Fe_{0.090}Al_{0.206}Si_{0.856}O_3$ bdg (this study); purple diamonds, gF12A28: $Mg_{0.718}Fe_{0.123}Al_{0.281}Si_{0.878}O_3$ bdg (this study) The data are normalized by the κ and ρ of bdg at ambient conditions (κ_0 = 5.1 W/m/K and ρ_0 = 4.11 g/cm^3) (Osako and Ito, 1991). Red and purple broken lines are the obtained linear approximation line, which gives g=4.96 ± 0.51 and 5.12 ± 0.78 calculated from Eq. (5-8), respectively.

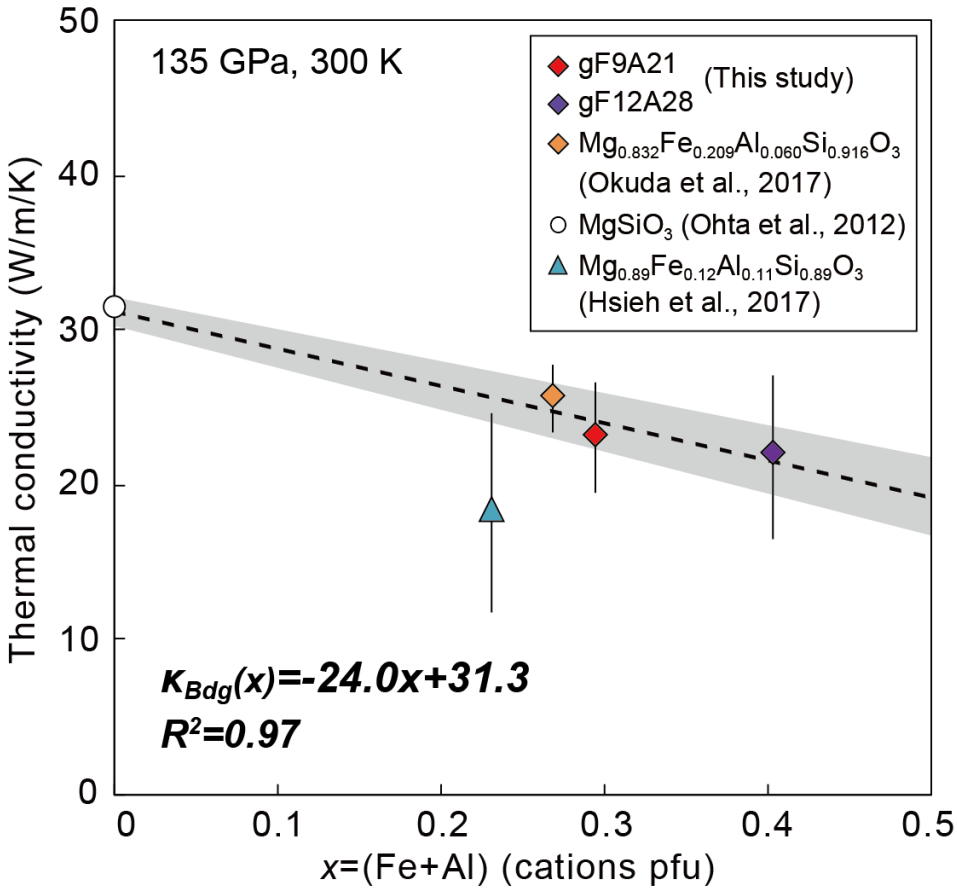

Fig. 5-5. Impurity effect on the lattice thermal conductivity of bdg at 135 GPa, 300 K. Orange, red, purple, blue and open symbols indicate the κ_{latt} of $Mg_{0.832}Fe_{0.209}Al_{0.060}Si_{0.916}O_3$ bdg (Okuda et al., 2017), $Mg_{0.848}Fe_{0.090}Al_{0.206}Si_{0.856}O_3$ bdg (this study), $Mg_{0.718}Fe_{0.123}Al_{0.281}Si_{0.878}O_3$ bdg (this study), $Mg_{0.89}Fe_{0.12}Al_{0.11}Si_{0.89}O_3$ bdg (Hsieh et al., 2017) and $MgSiO_3$ bdg (Ohta et al., 2012), respectively. Broken line indicates the obtained linear approximation line.

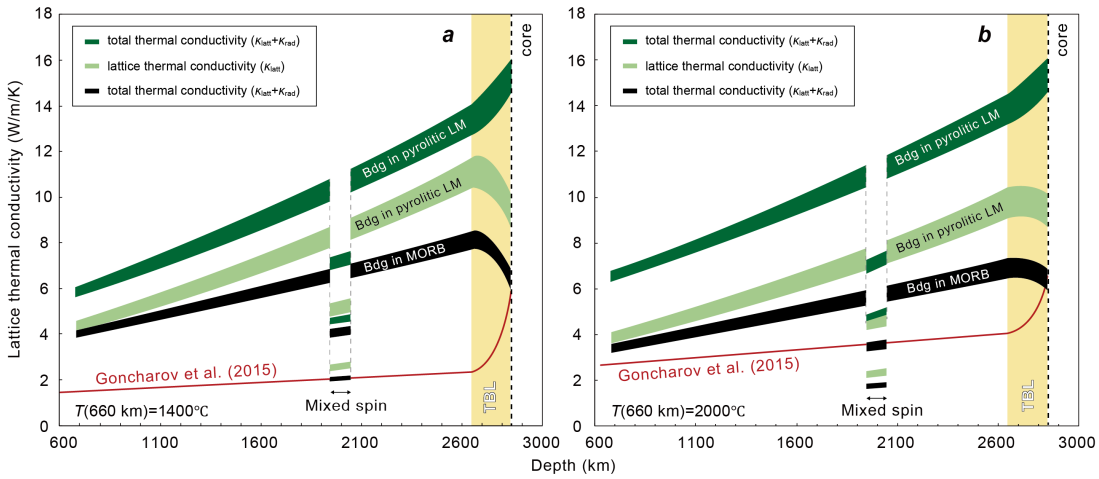

Fig. 5-6. Lattice thermal conductivity (κ_{latt}) and total thermal conductivity ($\kappa_{latt}+\kappa_{rad}$) profile of bdg in the Earth's lower mantle. a: using geotherm with the temperature at 660 km depth (T(660 km)) =1400 °C, b: using geotherm with T(660 km) =2000 °C (Brown and Shankland, 1981). Green and black bands indicate the estimated κ_{latt} of bdg in pyrolitic lower mantle and in MORB, respectively. Dark green and black bands indicate the estimated total κ of bdg in pyrolitic lower mantle and in MORB, respectively. Note that the estimated κ_{latt} and total κ of bdg in MORB are the same. Red curve indicates the κ_{rad} of bdg (Goncharov et al., 2015). Black broken line indicates the CMB, and yellow band indicates the 200 km thick thermal boundary layer (TBL) above the CMB (Lay et al., 2008).

5.9. Supplemental material

S5-1. Microprobe analyses of the used bdg samples

Microprobe analysis on starting material of gF9A21 was also conducted in Sinmyo et al. (2011). Here we provide the EDS analysis on starting material of gF12A28 (Table S5-1). We collected the EDS data from three different places to check the chemical homogeneity of the starting material, which errors calculated from the standard deviation of the obtained atm% of each element were below 10%.

We also investigated the chemical homogeneity of the bdg sample after the thermal conductivity measurement (Fig. S5-1). It can be seen from Fig. S5-1*d*, *f* that there is a SiO_2-enriched portion in the middle part of the sample. However, since the total area of this portion was only 5%, we consider that the effect of the SiO_2 on the thermal conductivity measurement of bdg is negligible.

Table S5-1. EDS analyses of gel starting material of gF12A28

	position1			position2			position3				
Elements	atm%	error (wt%)	wt%	atm%	error (wt%)	wt%	atm%	error (wt%)	wt%	STDEV of atm%	error of atm% (%)
Mg	16.83	1.84	18.8	16.58	1.88	18.84	16.45	1.89	18.66	0.19	1.16
Fe	2.88	0.46	7.39	2.58	0.41	6.21	2.38	0.41	6.22	0.25	9.63
Al	6.56	0.75	8.17	6.61	0.78	8.34	6.57	0.78	8.27	0.03	0.40
Si	20.56	2.03	26.55	19.33	1.99	25.39	19.73	2.06	25.87	0.63	3.16
O	53.15	7.35	39.09	55.09	7.89	41.21	54.87	7.93	40.98	1.06	1.95

STDEV of atm%, error of atm%: the standard deviation and error of atm% calculated from the atm% value in position 1, 2 and 3.

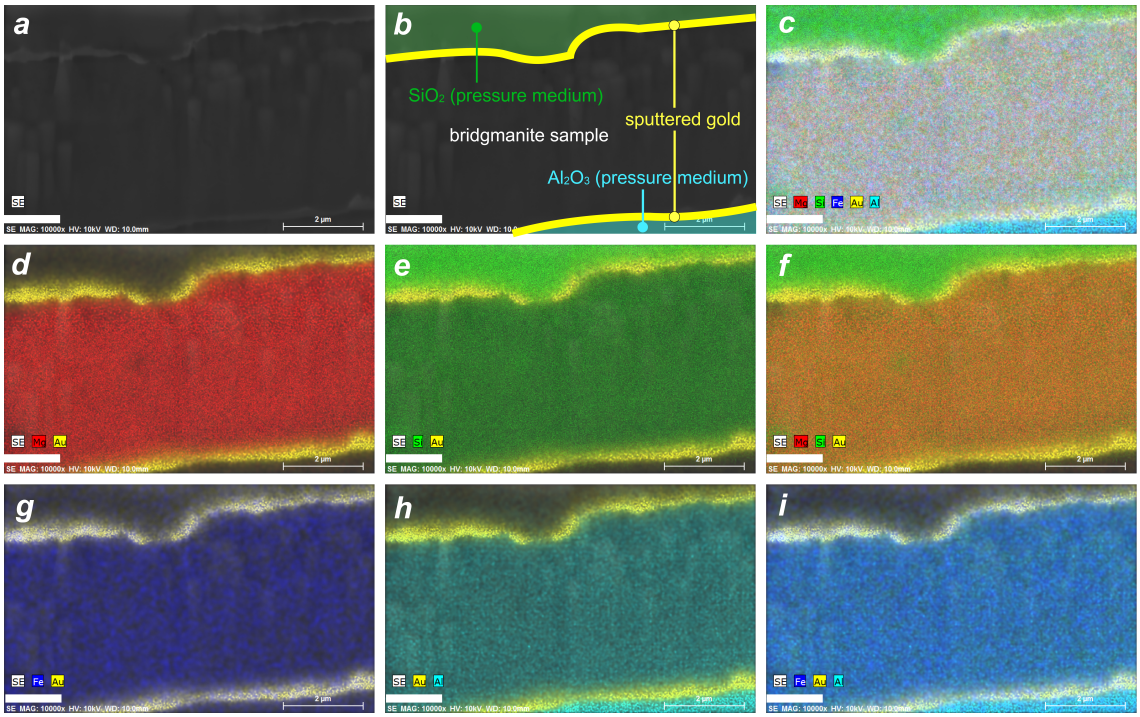

Fig. S5-1 X-ray maps of the recovered bdg sample gF9A21 after thermal conductivity measurement in run #2. Red, green, dark blue, light blue and yellow region illustrates mapping results of Mg, Si, Fe, Al and Au.

S5-2. Correction of the sample thickness

For the correction of thickness of our bdg sample under high pressure, we used the third-order Birch-Murnaghan EoS of gF9A21 obtained in this study from the fit of compressibility data with pressure above 29 GPa. However, since our collected compressibility data showed softening in V in the pressure range of 20 GPa to 31 GPa, the thickness of bdg in 24 GPa and 26 GPa (κ_{latt} data we regarded as κ_{MS}, see *section 5.4.5*) estimated from the EoS of gF9A21 is questionable. Here we tested how much the κ_{latt} alters by changing the P-V relation for the correction of bdg thickness for the κ_{latt} of gF9A21 obtained at 24 GPa in run #2, and that of gF12A28 obtained at 26 GPa in run #3.

We calculated the κ_{latt} by using P-V relation of 182-1.06P (Å^3), which is the linear fitting result of our obtained compressibility data in this pressure range (Fig. S5-2). The obtained κ_{latt} by using P-V relation of 182-1.06P (Å^3) altered up to 1.2% from that estimated from the third-order Birch-Murnaghan (BM) EoS of gF9A21 (Table S5-2), which is within the estimated error bar of κ_{latt} from the temperature history curve-fitting error and sample thickness error (Table 5-1). Since the P-V relation of 182-1.06P (Å^3) is empirical, we avoided using this relation to estimate the thickness of bdg at high pressure. Taking into account that the difference in κ_{latt} were within the error bar of κ_{latt}, we used the obtained EoS for sample thickness correction for each data.

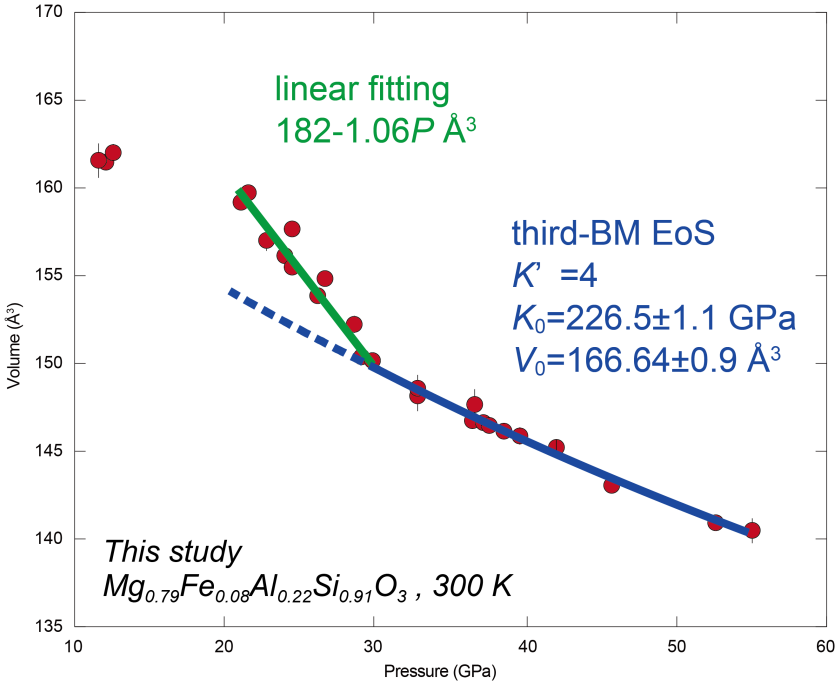

Fig. S5-2. *P-V* relation of gF9A21. Blue curve, fit of third Birch-Murnaghan EoS; green line, linear fit in the pressure range of 20 GPa to 31 GPa.

Table S5-2. Lattice thermal conductivity estimated from *P-V* relation based on linear fit and third-Birch Murnaghan EoS

			linear fit				third-order BM fit				
Sample	run#	Pressure (GPa)	V (Å^3)	Reduction rate of d at high P (%)	ρ_{bdg} (kg/m^3)	κ_{bdg} (W/(m*K))	V (Å^3)	Reduction rate of d at high P (%)	ρ_{bdg} (kg/m^3)	κ_{bdg} (W/(m*K))	κ_{bdg} difference (%)
gF9A21	2	24	156.58	97.987	4378.1	4.33	152.50	97.171	4495.2	4.38	1.2
gF12A28	3	26	154.45	97.561	4482.8	3.75	151.56	96.982	4568.4	3.78	0.8

S5-3. Data quality of each thermal conductivity measurement

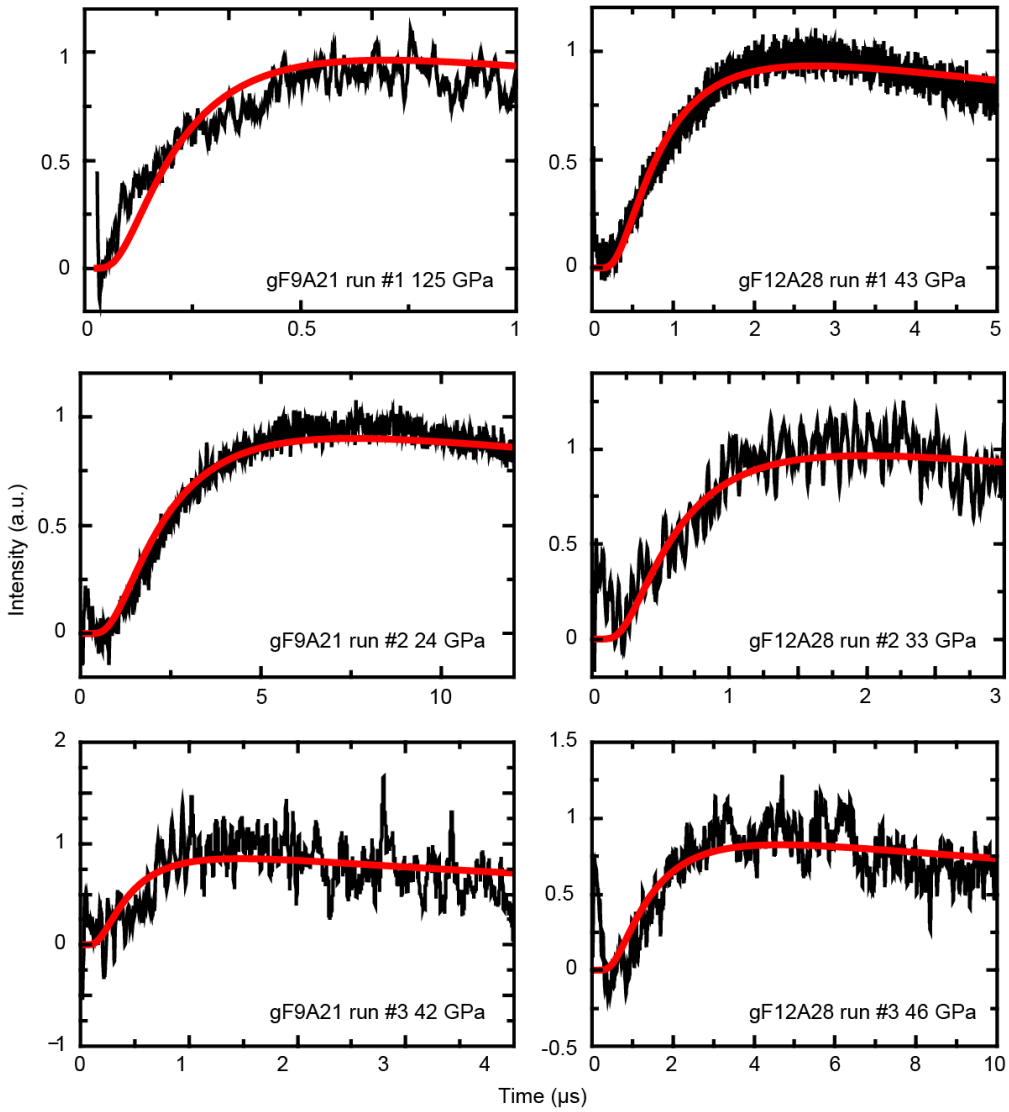

Fig. S5-3. The obtained temperature history curves in each run.

S5-4. Disordered lattice in the mixed spin state

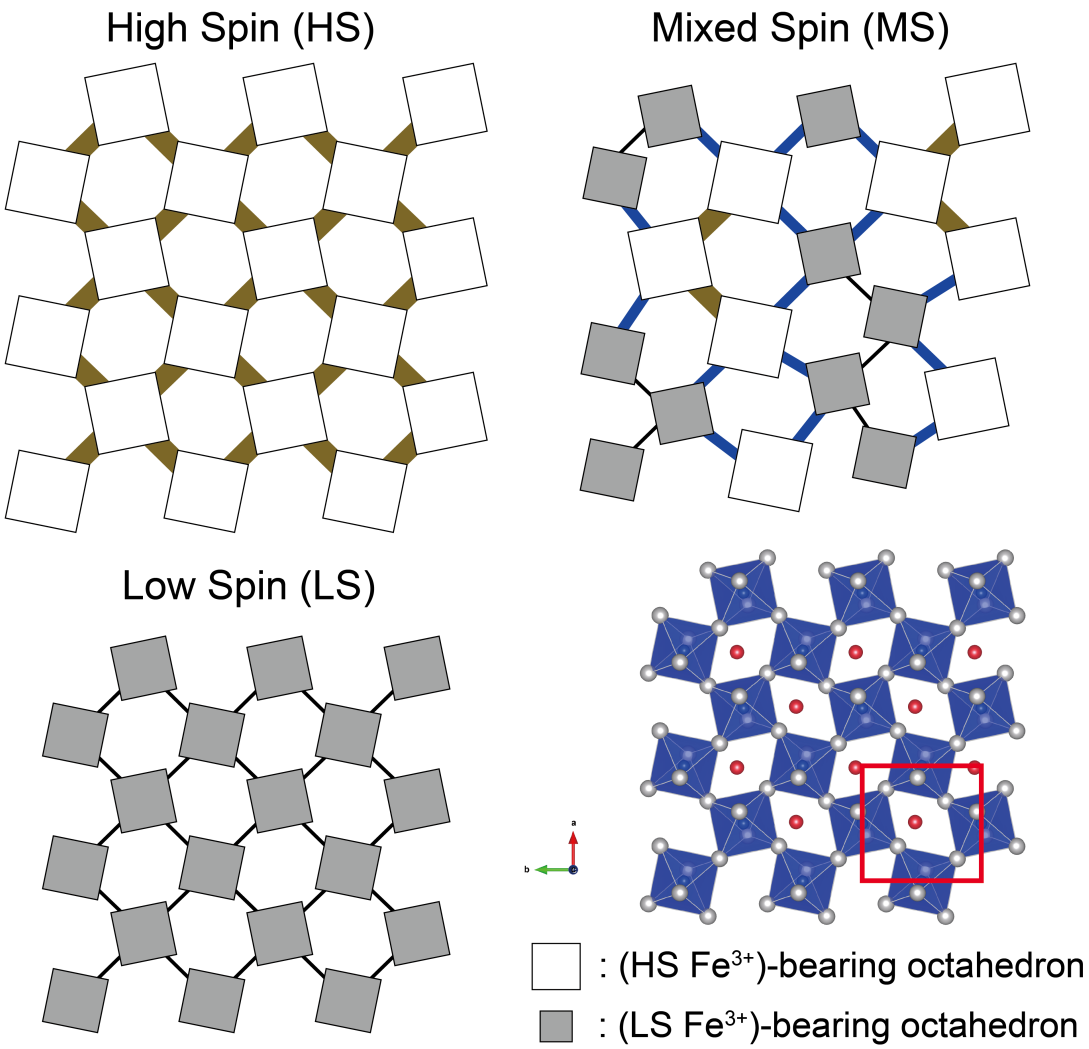

Fig. S5-4. Explanation of the disordered lattice in the mixed spin state. Cube indicates the FeO_6 octahedron. For simplicity, SiO_6 is not written in this figure. White and gray cubes indicate the FeO_6 octahedron with HS-Fe and LS-Fe, respectively. Brown, blue and black line indicates the different bond length between FeO_6 octahedrons with HS-HS, HS-LS, LS-LS, respectively. Figure in the lower right is the crystal structure of bdg as seen from directly above the *c*-axis, written by VESTA (Momma and Izumi, 2008). Red rectangle shows the unit cell of bdg.

S5-5. Tilting angle of octahedral Φ of bdg used in Okuda et al. (2017)

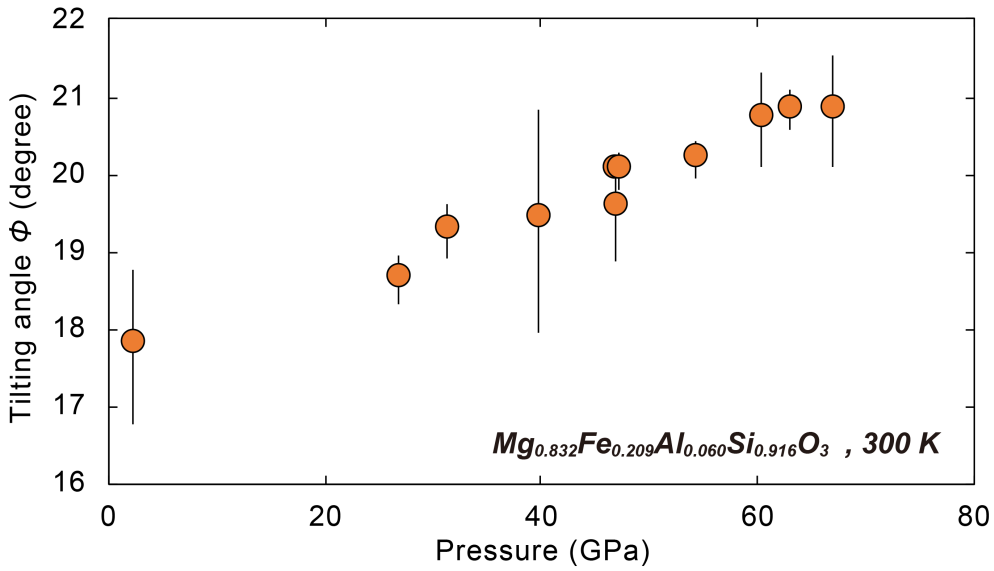

Fig. S5-5. Calculated Φ of $Mg_{0.832}Fe_{0.209}Al_{0.060}Si_{0.916}O_3$ in Okuda et al. (2017), Chapter 2.

S5-6. Pressure-compositional dependence of the lattice thermal conductivity of bdg at 300 K

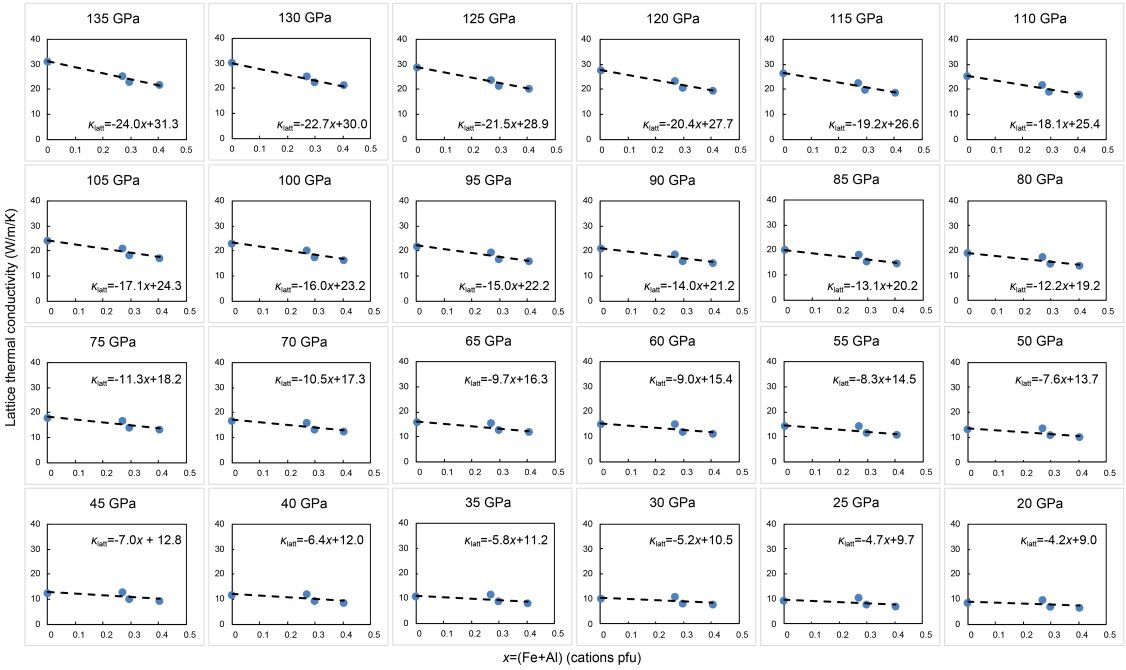

Fig. S5-6-1. Pressure-compositional dependence of the $\kappa_{bdg,x}(P, 300\ K)$ at pressure from 20 to 135 GPa in 5 GPa steps. Broken lines indicate the obtained linear fitting results.

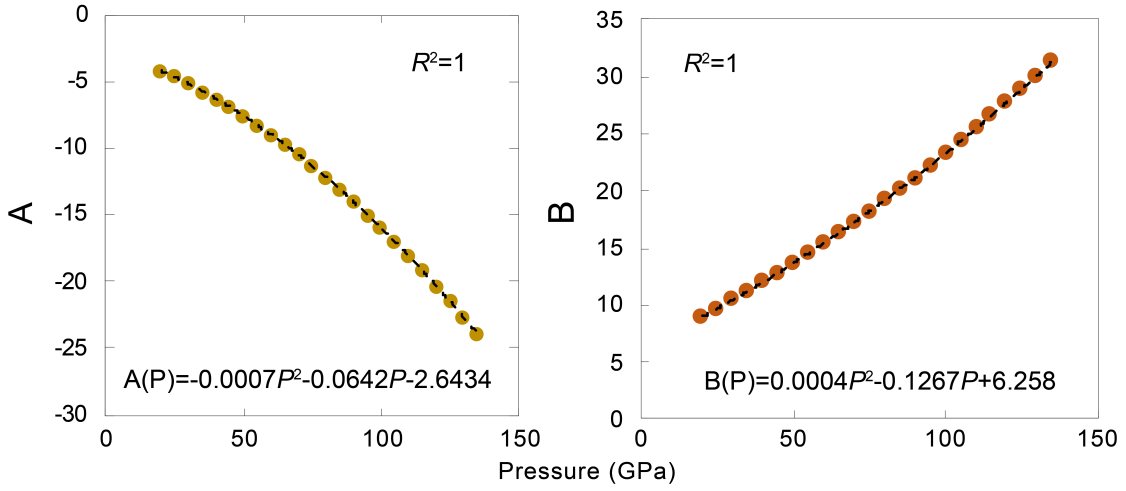

Fig. S5-6-2. Pressure dependence of coefficients A and B when $\kappa_{bdg,x}(P, 300\ K)=A(P)x+B(P)$. Black broken line indicates the fitting with a quadratic function.

Table S5-6. Coefficients of the linear approximation $\kappa = Ax + B$ for lattice thermal conductivity of bdg at high-P, 300 K

Pressure (GPa)	A	B
135	-23.951	31.292
130	-22.662	30.039
125	-21.502	28.855
120	-20.358	27.693
115	-19.233	26.552
110	-18.132	25.431
105	-17.058	24.332
100	-16.015	23.255
95	-15.004	22.199
90	-14.030	21.166
85	-13.092	20.154
80	-12.193	19.164
75	-11.332	18.196
70	-10.511	17.250
65	-9.728	16.326
60	-8.983	15.423
55	-8.273	14.542
50	-7.599	13.682
45	-6.957	12.842
40	-6.346	12.023
35	-5.764	11.225
30	-5.209	10.447
25	-4.677	9.689
20	-4.169	8.952

S5-7. κ ratio between $\kappa_{HS,\,LS}$ and κ_{MS}

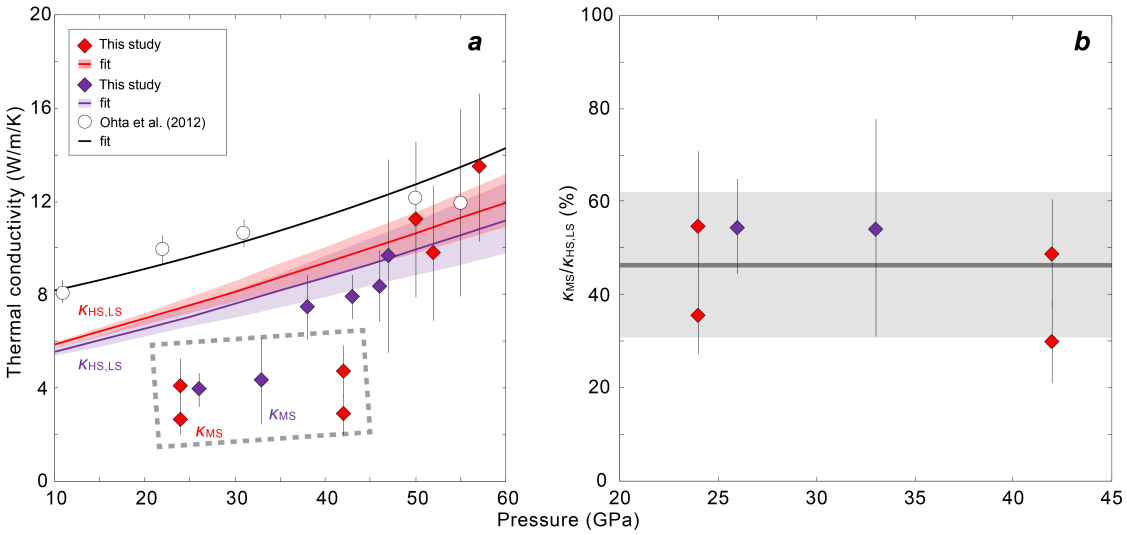

Fig. S5-7. (a): Lattice thermal conductivity of bdg at 10−60 GPa, 300 K. (b): κ ratio between $\kappa_{HS,\,LS}$ and κ_{MS}. Open, red, purple symbols indicate the κ_{latt} of $MgSiO_3$ bdg (Ohta et al., 2012), $Mg_{0.848}Fe_{0.090}Al_{0.206}Si_{0.856}O_3$ bdg (this study) and $Mg_{0.718}Fe_{0.123}Al_{0.281}Si_{0.878}O_3$ bdg (this study), respectively. Black, red and purple curves indicate the approximation curve of $MgSiO_3$ bdg (Ohta et al., 2012), $Mg_{0.848}Fe_{0.090}Al_{0.206}Si_{0.856}O_3$ bdg (this study) and $Mg_{0.718}Fe_{0.123}Al_{0.281}Si_{0.878}O_3$ bdg (this study) respectively, calculated by Eqs. (5-7, 5-8). We regarded κ_{latt} data inside the broken square window as that when Fe is in the MS state (κ_{MS}). The gray band indicates the standard deviation of the obtained $\kappa_{MS}/\kappa_{HS,\,LS}$ data, which was obtained to be 46 ± 16%.

S5-8. Effect of temperature difference of bdg in the subducted MORB on its lattice thermal conductivity

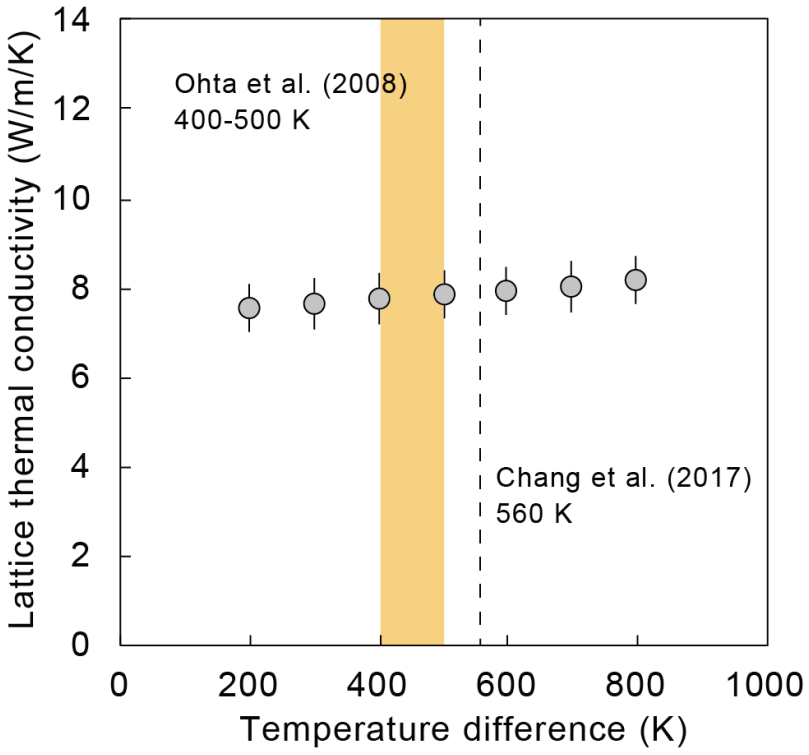

Fig. S5-8. The effect of the temperature difference between the subducted MORB and the surrounding lower mantle on the lattice thermal conductivity of bdg in subducted MORB at CMB conditions. Gray circle indicates the lattice thermal conductivity of bdg in subducted MORB with temperature difference between such MORB and the surrounding lower mantle as 200−800 K. Orange band and black broken like indicate the suggested temperature differences of 400−500 K in the lowermost mantle (Ohta et al., 2008), and 560 K in the top of the lower mantle (Chang et al., 2017), respectively.

Supplemental references

Chang, Y. Y., Hsieh, W. P., Tan, E., Chen, J., 2017. Hydration-reduced lattice thermal conductivity of olivine in Earth's upper mantle. Proc. Natl. Acad. Sci. 114, 4078–4081.

Momma, K., Izumi, F., 2011. VESTA 3 for three-dimensional visualization of crystal, volumetric and morphology data. J. Appl. Crystallogr. 44, 1272-1276.

Ohta, K., Hirose, K., Lay, T., Sata, N., Ohishi, Y., 2008. Phase transitions in pyrolite and MORB at lowermost mantle conditions: Implications for a MORB-rich pile above the core–mantle boundary. Earth. Planet. Sci. Lett. 267, 107–117.

Ohta, K., Yagi, T., Taketoshi, N., Hirose, K., Komabayashi, T. Baba, T., Ohishi, Y., Hernlund, J., 2012. Lattice thermal conductivity of $MgSiO_3$ perovskite and post-perovskite at the core-mantle boundary. Earth Planet. Sci. Lett. 349-350, 109–115.

Okuda, Y., Ohta, K., Yagi, T., Sinmyo, R., Wakamatsu, T., Hirose, K., Ohishi, Y., 2017. The effect of iron and aluminum incorporation on lattice thermal conductivity of bridgmanite at the Earth's lower mantle. Earth Planet. Sci. Lett. 474, 25–31.

Sinmyo, R., Hirose, K., Muto, S., Ohishi, Y., Yasuhara, A., 2011. The valence state and partitioning of iron in the Earth's lowermost mantle. J. Geophys. Res. 116, B07205.

Chapter 6. Thermal conductivity of Fe-bearing post-perovskite in the Earth's lowermost mantle

This chapter was updated from the published article as *"Thermal conductivity of Fe-bearing post-perovskite in the Earth's lowermost mantle"* by **Yoshiyuki Okuda**, Kenji Ohta, Akira Hasegawa, Takashi Yagi, Kei Hirose, Saori I. Kawaguchi, Yasuo Ohishi (2020) Earth and Planetary Science Letters, **547**, 116-466. https://doi.org/10.1016/j.epsl.2020.116466

Abstract

The thermal conductivity of post-perovskite (ppv), the highest-pressure polymorph of $MgSiO_3$ in the Earth's mantle, is one of the most important transport properties for providing better constraints on the temperature profile and dynamics at the core-mantle boundary (CMB). Incorporation of Fe into ppv can affect its conductivity, which has never been experimentally investigated. Here we determined the lattice thermal conductivities of ppv containing 3 mol% and 10 mol% of Fe at high *P-T* conditions – of pressures up to 149 GPa and 177 GPa, respectively, and temperatures up to 1560 K – by means of the recently developed pulsed light heating thermoreflectance technique combining continuous wave heating lasers. We found that the incorporation of Fe into ppv moderately reduces its lattice thermal conductivity as it increases the Fe content. The bulk conductivity of ppv dominant pyrolite is estimated as 1.5 times higher than that of pyrolite consisting of bridgmanite and ferropericlase in the lower mantle, which agrees with the traditional view that ppv acts as a better heat conductor than bridgmanite in the Earth's lowermost mantle.

6.1. Introduction

The heat flow across the core-mantle boundary (CMB), an extreme thermal boundary layer in the lowermost mantle, drives various geophysical-chemical phenomena in the deep mantle. Heat transport in the Earth's interior predominantly takes place by convection, although the thermal boundary layer at the CMB is one of the important exceptions: it carries heat by conduction only. The thermal conductivity (κ) of the lower mantle minerals is fundamental information for understanding the heat transport at the base of the mantle, and thus requires constraints. (Fe,Al)-bearing $MgSiO_3$ post-perovskite (ppv) is thought to be one of the most abundant minerals in the lowermost mantle. Mg-pure perovskite called bridgmanite (bdg) undergoes a phase transition into ppv above 125 GPa and 2500 K, forming a stacked SiO_6-octahedral sheet structure, which is thought to be the origin of the D″ seismic discontinuity (Murakami et al., 2004; Oganov and Ono, 2004; Tsuchiya et al., 2004). There are three carriers of heat transfer via conduction, which are phonon, electron and photon, referred to as lattice, electronic and radiative thermal conductions, respectively. Total thermal conductivity is given by the summation of these conductivities. Among them, electronic conduction by free electron only plays an important role in metal. Conversely, phonon and photon predominantly carry heat through non-metallic minerals.

Studies investigating the κ of ppv are scarce. Experimental study on the lattice thermal conductivity (κ_{latt}) of ppv is so far limited to the report by Ohta et al. (2012). The authors suggested that $MgSiO_3$ ppv is twice as conductive as bdg with Mg-endmember composition; the κ_{latt} of $MgSiO_3$ bdg and ppv at the CMB *P*-*T* conditions

(135 GPa, 3700 K) was estimated to be 9.0±1.6 W/m/K and 16.8±3.7 W/m/K, respectively. Such a high κ of ppv was predicted by Hofmeister (2007), and was also presumed from the measurement of $Ca_{1-x}Sr_xIrO_3$ analogs (e.g., Keawprak et al., 2009). Recent calculations of κ of ppv are also in concurrence with this view (Haigis et al., 2012; Ammann et al., 2014; Dekura and Tsuchiya, 2019).

It is well known that chemical impurities in a material, such as Fe, reduces its κ_{latt} (e.g., Slack, 1964). A number of studies have focused on the impurity effect on the κ_{latt} of the lower mantle minerals (e.g., Manthilake et al., 2011; Ammann et al., 2014; Ohta et al., 2014; Stackhouse et al., 2015; Okuda et al., 2017; Ohta et al., 2017; Hsieh et al., 2017, 2018; Hasegawa et al., 2019a; Okuda et al., 2019). Recent κ_{latt} measurements on ferropericlase (fp) revealed that incorporation of Fe in MgO component caused significant κ_{latt} reduction by an order of magnitude (Ohta et al., 2017; Hsieh et al., 2018). In contrast, bdg seems to show far less compositional dependence on its κ (Okuda et al., 2017; Hsieh et al., 2017; Chapters 2,5). Fe in the lower mantle ppv is thought to be depleted due to the poor Fe^{3+} capacity under a reduced environment (Sinmyo et al., 2011); still, theoretical calculation on the κ_{latt} of ppv implied that even a small amount of Fe could significantly reduce its κ (Ammann et al., 2014). From the dearth of relevant data on the κ of ppv, its P, T and x (compositional)-dependencies are matters of great interest and there is a demand to constrain them. Moreover, for highly conductive material, the effect of grain boundary scattering on its κ_{latt} may not be negligible, especially for a tiny sample. For instance, the κ_{latt} of polycrystalline MgO periclase at room temperature was much lower than that of single crystal (Dalton et al., 2013; Imada et al., 2014). Taking into account that ppv is thought to be a good heat

conductor (e.g., Ohta et al., 2012), it is important to consider carefully this effect on the κ of ppv.

Here we determined the κ_{latt} of Fe-bearing ppv at high *P*-*T* conditions in a laser-heated diamond anvil cell (LHDAC). Our results indicate that the κ of ppv would be moderately reduced by Fe incorporation. We estimate the κ of ppv at the actual Earth's lower mantle with consideration of its grain boundary scattering effect.

6.2. Experimental Methods

We used gel starting materials with two different chemical compositions as $Mg_{0.97}Fe_{0.03}SiO_3$ (F3) and $Mg_{0.90}Fe_{0.10}SiO_3$ (F10) (Table S6-1). F3 and F10 were dehydrated at 1000 K and 1273 K for 1 day and an hour respectively, in a H_2-CO_2 gas-mixing furnace at Tokyo Institute of Technology in which oxygen fugacity was controlled to be slightly above the iron-wüstite buffer. $Fe^{3+}/\Sigma Fe$ of F10 was determined by electron energy-loss near-edge structure (ELNES) measurement to be 0.19±0.10 (Ohta et al., 2008a). Although the $Fe^{3+}/\Sigma Fe$ of F3 was not determined, it is likely that F3 has a $Fe^{3+}/\Sigma Fe$ ratio similar to that of F10, considering that the valence state of Fe in ppv would not greatly change from that of the starting material (Sinmyo et al., 2011). The gel starting materials were dehydrated in a vacuum for more than a day before they were loaded into a sample chamber.

For DAC experiments, we used 120 and 90 μm beveled diamond anvils (Table 6-1). The disked gel starting material, coated with gold for a pressure marker and κ

measurement, was placed between Al_2O_3 layers as a pressure medium and thermal insulator in a 40 or 30 μm hole of a pre-indented Re gasket. After compression to a high pressure of interest at room temperature, sample synthesis and phase identification were performed at BL10XU, SPring-8. About 30 μm areas were heated from both sides with a couple of 100 W single-mode Yb fiber lasers. In each synthesis, temperature was determined by thermal radiation spectra. During the heating, temperature was kept at 2000−2500 K for 1−2 hrs. Subsequently, we collected the X-ray diffraction pattern of the sample and yielded only ppv, gold and pressure medium peaks in each run (Fig. 6-1a; see Fig. S6-1 for each collected pattern). The energy of the X-ray beam was 30 keV, and an imaging plate was used to collect the XRD patterns. The obtained unit cell volume of ppv were in a good agreement with a previously reported equation of state of Fe-bearing ppv (Fig. 6-1b). Thermal diffusivities of F3 and F10 ppv were measured in a DAC by thermoreflectance technique (Yagi et al., 2011) combining continuous wave heating lasers (Hasegawa et al., 2019b). We performed two separate measurements on samples F3 and F10, respectively (Table 6-1).

The thermal diffusivity of ppv was determined by obtaining the transient temperature curves at each pressure (Fig. 6-2a; see Fig. S6-2 for obtained transient temperature curves in each run). Laser spot size of the thermoreflectance probe laser was less than 5 μm, which is sufficiently smaller than those of the pump laser and continuous wave fiber laser of both 25−30 μm in diameter. Collected curves were fitted by the one-dimensional thermal conduction equation in order to estimate the heat diffusion time (τ) through the Au-sample-Au layers:

$$T(t) = \bar{T}\sqrt{\frac{\tau}{\pi t}}\sum_{n=0}^{\infty}\gamma^{2n}exp\left[-\frac{(2n+1)^2}{4}\frac{\tau}{t}\right], \qquad (6\text{-}1)$$

where $T(t)$ is temperature as a function of time (t), $\bar{T}$ is a constant, and γ is a fitting parameter describing heat effusion to the pressure medium. We took into account a three-layer heat diffusion model, namely heat diffusion through the sputtered gold layers, and extracted the thermal diffusivity of ppv (D_{ppv}) from the following equations:

$$D_{\mathrm{ppv}} = \frac{\frac{\Gamma}{6}+1+\frac{1}{\Gamma}}{(\Gamma+2)\frac{\tau}{6}-(\Gamma+\frac{4}{3})\frac{d_{\mathrm{Au}}^2}{D_{\mathrm{Au}}}} d_{\mathrm{ppv}}^2, \quad (6\text{-}2)$$

$$\Gamma = \frac{C_{\mathrm{ppv}} d_{\mathrm{ppv}}}{C_{\mathrm{Au}} d_{\mathrm{Au}}}, \quad (6\text{-}3)$$

where D_{Au} is thermal diffusivity of Au, d_{ppv}, d_{Au} are thickness of ppv and Au respectively, and C_{ppv}, C_{Au} are heat capacity per unit volume ($C = \rho C_{\mathrm{P}}$) of ppv and Au, respectively. D_{Au} at room-T and high-P was calculated from that at ambient conditions of 127 mm^2/s (Ho et al., 1972), and its pressure derivative of 4%/GPa (Ross et al., 1984). The temperature dependence of D_{Au} has never been investigated under high pressure. Temperature derivative of the thermal diffusivity of metal strongly depends on the material (e.g., positive derivative for platinum (Martin et al., 1967) and negative for copper (Sidles & Danielson, 1954)). Still, taking into account the negligible effect of D_{Au} on yielding D_{ppv} (see supporting information S6-3), the calculated room temperature and high pressure D_{Au} was also applied to the high temperature D_{ppv} estimation. We used the supplied value of C_{Au} at high pressure in Tsuchiya (2003). Thermal diffusivity measurements were all conducted at the National Institute of Advanced Industrial Science and Technology.

In addition to room temperature measurements, the high-temperature thermal diffusivity measurements were performed on the F10 ppv sample. Temperature was measured by fitting Planck radiation curves to the observed thermal radiation spectrum

(Fig. S6-4-1). Wavelengths between 640 nm and 740 nm were used for the fitting. The temperature uncertainty u_T was estimated from the following:

$$u_T = \sqrt{{u_{fit}}^2 + {u_{str}}^2}, \quad (6\text{-}4)$$

where u_{fit} and u_{str} are temperature uncertainties in Planck function fitting and temperature structure in the sample (supporting information S6-4).

κ is provided by the product of thermal diffusivity D, density ρ and isobaric specific heat C_P as the following:

$$\kappa = D\rho C_P. \quad (6\text{-}5)$$

Density was calculated from the Keane equation of state of $MgSiO_3$ ppv (Sakai et al., 2016), in which the Grüneisen parameter was carefully determined by their LHDAC study. We used the formula weight of 101.34 and 103.55 for F3 and F10, respectively. C_P was derived from the Debye model with supplied thermoelastic parameters (Sakai et al., 2016). Pressure calibration was based on the lattice volume of Au (Tsuchiya, 2003) and Raman shift of the diamond anvil (Akahama and Kawamura, 2004). For pressure at high *P-T* conditions, thermal pressure of the ppv sample was also considered, which was estimated from a similar experimental setup on the ppv sample (see supporting information S6-5 for details). All the experimental conditions in each run are summarized in Table 6-1.

Thicknesses of the recovered sample and Au layers were measured after the thermal diffusivity measurements. We obtained a cross-section of the heated portion for ppv synthesis by using a focused ion beam apparatus. Subsequently, thicknesses of the sample and Au layers were observed with a scanning electron microscope (SEM) (Fig. 6-2b). Those thicknesses at high *P-T* conditions were estimated after correction of

pressure-induced amorphization based on the fourth Birch Murnaghan equation of state of $MgSiO_3$ glass (see supporting information S6-6).

6.3. Results

6.3.1. Room temperature thermal conductivity measurements

We conducted thermal diffusivity measurements on Fe-bearing ppv under high pressure and ambient temperature. Two separate diffusivity measurements were carried out for F3 and F10 ppv, from 122 to 149 GPa, and from 135 GPa to 177 GPa, respectively. All measurements were performed upon decompression from the synthesized pressure of ppv samples. Figure 6-3 shows the κ_{latt} of ppv as a function of pressure obtained by Eq. (6-5), with reported κ of $MgSiO_3$ ppv (Ohta et al., 2012; Ammann et al., 2014). The κ values of $MgSiO_3$ bdg and Fe 21%, Al 6%-bearing bdg are also plotted for comparison (Ohta et al., 2012; Okuda et al., 2017). κ_{latt} of F3 and F10 ppv both increased monotonically with increasing pressure: those values increased from 36.5±5.7 W/m/K at 122 GPa to 50.0±17.8 W/m/K at 149 GPa, and from 32.2±3.0 W/m/K at 135 GPa to 52.8±11.7 W/m/K at 177 GPa, respectively.

Incorporation of Fe in minerals potentially reduces the κ_{latt} due to the additional phonon scattering, mass disorder, and weaker chemical bonds. The magnitude of the impurity effect on κ seems to depend on the mineral. κ_{latt} of MgO was reported to be strongly reduced by Fe-Mg substitution (Ohta et al., 2017; Hsieh et al., 2018; Hasegawa et al., 2019a); the κ_{latt} of $(Mg_{0.82}Fe_{0.19})O$ at 135 GPa and 300 K estimated as 13.5±2.2

W/m/K (Ohta et al., 2017) was extremely low compared to that of the Fe-free one at the same *P,T* conditions, which was determined to be 377 W/m/K (Dalton et al., 2013). On the other hand, the effect of additional phonon scattering due to Fe in bdg was found to be minimal (Okuda et al., 2017; Hsieh et al., 2017); Okuda et al. (2017) suggested that incorporation of 20 mol% of Fe and 6 mol% of Al only reduces 19% of the κ_{latt} of bdg from that of the Mg-pure composition at 135 GPa. Our obtained κ_{latt} of Fe-bearing ppv samples F3 and F10 were both fairly low compared to that of Fe-free ppv in the experimental study (Ohta et al., 2012) and DFT calculation (Ammann et al., 2014) (Fig. 6-3). At 135 GPa and 300 K, the κ_{latt} of F3 and F10 ppv were 44.8±6.9 W/m/K and 32.2 ± 3.0 W/m/K, respectively, which is 28% and 48% lower than that of $MgSiO_3$ ppv, determined to be 61.8 ± 13.6 W/m/K (Ohta et al., 2012), respectively. These reduced values are reasonable when taking into account that additional phonon scattering by Fe would be stronger in a more symmetrical mineral; ppv has better symmetricity than bdg, while it is poorer than that of fp. The κ_{latt} of $MgSiO_3$ ppv estimated by molecular dynamics (MD) calculation yielded significantly higher values than the other estimations, which were reported to be 167 ± 25 W/m/K at 135 GPa and 300 K (Haigis et al., 2012). The most recent MD calculation based on first principle showed similar results of 148 ± 13 W/m/K at 135 GPa and 300 K (Dekura and Tsuchiya, 2019). Such large conductivity differences may be due to the strong grain boundary scattering (discussed later in *section 6.4.1*). According to Ammann et al. (2014), the reduction of κ_{latt} of ppv quickly saturates with increasing Fe content. Calculated κ of ppv along *a*-axis at 135 GPa and 2000 K showed reduction from the Mg-endmember value by 34% and 48% when increasing Fe content to 0.01 and 0.1, respectively. Results for *b*-axis κ at the same conditions showed a similar reduction as well, which was 29% and 42%

respectively. These trends are in accordance with our results in which the increase of Fe content from 3 mol% to 10 mol% in this study showed 28% and 48% lower κ than $MgSiO_3$ ppv (Ohta et al., 2012).

6.3.2. High-temperature thermal conductivity measurements

In runs #3 and #4, thermal diffusivity measurements under high *P-T* conditions were also carried out at 138 GPa up to 1558 K, and 177 GPa up to 1070 K, respectively (Table 6-1). The thermoreflectance technique combined with continuous wave heating lasers was used for the measurements (Hasegawa et al., 2019b), which can measure the lattice component. The measured thermal diffusivity at 138 GPa dropped from 15.1±1.4 mm^2/s at room temperature to 4.2±0.4 mm^2/s at 1558 K (Fig. 6-4a). At a higher pressure of 177 GPa, we also observed a similar decrease in diffusivity, from 20.3±0.5 mm^2/s at 300 K to 6.5±0.2 mm^2/s at 1070 K. The κ of F10 ppv at high *P-T* conditions was estimated by Eq. (6-5) from our measured diffusivity with the estimated density and heat capacity from the supplied thermal equation of state (Sakai et al., 2016) and theoretical calculation (Metsue and Tsuchiya, 2011) (Table 6-1). As a result, both κ at 138 GPa and 177 GPa were reduced with increasing temperature, from 40.1±3.7 W/m/K at room temperature to 27.2±2.7 W/m/K at 1558 K, and from 52.8±11.2 W/m/K to 42.1±9.75 W/m/K at 1070 K, respectively (Fig. 6-4b). As mentioned earlier, there is a huge gap in κ results between experimental studies (Ohta et al., 2012; this study) and theoretical studies (Haigis et al., 2012; Dekura and Tsuchiya, 2019) at room temperature. In contrast, κ result at high-*T* shows a moderate agreement (Fig. 6-4b).

The rate of decrease on κ of F10 ppv is much smaller than its diffusivity. This is due to the higher heat capacity at high temperature conditions (see Table 6-1), which cancels out the effect of strong reduction of diffusivity at high-T to some extent.

6.4. Discussion

6.4.1. Grain boundary effect on lattice thermal conductivity of ppv

The following density-temperature κ_{latt} model has been used to evaluate the effect of phonon-phonon scattering as well as other scattering factors such as impurities (e.g., Manthilake et al., 2011; Ohta et al., 2012; Okuda et al., 2017; 2019):

$$\kappa = \kappa_0 \left(\frac{\rho}{\rho_0}\right)^g \left(\frac{T_0}{T}\right)^a. \quad (6\text{-}6)$$

When the grain size of the sample is comparable to the mean-free path of phonons, grain boundary scattering needs to be considered separately from other phonon-scattering mechanisms. For example, the reported thermal conductivity of MgO periclase at 300 K in experiments using a polycrystalline sample (Imada et al., 2014) was much lower than that using a single crystal sample (Dalton et al., 2013), and by *ab initio* calculation results (e.g., Dekura and Tsuchiya, 2019), which can be regarded as that of a perfect single crystal. This was attributed to the effect of phonon grain boundary scattering, of which the effect on κ can be quantified by the following equation (Smith et al., 2003):

$$\kappa_{\mathrm{poly}}^{-1} = \kappa_{\mathrm{single}}^{-1} + nR_{\mathrm{GB}}, \quad (6\text{-}7)$$

where κ_{poly}, κ_{single} are the κ of polycrystalline and a single crystal sample, respectively, R_{GB} and n are grain boundary thermal resistance and the number of grain boundaries per unit length along heat flow, respectively. In order to quantify R_{GB} of ppv and to evaluate the grain boundary effect on our measured κ_{latt} of ppv, we need information on κ_{single} of ppv and the grain size of our ppv sample.

The direct observation of the grain size of a ppv sample is difficult since ppv is unquenchable to ambient conditions. Moreover, currently there is no available literature about the grain growth rate of $MgSiO_3$ ppv. Therefore, we estimated the grain size of our ppv sample by multiplying the estimated grain size of bdg synthesized at the same *P-T* conditions using the grain growth kinetics of $MgSiO_3$ perovskite (pv) (Yamazaki et al., 1996), and the grain growth rate ratio between pv and ppv of $CaIrO_3$ analog (Yoshino and Yamazaki, 2007). Note that our ppv sample contains a certain amount of Fe, but in the present situation it is difficult to quantify the effect of Fe on grain growth of ppv due to a lack of available data. Therefore, we assumed that the grain growth rate of Fe-bearing ppv is the same as that of Mg-endmember composition. Grain size G can be calculated by the following rate equation:

$$G^n - G_0^n = k_0 e^{-\frac{H^*}{RT}} t, \qquad (6\text{-}8)$$

where G_0 is the initial average grain size, n is the grain growth exponent, k_0 is the pre-exponential factor of growth rate constant, H^* is the activation energy of grain growth, R is gas constant, T is temperature, and t is heating duration. We used the reported values of n, $\log k_0$ and H^* for $MgSiO_3$ pv (Yamazaki et al., 1996) of 10.6±1.0, -57.4±5.9 $m^{10.6}/s$ and 320.8±33.9 kJ/mol, respectively. Since we used gel starting material, G_0 was assigned to be 0. T was set to 2000 K, which is the sample synthesis temperature in the present study. The grain growth ratio of ppv to pv (G_{ppv}/G_{pv}) at 2000 K for a heating

duration of 2 hrs was calculated to be 0.24 from the equation below, provided k_0, n and H^* values of $CaIrO_3$ analog had pv and ppv structure (Yoshino and Yamazaki, 2007):

$$\frac{G_{\mathrm{ppv}}}{G_{\mathrm{pv}}} = \frac{\left(k_{0\mathrm{ppv}} e^{-\frac{H^*_{\mathrm{ppv}}}{RT}} t\right)^{\frac{1}{n_{\mathrm{ppv}}}}}{\left(k_{0\mathrm{pv}} e^{-\frac{H^*_{\mathrm{pv}}}{RT}} t\right)^{\frac{1}{n_{\mathrm{pv}}}}} . \qquad (6\text{-}9)$$

The grain size of ppv in our experiments was estimated as 0.34 μm (Fig. S6-7; supporting information S6-8). Considering the error of n, k_0 and H^* values, extreme cases were also calculated in order to determine the maximum and minimum grain size, obtained as 1.29 μm and 0.04 μm, respectively.

R_{GB} of ppv was determined from the previously reported κ results on $MgSiO_3$ ppv. The ppv sample used in Ohta et al. (2012) was a polycrystalline sample, while the κ results from first principle calculation (Dekura and Tsuchiya, 2019) can be regarded as that of an infinite size single crystal because of the applied periodic boundary condition. Therefore, we regarded the κ results obtained in Ohta et al. (2012) as κ_{poly}, and the theoretical calculation results (Dekura and Tsuchiya, 2019) as κ_{single} in Eq. (6-7). We used the authors' supplied κ data at 135 GPa and 300 K, which were κ_{poly} =61.8±13.6 W/m/K and κ_{single} =148±13 W/m/K, respectively. Ppv samples used in Ohta et al. (2012) were synthesized in a similar way to our experiments: using the gel starting material and heated at 2000 K for 1 hr. Accordingly, it is likely that the grain size of their ppv sample was comparable to our estimated grain size. As a result, R_{GB} was calculated to be $(3.2\pm1.2)\times10^{-9}$ m^2K/W when using a grain size of 0.34 μm (Fig. S6-5). The use of an estimated maximum/minimum grain size of 1.29 μm and 0.04 μm in Eq. (6-8) gave the R_{GB} as $(1.2\pm0.5)\times10^{-8}$ m^2K/W (maximum R_{GB}) and $(4.2\pm1.6)\times10^{-10}$ m^2K/W (minimum R_{GB}), respectively. By rearranging Eq. (6-6), κ_{poly} can be written as follows:

$$\kappa_{\text{poly}} = \gamma\kappa_{\text{single}}, \quad (6\text{-}10)$$

where γ is the grain boundary effect coefficient on thermal conductivity, $1/(1+nR_{GB}/R_{single})$. The grain boundary effect at high *P-T* conditions was also evaluated using the κ data at 1000 K, 2000 K and 3000 K calculated by Dekura and Tsuchiya (2019), each of which were assigned to be the κ_{single} at high-*T*. We used the R_{GB} of $(3.2\pm1.2)\times10^{-9}$ m^2K/W estimated above (see Fig. S6-9 for γ estimated from maximum/minimum grain size).

Figure 6-5a shows the ratio of nR_{GB} and R_{single}, which indicates that the smaller the grain size, the larger the contribution of R_{GB}. nR_{GB} would be larger than R_{single} when the grain size is below 0.5±0.2 μm at 300 K, and below 0.08±0.01 μm at 3000 K. The estimated γ of ppv at different temperature and grain size indicates that the κ_{latt} of ppv at CMB *P-T* conditions (135 GPa, 3000 K) would be reduced by 20% due to the grain boundary scattering of phonon when its grain size is 0.3±0.2 μm, and by 50% when it is 0.05±0.02 μm (Fig. 6-5b). The γ difference between 300 K and 2000 K was remarkable, whereas the difference between 2000 K and 3000 K was mostly within the error bar. This shows that the effect of phonon grain-boundary scattering would be weaker as *T* increases, because at high-*T* the phonon-phonon interaction becomes stronger and the mean free path of phonons decreases.

Here, the grain size of the lower mantle minerals estimated by numerical modeling ranges over at least two orders of magnitude, which is from 10^{-2} mm to 10^{0} mm (e.g., Solomatov et al., 2002; see supporting information S6-10). A recent study by Glišovic´ et al. (2015) estimated a possible grain size of the lower mantle inferred from seismic tomography and mantle rheology, which ranges from ~10^{-2} mm to ~10^{1} mm. Interestingly, they also mentioned that the grain size of ppv in the D" layer may be even

larger than 10 mm due to the bdg to ppv transformation. After the transformation, the grain boundary migration is thought to increase the grain size, which is thought to lead to post- polymorphic phase transformation close in size (or even larger due to a higher *T*) to that before the phase transformation (supporting information S6-10). Taking into account thermal conductivity of ppv would be reduced by only ~1% even with the grain size of ~ 10^{-3} mm (Fig. 6-5c), the effect of grain boundary scattering on the thermal conductivity of ppv is likely to be negligible in the actual lower mantle.

Figure 6-5 indicates that the ppv used in experimental studies can easily be affected by grain boundaries. Our estimated ppv sample grain size of 0.34 μm gives the γ value of 0.39±0.14 at room temperature, i.e., a significant reduction of κ_{latt} by 61±14% due to grain boundary scattering. On the other hand, temperatures of 1000 K, 2000 K and 3000 K with the same ppv grain size yield the γ values of 0.75±0.07, 0.87±0.04 and 0.92±0.03, respectively. This suggests that we need to consider carefully our evaluation of the temperature effect on the κ_{latt} of ppv from our obtained data.

6.4.2. Pressure and temperature dependences of the thermal conductivity of Fe-bearing ppv

We adopted the density-temperature κ_{latt} model described in Eq. (6-6) for an extrapolation to the lowermost mantle *P*-*T* conditions. The pressure dependence of κ_{latt} of ppv at room temperature was estimated from the following:

$$g = \left(\partial \ln \kappa_{\mathrm{ppv}} / \partial \ln \rho\right)_T. \qquad (6\text{-}11)$$

The calculated *g* values for F3 and F10 ppv were 6.0±0.3 and 7.8±0.5, respectively (Fig. S6-11). In the previous section, we insisted that the grain boundary effect would have significant influence on the κ_{latt} of ppv in experimental studies

conducted at room temperature. For the correction of the effect of grain boundary scattering, we used the γ value of 0.39±0.14, 0.75±0.06 and 0.83±0.05 at 300, 1000 and 1500 K, respectively (Fig. S6-12). We obtained the a value of 0.65±0.04 for F10 ppv at 138 GPa. Though there are only two data for the κ_{latt} of F10 ppv at 177 GPa, the fitting to Eq. (6-6) yielded the a value of 0.69, which is within the uncertainty of that at 138 GPa (Fig. 6-6).

6.4.3. Thermal conductivity of ppv with pyrolitic composition

Fe content in ppv in the pyrolitic lower mantle is thought to be lower than that in bdg due to its poor capacity of Fe^{3+}. According to Sinmyo et al. (2011), bdg in the pyrolitic mantle contains Fe of 0.114(6) in pfu, whereas ppv contains 0.036(11) in pfu. This Fe amount is fairly in accordance with our F3 ppv composition, thus it replicates the ppv in the Earth's lowermost mantle well. For the reference value κ_0 in Eq. (6-6), the κ_{latt} datum of F3 ppv collected at 122 GPa and 300 K was corrected from the γ value at room-T of 0.39±0.14. The calculated κ of 59.8±9.3 W/m/K was set for the κ_0. T_0 and ρ_0 were set as 300 K and 5.47 g/cm^3, and g value of 6.0±0.3 was used. For the a value, we assumed that the temperature dependences of κ_{latt} for F3 and F10 ppv are the same, and used that of 0.65±0.04. We assumed a typical temperature gradient in the thermal boundary layer above the CMB of 7 K/km, the thickness of 200 km, and the CMB temperature of 3700 K (Lay et al., 2008; Tateno et al., 2009). Here, the radiative thermal conductivity (κ_{rad}) of ppv and its electronic contribution from the measured electronic conductivity of ~10^2 S/m (Ohta et al., 2008a) is thought to be negligible at our measured temperature condition, so we simply regarded our obtained κ data at high-T as κ_{latt}. Our estimated depth profile of the κ_{latt} of ppv with pyrolitic composition

increases monotonically with depth up to the top of the thermal boundary layer above the CMB, which increases from 16.6±1.4 W/m/K at a depth of 2450 km, to 18.0±1.4 W/m/K at a depth of 2650 km (Fig. 6-7a). However, this turns into a decrease through the thermal boundary layer to 14.0±1.3 W/m/K at the CMB, which is 1.5±0.1 times higher than that of bdg with pyrolitic composition (Fe 10 mol%, Al 10 mol%) estimated in Okuda et al. (2019). We also calculated the bulk κ_{latt} of pyrolite using Hashin-Shtrikman averaging (Hashin and Shtrikman, 1962) with κ_{latt} of ppv (this study) or bdg (Okuda et al., 2019; Chapter 5), and fp (Ohta et al., 2017), assuming volume ratio on pyrolite mineralogy of 80% and 20%, respectively. Here, since lower mantle fp is thought to contain ~20 mol% Fe (Sinmyo et al., 2011), we used the reported κ results of $(Mg_{0.81}Fe_{0.19})O$ fp (Ohta et al., 2017). The total κ of pyrolite was estimated by the summation of our estimated bulk κ_{latt} and the recently reported κ_{rad} of pyrolite (Lobanov et al., 2020) (Fig. 6-7b). Similar to the trend seen in the κ_{latt} of ppv, we found that the total κ of pyrolite for both ppv+fp and bdg+fp aggregates increases with depth up to the uppermost thermal boundary layer, and then decreases in this region due to a weak increase of κ_{rad} compared to the strong reduction of κ_{latt} along the steep temperature gradient in the thermal boundary layer (Fig. 6-7b). The κ of ppv+fp at the CMB was estimated as 12.8±1.3 W/m/K, and that of bdg+fp as 9.4±0.8 W/m/K. The recent κ measurement of ppv+fp pyrolite in a DAC showed a conductivity value of 3−10 W/m/K at 124 GPa and 2000−3000 K (Geballe et al., 2020), which is much lower than our estimated κ of ppv+fp at the CMB. However, since only one datum was reported for the κ of ppv+fp aggregate, and there are many possible reasons for this difference (e.g., the effect of $CaSiO_3$ perovskite; grain boundary scattering; spin transition of Fe in ferropericlase; chemical composition; see supporting information S6-14), it is difficult

to simply compare them. Ohta et al. (2012) estimated the κ of $MgSiO_3$ (perovskite or ppv) +MgO aggregates as 11.0±2.0 W/m/K and 17.8±3.9 W/m/K, respectively. In other words, the phase transition from $MgSiO_3$ perovskite to ppv enhances the bulk κ by a factor of 1.6±0.5. Our estimated total κ of pyrolite shows that transformation from bdg to ppv in pyrolite increases its bulk κ by a factor of 1.5±0.3 in the lower mantle (Fig. 6-7b), which is a ratio consistent with that reported in Ohta et al. (2012). The ~1.5 times higher bulk κ with the transformation of bdg to ppv creates a lateral thermal heterogeneity on CMB heat flux, with lateral variations of ~30 mW/m^2 with simply adopting a typical temperature gradient of 7 K/km (Lay et al., 2008). This heat flux variation should be larger since conductive ppv forms in the lower-*T* regions above the CMB, where the thermal gradients are greater than the poorly conductive bdg-dominant regions. Such enhanced lateral heat flux variation due to the bdg to ppv transformation in the pyrolitic lower mantle can affect the flow in the outer core, which is thought to influence the frequency of geomagnetic reversals (e.g., Olson, 2016). Also, it is worth mentioning that the estimated κ of 12.8±1.3 W/m/K of ppv+fp aggregate is ~1.3 times higher than the conventionally used lowermost mantle κ of 10 W/m/K (e.g., Lay et al., 2008), the conductivity difference of which may also affect lower mantle dynamics.

The constraint of the abundance of ppv as a function of depth in the Earth's lower mantle is important for a better understanding of the κ-depth profile since our result implies that ppv enhances the bulk mantle κ. However, there is a discrepancy in the results of the transition pressure of Fe-bearing ppv. Tateno et al. (2007) showed that the incorporation of Fe into ppv would not change the onset transition pressure, but expand the pressure of completion of the transition, i.e., the expansion of the stable *P*-*T* region of bdg phase due to Fe incorporation. In contrast, a different experimental study using a

similar sample composition as Tateno et al. (2007) suggested that the presence of Fe would reduce the onset pressure to 85 GPa, yet would not affect the offset pressure (Dorfman et al., 2013), i.e., the wider stable *P-T* region of ppv phase in an Fe-bearing system. Incorporation of aluminum may also affect the κ of ppv, however, currently, there is no research focused on (Fe,Al)-bearing ppv. Ppv in the pyrolitic mantle is considered to contain a certain amount of Al, such as 0.08 in pfu (Sinmyo et al., 2011). Further investigations into the incorporation effects of impurities such as Fe, Al on the physical properties of the Earth's lower mantle minerals in a sequence are important to carry out in the future.

6.5. Conclusions

We measured the κ of $(Mg_{0.97}Fe_{0.03})SiO_3$ and $(Mg_{0.90}Fe_{0.10})SiO_3$ ppv up to 149 GPa and 177 GPa, respectively. Both conductivities showed moderately lower values than that of the experimentally measured $MgSiO_3$ ppv (Ohta et al., 2012). Based on the previous studies, we quantified the effect of grain boundary scattering on the κ_{latt} of ppv; that of the ppv synthesized in a DAC (~135 GPa, heating for ~1 hr at ~2000 K) at 300 K would be reduced by 61±14% due to the effect, implying that we need to consider carefully the results obtained from room temperature measurements on highly conductive minerals. On the other hand, the grain boundary effect is insignificant for the κ_{latt} of typical lower mantle ppv, which would be reduced by only ~10%. We found that

the bulk conductivity of ppv+fp aggregate is 1.5 times higher than that of bdg+fp in the lower mantle, which can affect lower mantle dynamics.

6.6. References

Akahama, Y., Kawamura, H., 2004. High-pressure Raman spectroscopy of diamond anvils to 250 GPa: Method for pressure determination in the multimegabar pressure range. J. Appl. Phys., 96, 3748–3751.

Ammann, M. W., A. M. Walker, S. Stackhouse, J. Wookey, A. M. Frost, J. P. Brodholt, D. P. Dobson., 2014. Variation of thermal conductivity and heat flux at the Earth's core mantle boundary. Earth Planet. Sci. Lett., 390, 175–185.

Dalton, D. A., W.-P. Hsieh, G. T. Hohensee, D. G. Cahill, A. F. Goncharov, 2013. Effect of mass disorder on the lattice thermal conductivity of MgO periclase under pressure. Sci. Rep., 3, 2400.

Dekura, H., Tsuchiya, T., 2019. Lattice thermal conductivity of $MgSiO_3$ post-perovskite under the lowermost mantle conditions from *ab initio* anharmonic lattice dynamics. Geophys. Res. Lett., 46, 12919–12926.

Dorfman, S.M., Meng, J., Prakapenka, V.B., Duffy, T.S., 2013. Effects of Fe-enrichment on the equation of state and stability of $(Mg,Fe)SiO_3$ perovskite. Earth Planet. Sci. Lett., 361, 249–257.

Geballe, Z. M., Sime, N., Badro, J., van Keken, P. E., Goncharov, A. F., 2020. Thermal conductivity near the bottom of the Earth's lower mantle: Measurements of pyrolite up to 120 GPa and 2500 K. Earth Planet. Sci. Lett., 536, 116161.

Glišovic, P., Forte, A.M., Ammann, M.W., 2015. Variations in grain size and viscosity based on vacancy diffusion in minerals, seismic tomography, and geodynamically inferred mantle rheology. Geophys. Res. Lett. 42, 6278–6286. http://dx.doi.org/10.1002/2015GL065142.

Haigis, V., M. Salanne, S. Jahn., 2012. Thermal conductivity of MgO, $MgSiO_3$ perovskite and post-perovskite in the Earth's deep mantle. Earth Planet. Sci. Lett., 355-356, 102–108.

Hasegawa. A., Ohta, K., Yagi, T., Hirose, K., Okuda, Y., Kondo, T., 2019a. Composition and pressure dependence of lattice thermal conductivity of (Mg,Fe)O solid solutions. C. R. Geoscience, 351, 229–235.

Hasegawa, A., Yagi, T., Ohta, K., 2019b. Combination of pulsed light heating thermoreflectance and laser-heated diamond anvil cell for *in-situ* high pressure-temperature thermal diffusivity measurements. Rev. Sci. Instrum., 90, 074901.

Hashin, Z., S. Shtrikman, 1962. A variational approach to the theory of the effective magnetic permeability of multiphase materials. J. Appl. Phys., 33, 3125–3131.

Ho, C. Y., R. W. Powell, P. E. Liley., 1972. Thermal conductivity of the elements. J. Phys. Chem. Ref. Data, 1, 279–422.

Hofmeister, A. M., M. Pertermann, J. M. Branlund., 2007. Properties of rocks and minerals -thermal conductivity of the Earth, in Treatise on Geophysics. Vol. 2: Mineral physics, pp. 543–578, Elsevier, Amsterdam, Netherlands.

Hsieh, W. P., Deschamps, F., Okuchi, T., Lin, J. F., 2017. Reduced lattice thermal conductivity of Fe-bearing bridgmanite in Earth's deep mantle. J. Geophys. Res. Sol. Earth, 122, 7, 4900–4917.

Hsieh, W.P., Deschamps, F., Okuchi, T., Lin, J.F., 2018. Effects of iron on the lattice thermal conductivity of Earth's deep mantle and implications for mantle dynamics. Proc. Natl. Acad. Sci. U.S.A., 4099–4104.

Imada, S., K. Ohta, T. Yagi, K. Hirose, H. Yoshida, H. Nagahara, 2014. Measurements of lattice thermal conductivity of MgO to core-mantle boundary pressures. Geophys. Res. Lett., 41, 4542–4547.

Keawprak, N., Tu, R., Goto, T., 2009. Thermoelasticity of $CaIrO_3$ ceramics prepared by spark plasma sintering. J. Chem. Soc. Japan, 117:466–469.

Komabayashi, T., Hirose, K., Sugimura, E., Sata, N., Ohishi, Y., Dubrovinsky, L.S., 2008. Simultaneous volume measurements of post-perovskite and perovskite in $MgSiO_3$ and their thermal equations of state. Earth Planet. Sci. Lett., 265, 515–524.

Lay, T., J. Hernlund, B. A. Buffett, 2008. Core–mantle boundary heat flow. Nat. Geosci., 1, 25–32.

Lobanov, S.S., Holtgrewe, N., Ito, G., Badro, J., Piet, H., Nabiei, F., Lin, J-F., Bayarjargal, L., Wirth, R., Schreiber, A., Goncharov, A.F., 2020. Blocked radiative heat transport in the hot pyrolitic lower mantle. Earth Planet. Sci. Lett., 537, 116176.

Manthilake, G.M., de Koker, N., Frost, D.J., McCammon, C.A., 2011. Lattice thermal conductivity of lower mantle minerals and heat flux from Earth's core. Proc. Natl. Acad. Sci. U.S.A., 108, 17901–17904.

Martin, J.J., Sidles, P.H., Danielson, G.C., 1967. Thermal Diffusivity of Platinum from 300° to 1200°K, J. App. Phys., 38, 3075.

Metsue, A., T. Tsuchiya, 2011. Lattice dynamics and thermodynamic properties of $(Mg,Fe^{2+})SiO_3$ postperovskite. J. Geophys. Res., 116, B08207.

Murakami, M., Hirose, K., Kawamura, K., Sata, N., Ohishi, Y., 2004. Post-perovskite phase transition in $MgSiO_3$. Science, 304, 855–858.

Nishio-Hamane, D., Yagi, T., 2009. Equations of state for postperovskite phases in the $MgSiO_3$–$FeSiO_3$–$FeAlO_3$ system. Phys. Earth Planet. Inter. 175, 145–150.

Oganov, A.R., and Ono, S., 2004. Theoretical and experimental evidence for a postperovskite phase of $MgSiO_3$ in Earth's D″ layer. Nature, 430, 445–448.

Ohta, K., Onoda, S., Hirose, K., Sinmyo, R., Shimizu, K., Sata, N., Ohishi, Y., Yasuhara, A., 2008a. The electrical conductivity of post-perovskite in Earth's D″ layer. Science, 320, 89–91.

Ohta, K., Hirose, K., Lay, T., Sata, N., Ohishi, Y., 2008b. Phase transitions in pyrolite and MORB at lowermost mantle conditions: Implications for a MORB-rich pile above the core-mantle boundary. Earth Planet. Sci. Lett., 267, 107–117.

Ohta, K., T. Yagi, N. Taketoshi, K. Hirose, T. Komabayashi, T. Baba, Y. Ohishi, J. Hernlund, 2012. Lattice thermal conductivity of $MgSiO_3$ perovskite and post-perovskite at the core–mantle boundary. Earth Planet. Sci. Lett., 349-350, 109–115.

Ohta, K., Yagi, T., Hirose, K., 2014. Thermal diffusivities of $MgSiO_3$ and Al-bearing $MgSiO_3$ perovskites, Am. Mineral, 99, 94–97.

Ohta, K., Yagi, T., Hirose, K., Ohishi, Y., 2017. Thermal conductivity of ferropericlase in the Earth's lower mantle. Earth Planet. Sci. Lett., 465, 29–37.

Okuda, Y., Ohta, K., Yagi, T., Sinmyo, R., Wakamatsu, T., Hirose, K., Ohishi, Y., 2017. The effect of iron and aluminum incorporation on lattice thermal conductivity of bridgmanite at the Earth's lower mantle. Earth Planet. Sci. Lett., 474, 25–31.

Okuda, Y., Ohta, K., Sinmyo, R., Hirose, K., Yagi, T., Ohishi, Y., 2019. Effect of spin transition of iron on the thermal conductivity of (Fe, Al)-bearing bridgmanite. Earth Planet. Sci. Lett., 520, 188–198.

Olson, P., 2016. Mantle control of the geodynamo: consequences of top-down regulation. Geochem. Geophys. Geosyst. 17, 1935–1956.

Ross, R. G., P. Andersson, B. Sundqvist, G. Bäckström, 1984. Thermal conductivity of solids and liquids under pressure. Rep. Prog. Phys., 47, 1347–1402.

Sakai, T., Dekura, H., Hirao, N., 2016. Experimental and theoretical thermal equations of state of $MgSiO_3$ post-perovskite at multi-megabar pressures. Sci. Rep., 6, 22652.

Sidles, P.H., Danielson, G.C., 1954. Thermal Diffusivity of Metals at High Temperatures. J. App. Phys., 25, 58, https://doi.org/10.1063/1.1721521.

Sinmyo, R., Hirose, K., Muto, S., Ohishi, Y., Yasuhara, A., 2011. The valence state and partitioning of iron in the Earth's lowermost mantle. J. Geophys. Res., 116, B07205.

Slack, G., 1964. Thermal conductivity of pure and impure silicon, silicon carbide, and diamond. J. App. Phys., 35, 3460–3466.

Smith, D. S., S. Fayette, S. Grandjean, C. Martin, R. Telle, T. Tonnessen, 2003. Thermal resistance of grain boundaries in alumina ceramics and refractories. J. Am. Ceram. Soc., 86, 105–111.

Solomatov, V. S., El-Khozondar, R., Tikare, V., 2002. Grain size in the lower mantle: constraints from numerical modeling of grain growth in two-phase systems. Phys. Earth Planet. Inter., 129(3−4), 265−282.

Stacey, F., 1992. In: Physics of the Earth, 3rd ed. Brookfield, Brisbane, Australia.

Stackhouse, S., Stixrude, L., Karki, B., 2015. First-principles calculations of the lattice thermal conductivity of the lower mantle. Earth Planet. Sci. Lett., 427, 11–17.

Tateno, S., Hirose, K., Sata, N., Ohishi, Y., 2007. Solubility of FeO in $(Mg,Fe)SiO_3$ perovskite and the post-perovskite phase transition. Phys. Earth Planet. Inter. 160, 319–325.

Tateno, S., Hirose, K., Sata, N., Ohishi, Y., 2009. Determination of post-perovskite phase transition boundary up to 4400 K and implications for thermal structure in D″ layer. Earth Planet. Sci. Lett., 277, 130–136.

Tsuchiya, T., 2003. First-principles prediction of the *P–V–T* equation of state of gold and the 660-km discontinuity in Earth's mantle. J. Geophys. Res, 108 (B10), 2462.

Tsuchiya, T., Tsuchiya, J., Umemoto, K., Wentzcovitch, R.M., 2004. Phase transition in $MgSiO_3$ perovskite in the earth's lower mantle, Earth Planet. Sci. Lett., 224, 241–248.

Yagi, T., K. Ohta, K. Kobayashi, N. Taketoshi, K. Hirose, T. Baba, 2011. Thermal diffusivity measurement in a diamond anvil cell using a light pulse thermoreflectance technique. Meas. Sci. Technol., 22, 024011.

Yamazaki, D., T. Kato, E. Ohtani, M. Toriumi, 1996. Grain growth rates of $MgSiO_3$ perovskite and periclase under lower mantle conditions. Science, 274, 2052–2054.

Yoshino, T., Yamazaki, D., 2007. Grain growth kinetics of $CaIrO_3$ perovskite and post-perovskite, with implications for rheology of D″ layer. Earth Planet. Sci. Lett., 255, 485–493.

Table 6-1. Experimental conditions of the thermal conductivity measurement of $(Mg_{1-x},Fe_x)SiO_3$ ppv

Run#	Fe content x (pfu)	culet size (μm)	Synthesized Pressure (GPa)	Pressure (GPa)	Temperature (K)	D_{ppv} (mm^2/s)	κ_{ppv} (W/(m*K))	Pressure error (GPa)	Thermal pressure (GPa)
1	0.03	120	135.1	135.1*	300	16.5(26)	44.8(69)	6.8*	-
				121.9	300	13.4(22)	36.5(57)	12.2	-
2	0.03	120	148.6	148.6*	300	19.4(69)	50.0(178)	7.4*	-
3	0.10	120	138.2	138.2*	300	15.1(14)	40.1(37)	6.9*	-
				142.2	1458(106)	5.3(5)	35.2(35)	14.2	4.1
				142.7	1558(114)	4.2(4)	27.8(28)	14.3	4.7
				134.7	300	12.1(11)	32.2(30)	13.5	-
4	0.10	90	176.6	176.6*	300	20.3(5)	52.8(117)	17.7	-
				179.5	1070(79)	6.5(2)	42.9(101)	17.9	2.9

*Pressure calibration based on the EoS of gold (Tsuchiya, 2003).

We used typical values of 10% and 5% for pressure errors with pressure calibration using Raman spectroscopy of diamond and EoS of gold, respectively.

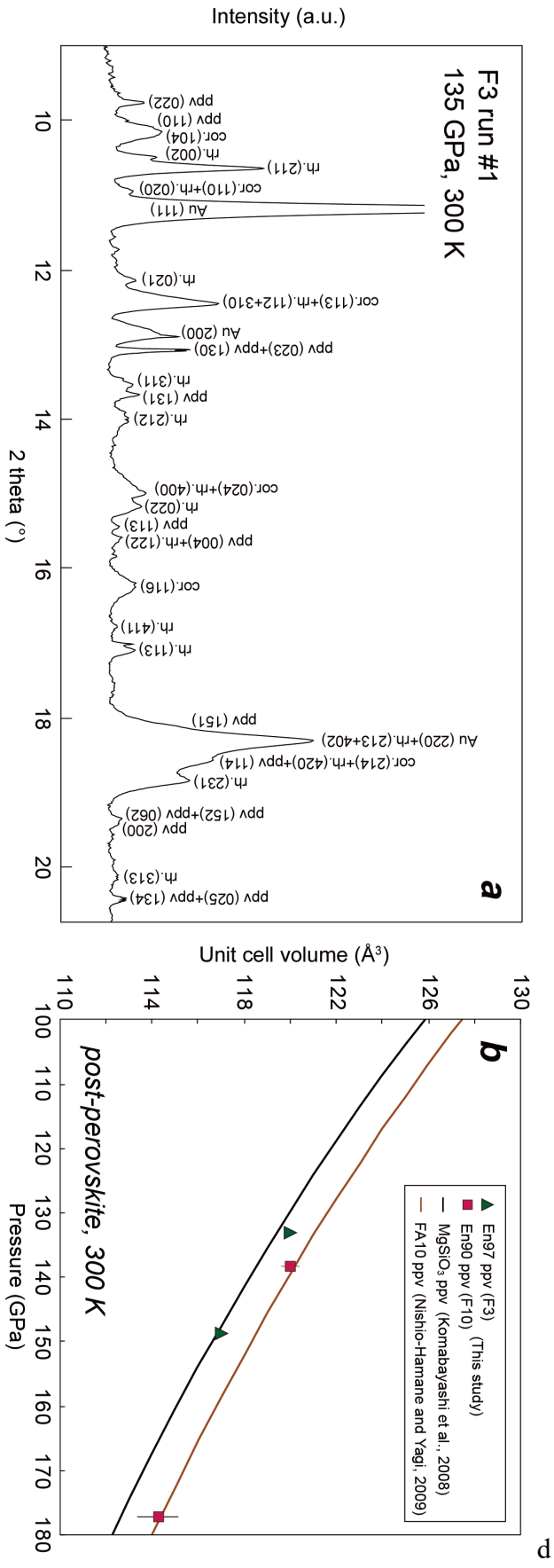
Intensity (a.u.)
F3 run #1
135 GPa, 300 K
a
ppv (025)+ppv (134)
rh.(313)
ppv (200)
ppv (152)+ppv (062)
rh.(231)
cor.(214)+rh.(420)+ppv (114)
Au (220)+rh.(213+402)
ppv (151)
rh.(411)
rh.(113)
cor.(116)
ppv (004)+rh.(122)
ppv (113)
rh.(022)
cor.(024)+rh.(400)
rh.(212)
ppv (131)
rh.(311)
ppv (023)+ppv (130)
Au (200)
cor.(113)+rh.(112+310)
rh.(021)
Au (111)
cor.(110)+rh.(020)
rh.(211)
rh.(002)
cor.(104)
ppv (110)
ppv (022)
2 theta (°)
10
12
14
16
18
20
Unit cell volume (Å³)
110
114
118
122
126
130
b
post-perovskite, 300 K
En97 ppv (F3) (This study)
En90 ppv (F10) (This study)
MgSiO3 ppv (Komabayashi et al., 2008)
FA10 ppv (Nishio-Hamane and Yagi, 2009)
Pressure (GPa)
100
110
120
130
140
150
160
170
180

d

Fig. 6-1. (a) XRD pattern of ppv sample F3 after the synthesis in run #1. The numbers in the figure indicate Miller indices. The notations of ppv, Au, cor. and rh. in the figure denote diffraction peaks from post-perovskite phase, gold as a pressure marker, corundum and Rh_2O_3(II)-type Al_2O_3 as pressure mediums, respectively. (b) Obtained unit cell volumes of ppv in each run. Green triangles and pink squares, F3 and F10 ppv (this study); solid and broken black curves, the Equations of state of $MgSiO_3$ ppv provided in Komabayashi et al. (2008); red curve, Fe and Al 10% ppv (Nishio-Hamane and Yagi, 2009).

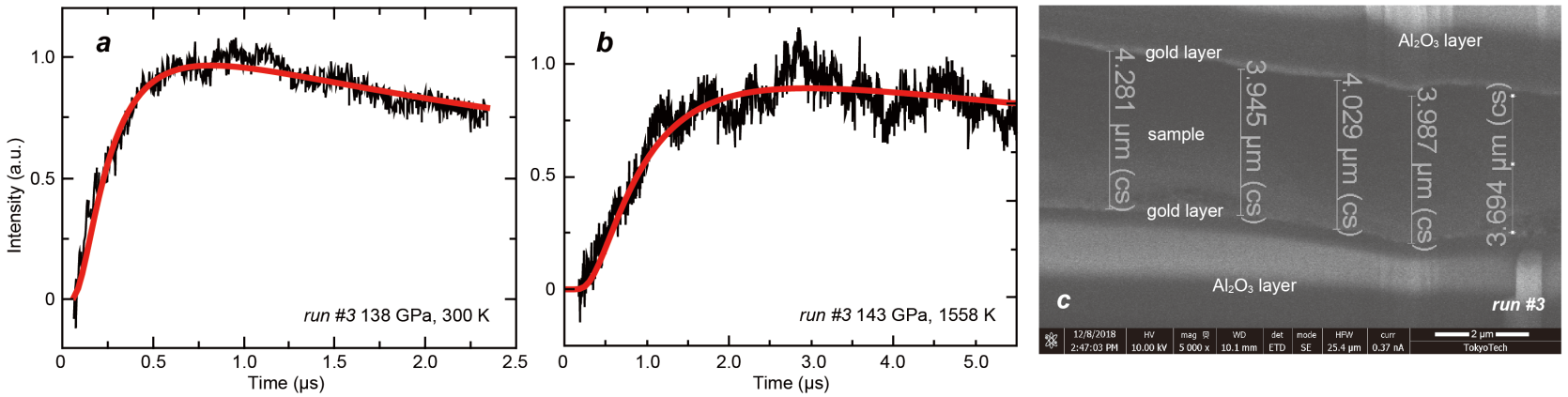
a
b
c
Intensity (a.u.)
Time (μs)
run #3 138 GPa, 300 K
run #3 143 GPa, 1558 K
gold layer
sample
gold layer
Al2O3 layer
Al2O3 layer
4.281 μm (cs)
3.945 μm (cs)
4.029 μm (cs)
3.987 μm (cs)
3.694 μm (cs)
run #3

Fig. 6-2. (a) Typical temperature history curve obtained in this study at room-*T*, and (b) at high-*T*. Red curve is the fitting curve, which gives thermal diffusion time τ. (c) FE-SEM image of a cross-section of the recovered sample in run #3. Note that the apparent thickness shown in this figure is different from the actual sample thickness due to its acquisition from an oblique direction to the sample stage. cs in the figure denotes cross-section, meaning that the thicknesses displayed are corrected values from the slanting stage mentioned above.

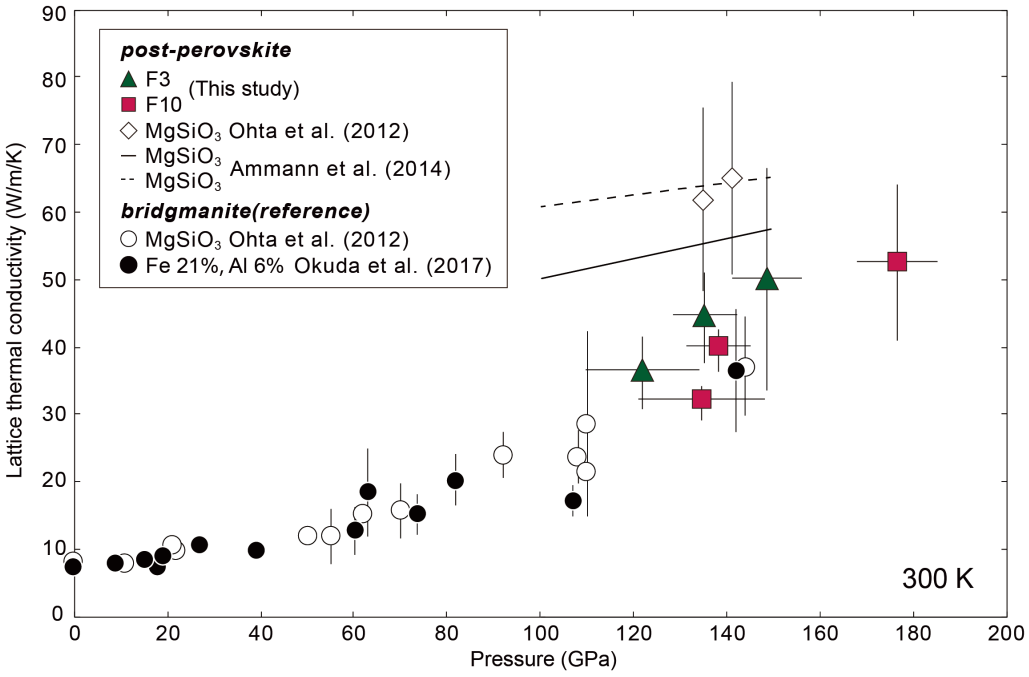

Fig. 6-3. Lattice thermal conductivity of ppv as a function of pressure at room temperature. Green triangles and pink squares, F3 and F10 ppv respectively (this study); open diamonds, $MgSiO_3$ ppv (Ohta et al., 2012); solid and broken lines, $MgSiO_3$ ppv (Ammann et al., 2014) using potentials from Oganov and Ono (2004) and Murakami et al. (2004), respectively; open and solid circles, $MgSiO_3$ and $Mg_{0.832}Fe_{0.209}Al_{0.060}Si_{0.916}O_3$ bdg respectively (Ohta et al., 2012; Okuda et al., 2017). Note that data of Haigis et al. (2012) and Dekura and Tsuchiya (2019) at 135 GPa, 300 K are not plotted in this figure because they are way above the other plots.

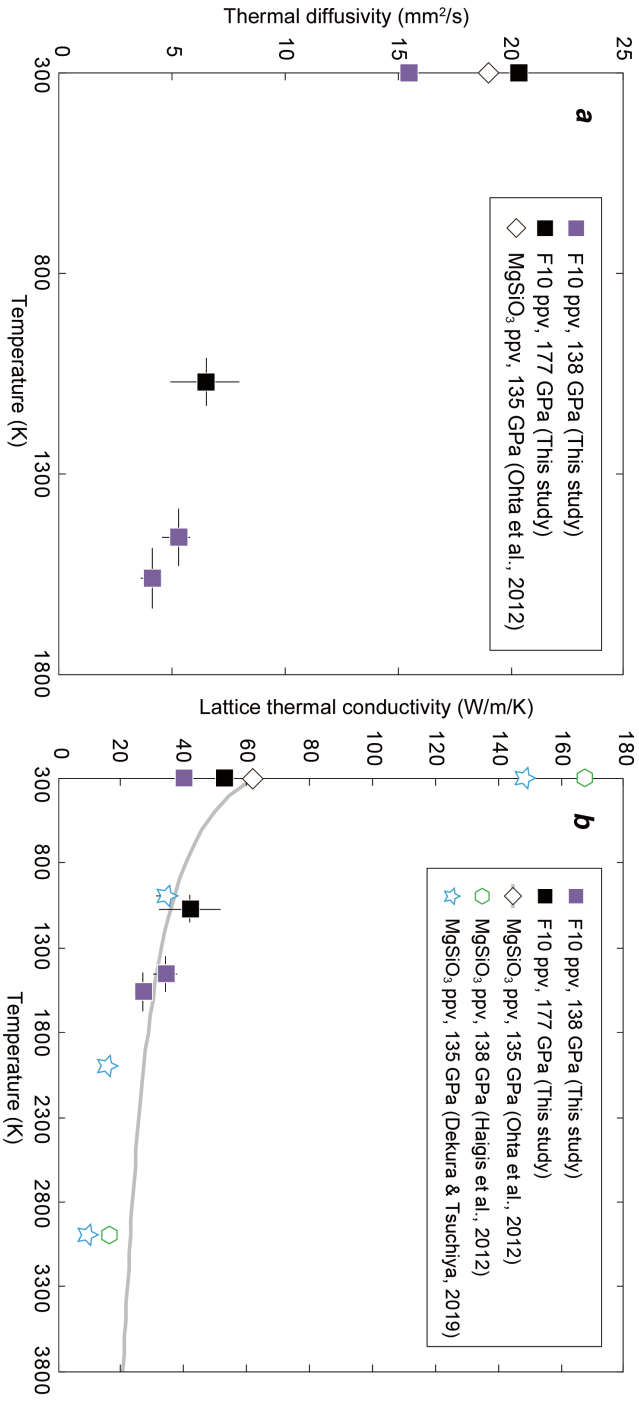

Fig. 6-4. (a) High temperature thermal diffusivity of F10 ppv. Purple and black squares are data obtained in runs #3 and #4 respectively. Open diamond is the diffusivity datum of $MgSiO_3$ ppv (Ohta et al., 2012). (b) High temperature lattice thermal conductivity of F10 ppv. Purple and black squares are data obtained in runs #3 and #4 respectively.

Open diamond, green open hexagons and blue open stars are the reported conductivity of $MgSiO_3$ ppv determined experimentally (Ohta et al., 2012), by MD simulation (Haigis et al., 2012), and MD simulation based on first principle (Dekura and Tsuchiya, 2019), respectively. Gray curve indicates the high temperature lattice thermal conductivity of $MgSiO_3$ ppv estimated in Ohta et al. (2012).

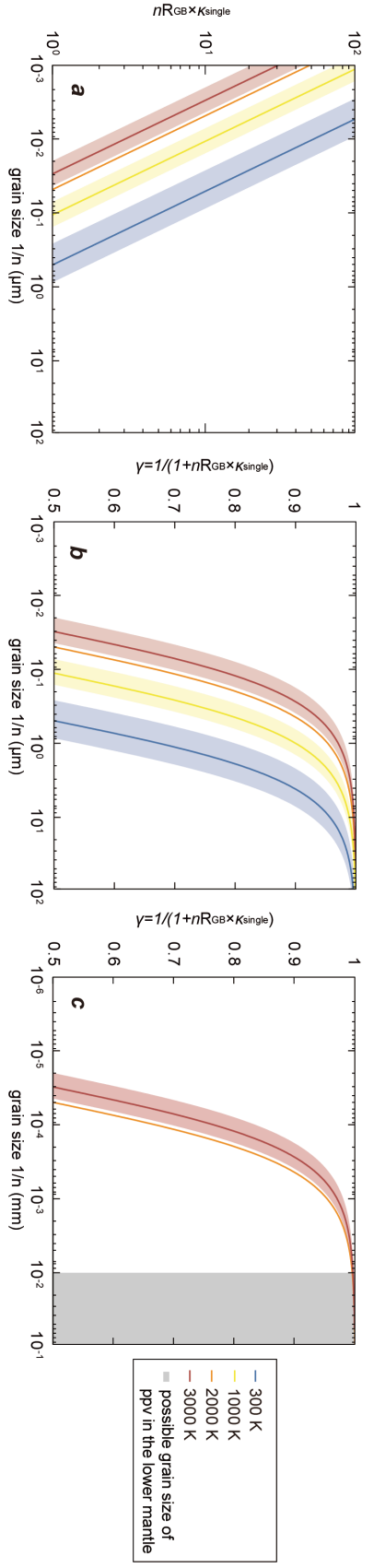
a
b
c
nRGB×κsingle
γ=1/(1+nRGB×κsingle)
grain size 1/n (μm)
grain size 1/n (mm)
300 K
1000 K
2000 K
3000 K
possible grain size of ppv in the lower mantle

Fig. 6-5. (a) nR_{GB}/R_{single} and (b) grain boundary effect coefficient γ on lattice thermal conductivity of ppv at 135 GPa as a function of its grain size. Blue, yellow, orange and red curves show the nR_{GB}/R_{single} or γ at 300, 1000, 2000 and 3000 K, respectively. Bands indicate estimated errors at 300, 1000 and 3000 K respectively. For simplicity, error of the nR_{GB}/R_{single} or γ at 2000 K is not shown (see Fig. S6-9). (c) γ of ppv in the Earth's lower mantle. Gray band indicates the possible grain size of ppv estimated in previous studies (Solomatov et al., 2002; Glišovic´ et al., 2015; see supporting information S6-10).

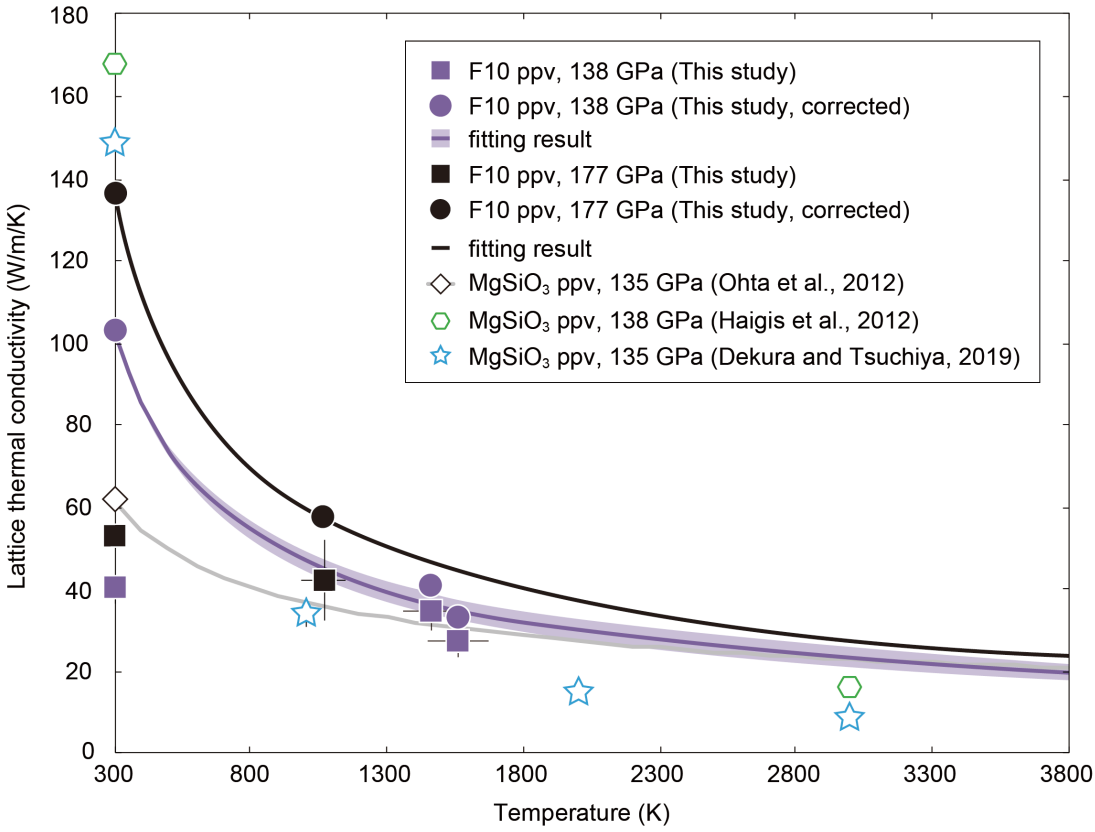

Fig. 6-6. High temperature lattice thermal conductivity of F10 ppv. Purple and black squares are data obtained in runs #3 and #4 respectively. Open diamond, green open hexagons and blue open stars are the reported conductivity of $MgSiO_3$ ppv determined in Ohta et al. (2012), Haigis et al. (2012) and Dekura and Tsuchiya (2019), respectively. Gray curve indicates the high temperature lattice thermal conductivity of $MgSiO_3$ ppv estimated in Ohta et al. (2012). Purple and black circles indicate the high temperature thermal conductivity of F10 ppv after the correction of the effect of grain boundary scattering obtained in runs #3 and #4, respectively. Purple band shows the fitting result by Eq. (6-6).

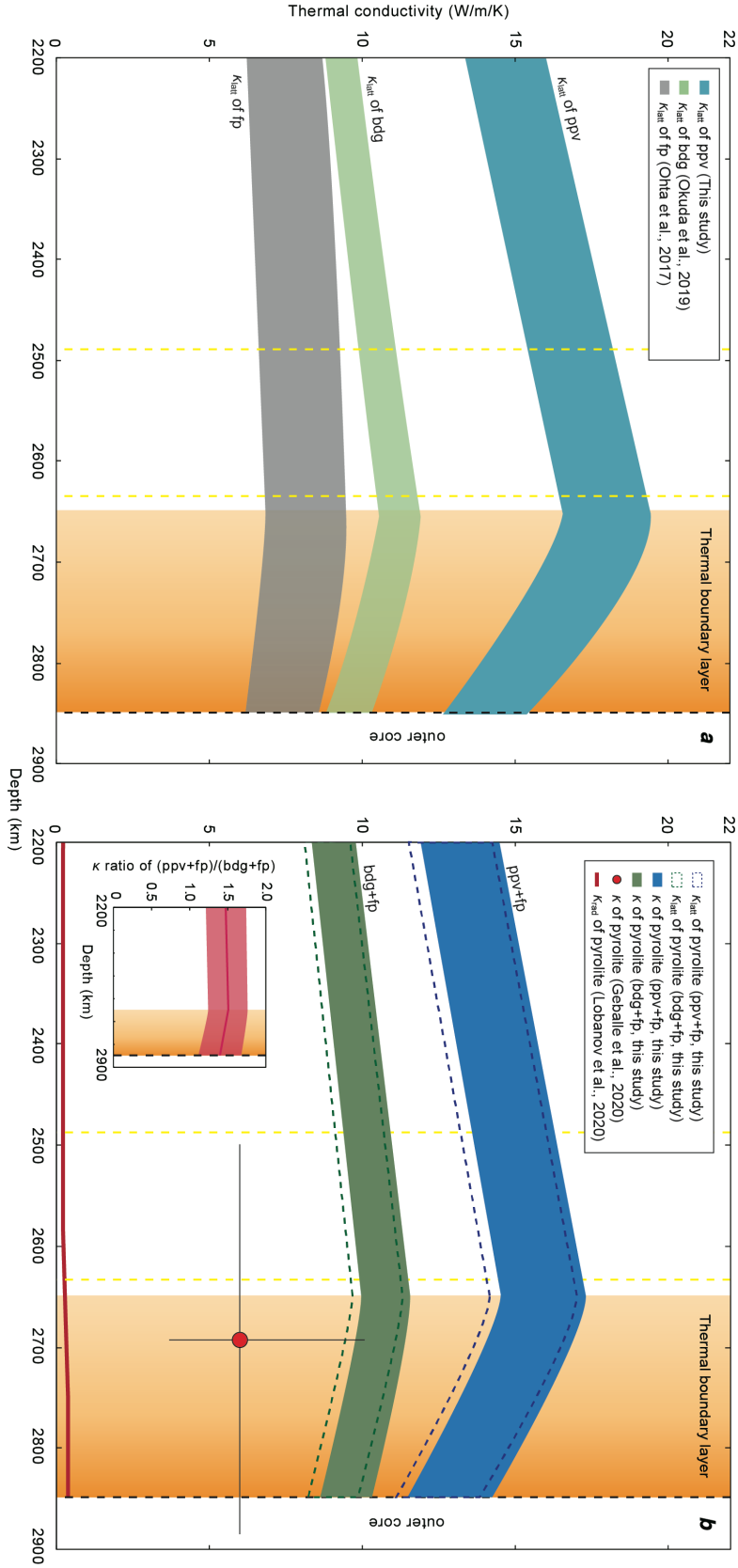
Thermal conductivity (W/m/K)
Depth (km)
a
b
Thermal boundary layer
outer core
κ_{latt} of ppv (This study)
κ_{latt} of bdg (Okuda et al., 2019)
κ_{latt} of fp (Ohta et al., 2017)
κ_{latt} of ppv
κ_{latt} of bdg
κ_{latt} of fp
κ_{latt} of pyrolite (ppv+fp, this study)
κ_{latt} of pyrolite (bdg+fp, this study)
κ of pyrolite (ppv+fp, this study)
κ of pyrolite (bdg+fp, this study)
κ_{rad} of pyrolite (Lobanov et al., 2020)
ppv+fp
bdg+fp
κ ratio of (ppv+fp)/(bdg+fp)

Fig. 6-7. (a) κ_{latt} of lower mantle minerals with pyrolitic composition. Blue, green and gray bands indicate the estimated κ_{latt} of ppv, bdg and fp, respectively. (b) Thermal conductivity of pyrolite. Blue and green broken lines indicate the estimated bulk κ_{latt} of pyrolite with ppv+fp, and bdg+fp, respectively. Blue and green bands indicate the estimated bulk total κ ($=\kappa_{latt}+\kappa_{rad}$) of pyrolite with ppv+fp, and bdg+fp, respectively. Red line indicates the κ_{rad} of pyrolite (Lobanov et al., 2020). Red circle indicates the κ of pyrolite by direct measurement (Geballe et al., 2020). Yellow broken lines indicate the suggested onset and offset bdg to ppv phase transition depth in the pyrolitic lower mantle (Ohta et al., 2008b). Orange band indicates the 200 km thick thermal boundary layer above the CMB (Lay et al., 2008). Inset: κ ratio of pyrolite with ppv+fp, and bdg+fp.

6.8. Supplemental material

S6-1. Chemical composition and XRD patterns

Table S6-1. Mg/(Mg+Fe) ratio of gel starting material

F3	F10
0.971(2)	0.89*

*Ohta et al. (2008)

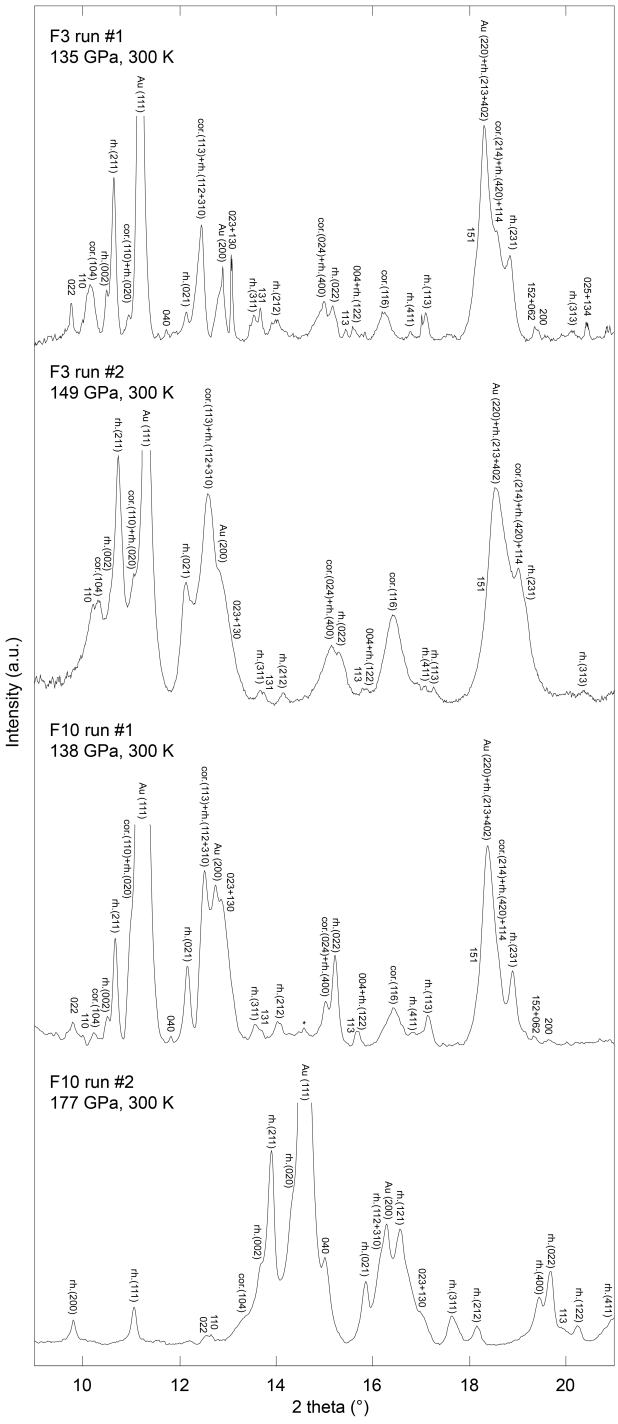

Fig. S6-1. Obtained XRD patterns in each run.

The numbers in the figure indicate Miller indices of ppv. The notations Au, cor. and rh. in the figure denote diffraction peaks from gold for pressure marker, Al_2O_3 corundum and Rh_2O_3-type Al_2O_3 as pressure mediums, respectively. * indicates an unknown peak.

S6-2. Temperature history curves

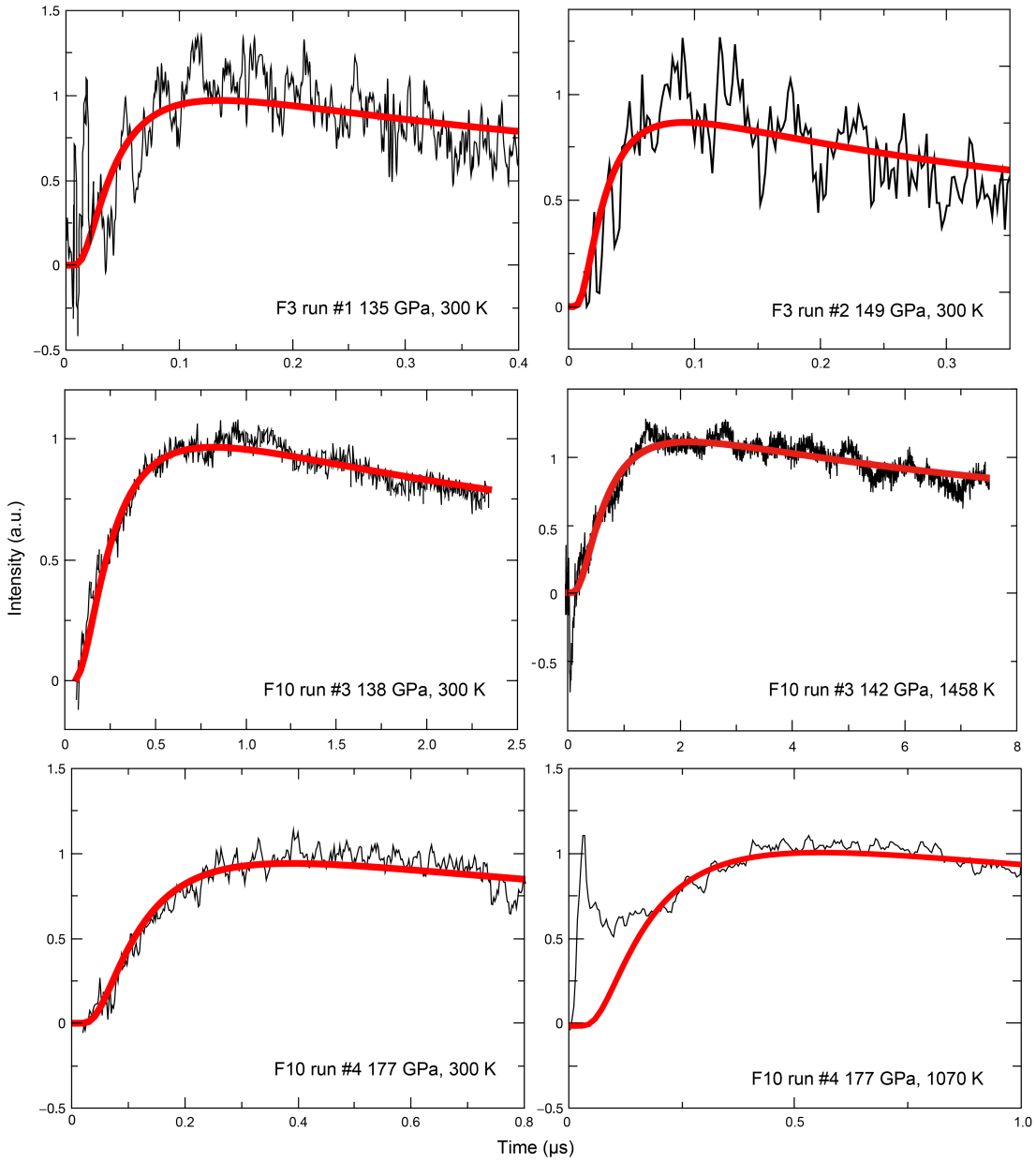

Fig. S6-2-1. Obtained temperature history curves in each run.

Red curves are the fitting curve of thermal diffusion equation (Eq. 6-1 in the main text). The spike near t=0 in the thermoreflectance signal at high-T shown in Fig.S6-2 for signals of F10 ppv in run #3 at 1458 K, and in run #4 at 1070 K, often appears during the measurement. This spike is generally attributed to two events: 1) the heat transfer

from the bottom of the sample as photons near light speed, and 2) the elastic effect due to the pulse laser heating (described in detail in Hofmeister, 2015). We can often minimize this spike by slightly changing the measured portion in the sample (e.g., move the portion ~0.1 μm in the lateral direction). Though, under high-T measurement, we could not change the measured portion during laser heating, since this can cause the temperature to skyrocket, crucially damaging both the sample and the diamond anvil. The presence of such a spike makes the quality in obtained thermoreflectance signal worse, but the uncertainty of the yielded thermal conductivity still only increased by ~1%. Also, we show that the time interval employed in the fitting would not affect the yielded thermal diffusion time, which difference was ~0.02% and was within the errors.

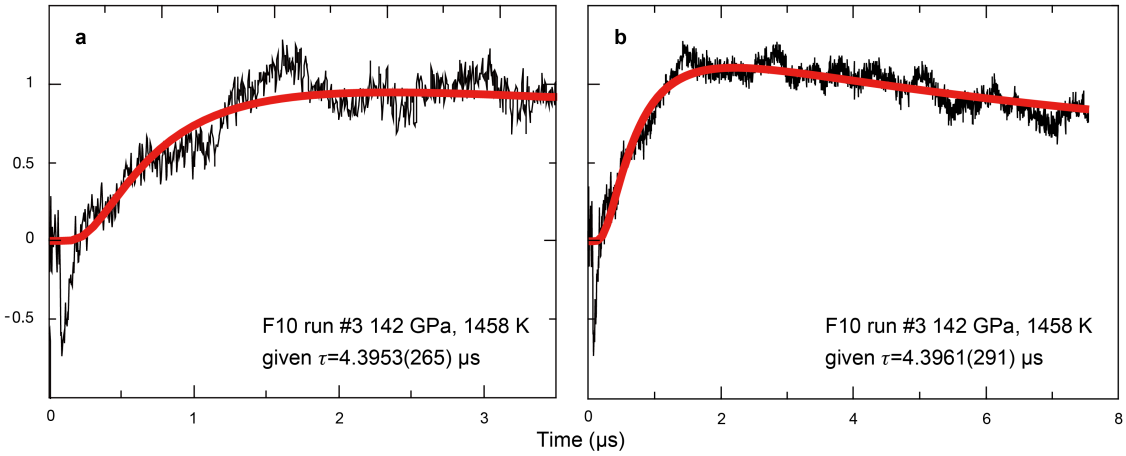

Fig. S6-2-2. The Difference in the obtained thermal diffusion time by changing fitting time intervals. TR signal of F10 ppv in run #3 at 1458 K are shown with different time range: (a) 3.5 μs, and (b) 7.6 μs. Red curves are the fitting curve of the thermal diffusion equation (Eq. 6-1 in the main text).

S6-3. Effect of Au layers on the estimation of the thermal conductivity of ppv

For thermal conductivity measurements on non-metal minerals using the rear heating, front detection (RF)-type thermoreflectance technique, metal layers should be placed on both sides of the sample. Gold, platinum and aluminum were used for such metal layers in previous studies (e.g., Okuda et al., 2017; Ohta et al., 2012). Here, since platinum and aluminum are likely to react with iron in silicates under high temperature, gold was chosen for metal layers in κ measurements on Fe-bearing minerals (Okuda et al., 2017, 2019; Hasegawa et al., 2019).

The available data on pressure-temperature dependence of the thermal diffusivity of gold are scarce. To the best of our knowledge, its pressure dependence was investigated only by Ross et al. (1984), and the pressure was applied only up to a few GPa. Moreover, the temperature effect has not been tested so far, thus we need careful tests examining to what extent the uncertainty of the thermal diffusivity of Au layers affects our estimation of κ_{ppv}. Recent measurement of the thermal conductivity of Pt at a high pressure of 56 GPa showed that the change in temperature from 300 K to 1565 K would only alter the conductivity from 38.2 W/m/K to 37.7 W/m/K (Hasegawa et al., 2019b). Here, when we changed the thermal conductivity of Au from 500 W/m/K to 5 W/m/K, our estimated κ_{ppv} only shifted by up to 2% in each run. This small effect of Au layers on the estimation of κ_{ppv} is mainly due to the difference in thickness between the ppv sample and Au layers (Table S6-2). Thus, we emphasize that the effect of unreliability in the thermal conductivity of Au at high-T condition would be very trivial to our κ_{ppv} estimation.

Table S6-2. Thickness of the sample and Au layers

Run#	Sample thickness (μm)	Au layer thickness (μm)
1	1.74(12)	0.17(2)
2	1.74(31)	0.10(1)
3	5.08(16)	0.18(3)
4	4.11(43)	0.12(3)

S6-4. Estimation of temperature uncertainty in high-P,T thermal conductivity measurements

Temperature uncertainty u_T was estimated as follows (also explained in Hasegawa et al., 2019b):

$$u_T = \sqrt{{u_{fit}}^2 + {u_{str}}^2}, \qquad \text{(Eq. 6-3 in the main text)}$$

where u_{fit} and u_{str} are temperature uncertainties in Planck's law curve fitting and temperature structure in the sample. u_{fit} was obtained from the Planck fitting error (Fig. S6-4-1); we first derived the standard deviation of the residuals between the measured radiation spectrum and the best fit curve, and then we considered the maximum distribution of the Planck's law fitting curve as u_{fit}.

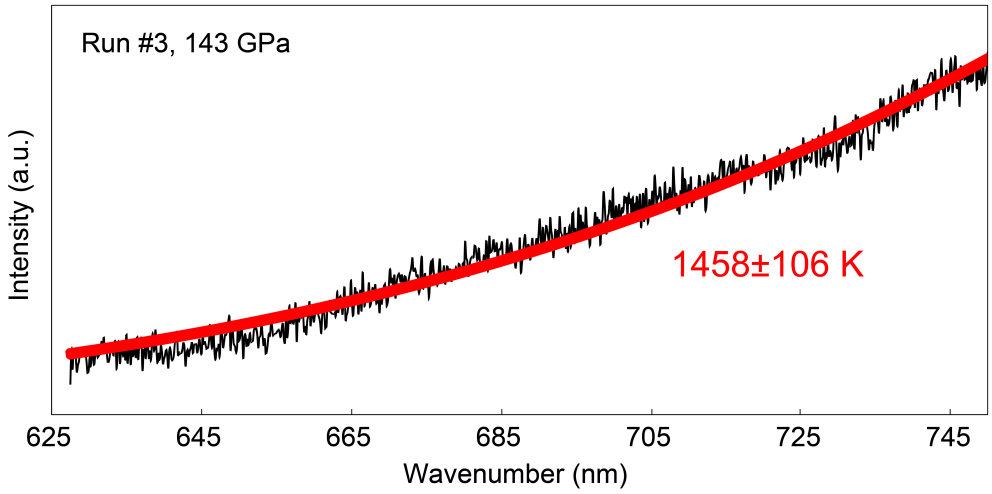

Fig. S6-4-1. Planck fitting to the obtained thermal radiation spectrum. Red curve shows the Planck fitting result.

We also quantified the temperature uncertainty from the temperature difference in the sample caused by the double-sided laser heating using finite element method

analysis (COMSOL). We applied a Gaussian laser on the sample surface. The values used for simulation are supplied in Table S6-3.

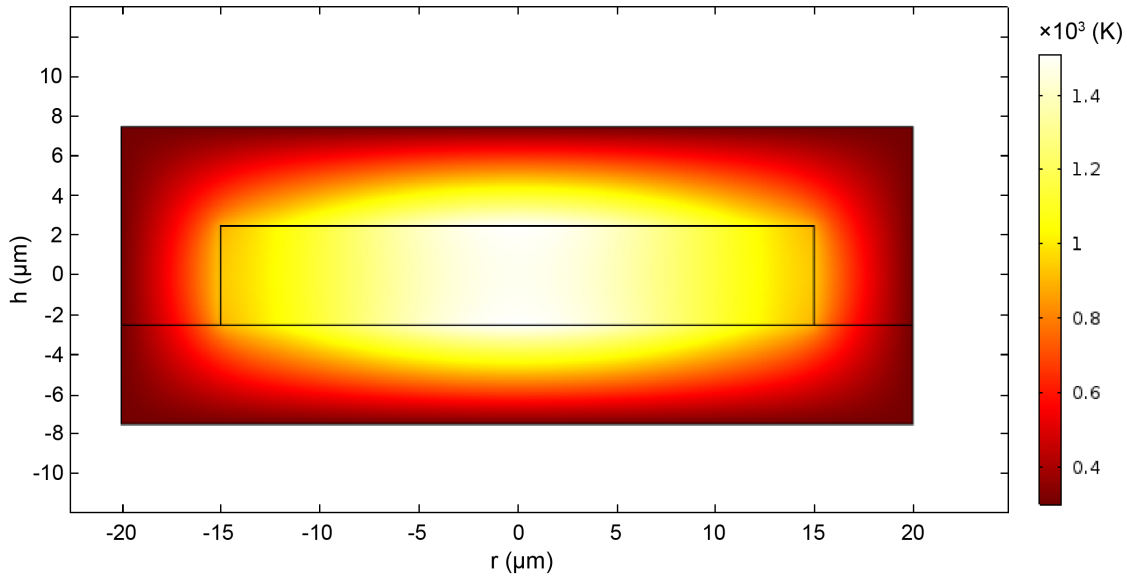

Fig. S6-4-2. Simulated temperature distribution of the ppv sample at 135 GPa, 1500 K in a LHDAC. Different colors indicate the temperature difference.

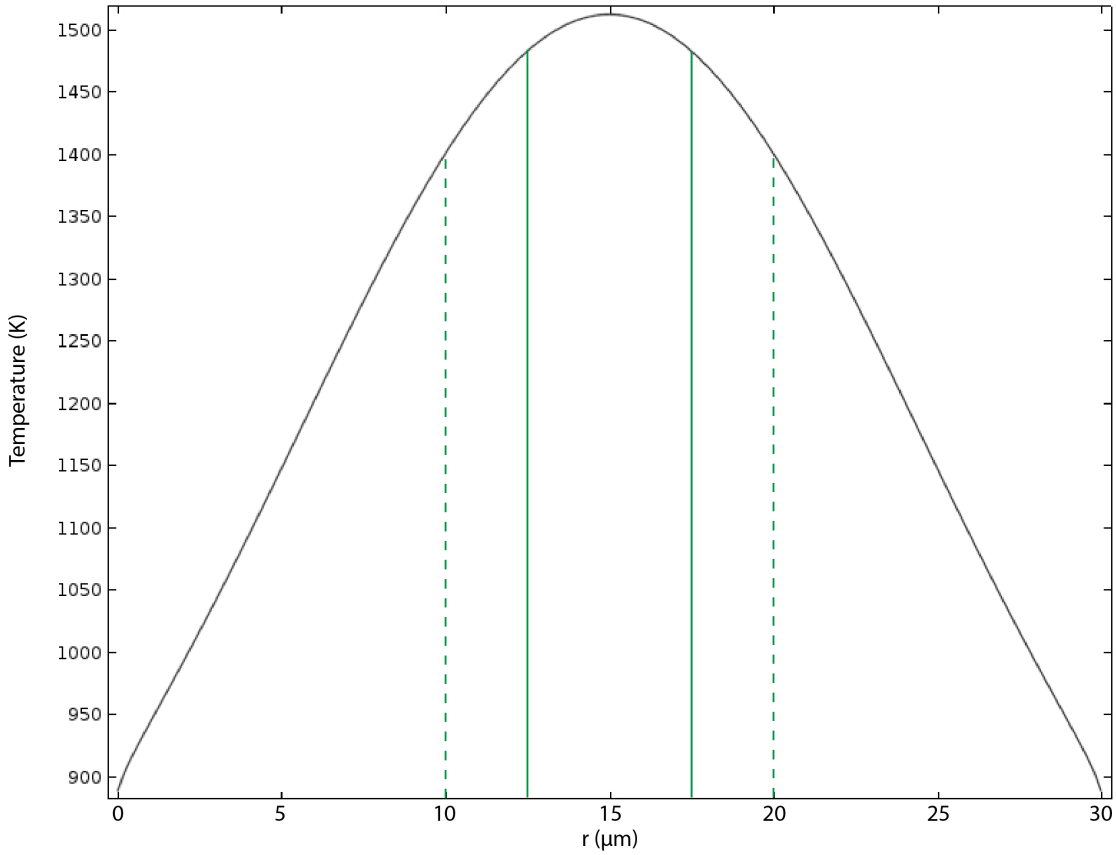

Fig. S6-4-3. Simulated temperature distribution of the ppv sample at 135 GPa, 1500 K in LHDAC. Green solid lines indicate the spot size of the probe laser, and green broken lines indicate the range we used for estimating the temperature difference in the lateral direction.

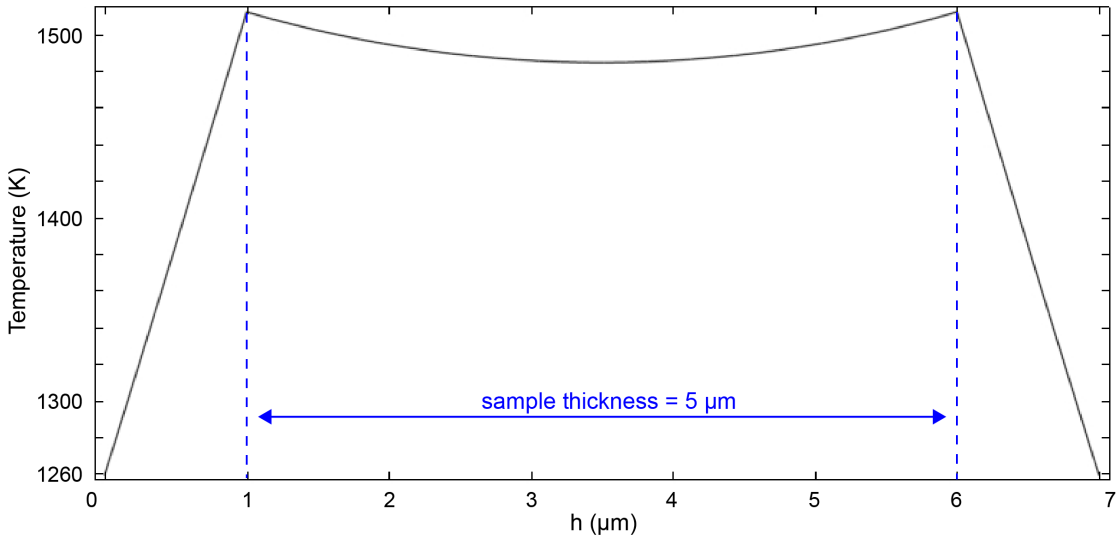

Fig. S6-4-4. Simulated temperature distribution of the ppv sample at 135 GPa, 1500 K in LHDAC.

Table S6-3. Used parameters for simulating temperature structure in the ppv sample

sample thickness (μm)	sample radius (μm)	thickness of pressure medium (μm)	sample chamber radius (μm)	laser power (W/m^2)	laser spot size* (μm)	laser absorption coefficient	κ of sample (W/m/K)	κ of pressure medium (W/m/K)
5	15	10	20.0	1000	15	0.15	40	6

*Gaussian laser was applied to the sample surfaces

As a result, the temperature uncertainties in the lateral and axial direction u_{lat} and u_{axi} were obtained to be 1.9 and 6.8%, respectively. We estimated the u_{str} by using the following equation, with which it was calculated to be 7.1%.

$$u_{str} = \sqrt{{u_{axi}}^2 + {u_{lat}}^2} \qquad \text{(S6-4-1)}$$

As a consequence, the typical u_T calculated from the above was 7.2%.

S6-5. Thermal pressure

We calculated the thermal pressure of ppv (P_{th}) from an experiment conducted in a similar experimental setup as in this study (Hirose et al., 2006), which determined pressure at high-*P,T* conditions using the Au pressure scale (Tsuchiya, 2003). We used the data of run #2 in Hirose et al. (2006), of which the *P,T* conditions are summarized in the table below.

Table S6-4. Pressure-temperature relation on ppv syntheses in Hirose et al. (2006)

Temperature (K)	Pressure (GPa)	$(P_0+P_{th})/P_0$
300	104.5	1.00
1340	107.5	1.03
2330	112.2	1.07

Pressure calibration based on the EoS of gold (Tsuchiya, 2003).

We set the pressure at room temperature of 104.5 GPa as P_0, and the pressure change at high temperature $(P_0+P_{th})/P_0$ was plotted as a function of temperature, subsequently fit by quadratic function of temperature (Fig. S6-5). The $(P_0+P_{th})/P_0$ of ppv was obtained as the following equation:

$$\frac{(P_0+P_{th})}{P_0} = 8.8e-09T^2 + 1.30T^5 + 1.0. \quad \text{(S6-5-1)}$$

We assumed that the $(P_0+P_{th})/P_0$ obtained in Eq. (S6-5-1) does not change by pressure and calculated each P_{th} at each room temperature-pressure P_0 in our high temperature experiments.

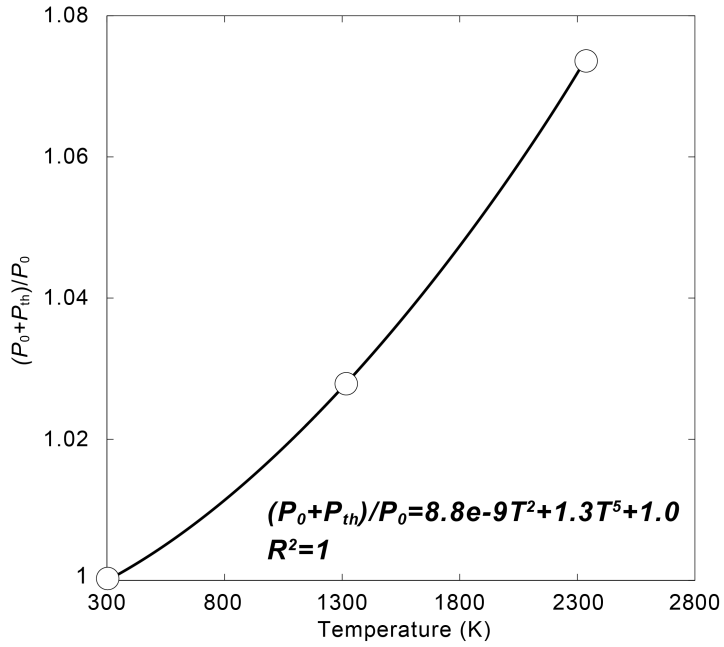

Fig. S6-5. Change in the pressure of ppv sample at high temperature. White circle, the $(P_0+P_{th})/P_0$ value calculated from run #2 in Hirose et al. (2006); black curve, the quadratic function fitting result.

S6-6. Estimation of the sample thickness at high-P

Sample thickness at ambient condition was obtained by observing its cross-section with FE-SEM. However, it is well known that ppv becomes amorphous under decompression. Nevertheless, the transition pressure is unknown, and the effect of such amorphization on its pressure is unquantifiable. Therefore, the ppv sample thickness at high-*P* was estimated from the equation of state of ppv (Sakai et al., 2016), and its uncertainty was calculated from the following:

$$u_d = \sqrt{{u_{meas}}^2 + {u_{amor}}^2}, \qquad \text{(S6-6-1)}$$

where u_{meas} and u_{amor} are sample thickness uncertainties calculated from standard deviation, and the volume difference between ppv and $MgSiO_3$ glass.

The compressibility of $MgSiO_3$ glass provided in Matsui et al. (1982) (Table S6-5) was fit by fourth order Birch Murnaghan (BM4) equation of state (Fig. S6-6-1), giving the fitting parameters K_0, K_0' and K_0" of 42.1 GPa, 10.5 and -1.26 GPa^{-1}, respectively.

Table S6-5. Compressibility of $MgSiO_3$ glass in Matsui et al. (1982)

Pressure (GPa)	V/V_0	Density (g/cm^3)
0	1	2.49
26(7)	0.8	3.11
70(23)	0.7	3.56
175(30)	0.6	4.15

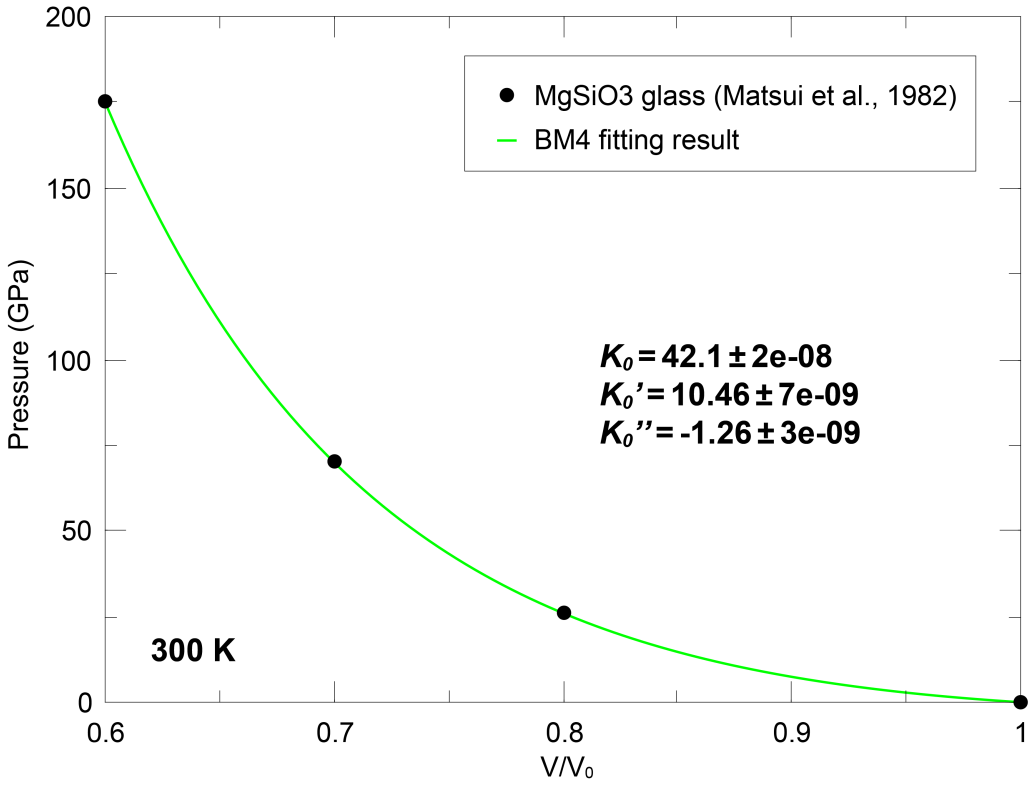

Fig. S6-6-1. BM4 fitting result on the compressibility of $MgSiO_3$ glass at room temperature. Black circle indicates the measured V/V_0 data of $MgSiO_3$ glass at high pressure (Matsui et al., 1982), and the green curve indicates the BM4 fitting results.

We used the obtained BM4 equation of state of $MgSiO_3$ glass (Matsui et al., 1982) and equation of state of ppv (Sakai et al., 2016; Komabayashi et al., 2008) to calculate the change in sample thickness d/d_0 at high pressure (Fig. S6-2), calculated from its volume change V/V_0 as the following:

$$d/d_0 = \left\{1 - \frac{1}{3}(1 - V/V_0)\right\}. \qquad \text{(S6-6-2)}$$

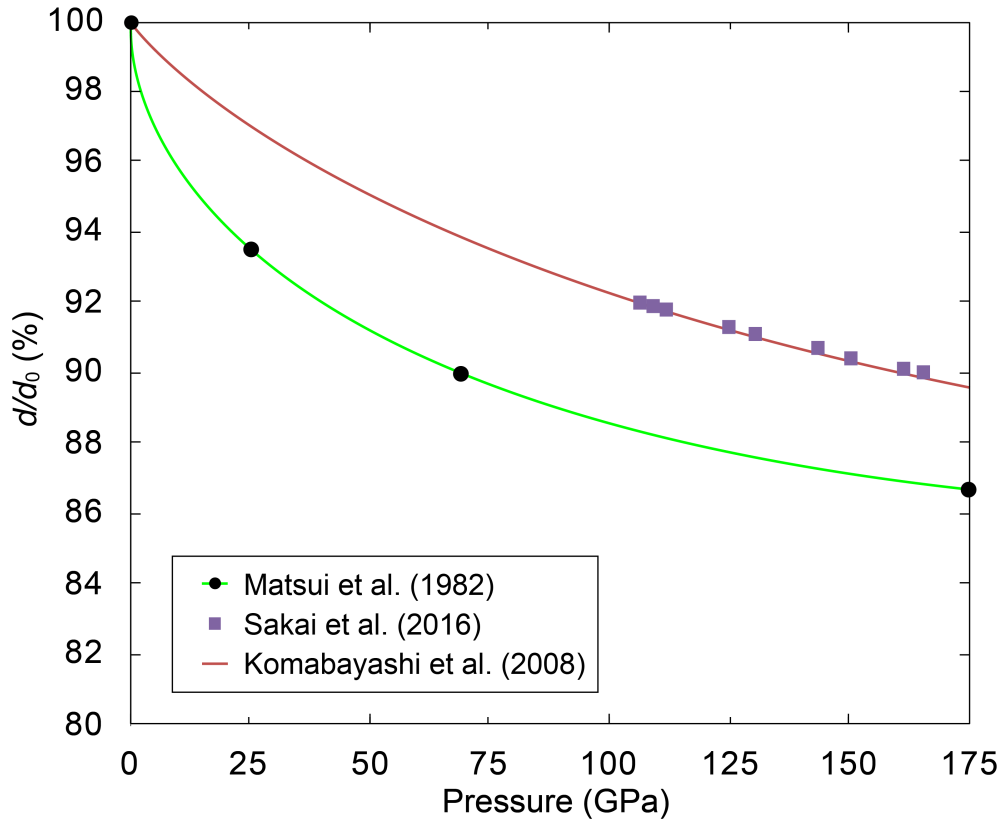

Fig. S6-6-2. Sample thickness at high pressure. Green, red curves and purple symbols indicate the estimated sample thickness at high pressure from the equations of state of $MgSiO_3$ glass (Matsui et al., 1982) and ppv (Komabayashi et al., 2008; Sakai et al., 2016), respectively.

S6-7. Evaluation of the estimated grain size of ppv in this study

The grain size of ppv in our experiments was estimated as 0.34 μm (Fig. S6-7).

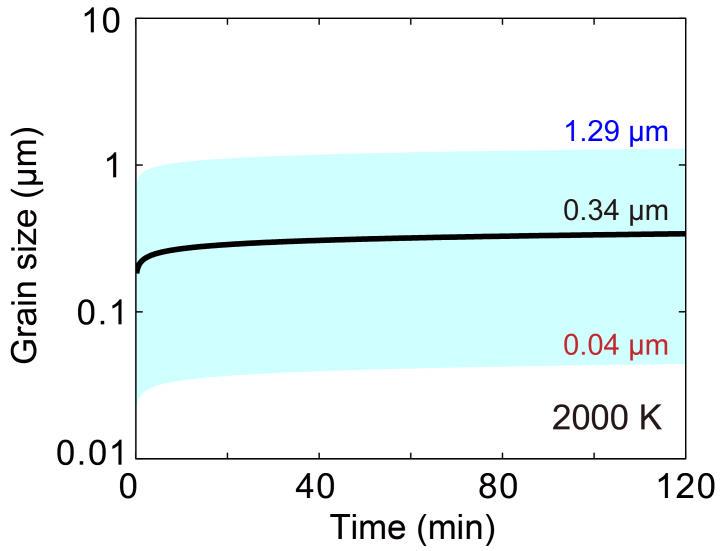

Fig. S6-7. Grain size of ppv as a function of time when heated at 2000 K. Black curve, the grain size of ppv; light blue band, calculated error of grain size. Estimated average grain size of ppv when heated at 2000 K and 2 hrs is 0.34 μm, with upper limit grain size 1.29 μm and lower limit grain size 0.04 μm.

Note that the estimated grain size is larger than the apparent size of amorphous grain of the sample used in Hirose et al. (2005) of ~0.1 μm, which was synthesized from MORB composition gel starting material above ppv-stable *P,T* conditions and analyzed after cold decompression. This difference may be caused because our used ppv sample was synthesized as a single phase, i.e., was synthesized without other phases such as ppv synthesized in MORB composition. Since the presence of other major minerals decelerates the grain growth of ppv (e.g., Yamazaki et al., 1996), it is reasonable that our estimated grain size is slightly larger than the apparent grain size observed in Hirose et al. (2005).

S6-8. Grain boundary effect coefficient of ppv

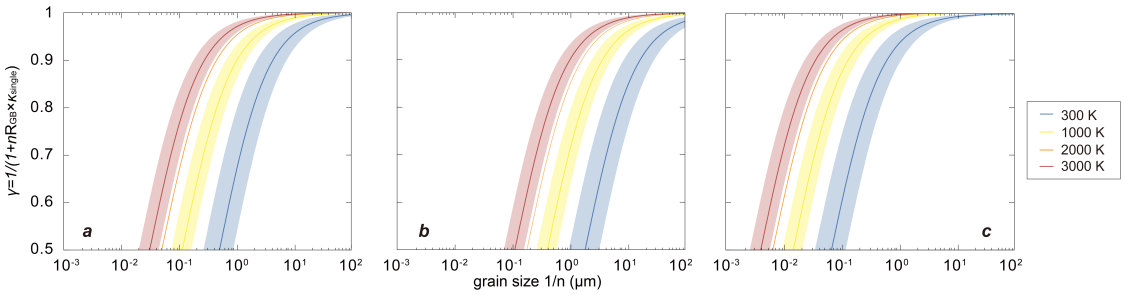

Fig. S6-8. Estimated grain boundary effect coefficient of ppv γ from different R_{GB} as (a) 3.5×10^{-9} m^2K/W, (b) 1.3×10^{-8} m^2K/W and (c) 4.5×10^{-10} m^2K/W. Blue, orange, yellow and red curves show the γ at 300 K, 1000 K, 2000 K and 3000 K, respectively. Bands indicate the estimated errors.

S6-9. Estimation of the grain size of ppv in the Earth's lower mantle

Estimation on the *in situ* grain size in the mantle is challenging. The grain size of pyroxenes and garnets in direct samples from the mantle, kimberlite, typically ranges from 0.5−10 mm (Kopylova et al., 1999). Determining the possible variability of grain size in the lower mantle is further complicated by the lack of natural samples. Numerical modeling assuming the rate-limiting process is silicon diffusion yielded the possible grain size of bridgmanite of 10^{-1}−10^{0} mm (Solomatov et al., 2002). Solomatov et al. (2002) also calculated the grain size of bridgmanite in the Earth's lower mantle using the static grain growth kinetics of $MgSiO_3$ pv (Yamazaki et al., 1996). With a very simple model, the calculated grain size was ~10 to 50 μm, assuming a temperature of 2000−3000 K. Note that this estimation is based on a very simple model, in which the calculated grain size should be an underestimation since it omits other mechanisms.

Table S6-6. Possible grain size of the lower mantle minerals.

Reference	Estimated method	Estimated grain size (mm)
Solomatov et al. (2002)	Calculated from a simple grain growth model *	10^{-2}-10^{0}
Solomatov et al. (2002)	Numerical modeling**	10^{-1}-10^{0}
Glišovic´ et al. (2015)	Inferred from effective viscosity***	10^{-2}-10^{1}

* $d \propto t^{1/n}$ with n ~11, T =2000-3000 K derived from experimental study (Yamazaki et al., 1996)

** $d \propto t^{1/n}$ with n ~3, T =2000 K, assuming that rate limiting process is Si diffusion.

*** with vacancy diffusion rate, lateral T variation derived from seismic data, and reported geotherms.

A recent study by Glišovic´ et al. (2015) estimated a possible grain size of the lower mantle inferred from seismic tomography and mantle rheology, which ranges from ~10^{-2} mm to ~10^{1} mm. They also insisted that the grain size of ppv in the D" layer may be even larger than 10 mm due to the bdg to ppv transformation (detailly described in Solomatov and Reese, 2008). To summarize, so far, the estimation of the lower mantle grain size varies over three orders of magnitude, which is from 10^{-2}−10^{1} mm.

S6-10. Density dependence of the lattice thermal conductivity of ppv

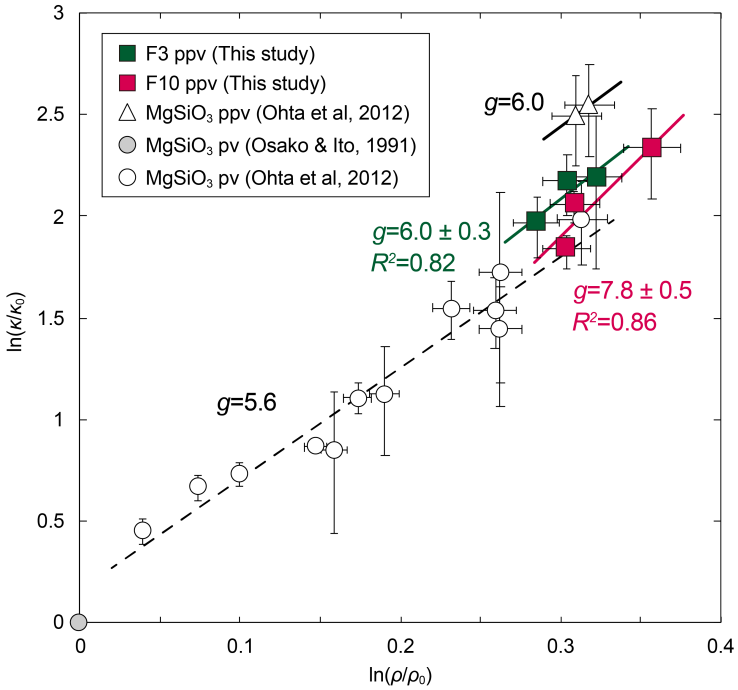

Fig. S6-10. Lattice thermal conductivity of ppv as a function of density at room temperature. Green and pink squares, F3 and F10 ppv respectively (this study); open triangles, $MgSiO_3$ ppv (Ohta et al., 2012); open circles, $MgSiO_3$ pv (Ohta et al., 2012); gray circle, $MgSiO_3$ pv at ambient condition (Osako and Ito, 1991).

S6-11. Temperature dependence of the grain boundary effect coefficient

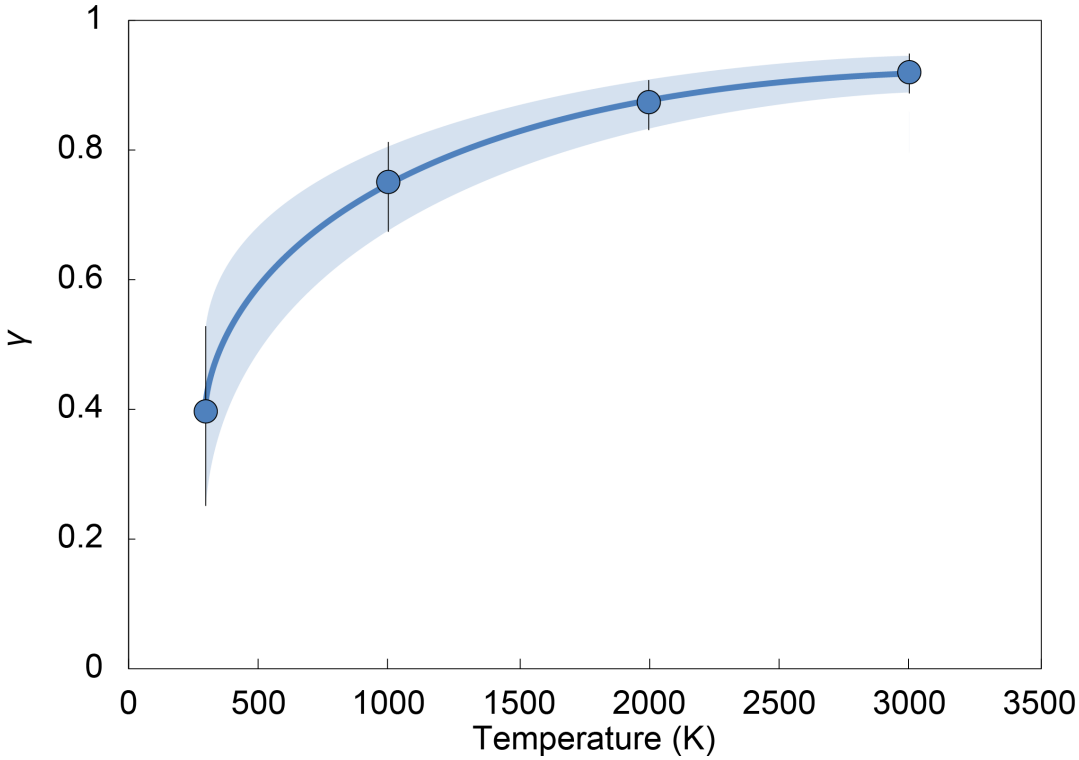

Fig. S6-11. Temperature dependence of the grain boundary effect coefficient on thermal conductivity when using grain size of 0.37 μm. Band indicates the estimated error.

S6-12. Estimation of the thermal conductivity of bdg with pyrolitic composition

In order to calculate the thermal conductivity of bdg with pyrolitic composition, we used the compositional dependence of lattice thermal conductivity of bdg provided in Okuda et al. (2019) as follows:

$$\kappa_{\mathrm{bdg}} = -24.0x + 31.3, \qquad \text{(S6-12-1)}$$

where x is the summation of Fe and Al content in per formula unit, κ_{bdg}, x is the lattice thermal conductivity of bdg with Fe+Al = x (pfu), respectively. We adopted x=0.2, i.e., Fe and Al content of 10 mol.% respectively, for lattice thermal conductivity of bdg with pyrolitic composition. When considering the radiative thermal conductivity of bdg with pyrolitic composition, currently there are three previous reports on the κ_{rad} measurement of bdg (Keppler et al., 2008; Goncharov et al., 2008; Goncharov et al., 2015). κ_{rad} measurement on $(Mg_{0.892}Fe^{2+}_{0.059}\ Fe^{3+}_{0.042})(Si_{0.972}Al_{0.028})O_3$ at high pressures by Keppler et al. (2008) suggested that κ_{rad} is approaching ~5 W/m/K at the CMB conditions (light blue curve in the figure above), and similar optical measurements on $(Mg_{0.94}Fe_{0.06})SiO_3$ bdg ($Fe^{3+}/\Sigma Fe$ = 0.45) showed a similar κ_{rad} (Goncharov et al., 2015). On the other hand, $(Mg_{0.9}\ Fe_{0.1})SiO_3$ bdg with $Fe^{3+}/\Sigma Fe$ = 0.11 exhibited a smaller κ_{rad} of about 2.2 W/m/K at the CMB (Goncharov et al., 2008, dashed red curve in the figure above). Since the iron contents in the bdg samples of Keppler et al. (2008) and Goncharov et al. (2008) are the same but the $Fe^{3+}/\Sigma Fe$ ratios are different, it is conceivable that Fe^{3+} promotes radiative thermal conduction in bdg. However, Fe^{3+} enhances the Fe^{2+}–Fe^{3+} charge transfer absorption band in the middle of the visible range, resulting in the reduction of the κ_{rad}. Thus, the discrepancy of the results between Keppler et al. (2008) and Goncharov et al. (2008) may be attributed to the uncertainty in sample thickness used in the measurements of Keppler et al. (2008), which was also discussed in Okuda et al.

(2017). The difference between Goncharov et al. (2008) and Goncharov et al. (2015) may be due to both the Fe content and $Fe^{3+}/\Sigma Fe$ ratio. Fe and Al-bearing bdg in the Earth's lower mantle is likely to have a $Fe^{3+}/\Sigma Fe$ ratio of about 0.5, which is independent of the oxygen fugacity (Frost et al., 2004; Sinmyo et al., 2011). Here we use the data of Goncharov et al. (2015) for the κ_{rad} ($Fe^{3+}/\Sigma Fe$ ratio=0.45) instead of Goncharov et al. (2008) ($Fe^{3+}/\Sigma Fe$ ratio=0.11).

S6-13. Effect of the spin transition of Fe in ferropericlase and other factors on the thermal conductivity of pyrolite

We estimated the thermal conductivity of bdg+fp and ppv+fp aggregate in the lower mantle from 2200 km depth to the CMB (Fig. 6-7b). Here, for the estimation below 2200 km, we need to carefully consider the effect of the spin transition of Fe in fp. A theoretical study showed that HS to LS transition of Fe in fp occurs with a depth range of 800 km−2130 km in the Earth's lower mantle (Tsuchiya et al., 2006). Ohta et al. (2017) showed that the lattice thermal conductivity of $(Mg_{0.81}Fe_{0.19})O$ fp exhibits an anomalous reduction in the pressure range where Fe in fp is in the mixed-spin state, which was even halved among some of their data. Their results imply that the thermal conductivity of fp depends on its spin fraction, though such quantitative data has not been reported so far.

As mentioned earlier, since the spin transition in fp is thought to occur in a very wide range, it is necessary to quantitatively determine the relation between HS (or LS) fractions and thermal conductivity but is still an open question. Therefore, it is difficult to accurately determine the thermal conductivity of the lower mantle below 2200 km from the thermal conductivities of each of the lower mantle minerals.

Very recently, Geballe et al. (2020) measured the high *P-T* thermal conductivity of pyrolite from 40 to 124 GPa at ~2500 K. In order to see the effect of the spin transition of fp on the bulk thermal conductivity of pyrolite, we calculated the thermal conductivity of bdg+fp aggregate at a shallower depth (from 1000 km) in the same manner as described in the main manuscript (Fig. S6-13-1).

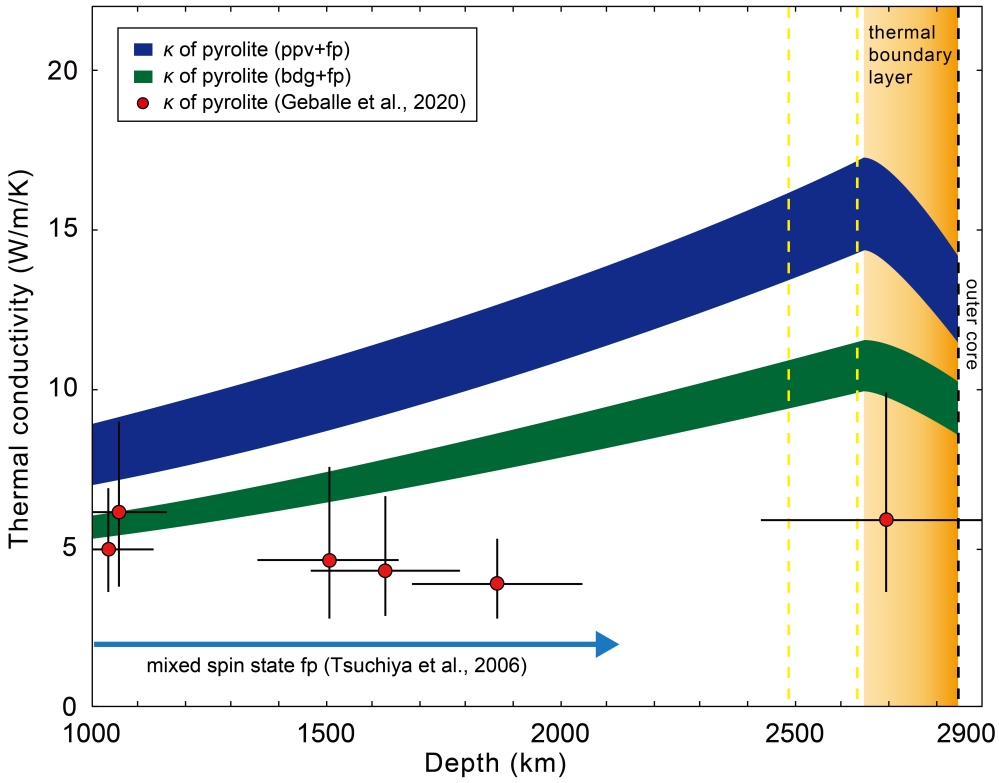

Fig. S6-13-1. Estimated thermal conductivity of pyrolite in the lower mantle. Blue and green bands indicate the estimated bulk total κ ($=\kappa_{latt}+\kappa_{rad}$) of pyrolite with ppv+fp, and bdg+fp, respectively. Red circles indicate the κ of pyrolite by direct measurement (Geballe et al., 2020). Yellow broken lines indicate the suggested onset and offset bdg to ppv phase transition depth in the pyrolitic lower mantle (Ohta et al., 2008b). Blue arrow indicates the suggested depth range where Fe in fp is in the mixed spin state (Tsuchiya et al., 2006). Orange band indicates the 200 km thick thermal boundary layer above the CMB (Lay et al., 2008).

We found that our "simply" estimated thermal conductivity of bdg+fp pyrolite at ~1000 km depth, without considering the spin state of fp, is in good agreement with that in Geballe et al. (2020). However, it starts to differ at deeper depth due to the apparently negative pressure-dependence of κ in Geballe et al. (2020). We expected this to be the

effect of the mixed-spin Fe in fp, so we calculated the bulk thermal conductivity of bdg+fp using the *halved* κ_{latt} value of fp reported in Ohta et al. (2017), which should be an underestimation of the bulk total κ. However, we could not explain the reduced κ data in Geballe et al. (2020) even when using the halved κ_{latt} of fp (Fig. S6-13-2). The difference between our estimation and that of Geballe et al. (2020) cannot be explained by the effect of the spin transition of Fe in fp alone, indicating there may be other factors causing the suppressed κ of pyrolite in Geballe et al. (2020).

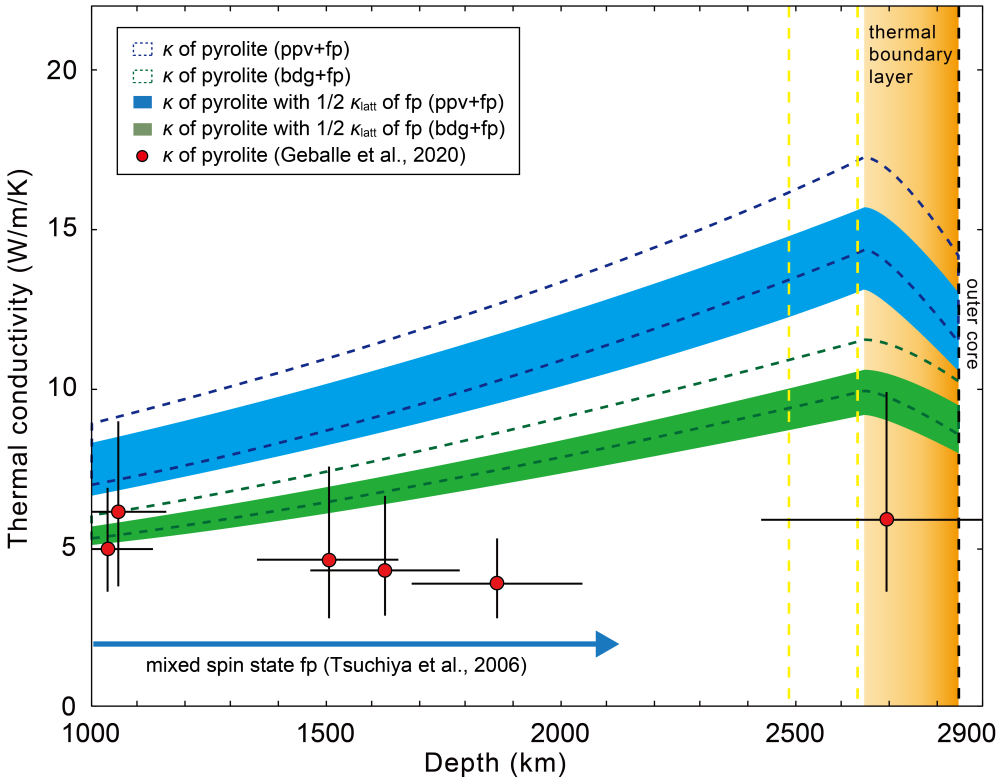

Fig. S6-13-2. Estimated thermal conductivity of pyrolite in the lower mantle. Blue and green broken lines indicate the estimated bulk total κ ($=\kappa_{latt}+\kappa_{rad}$) of pyrolite with ppv+fp, and bdg+fp, respectively. Blue and green bands indicate the estimated bulk total κ ($=\kappa_{latt}+\kappa_{rad}$) of pyrolite with ppv+fp, and bdg+fp, respectively, with the halved value of the κ_{latt} of fp due to the mixed spin state of Fe. Red circles indicate the κ of

pyrolite by direct measurement (Geballe et al., 2020). Yellow broken lines indicate the suggested onset and offset bdg to ppv phase transition depth in the pyrolitic lower mantle (Ohta et al., 2008b). Blue arrow indicates the suggested depth range where Fe in fp is in the mixed spin state (Tsuchiya et al., 2006). Orange band indicates the 200 km thick thermal boundary layer above the CMB (Lay et al., 2008).

Also, in Geballe et al. (2020), since there is only one datum at the pressure range where the $MgSiO_3$ component is stable as ppv, and they lack the phase identification whether $MgSiO_3$ component has sufficiently underwent bridgmanite to post-perovskite transition, it is difficult to simply compare our estimated thermal conductivity of ppv+fp pyrolite and their results. Additional reason may be attributed to the following:

1) The effect of Ca-perovskite

So far there are no reports on the κ of Ca-perovskite, so one may attribute the κ difference to this mineral. However, since the volume ratio of the Ca-perovskite in pyrolite is only ~5%, it may be difficult to explain a huge difference between our estimation and results in Geballe et al. (2020).

2) The effect of grain boundary scattering

According to the supplemental material S1 in Geballe et al. (2020), their pyrolite sample was synthesized in a DAC from a glass starting material, and heated at ~2500 K for several minutes. Here, the grain growth of post-perovskite is much slower than that of bridgmanite (e.g., Yoshino&Yamazaki, 2007). Our post-perovskite samples were heated at ~2500 K for more than 1 hr and were estimated to be ~0.3 μm (Fig. S6-7). Other phases such as fp and Ca-perovskite should also hinder grain growth of ppv in

their sample. This may have resulted in a small grain size of post-perovskite of <0.1 μm, which would reduce its thermal conductivity due to the grain boundary scattering even at high-*T* (Fig. 6-5 in our main manuscript). This can sufficiently explain the reason for the suppressed thermal conductivity of pyrolite at 124 GPa in Geballe et al. (2020).

3) The effect of Al

For the simplicity of interpreting our results, we used ppv samples without Al. In contrast, starting material used in Geballe et al. (2020) was a pyrolite composition, which includes ~4 wt% of Al_2O_3. Since Al may change the site-distribution of Fe in ppv, which may affect the thermal conductivity, measurement of (Fe,Al)-bearing ppv may contribute to a better understanding of the thermal conductivity of the lower mantle.

4) Uncertainty in our measured temperature dependence coefficient

We succeeded in high *P*-*T* thermal conductivity measurement of ppv up to ~1550 K, and obtained the temperature coefficient *a* of 0.65 in the following density-temperature κ_{latt} model (e.g., Manthilake et al., 2011; Ohta et al., 2012):

$$\kappa = \kappa_0 \left(\frac{\rho}{\rho_0}\right)^g \left(\frac{T_0}{T}\right)^a. \qquad \text{(Eq. 6-6 in the main manuscript)}$$

However, the achieved temperature was still far from the temperature at the CMB of ~3500 K. Hasegawa et al. (2019b) succeeded in collecting the thermal conductivities of platinum and iron up to ~60 GPa and ~2000 K, using the same method as the present study. A linearly polarized continuous wave fiber laser (KKFL-20, KIMMON KOHA)

with a wavelength of 1064 nm – which is the wavelength generally used for laser heating (e.g., Hirao et al., 2020) – and a maximum output power of 20 W was used to generate high temperature. Since the absorption coefficient of this laser for platinum is relatively high (higher than gold, which is mentioned later), less power is needed to generate high-T. This also reduces temperature fluctuations during high-T measurement. However, it is known that platinum is highly reactive with Fe in Fe-bearing minerals at high-T condition. Therefore, we used gold instead of platinum as a laser absorber, which is often used for thermal conductivity measurements on Fe-bearing minerals (e.g., Okuda et al., 2017; Hasegawa et al., 2019a). This can minimize reactions between the laser absorber and our Fe-bearing sample. However, gold is highly reflective of a wide range of the pump laser beam. This made it difficult to generate high-T above 2000 K with a maximum output power of 20 W. Unfortunately, since the beam time of synchrotron X-ray radiation facility is limited, we could not conduct further measurements.

The κ_{latt} model explains that the temperature dependence of thermal conductivity obeys a T^{-a} relation, which assumes the reduction of mean phonon free path mainly by lattice vibrations. It is known that silicates show a weaker temperature dependence on its lattice thermal conductivity than those for simple pure oxides that obey T^{-1} relation (e.g., Hofmeister, 1999). For example, Manthilake et al. (2011) showed that the temperature dependence coefficient of pure-Mg perovskite is 0.76, but it falls to 0.24 when containing 5 mol.% of Fe. We estimated the thermal conductivity of ppv+fp with stronger temperature dependence in Fig. S6-13-3, to evaluate the uncertainty in our measured temperature dependence coefficient.

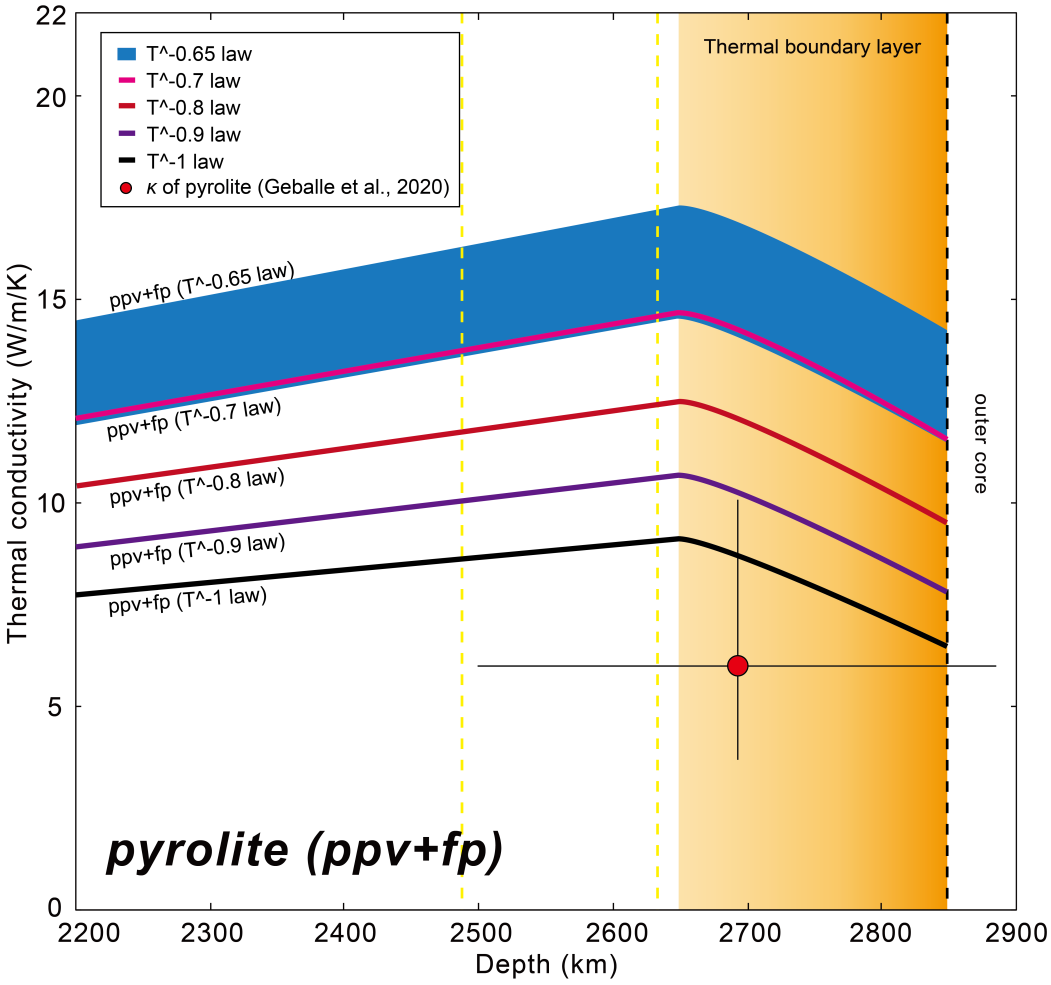

Fig. S6-13-3. Estimated thermal conductivity of ppv+fp aggregate using different temperature dependence. Blue band indicates the estimated bulk total κ ($=\kappa_{latt}+\kappa_{rad}$) of pyrolite with ppv+fp using $T^{-0.65}$ law. Pink, red, purple and black curves indicate the estimated κ of pyrolite using T^{-a} law of a=0.7, 0.8, 0.9, and 1, respectively. Red circle indicates the κ of pyrolite by direct measurement (Geballe et al., 2020). Yellow broken lines indicate the suggested onset and offset bdg to ppv phase transition depth in the pyrolitic lower mantle (Ohta et al., 2008b). Orange band indicates the 200 km thick thermal boundary layer above the CMB (Lay et al., 2008).

We found that the estimated thermal conductivity even with a strong T dependence of a=0.8 does not match that of Geballe et al. (2020).

Again, so far it is very difficult to interpret the thermal conductivity of pyrolite (Geballe et al., 2020), thus, we expect to carry out systematic studies on the thermal conductivity of lower mantle minerals in the future.

Supplemental references

Frost, D.J., Liebske, C., Langenhorst, F., McCammon, C.A., Trønnes, R.G., Rubie, D.C., 2004. Experimental evidence for the existence of iron-rich metal in the Earth's lower mantle. Nature 428, 409–412.

Geballe, Z. M., Sime, N., Badro, J., van Keken, P. E., Goncharov, A. F., 2020. Thermal conductivity near the bottom of the Earth's lower mantle: Measurements of pyrolite up to 120 GPa and 2500 K. Earth Planet. Sci. Lett., 536, 116161.

Glišovic, P., Forte, A.M., Ammann, M.W., 2015. Variations in grain size and viscosity based on vacancy diffusion in minerals, seismic tomography, and geodynamically inferred mantle rheology. Geophys. Res. Lett. 42, 6278–6286. http://dx.doi.org/10.1002/2015GL065142.

Goncharov, A.F., Haugen, B.D., Struzhkin, V.V., Beck, P., Jacobsen, S.D., 2008. Radiative conductivity in the Earth's lower mantle. Nature 456, 231–234.

Goncharov, A., Lobanov, S., Tan, X., Hohensee, G., Cahill, D., Lin, J.-F., Thomas, S.-M., Okuchi, T., Tomioka, N., 2015. Experimental study of thermal conductivity at high pressures: implications for the deep Earth's interior. Phys. Earth Planet. Inter. 247, 11–16.

Hasegawa. A., Ohta, K., Yagi, T., Hirose, K., Okuda, Y., Kondo, T., 2019a. Composition and pressure dependence of lattice thermal conductivity of (Mg,Fe)O solid solutions. C. R. Geoscience, 351, 229–235.

Hasegawa, A., Yagi, T., Ohta, K., 2019b. Combination of pulsed light heating thermoreflectance and laser-heated diamond anvil cell for *in-situ* high pressure-temperature thermal diffusivity measurements. Rev. Sci. Instrum., 90, 074901.

Hirao N, Kawaguchi SI, Hirose K, Shimizu K, Ohtani E, Ohishi Y (2020) New developments in high-pressure X-ray diffraction beamline for diamond anvil cell at SPring-8. Matter Radiat Extremes 5: 018403.

Hirose, K., Takafuji, N., Sata, N., Ohishi, Y., 2005. Phase transition and density of subducted MORB crust in the lower mantle. Earth Planet. Sci. Lett., 237, 239–251.

Hirose, K., Sinmyo, R., Sata, N., Ohishi, Y., 2006. Determination of post-perovskite phase transition boundary in $MgSiO_3$ using Au and MgO pressure standards. Geophys. Res. Lett., 33, L01310, doi:10.1029/2005GL024468.

Hofmeister, A.M., 1999. Mantle values of thermal conductivity and the geotherm from phonon lifetimes. Science 283, 1699–1706.

Keppler, H., Dubrovinsky, L.S., Narygina, O., Kantor, I., 2008. Optical absorption and radiative thermal conductivity of silicate perovskite to 125 gigapascals. Science 322, 1529–1532.

Komabayashi, T., Hirose, K., Sugimura, E., Sata, N., Ohishi, Y., Dubrovinsky, L.S., 2008. Simultaneous volume measurements of post-perovskite and perovskite in $MgSiO_3$ and their thermal equations of state. Earth Planet. Sci. Lett., 265, 515–524.

Kopylova, M.G., Russell, J.K., Cookenboo, H., 1999. Petrology of peridotite and pyroxenite xenoliths from the Jericho kimberlite: Implications for the thermal state of the mantle beneath the slave craton. Northern Canada, J. Petrol., 40(1), 79–104, doi:10.1093/petroj/40.1.79.

Lay, T., Hernlund, J., Buffett, B., 2008. Core–mantle boundary heat flow. Nat. Geosci. 1, 25–32.

Manthilake, G.M., de Koker, N., Frost, D.J., McCammon, C.A., 2011. Lattice thermal conductivity of lower mantle minerals and heat flux from Earth's core. Proc. Natl. Acad. Sci. USA 108, 17901–17904.

Matsui, Y., Kawamura, K., and Syono, Y., 1982. Molecular Dynamics Calculations Applied to Silicate Systems: Molten and Vitreous $MgSiO_3$ and Mg_2SiO_4 under Low and High Pressures. High Pressure Research in Geophysics, 511–524

Ohta, K., Onoda, S., Hirose, K., Sinmyo, R., Shimizu, K., Sata, N., Ohishi, Y., Yasuhara, A., 2008a. The electrical conductivity of post-perovskite in Earth's D″ layer. Science, 320, 89–91.

Ohta, K., Hirose, K., Lay, T., Sata, N., Ohishi, Y., 2008b. Phase transitions in pyrolite and MORB at lowermost mantle conditions: Implications for a MORB-rich pile above the core-mantle boundary. Earth Planet. Sci. Lett., 267, 107–117.

Ohta, K., T. Yagi, N. Taketoshi, K. Hirose, T. Komabayashi, T. Baba, Y. Ohishi, J. Hernlund, 2012. Lattice thermal conductivity of $MgSiO_3$ perovskite and post-perovskite at the core–mantle boundary. Earth Planet. Sci. Lett., 349-350, 109–115.

Ohta, K., Yagi, T., Hirose, K., Ohishi, Y., 2017. Thermal conductivity of ferropericlase in the Earth's lower mantle. Earth Planet. Sci. Lett. 465, 29–37.

Okuda, Y., Ohta, K., Yagi, T., Sinmyo, R., Wakamatsu, T., Hirose, K., Ohishi, Y., 2017. The effect of iron and aluminum incorporation on lattice thermal conductivity of bridgmanite at the Earth's lower mantle. Earth Planet. Sci. Lett., 474, 25–31.

Okuda, Y., Ohta, K., Sinmyo, R., Hirose, K., Yagi, T., Ohishi, Y., 2019. Effect of spin transition of iron on the thermal conductivity of (Fe, Al)-bearing bridgmanite. Earth Planet. Sci. Lett., 520, 188–198.

Osako, M., Ito, E., 1991. Thermal diffusivity of $MgSiO_3$ perovskite. Geophys. Res. Lett., 18, 239–242.

Ross, R. G., P. Andersson, B. Sundqvist, G. Bäckström, 1984. Thermal conductivity of solids and liquids under pressure. Rep. Prog. Phys., 47, 1347–1402.

Sakai, T., Dekura, H., Hirao, N., 2016. Experimental and theoretical thermal equations of state of $MgSiO_3$ post-perovskite at multi-megabar pressures. Sci. Rep., 6, 22652, doi: 10.1038/srep22652.

Sinmyo, R., Hirose, K., Muto, S., Ohishi, Y., Yasuhara, A., 2011. The valence state and partitioning of iron in the Earth's lowermost mantle. J. Geophys. Res. 116, B07205.

Solomatov, V. S., El-Khozondar, R., Tikare, V., 2002. Grain size in the lower mantle: constraints from numerical modeling of grain growth in two-phase systems. Phys. Earth Planet. Inter., 129(3−4), 265−282.

Solomatov, V. S., Reese, C. C., 2008. Grain size variations in the Earth's mantle and the evolution of primordial chemical heterogeneities. J. Geophys. Res., 113, B07408, doi:10.1029/2007JB005319.

Tsuchiya, T., 2003. First-principles prediction of the *P–V–T* equation of state of gold and the 660-km discontinuity in Earth's mantle. J. Geophys. Res, 108 (B10), 2462.

Tsuchiya, T., Wentzcovitch, R.M., da Silva, C.R., de Gironcoli, S., 2006. Spin transition in magnesiowüstite in Earth's lower mantle. Phys. Rev. Lett. 96, 198501.

Yamazaki, D., T. Kato, E. Ohtani, M. Toriumi, 1996. Grain growth rates of $MgSiO_3$ perovskite and periclase under lower mantle conditions. Science, 274, 2052–2054.

Yoshino, T., Yamazaki, D., 2007. Grain growth kinetics of $CaIrO_3$ perovskite and post-perovskite, with implications for rheology of D″ layer. Earth Planet. Sci. Lett., 255, 485–493.

Chapter 7. A cylindrical SiC heater for an externally heated diamond anvil cell to 1500 K

This chapter was updated from the article as *"A cylindrical SiC heater for an externally heated diamond anvil cell to 1500 K"* by **Yoshiyuki Okuda**, Seiji Kimura, Kenji Ohta, Yohan Park, Tatsuya Wakamatsu, Izumi Mashino, Kei Hirose Review of Scientific Instruments, *in press*.

Abstract

Semiconductor-based heaters for diamond anvil cells (DACs) have advantages over metal wire heaters in terms of repeated use and the ability to reach higher temperatures. We introduce a cylindrical SiC heater for an externally heated DAC (EHDAC) that works satisfactorily at temperatures up to 1500 K and pressures around 90 GPa. The heater is reusable and inexpensive, and only slight modifications to the DAC are required to fit the heater. Experiments on melting of NaCl and gold are conducted at ambient pressure to test the temperature accuracy of the EHDAC system, and resistance measurements on iodine at high pressures and temperatures are performed to assess the heater assembly. These test runs show that uniform and accurate temperature can be maintained by the EHDAC assembly, which has potential applications to a variety of transport property measurements.

7.1. Introduction

Diamond anvil cells (DACs) allow static high-pressure experiments to be conducted at pressures equivalent to that at the center of the Earth (Tateno et al., 2010). For DAC experiments at high temperatures, three heating methods have been developed: laser heating (LHDACs), internal resistive heating (IHDACs), and external resistive heating (EHDACs) (Hazen and Finger, 1981; Liu and Bassett, 1975; Ming and Bassett, 1974).

Laser heating is capable of generating ultrahigh temperatures above 2000 K and even exceeding 10000 K (McWilliams et al., 2015), but it has the disadvantage of potentially creating large temperature gradients in both the axial and lateral directions in DAC samples (Rainey et al., 2013). Recent studies have attempted to minimize axial gradients through the use of double-sided laser heating with two independent laser heads (Hirao et al., 2020). For silicate samples, it has been found that placing laser absorbers on each side of the sample can minimize the axial temperature gradient (Sinmyo and Hirose, 2010). A significant advance in laser shaping through the use of a flat-top beam shaper has improved laser heating in the lateral direction (Hirao et al., 2020; Ohishi et al., 2008; Prakapenka et al., 2008), as well as the technique for mapping the temperature gradient in an LHDAC (Du et al., 2013a). However, a problem remains with regard to the stability of heating, and the temperature of the sample often fluctuates in time by 100–200 K, which makes experiments requiring precise temperature determination difficult.

In the IHDAC method, heat is generated by inducing a current in a heater inside the sample chamber of the DAC. This method was originally applied to metallic samples (Boehler, 1986; Inoue et al., 2020; Komabayashi et al., 2009; Liu and Bassett, 1975; Sinmyo et al., 2019; Suehiro et al., 2019), but has also been extended to nonmetallic samples. In the study reported in Zha and Bassett (2003), an internal rhenium strip heater was used, with a small MgO sample placed at its center, and it was found that a temperature of ~3000 K could be generated at a pressure of 10 GPa. Another study found that a cylindrical boron-doped diamond resistive heater was capable of heating a silicate/oxide material to 3500 K with a minimal temperature gradient (±35 K/40 μm) (Ozawa et al., 2018). However, the complicated sample loading procedure required with IHDACs hinders their practical application.

The EHDAC method produces stable and homogeneous heating (Bassett et al., 1993). Although the temperatures that can be obtained using EHDACs remain lower than those from laser heating, they have been increased through the use of a vacuum chamber and/or the injection of an inert gas (for a review, see Bassett et al., 1993). Metallic heaters such as those based on molybdenum (Bassett et al., 1993), nichrome (Mondal et al., 1999), tungsten (Pasternak et al., 2008; Petitgirard et al., 2009), platinum (Ohta et al., 2012), platinum–rhodium (Jenei et al., 2013; Lai et al., 2020), and other alloys (Dubrovinskaia and Dubrovinsky, 2003), have conventionally been used for EHDAC experiments. The heating assembly consists of a coiled wire with a ceramic insulating shell that is placed around the diamond anvil (Dubrovinskaia and Dubrovinsky, 2003; Hazen and Finger, 1981; Jenei et al., 2013; Lai et al., 2020; Ohta et al., 2012). This enables experiments to be performed with relatively homogeneous and temperature-accurate heating. The resistance of the metallic heater increases with

increasing temperature, which also stabilizes the heating process. However, breakdown often occurs at temperatures of ~1000 K, mainly due to sublimation or melting of selectively overheated weak portions of the coil (e.g., at sharp bends). In addition, the use of precious metals for the wire material makes experiments expensive.

Semiconductors, with their typically high sublimation and/or melting temperatures, have potential as alternative heater materials capable of generating stable temperatures above 1300 K. However, to the best of our knowledge, graphite, which has an ultrahigh sublimation temperature of ~3900 K (Whittaker, 1978), is the only nonmetallic material that has so far been used as the heating element in an EHDAC (Table 7-1).

So far, three different designs have been developed: (1) a graphite sheet heater surrounding the whole gasket (Liermann et al., 2009; Miyagi et al., 2013; Shen et al., 2007); (2) a graphite sheet surrounding the diamond anvils (Mijiti et al., 2018); and (3) two thin graphite ring heaters directly in contact with the diamond anvils and connected by graphite sheets (Du et al., 2013b). All these heaters are designed to be very small (a few millimeters in size) and are directly in contact with gaskets or diamond anvils, which enables efficient heating via thermal conduction under vacuum conditions. However, as previously shown (Miyagi et al., 2013), a large temperature gradient will be created between the sample and the heater owing to their very small separation (~0.5 mm), especially at high temperatures. Consequently, the temperature read from a thermocouple (TC) will be highly location-dependent and can differ greatly from the actual temperature of the sample. Heat loss from the TC may also affect temperature measurements. By contrast, a relatively large cylindrical heater assembly, such as a metal wire heater coiled

around a cylindrical ceramic (Dubrovinskaia and Dubrovinsky, 2003; Hazen and Finger, 1981; Jenei et al., 2013; Komabayashi et al., 2008) will heat the entire gasket with a separation (~5 mm) that is sufficient to minimize the location dependence of the TC and allow more accurate temperature measurements.

A cylindrical heater assembly based on a semiconductor material would overcome the disadvantages of metal wire heaters, namely, their breakdown at high temperatures and their high cost. Also, with such a heater assembly, the temperature measured by the TC would not be dependent on location (which, although it has not been observed, is a potential disadvantage of graphite heaters). To develop a cylindrical semiconductor heater, we tested two heater materials, namely, graphite and silicon carbide (SiC). We found that graphite is not a suitable material; on the other hand, we achieved homogeneous and stable heating up to 1500 K at a pressure of around 90 GPa with a cylindrical SiC heater. Our newly developed heater assembly can be easily coupled with a standard DAC setup, thereby facilitating various high-pressure, high-temperature experiments with highly accurate temperature measurements at low cost, with potential for widespread application.

7.2. Methods

A graphite rod was machined in a vice to produce a cylindrical shape [7.5 mm outer diameter (OD), 6.5–7.2 mm inner diameter (ID), and 6 mm thickness], which was

then reinforced with a ceramic insulator. Additional holes were drilled in the axial direction to allow the insertion of molybdenum electrodes (Fig. S7-1, supplementary material). The cylindrical SiC heater (OD 12 mm OD, 7 mm ID, and 5–6 mm thickness) was cut and filed from an A-14 type Siliconit SiC heater rod (14 mm OD, 4 mm ID; http://www.siliconit.co.jp/index.html) using a diamond saw and a diamond file. The amount of material needed for one heater costs ~1 USD. Owing to the large contact resistance of SiC, we could not use the same method for introducing electrodes as we did with the graphite heater. Instead, the cylindrical SiC heater and graphite sheets were pressure-bonded by squeezing the DAC while pressurizing the sample [Fig. 7-1(a)], in an approach originally used by Du et al. (2013b) A bunch of four copper leads (each of 1 mm diameter) was connected to the graphite sheets (see Fig. S7-2, supplementary material for details in their preparation). Convex-shaped silicon nitride (Si_3N_4) seats with low thermal conductivity (~1 W m^{-1} K^{-1}) were used to minimize the axial heat loss. We also designed a new symmetrical DAC made of stainless steel and suitable for resistive heating [Fig. 7-1(b)]. Four holes were made in the cylinder side of the DAC through which the TCs could be inserted. Wide grooves were cut by electrical discharge machining to facilitate insertion of the electrodes. The thickness of the walls of the piston side of the DAC was 3.5 mm, which allowed the strength of the DAC to be maintained at high temperature.

Type-K and type-R TCs were cemented with Resbond 904 ceramic paste (Cotronics Corp.) to the pavilions of the diamond anvils for temperature measurement. The type-K TC was prepared from 0.10 mm nickel–chromium and nickel–Alumel wires, which were carefully twisted to create a junction. For the type-R TC, 0.10 mm platinum and 87% platinum–13% rhodium wires were welded to create a good junction.

All of the metal wires were purchased from Nilaco Co. (https://nilaco.jp/jp/), and, from the data supplied by the company, the intrinsic temperature accuracies of the type-K and type-R TCs were ±0.75% and ±0.25%, respectively. The DC power supply was a Takasago ZX-800LA. The temperature was monitored using a Graphtec GL240 data logger. The chamber was filled with argon gas to prevent oxidation of the diamond anvils (Fig. 7-2).

For high-pressure experiments, diamonds with a 300 or 120 μm culet were used. Samples were loaded into a 100 or 40 μm diameter sample chamber in a pre-indented rhenium/cubic boron nitride (cBN) composite gasket (hereinafter referred to simply as a cBN gasket) (Funamori and Sato, 2008) with inner gasket consisting of cBN+TiO_2 powder (Inoue et al., 2020; Suehiro et al., 2019) to minimize the pressure release that occurred on heating (see section 7.4.3 for details).

7.3. Heater Performance: Graphite vs SiC

Graphite shows a metal-like high electrical conductivity of ~10^5 S/m under ambient conditions, and this increases at high temperature. The use of a heater with a high resistance is important to reduce the current needed to generate high temperatures (Du et al., 2013b; Mijiti et al., 2018). To maximize the heater resistance, we attempted to reduce the wall thickness to 0.15 mm. However, the resistance was still not sufficient to generate temperatures above 600 K and also made the heater so fragile that it could not be

connected with the electrodes. We therefore conclude that graphite is not a suitable material for a cylindrical heater.

By contrast, we succeeded in generating temperatures up to 1500 K using the cylindrical SiC heater (Fig. 7-3). Each target temperature was stabilized within ~10 min, and the temperature fluctuations fell to within a few kelvin. In the test runs, two pairs of TCs were attached to the pavilions of the diamond anvils, and the temperature differences were all within 10 K (Fig. S7-3, supplementary material), revealing the precision of the temperature measurements in the present heater assembly. The cylindrical SiC heater yielded a linear power–temperature relation, which is similar to what was found in a previous study (Du et al., 2013b). The difference between the regression line and the value was ~5%, which may be due to slight differences in shape of the heaters used in different runs.

7.4. Discussion

7.4.1. Temperature accuracy

To test the temperature accuracy of our EHDAC system using the cylindrical SiC heater, we conducted an experiment on the melting of NaCl (melting temperature = 1074 K) and gold (melting temperature = 1337 K) under ambient pressure in a similar manner as that described in Du et al. (2013b). During heating, the temperature of the diamond was measured by the type-K TC cemented to one of the pavilions. The junction of the TC

was placed less than 1 mm away from the culet. The samples were a piece of gold cut from 10 μm thick foil and a NaCl pellet, each of which was loaded into a pre-indented rhenium gasket without a pressure medium. These samples were heated under ambient pressure and the temperature was gradually increased (~10 K/min) by increasing the power supplied to the heater. The melting temperatures were determined visually by an optical microscope. The criterion for melting adopted in this experiment was the transformation of the sample into a spherical shape.

We observed melting of NaCl at 1063 K, whereas the actual melting temperature of NaCl is 1074 K, which represents only a slight difference of ~1.40%. Also, our observed melting temperature of gold of 1337 K was a perfect match with the reference value, proving that our EHDAC is capable of performing an experiment with highly temperature-accurate heating. The measured temperature uncertainty u was calculated from the uncertainty obtained in this calibration experiment, u_{exp}, and the uncertainty originating from the temperature accuracy of the TC itself, u_{TC}, as follows:

$$u = \sqrt{\left(u_{\mathrm{exp}}\right)^2 + (u_{\mathrm{TC}})^2}\,. \qquad (7\text{-}1)$$

Here, we take u_{exp} as the maximum uncertainty of ±1.40%. With u_{TC} values of ±0.75% and ±0.25% for type-K and type-R TCs, respectively, the calculated temperature uncertainty u in our EHDAC assembly is at most ±1.6% when using a type-K TC and ±1.4% when using a type-R TC.

7.4.2. Degradation of the SiC heater

In the test runs for checking the power–temperature behavior of the SiC heater, all except for run #3 showed clear linear relations (applied voltage and current in each run is summarized in Table S7-1, supplementary material). In run #3, the current fluctuated wildly (±1.0 A) under voltage control and did not settle down within 10 min. Also, the total resistance of the SiC heater used in run #3 jumped at 1000 K and the temperature kept decreasing at the same applied power (Fig. 7-4).

In all the runs except run #3, the heater was first heated in an oxygen atmosphere. At high temperatures in an oxygen atmosphere, i.e., under high oxygen partial pressure (P_{O_2}) conditions, SiC is oxidized according to the following reaction (Narushima et al., 1989):

$$SiC(s) + 2O_2(g) \rightarrow SiO_2(s) + CO_2(g), \qquad (7\text{-}2)$$

where (s) and (g) indicates solid and gaseous states, respectively. Generally, materials will be oxidized and degraded under high-P_{O_2} conditions at high temperature. However, as can be seen from Eq. (7-2), oxidation of SiC produces solid SiO_2, which forms a passive film on the heater surface. This so-called passive oxidation prevents further oxidation of the heater material, which is thereby protected from damage. On the other hand, when the SiC heater is heated under low-P_{O_2} conditions of $<\sim 10^3$ Pa, such as in an argon atmosphere, oxidation of SiC occurs through the following reaction (Narushima et al., 1991):

$$SiC(s) + O_2(g) \rightarrow SiO(g) + CO(g). \qquad (7\text{-}3)$$

In this so-called active oxidation reaction, rather than the stable solid SiO_2, gaseous SiO is produced. Consequently, no passive protective film is formed on the heater, which

therefore undergoes further damage as oxidation proceeds. We attribute the unstable heating in run #3 to degradation of the heater due to active oxidation. Therefore, as long as the SiC heater is to be used under low-P_{O_2} conditions such as an argon atmosphere, preheating under an oxygen atmosphere is an important step.

7.4.3. Pressure change at high pressure and temperature

Generally, high-temperature experiments using an EHDAC involve pressure changes, which are mainly due to thermal expansion of the DAC and weakening of the metal gasket and seat at high temperature: there can be a significant pressure increase by as much as 200% (Miyagi et al., 2013) or, conversely, a sudden drop to ambient pressure. We conducted an additional experiment to check how the pressure would change in our EHDAC system. First, we heated NaCl loaded into a pre-indented rhenium gasket with an initial thickness of 50 μm, and we found that the pressure dropped by ~20% at 1000 K. We then prepared a nonmetallic cBN gasket (Inoue et al., 2020; Suehiro et al., 2019) of initial thickness 48 μm, expecting a weaker pressure reduction because of its high strength and chemical inertness at high pressure and temperature. With this gasket, the pressure did not change greatly below 1200 K, but it did drop at 1300 K (Fig. 7-5). Assuming that the surrounding rhenium portion of the cBN gasket had weakened at 1300 K, we reduced the initial thickness of the pre-indented rhenium gasket to ~25 μm to minimize the pressure release. However, we could not prevent a pressure drop at 1500 K, which was the largest drop in our experiments. We thus conclude that although the use of a cBN gasket rather than a rhenium gasket alone can lessen the pressure reduction, experiments above 1300 K still require a gas membrane system to maintain the target

pressure. We never experienced gasket blowouts or failure of diamond anvils in our runs, even at a high pressure of ~90 GPa or a high temperature of 1500 K maintained for 30 min, and this may be due to the use of the cBN gasket.

7.4.4. Electrodes

$LaCrO_3$ and boron-doped diamond have also been used as heater materials in experiments at high pressures and temperatures using multi-anvil press (Tsujino et al., 2016; Xie et al., 2017). However, the high contact resistance of heaters using most semiconductors other than graphite makes it difficult to achieve a perfect connection between heater and electrodes and has hindered the development of heaters suitable for use with EHDACs. By contrast, the extreme hardness of SiC allows it to be fully pressure-bonded to carbon-sheet electrodes without physical breakdown, and heaters based on this material can be used again and again until complete degradation. We found that the heater sometimes split in two when the number of carbon sheets was too low. In total, four graphite sheets were required for a thick diamond anvil of ~2 mm, and three were enough for a thin anvil of ~1.5 mm. No reaction between the SiC heater and the graphite sheets was observed at temperatures up to 1500 K. By contrast, other semiconductor materials are prone to carbonization, and if these are to be used in heaters for EHDAC systems, an alternative approach to electrode connection will be required.

7.4.5. Application

Our simple EHDAC system can be integrated into most of laser optical systems with a 200 mm focal length lens, and can therefore be used for optical spectroscopy and

for measurements of physical properties such as thermal conductivity (Ohta et al., 2012; Yagi et al., 2011) and sound velocity (Wakamatsu et al., 2018) at high pressure and temperature using optical techniques. This system can also be used for synchrotron X-ray diffraction (XRD) measurements in the axial direction, but does not permit radial XRD owing to the strong peaks from SiC grains (Fig. S7-4, supplementary material). However, the use of a SiC heater divided vertically in two would provide a gap for the radial X-ray path. Since the heater is independent of the gasket, experiments demanding a complex gasket assembly such as electrical resistivity measurements should also be feasible.

To test the capability of our EHDAC system for resistance measurements, the resistance of iodine was measured up to 25 GPa and 1050 K. A cBN gasket with an initial rhenium gasket thickness of 20 μm and 300 μm culet diamond anvils were used. Iodine was loaded into the 100 μm diameter sample chamber (Fig. S7-5, supplementary material). Gold electrodes that were directly in contact with the sample were printed on the diamond anvil surface, which were connected with two platinum lead electrodes cut from a Pt foil that were not directly in contact with the sample. The pressure was determined from the Raman spectrum of the diamond anvils (Akahama and Kawamura, 2004). The electrical resistivity was measured by the quasi-four-terminal method, with impedance spectra being collected using a Hioki 3532-80 Chemical Impedance Analyzer and a Hioki Four-Terminal Probe 9500.

The electrical resistance of iodine has been reported to decrease continuously from 6 GPa to ~23 GPa. Both optical observations (Balchan and Drickamer, 1961) and the low resistance with a positive temperature dependence measured in low-temperature experiments (Sakai et al., 1982) have led to the suggestion that iodine becomes metallic

at these high pressures. In our experiments, the resistance of iodine under pressure at room temperature decreased continuously, with a significant drop by four orders of magnitude at 25 GPa [Fig. 7-6(a)], showing a metal-like resistance as reported in previous studies (Balchan and Drickamer, 1961; Sakai et al., 1982).

At 25 GPa, the electrical resistance of iodine showed a positive temperature dependence up to 800 K, indicating that it had transformed into a metallic phase [Fig. 7-6(b)]. The resistance dropped discontinuously at 960 K but retained a positive temperature dependence. The melting temperature of iodine has been reported to remain a constant ~1000 K at pressures in the range 6–8 GPa, indicating an almost flat pressure dependence above 6 GPa, although there is possibly a negative dependence at higher pressures (Brazhkin et al., 1999, 1991). The discontinuous drop in resistance at 960 K may be due to a transformation from solid metallic iodine to a metallic liquid, which is consistent with previous reports of atomic and metallic liquid iodine at high pressures (Brazhkin et al., 1999; Buontempo et al., 1998), and also implies a negative pressure dependence of the melting temperature of iodine.

7.5. Conclusions

We have developed a cylindrical semiconductor heater based on SiC that has allowed us to conduct temperature-accurate experiments in an EHDAC at high pressures and temperatures. Using a cBN gasket, we were able to achieve stable heating up to 1500 K without the occurrence of gasket blowouts. The temperature uncertainty in our EHDAC

system was estimated to be ~1.5%. The distinctive feature of the SiC heater is its hardness, allowing perfect pressure bonding to graphite sheet electrodes. Preheating in an oxygen atmosphere is necessary for the stable heating performance under an inert atmosphere. The SiC heater material is much cheaper than precious metal wires (~1 USD for a single heater). Our EHDAC system has a wide range of potential applications in combination with optical systems and complex gasket assemblies, allowing measurements of transport properties at high pressures and temperatures.

7.6. References

Akahama, Y., Kawamura, H., 2004. High-pressure Raman spectroscopy of diamond anvils to 250 GPa: Method for pressure determination in the multimegabar pressure range. J. Appl. Phys. 96, 3748–3751. https://doi.org/10.1063/1.1778482

Balchan, A.S., Drickamer, H.G., 1961. Effect of Pressure on the Resistance of Iodine and Selenium. J. Chem. Phys. 34, 1948–1949. https://doi.org/10.1063/1.1731798

Bassett, W.A., Shen, A.H., Bucknum, M., Chou, I., 1993. A new diamond anvil cell for hydrothermal studies to 2.5 GPa and from −190 to 1200 °C. Rev. Sci. Instrum. 64, 2340–2345. https://doi.org/10.1063/1.1143931

Boehler, R., 1986. The phase diagram of iron to 430 kbar. Geophys. Res. Lett. 13, 1153–1156. https://doi.org/10.1029/GL013i011p01153

Brazhkin, V. V., Popova, S. V., Voloshin, R.N., 1999. Pressure-temperature phase diagram of molten elements: selenium, sulfur and iodine. Phys. B Condens. Matter 265, 64–71. https://doi.org/10.1016/S0921-4526(98)01318-0

Brazhkin, V. V., Popova, S. V., Voloshin, R.N., Umnov, A.G., 1991. Metallization of liquid iodine under high pressure. High Press. Res. 6, 363–369. https://doi.org/10.1080/08957959208201044

Buontempo, U., Filipponi, A., Martínez-García, D., Postorino, P., Mezouar, M., Itié, J.P., 1998. Anomalous bond length expansion in liquid iodine at high pressure. Phys. Rev. Lett. 80, 1912–1915. https://doi.org/10.1103/PhysRevLett.80.1912

Du, Z., Amulele, G., Robin Benedetti, L., Lee, K.K.M., 2013a. Mapping temperatures and temperature gradients during flash heating in a diamond-anvil cell. Rev. Sci. Instrum. 84. https://doi.org/10.1063/1.4813704

Du, Z., Miyagi, L., Amulele, G., Lee, K.K.M., 2013b. Efficient graphite ring heater suitable for diamond-anvil cells to 1300 K. Rev. Sci. Instrum. 84, 024502. https://doi.org/10.1063/1.4792395

Dubrovinskaia, N., Dubrovinsky, L., 2003. Whole-cell heater for the diamond anvil cell. Rev. Sci. Instrum. 74, 3433–3437. https://doi.org/10.1063/1.1578151

Funamori, N., Sato, T., 2008. A cubic boron nitride gasket for diamond-anvil experiments. Rev. Sci. Instrum. 79, 053903. https://doi.org/10.1063/1.2917409

Hazen, R.M., Finger, L.W., 1981. High-temperature diamond-anvil pressure cell for single-crystal studies. Rev. Sci. Instrum. 52, 75–79. https://doi.org/10.1063/1.1136450

Hirao, N., Kawaguchi, S.I., Hirose, K., Shimizu, K., Ohtani, E., Ohishi, Y., 2020. New developments in high-pressure X-ray diffraction beamline for diamond anvil cell at SPring-8. Matter Radiat. Extrem. 5, 018403. https://doi.org/10.1063/1.5126038

Inoue, H., Suehiro, S., Ohta, K., Hirose, K., Ohishi, Y., 2020. Resistivity saturation of hcp Fe-Si alloys in an internally heated diamond anvil cell: A key to assessing the

Earth's core conductivity. Earth Planet. Sci. Lett. 543, 116357. https://doi.org/10.1016/j.epsl.2020.116357

Jenei, Z., Cynn, H., Visbeck, K., Evans, W.J., 2013. High-temperature experiments using a resistively heated high-pressure membrane diamond anvil cell. Rev. Sci. Instrum. 84. https://doi.org/10.1063/1.4821622

Komabayashi, T., Fei, Y., Meng, Y., Prakapenka, V., 2009. In-situ X-ray diffraction measurements of the γ-ε transition boundary of iron in an internally-heated diamond anvil cell. Earth Planet. Sci. Lett. 282, 252–257. https://doi.org/10.1016/j.epsl.2009.03.025

Komabayashi, T., Hirose, K., Sugimura, E., Sata, N., Ohishi, Y., Dubrovinsky, L.S., 2008. Simultaneous volume measurements of post-perovskite and perovskite in MgSiO3 and their thermal equations of state. Earth Planet. Sci. Lett. 265, 515–524. https://doi.org/10.1016/j.epsl.2007.10.036

Lai, X., Zhu, F., Zhang, J.S., Zhang, D., Tkachev, S., Prakapenka, V.B., Chen, B., 2020. An externally-heated diamond anvil cell for synthesis and single-crystal elasticity determination of Ice-VII at high pressure-temperature conditions. J. Vis. Exp. 2020, 1–14. https://doi.org/10.3791/61389

Liermann, H.P., Merkel, Ś., Miyagi, L., Wenk, H.R., Shen, G., Cynn, H., Evans, W.J., 2009. Experimental method for in situ determination of material textures at simultaneous high pressure and high temperature by means of radial diffraction in the diamond anvil cell. Rev. Sci. Instrum. 80. https://doi.org/10.1063/1.3236365

Liu, L.-G., Bassett, W.A., 1975. The melting of iron up to 200 kbar. J. Geophys. Res. 80, 3777–3782. https://doi.org/10.1029/JB080i026p03777

McWilliams, R.S., Dalton, D.A., Konôpková, Z., Mahmood, M.F., Goncharov, A.F., 2015. Opacity and conductivity measurements in noble gases at conditions of planetary and stellar interiors. Proc. Natl. Acad. Sci. U. S. A. 112, 7925–7930. https://doi.org/10.1073/pnas.1421801112

Mijiti, Y., Trapananti, A., Minicucci, M., Ciambezi, M., Coquet, J., Nataf, L., Baudelet, F., Di Cicco, A., 2018. Development of a high temperature diamond anvil cell for x ray absorption experiments under extreme conditions. Radiat. Phys. Chem. 108106. https://doi.org/10.1016/j.radphyschem.2018.12.026

Ming, L.C., Bassett, W.A., 1974. Laser heating in the diamond anvil press up to 2000°C sustained and 3000°C pulsed at pressures up to 260 kilobars. Rev. Sci. Instrum. 45, 1115–1118. https://doi.org/10.1063/1.1686822

Miyagi, L., Kanitpanyacharoen, W., Raju, S.V., Kaercher, P., Knight, J., MacDowell, A., Wenk, H.-R., Williams, Q., Alarcon, E.Z., 2013. Combined resistive and laser heating technique for in situ radial X-ray diffraction in the diamond anvil cell at high pressure and temperature. Rev. Sci. Instrum. 84, 025118. https://doi.org/10.1063/1.4793398

Mondal, T.K., Murugavel, S., Asokan, S., 1999. An automated, externally heated opposed anvil high pressure–high temperature system for electrical resistivity studies. Rev. Sci. Instrum. 70, 165–170. https://doi.org/10.1063/1.1149559

Narushima, T., Goto, T., Hirai, T., 1989. High-Temperature Passive Oxidation of Chemically Vapor Deposited Silicon Carbide. J. Am. Ceram. Soc. 72, 1386–1390. https://doi.org/10.1111/j.1151-2916.1989.tb07658.x

Narushima, T., Goto, T., Iguchi, Y., Hirai, T., 1991. High-Temperature Active Oxidation of Chemically Vapor-Deposited Silicon Carbide in an ArO2 Atmosphere. J. Am. Ceram. Soc. 74, 2583–2586. https://doi.org/10.1111/j.1151-2916.1991.tb06803.x

Ohishi, Y., Hirao, N., Sata, N., Hirose, K., Takata, M., 2008. Highly intense monochromatic X-ray diffraction facility for high-pressure research at SPring-8. High Press. Res. 28, 163–173. https://doi.org/10.1080/08957950802208910

Ohta, K., Yagi, T., Taketoshi, N., Hirose, K., Komabayashi, T., Baba, T., Ohishi, Y., Hernlund, J., 2012. Lattice thermal conductivity of MgSiO 3 perovskite and post-perovskite at the core-mantle boundary. Earth Planet. Sci. Lett. 349–350, 109–115. https://doi.org/10.1016/j.epsl.2012.06.043

Ozawa, H., Tateno, S., Xie, L., Nakajima, Y., Sakamoto, N., Kawaguchi, S.I., Yoneda, A., Hirao, N., 2018. Boron-doped diamond as a new heating element for internal-resistive heated diamond-anvil cell. High Press. Res. 38, 120–135. https://doi.org/10.1080/08957959.2018.1441407

Pasternak, S., Aquilanti, G., Pascarelli, S., Poloni, R., Canny, B., Coulet, M.V., Zhang, L., 2008. A diamond anvil cell with resistive heating for high pressure and high temperature x-ray diffraction and absorption studies. Rev. Sci. Instrum. 79. https://doi.org/10.1063/1.2968199

Petitgirard, S., Daniel, I., Dabin, Y., Cardon, H., Tucoulou, R., Susini, J., 2009. A diamond anvil cell for x-ray fluorescence measurements of trace elements in fluids at high pressure and high temperature. Rev. Sci. Instrum. 80, 1–6. https://doi.org/10.1063/1.3100202

Prakapenka, V.B., Kubo, A., Kuznetsov, A., Laskin, A., Shkurikhin, O., Dera, P., Rivers, M.L., Sutton, S.R., 2008. Advanced flat top laser heating system for high pressure research at GSECARS: Application to the melting behavior of germanium. High Press. Res. 28, 225–235. https://doi.org/10.1080/08957950802050718

Rainey, E.S.G., Hernlund, J.W., Kavner, A., 2013. Temperature distributions in the laser-heated diamond anvil cell from 3-D numerical modeling. J. Appl. Phys. 114, 204905. https://doi.org/10.1063/1.4830274

Sakai, N., Takemura, K., Tsuji, K., 1982. Electrical Properties of High-Pressure Metallic Modification of Iodine. J. Phys. Soc. Japan 51, 1811–1816. https://doi.org/10.1143/JPSJ.51.1811

Shen, G., Liermann, H.P., Sinogeikin, S., Yang, W., Hong, X., Yoo, C.S., Cynn, H., 2007. Distinct thermal behavior of GeO2 glass in tetrahedral, intermediate, and

octahedral forms. Proc. Natl. Acad. Sci. U. S. A. 104, 14576–14579. https://doi.org/10.1073/pnas.0703098104

Sinmyo, R., Hirose, K., 2010. The Soret diffusion in laser-heated diamond-anvil cell. Phys. Earth Planet. Inter. 180, 172–178. https://doi.org/10.1016/j.pepi.2009.10.011

Sinmyo, R., Hirose, K., Ohishi, Y., 2019. Melting curve of iron to 290 GPa determined in a resistance-heated diamond-anvil cell. Earth Planet. Sci. Lett. 510, 45–52. https://doi.org/10.1016/j.epsl.2019.01.006

Suehiro, S., Wakamatsu, T., Ohta, K., Hirose, K., Ohishi, Y., 2019. High-temperature electrical resistivity measurements of hcp iron to Mbar pressure in an internally resistive heated diamond anvil cell. High Press. Res. 39, 579–587. https://doi.org/10.1080/08957959.2019.1692008

Tateno, S., Hirose, K., Ohishi, Y., Tatsumi, Y., 2010. The Structure of Iron in Earth's Inner Core. Science (80-.). 330, 359–361. https://doi.org/10.1126/science.1194662

Tsujino, N., Nishihara, Y., Yamazaki, D., Seto, Y., Higo, Y., Takahashi, E., 2016. Mantle dynamics inferred from the crystallographic preferred orientation of bridgmanite. Nature 539, 81–84. https://doi.org/10.1038/nature19777

Wakamatsu, T., Ohta, K., Yagi, T., Hirose, K., Ohishi, Y., 2018. Measurements of sound velocity in iron–nickel alloys by femtosecond laser pulses in a diamond anvil cell. Phys. Chem. Miner. 45, 589–595. https://doi.org/10.1007/s00269-018-0944-3

Whittaker, A.G., 1978. The controversial carbon solid-liquid-vapour triple point. Nature 276, 695–696. https://doi.org/10.1038/276695a0

Xie, L., Yoneda, A., Yoshino, T., Yamazaki, D., Tsujino, N., Higo, Y., Tange, Y., Irifune, T., Shimei, T., Ito, E., 2017. Synthesis of boron-doped diamond and its application as a heating material in a multi-anvil high-pressure apparatus. Rev. Sci. Instrum. 88. https://doi.org/10.1063/1.4993959

Yagi, T., Ohta, K., Kobayashi, K., Taketoshi, N., Hirose, K., Baba, T., 2011. Thermal diffusivity measurement in a diamond anvil cell using a light pulse thermoreflectance technique. Meas. Sci. Technol. 22. https://doi.org/10.1088/0957-0233/22/2/024011

Zha, C.S., Bassett, W.A., 2003. Internal resistive heating in diamond anvil cell for in situ x-ray diffraction and Raman scattering. Rev. Sci. Instrum. 74, 1255–1262. https://doi.org/10.1063/1.1539895

7.7. Tables and Figures

Table 7-1. Previous studies of EHDACs with nonmetallic resistive heaters.

Heater material	Temperature achieved (K)	Pressure achieved (GPa)	Heater design	References
Graphite	620	13	Rhenium gasket sandwiched between two graphite sheets	Shen et al. (2007)
Graphite	1100	36	Rhenium gasket sandwiched between two graphite sheets	Liermann et al. (2009)[a]
Graphite	2273[b]	69	Rhenium gasket sandwiched between two graphite sheets	Miyagi et al. (2013)[a]
Graphite	1300	51	Ring-shaped graphite heaters directly in contact with both diamond anvils	Du et al. (2013)
Graphite	1300	5	Graphite sheet surrounding the diamond anvils	Mijiti et al. (2019)

[a]Design modified from that of Shen et al. (2007). [b]Combined with laser heating.

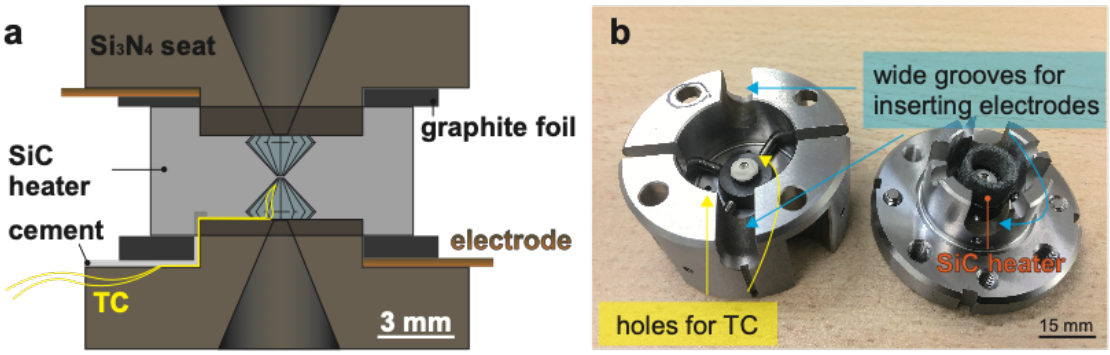

Fig. 7-1. (a) schematic and (b) photograph of the EHDAC assembly.

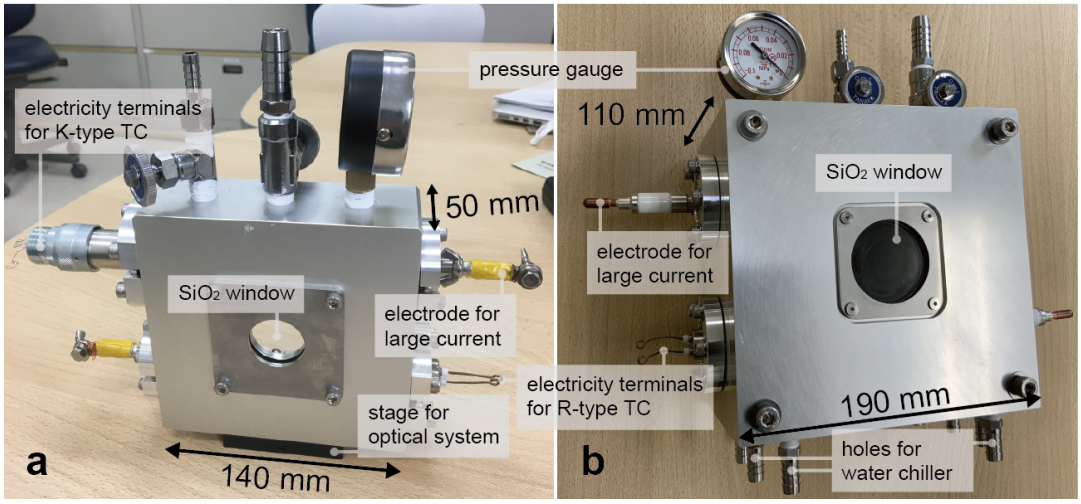

Fig. 7-2. (a) Chamber fitted with the optical system with a double-sided $f = 200$ mm lens. (b) Water-cooled built-in vacuum chamber with relatively large working distance.

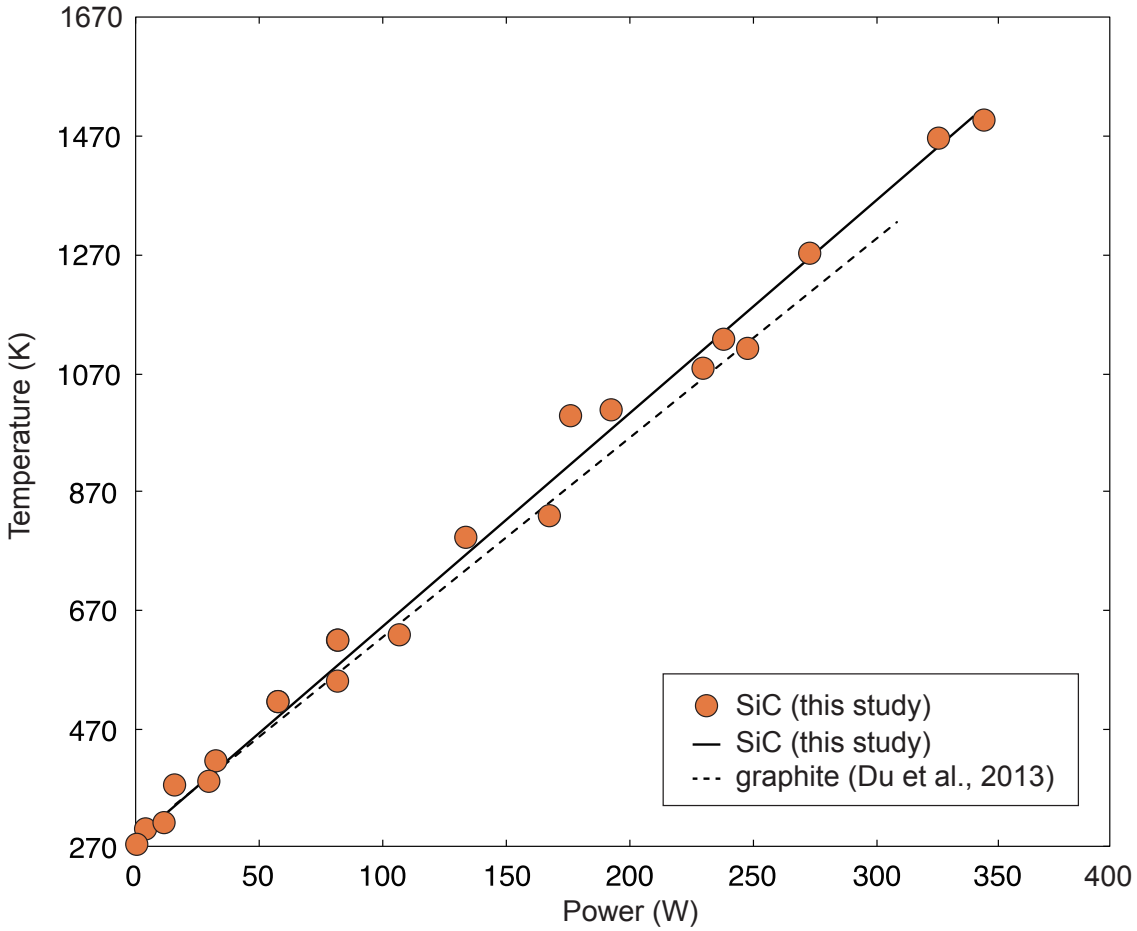

Fig. 7-3. Power–temperature relation in EHDACs using graphite and SiC heaters. The black solid line is the regression line of the power–temperature relation for the SiC heater, and the dashed line is that for the graphite heater reported in Du et al. (2013b).

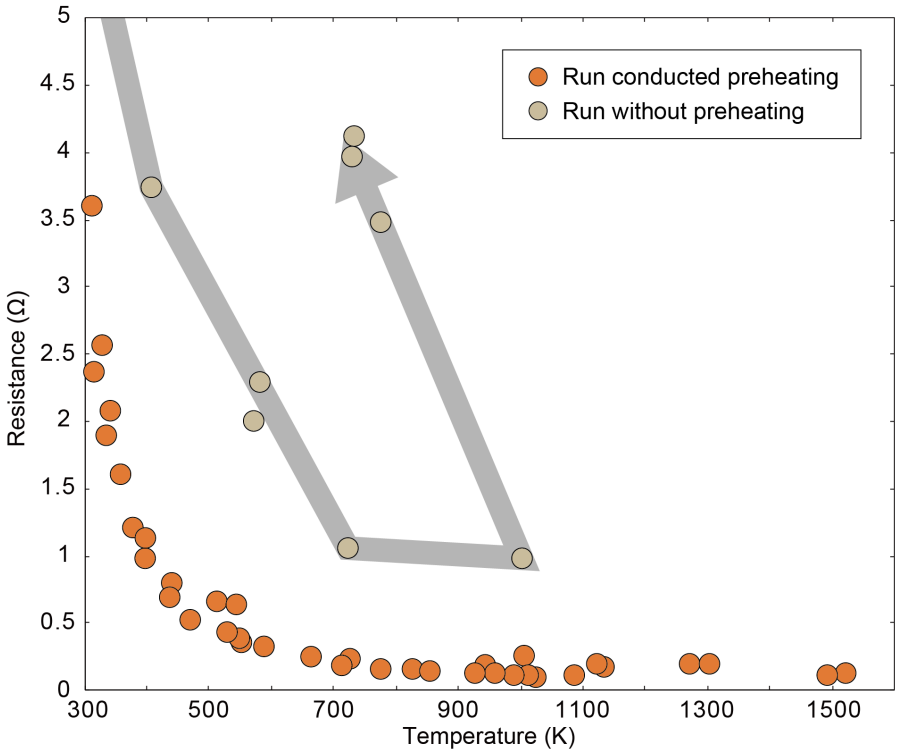

Fig. 7-4. Temperature dependence of the resistance of the SiC heater in the test runs. The gray arrow shows the resistance path of the heater during run #3 (the run conducted without preheating in an oxygen atmosphere).

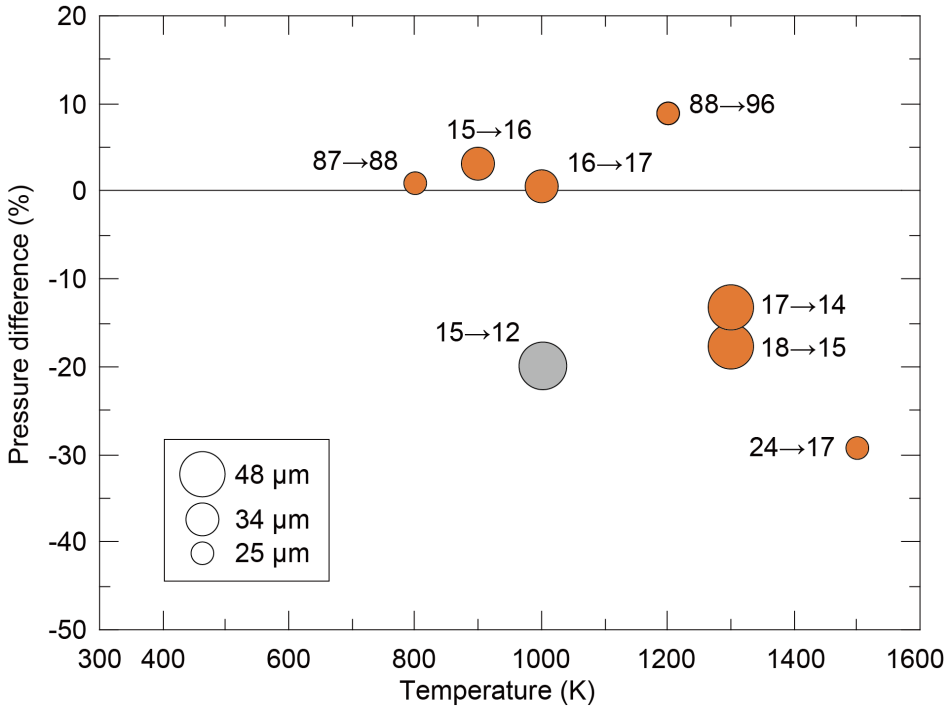

Fig. 7-5. Temperature dependence of pressure change after heating. Orange and gray symbols correspond to experimental runs using cBN and rhenium gaskets, respectively. The size of each symbol indicates the initial thickness of the pre-indented rhenium gasket. The numbers next to the symbols show the pressure change during heating. The pressure change found in Miyagi et al. (2013) is not plotted, since it is far greater than the other values.

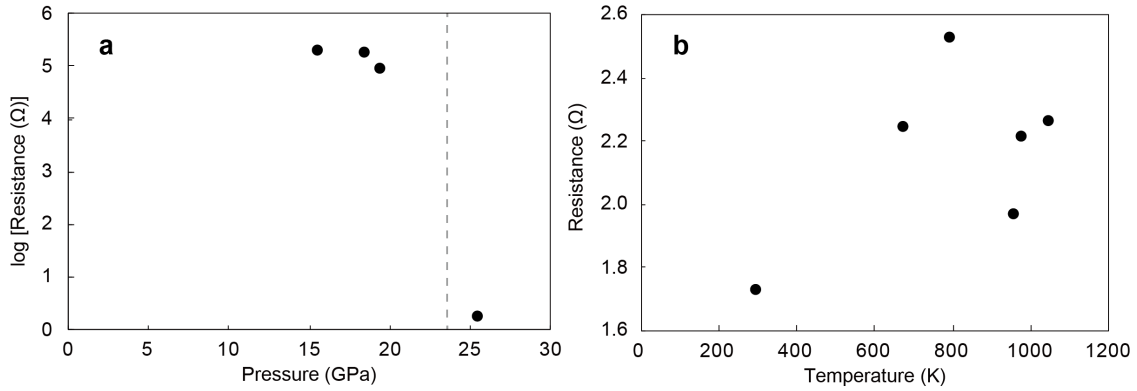

Fig. 7-6. High-pressure electrical resistance of iodine at (a) room temperature and (b) high temperatures. The vertical dashed line indicates the reported metal-transition offset pressure of iodine (Balchan and Drickamer, 1961; Sakai et al., 1982).

7.8. Supplemental material

Table S7-1. Applied voltage and current in each run.

Run #	Voltage (V)	Current (A)	Temperature (K)	Resistance (Ω)
1	7	3.0	318	2.37
	7.2	3.8	336	1.89
	7.2	5.9	379	1.22
	7.2	9.0	441	0.80
	7	7.1	399	0.98
	6.7	9.5	438	0.70
	6.3	12.0	471	0.53
	6.79	15.7	532	0.43
	6.65	19.9	589	0.33
	6.43	25.4	664	0.25
	6.07	30.2	715	0.20
	5.73	33.9	777	0.17
	5.7	36.1	828	0.16
	5.73	37.3	855	0.15
	5.7	40.4	929	0.14
	5.71	43.0	959	0.13
	5.64	47.8	1013	0.12
	5.2	36.1	675	0.14
	5.5	43.0	788	0.13
	5.5	44.0	839	0.12
	5.6	45.9	893	0.12
	5.68	48.7	960	0.12
	5.57	49.3	989	0.11
	5.47	50.0	1023	0.11
	5.51	53.0	1083	0.10
	5.35	52.4	1091	0.10
	5.25	51.9	1094	0.10
2	6.3	1.8	315	3.60
	7	2.7	328	2.56
	7.3	3.5	342	2.09
	7.6	4.7	360	1.62
	7.84	6.9	400	1.14
	7.92	9.9	447	0.80
	8.2	12.3	515	0.67
	7.2	11.4	549	0.63
	6.6	26.7	727	0.25
	6.6	35.0	943	0.19
	7	27.5	1008	0.25
	6.9	34.5	1127	0.20
	6.7	37.5	1133	0.18
	7.1	38.5	1273	0.18
	7.6	40.7	1308	0.19
	6.35	51.9	1493	0.12
	6.7	52.0	1523	0.13
3	14.6	3.9	410	3.74
	13.3	5.8	582	2.29
	13.3	6.6	573	2.02
	10.6	10.0	723	1.06
	11.3	11.4	1003	0.99
	14	3.4	733	4.12
	14.1	3.6	730	3.97
	15	4.3	778	3.49

Fig. S7-1. The tested cylindrical shape graphite ring heater with the wall thickness of 0.5 mm.

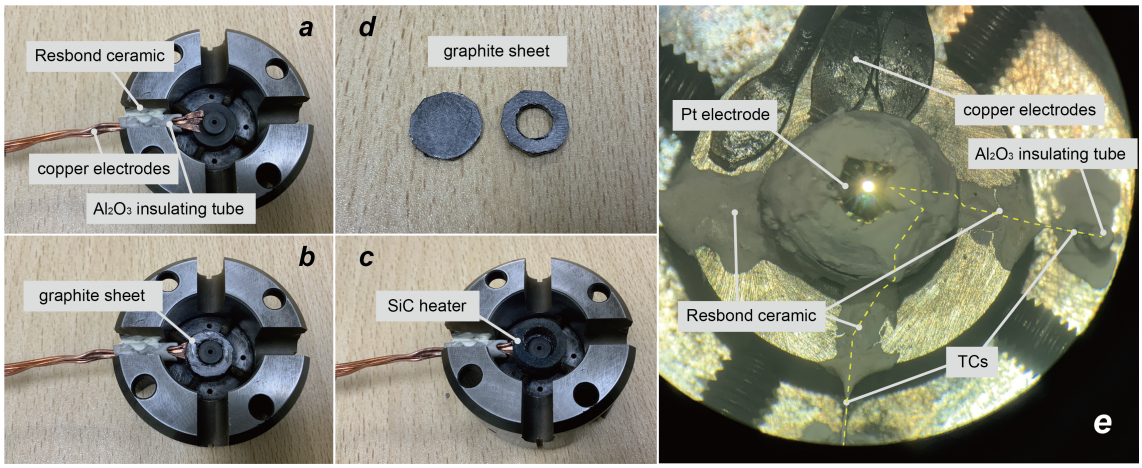

Fig. S7-2. Preparation procedure of (a)(b)(c) graphite sheets + copper electrodes, (d) shaping of graphite sheets, and (e) thermocouples. Yellow broken line in Fig. S7-2e shows the path of the thermocouple.

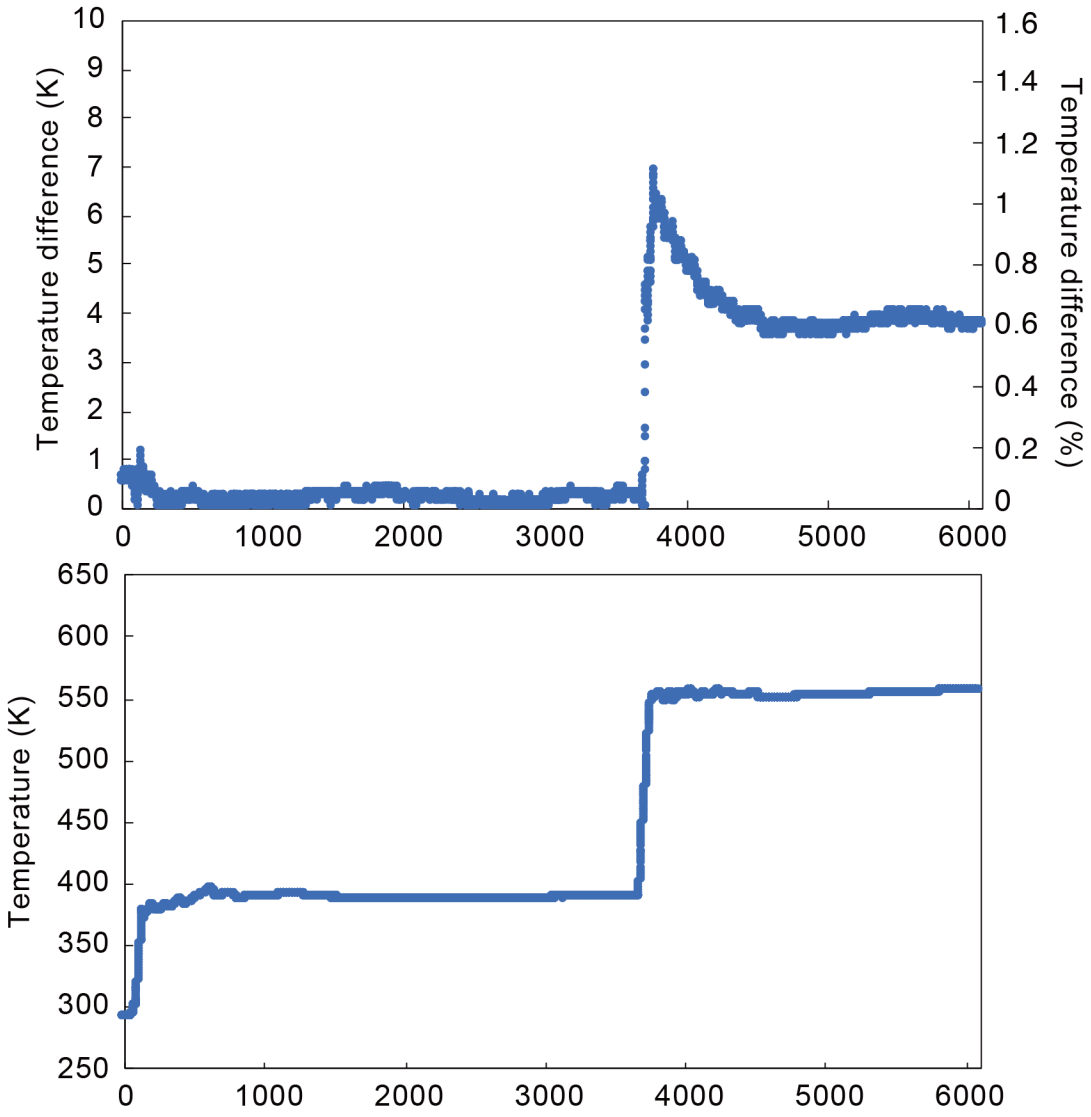

Fig. S7-3. Temperature difference of two TC in the EHDAC.

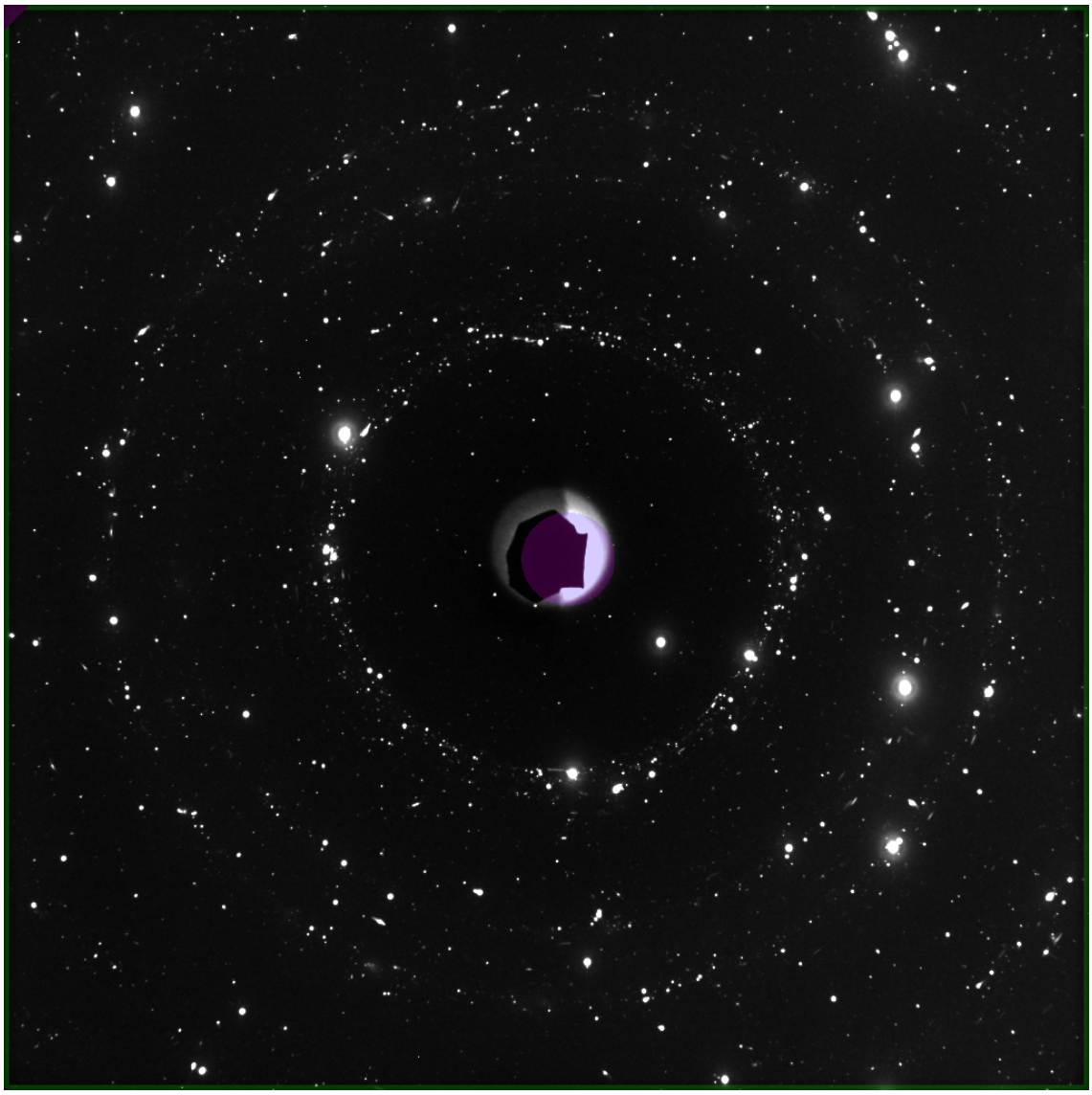

Fig. S7-4. 2D XRD pattern of the SiC heater. Spotty strong peaks were observed deriving from relatively large SiC grains. The XRD pattern was collected using a flat panel detector at BL10 XU, Spring-8, Japan.

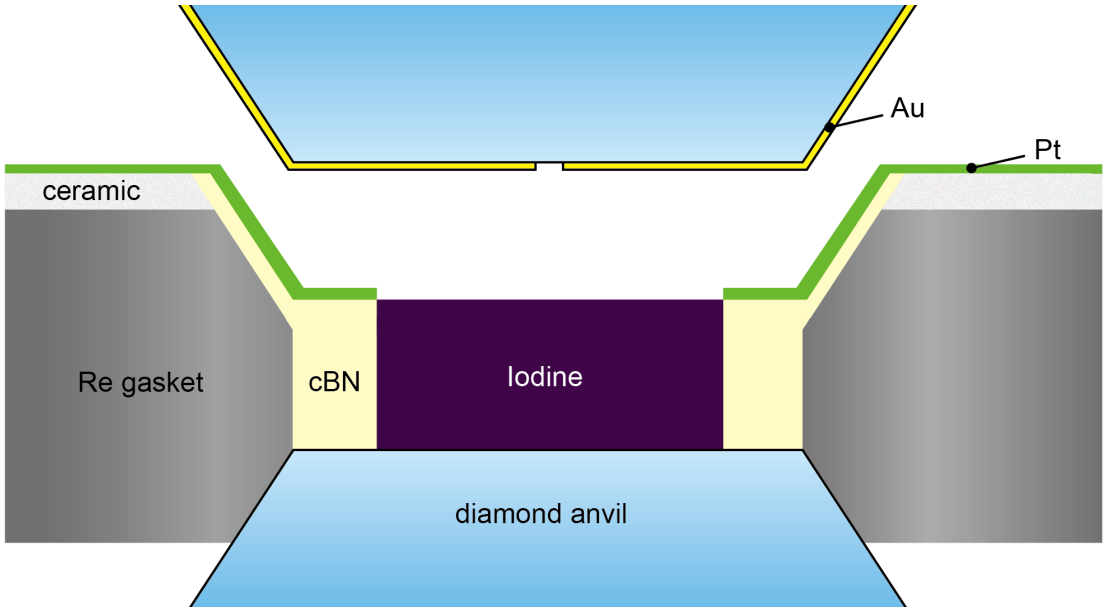

Fig. S7-5. Schematic of the sample chamber of electrical resistivity measurements in the EHDAC.

Chapter 8. Dry lower mantle inferred from the electrical conductivity of water-bearing bridgmanite

Abstract

The amount of water and its distribution in the Earth's interior is one of the most important fundamental information affecting various geophysical and chemical phenomena. Water concentration of the Earth's mantle is not well constrained, which is mainly caused by the unknown amount in the lower mantle. Here we carried out the electrical conductivity measurement on hydrous bridgmanite with 526 ± 139 ppm wt. H_2O at 30 GPa and up to 923 K using an externally heated diamond anvil cell. Similarly to other mantle minerals such as olivine, wadsleyite, and ringwoodite, we found that the electrical conductivity of bridgmanite significantly enhances by adding hydroxyl into its structure. To our knowledge the present study is the first laboratory measurement that quantified the effect of water incorporation on the electrical conductivity of bridgmanite. Extrapolation of the present results to lower mantle conditions derives the water content in lower mantle bridgmanite of less than 10 ppm wt. H_2O, corresponding to less than 0.02 times the ocean mass. Such a dry lower mantle can be a consequence of a secondary iron percolation to the core and/or ongoing hydrogen absorption of metallic iron in the lower mantle.

8.1. Introduction

Planetary accretion simulations suggest the possibility of massive volatiles such as water delivered to the Earth's building blocks (Morbidelli et al., 2000), which can be more than 100 ocean mass (Raymond et al., 2004). The amount of water and its distribution in the Earth's interior influence the thermoelectrical transport properties (Chang et al., 2017; Karato, 2013), rheological properties (Chen et al., 1998), deformation mechanism (Zhan, 2020), phase relations (Ghosh et al., 2013), and melting temperature (Fiquet, 2018; Hirose et al., 2019; Nomura et al., 2014) of the Earth's mantle and core, hence controlling the thermochemical evolution of the Earth. The oceanic water covers about 70% of the Earth's surface but only has 0.023 wt.% of the total mass of the Earth. An extensive amount of the Earth's water is thought to be dissolved into the anhydrous silicate minerals constituting the Earth's crust and the mantle as an impurity (Peslier et al., 2017), which could account for more than 80 % of the Earth's total water (Nestola and Smyth, 2015). Investigation of the water concentration in crustal and upper mantle origin natural samples gave precise regional water content in those regions (Bell and Rossman, 1992). The natural samples from the mantle transition zones are found but are not sufficient to estimate the average water content in these layers (Pearson et al., 2014; Wirth et al., 2007).

The electrical conductivity of minerals is highly sensitive to their water content (Karato, 1990). Combining with the electromagnetic observations, laboratory electrical conductivity measurements on minerals constituting the upper mantle and the transition zones, namely olivine (Wang et al., 2006; Yoshino et al., 2006), pyrope garnet (Dai and Karato, 2009a), orthopyroxene (Dai and Karato, 2009b), clinopyroxene and plagioclase

(Yang et al., 2012, 2011), wadsleyite and ringwoodite (Huang et al., 2005; Yoshino et al., 2008a; Yoshino and Katsura, 2012), have provided invaluable constraints on the water content of the Earth's interior. The water content in the mantle transition zones was found to be heterogeneous, ranging from 3000 to 6000 ppm wt. H_2O on average (Karato, 2013) and could be strongly hydrated with > 10000 ppm in some regions such as below central China or southwestern North USA (Khan and Shankland, 2012). This is moderately consistent with the water content of ringwoodite inclusion in natural diamond samples of more than 10000 ppm wt. H_2O (Pearson et al., 2014).

As the largest layer occupying more than half of the Earth's total volume, even a slight amount of water in the lower mantle greatly affects the total water abundance of the Earth (Peslier et al., 2017). Water concentration of a natural inclusion in superdeep diamond originated from the lower mantle has never been investigated (Zedgenizov et al., 2020), necessitating the laboratory electrical conductivity measurements on lower mantle minerals for water abundance estimation. Pyrolitic lower mantle is thought to consist of ~80% of (Fe,Al)-bearing bridgmanite and ~20% of ferropericlase (Hirose, 2002), and bridgmanite is thought to control the electrical conductivity of the Earth's lower mantle (Yoshino et al., 2008b). Extensive studies have conducted the laboratory electrical conductivity measurements on bridgmanite using a multi-anvil apparatus (MA) (Dobson, 2003; Katsura et al., 1998; Xu and McCammon, 2002; Yoshino et al., 2016, 2008b), and a diamond anvil cell (DAC) (Li and Jeanloz, 1990; Liu et al., 2018; Ohta et al., 2010a, 2010b, 2008; Peyronneau and Poirier, 1989; Potapkin et al., 2013; Shankland et al., 1993; Sinmyo et al., 2014) with various Fe and Al content. However, the effect of hydration on the electrical conductivity of bridgmanite has never been investigated. The amount of water in the Earth's lower mantle has relied on the information of the water solubility of

bridgmanite providing the upper boundary for actual water content, nevertheless, the reported values show a wide variation from <5 to ~4000 ppm wt. H_2O (Bolfan-Casanova et al., 2000; Litasov et al., 2003; Murakami et al., 2002; Ohtani, 2015).

Here we report high-*P,T* electrical conductivity of water-bearing bridgmanite at 30 GPa up to 923 K using an externally-heated diamond anvil cell (EHDAC) technique introduced in Chapter 7. To our knowledge, this is the first experiment reporting the hydration effect on the electrical conductivity of bridgmanite. Our results with a combination of geomagnetic observations imply a dry lower mantle containing less than 0.02 times the oceanic water in mass, which is much drier than the previous estimation of 0.2−4.5 (Peslier et al., 2017).

8.2. Methods

8.2.1. Sample preparation

The OT2463 bridgmanite sample was synthesized using a 3,000-ton Kawai-type MA apparatus (ORANGE-3000) at Ehime University, following a similar manner described in the previous study (Okuchi et al., 2015). The oxide mixtures of talc ($Mg_3Si_4O_{10}(OH)_2$), brucite ($Mg(OH)_2$), fayalite (Fe_2SiO_4), MgO, and Al_2O_3, were packed into an Au foil capsule and then loaded into a MgO container. Heating was performed for 12 hrs at 25 GPa and 1700 ℃ using a $LaCrO_3$ heater. The synthesis temperature was monitored with a W3Re-W25Re thermocouple. As a result, we obtained bridgmanite with a maximum crystal size of ~200 μm, with iron-depleted $(Mg_{0.97}Fe_{0.03})O$ ferropericlase and quench crystal, which of those phases were identified

by XRD measurement using a Rigaku RAPID II-V/DW (Fig. 8-1a). The chemical composition of bridgmanite was determined to be $Mg_{0.879(5)}Fe_{0.142(10)}Al_{0.106(3)}Si_{0.911(6)}O_3$ by Energy Dispersive Spectroscopy (EDS) analysis using JEOL JSM-6510LV in Ehime University.

The water content was determined from the Fourier Transform Infrared Spectroscopy (FTIR) measurement using the following equation (Paterson, 1982):

$$C_{\mathrm{OH}} = \frac{X_i}{150\xi}\int \frac{K(\nu)}{(3780-\nu)}d\nu, \qquad (8\text{-}1)$$

where C_{OH} is the concentration of hydroxyl in ppm wt. H_2O, ξ is an orientation factor, $K(\nu)$ is the absorption coefficient in cm^{-1} for a given wavenumber ν, and X_i is a density factor, respectively. FTIR spectra were collected using an FTIR spectrometer PerkinElmer Spectrum One at Ehime University under vacuum condition with BaF_2 window from six different locations with scanning 100 times per location in 25×25 μm^2 area. We used the *Xi* of bridgmanite with pyrolitic composition estimated in a previous study of 2123 ppm wt. H_2O (Litasov et al., 2003). The average water content was calculated to be 526 ± 139 ppm wt. H_2O. When OH hydroxyl distribution is anisotropic in non-cubic crystal, the infrared absorption spectrum depends on the crystal orientation. The unpolarized FTIR spectroscopy in some anisotropic mineral is argued to be unreliable (Bell et al., 2003; Libowitzky and Rossman, 1996). The crystal structure of bridgmanite is orthorhombic, so calculating three independent absorption spectra with polarized analysis is necessary for rigorous estimation. Withers (2013) showed an alternative way to strictly analyze FTIR spectrum of anisotropic crystal with unpolarized spectroscopy measurement using the following calculation:

$$A_{\mathrm{tot}} = \frac{\alpha}{d} = -\log_{10}\left[\left(3T_{\mathrm{avg}} - 2T_{\mathrm{max}}\right)\left(2T_{\mathrm{min}} + 2T_{\mathrm{max}} - 3T_{\mathrm{avg}}\right)\left(3T_{\mathrm{avg}} - 2T_{\mathrm{min}}\right)\right], \qquad (8\text{-}2)$$

where A_{tot} is the principal absorbance, α is total absorption coefficient, d is sample thickness, and T_{avg}, T_{max}, and T_{min} are the average, maximum, and minimum transmittance at each frequency, respectively. The calculated α as a function of wavenumber did not alter from that calculated based on Paterson (1982), indicating that the OH hydroxyl distribution in the OT2463 bridgmanite is almost isotropic. The water content using Eq. (8-2) (Withers, 2013) was estimated as ~534 ppm wt. H_2O, which is consistent with that calculated based on Paterson (1982).

We observed a minor amount of brucite in our single-crystal bridgmanite sample (Figs. 8-1,8-2) as reported in previous studies (Bolfan-Casanova et al., 2000; Litasov et al., 2003). Nevertheless, brucite does not decompose at the *P,T* conditions conducted in the present study (Duffy et al., 1991), and the volume fraction of brucite should not be enough to interconnect a three-dimensional network in our sample. Besides, the electrical conductivity of brucite at ambient and at high-*P,T* conditions is reported to be lower than that of bridgmanite (Fuji-Ta et al., 2007; Ohta et al., 2008; Sinmyo et al., 2014), so the presence of brucite should not affect the measured electrical conductivity.

8.2.2. Electrical conductivity measurements

The high-*P,T* electrical conductivity measurement was conducted using an EHDAC with SiC heater introduced in *Chapter 7*. A rhenium (Re) + cubic boron nitride (cBN) composite gasket (Funamori and Sato, 2008; Inoue et al., 2020; Suehiro et al., 2019) with an initial rhenium gasket thickness of 25 μm, and 120 μm culet diamond anvils were used. The cBN insulating layers were prepared on both sides of the gasket. A single crystal bridgmanite sample OT2463 polished to ~15×15×20 μm^3, then loaded

into a 20 μm diameter-sample chamber without a pressure medium. Gold electrodes that were directly in contact with the sample were sputtered on both sides of the diamond anvil surfaces, which of those initial thicknesses were both 1 μm. These were connected with platinum lead electrodes cut from a 10 μm thick Pt foil (Fig. 8-3). Type-K TC was placed in the pavilion of the diamond anvil to monitor the sample temperature. The electrical insulations of Pt electrodes and TC were carried out using the Resbond 919 ceramic paste (Cotronics Corp.). The entire DAC assembly was dried in a vacuum furnace at 140 ℃ right before the sample loading and the electrical conductivity measurement.

The electrical conductivity (σ) was calculated from the measured sample resistance R, and the sample geometry of the length (l) between the electrodes and the cross-sectional area parallel to the electrodes:

$$\sigma = l/RS. \quad (8\text{-}3)$$

The electrical resistance was measured by the quasi-four-terminal method, with impedance spectra being collected using a HIOKI 3532-80 Chemical Impedance Analyzer and a HIOKI Four-Terminal Probe 9500. The pressure was determined from a Raman spectrum of the diamond anvil (Akahama and Kawamura, 2004). We used a typical value of 10% for pressure errors. The recovered sample geometry was measured by a scanning electron microscope (SEM) after milling with a focused Ga ion beam (FIB) using VERSA 3D in the University of Tokyo and corrected for pressure using the reported thermal equation of state of (Fe,Al)-bearing bridgmanite (Sun et al., 2018) (Fig. 8-4). The errors in our conductivity measurements are calculated from the uncertainty in the sample geometry, which was ~16%.

8.3. Results and Discussion

We have conducted five independent experimental sets and succeeded in one run (Table 8-1). We first pressurized the sample to 28 GPa at room temperature. Subsequently, the sample resistance was measured with increasing temperature from 288 to 923 K. The pressure was increased to 30 GPa after the heating, so we treated our data as 30 GPa and extended the pressure uncertainty at lower pressure. The collected spectra showed three impedance arcs (Fig. 8-5), which is usually observed in frequency dependent electrical conductivity measurements (Bauerle, 1969; Roberts and Tyburczy, 1991). The three resistive mechanisms are generally attributed to the grain interiors (sample resistance), grain boundaries, and electrodes such as contact resistance, which was first described in Bauerle (1969). The use of low-frequency data is also bothered since the contribution of proton conduction is suggested to be underestimated due to the effect of polarization (Roberts and Tyburczy, 1991). We obtained the sample resistance by fitting our data measured at frequencies of ~10^4−10^6 Hz because the effect of grain boundary and electrodes are dominant for the collected conductivities at lower frequencies (Bauerle, 1969; Karato, 2013; Roberts and Tyburczy, 1991; Yoshino, 2010).

Figure 8-6 shows an Arrhenius plot of the measured electrical conductivity. At 288−723 K, the logarithm of the electrical conductivity increased linearly with decreasing reciprocal temperature. The calculated conductivity was about 6×10^{-3} S/m at room temperature, which was more than one order of magnitude higher than that of

$Mg_{0.9}Fe_{0.1}SiO_3$ (Ohta et al., 2010b) and $Mg_{0.83}Fe_{0.21}Al_{0.06}Si_{0.91}O_3$ (Sinmyo et al., 2014) bridgmanite at identical pressure. The conductivity increased to 7×10^{-2} S/m by increasing temperature to 723 K. At higher temperature, the reciprocal temperature dependence of the logarithm of the electrical conductivity showed a steeper slope (Fig. 8-6). The calculated conductivity was enhanced to ~1×10^{0} S/m at 923 K.

The electrical conductivity σ of a semiconductor can be expressed by the Arrhenian formula:

$$\sigma = \sigma_0 \exp\left(-\frac{\Delta H}{kT}\right), \qquad (8\text{-}4)$$

where σ_0 is the pre-exponential factor, ΔH is the activation enthalpy, k is the Boltzmann constant, and T is the temperature. We analyzed the ΔH by fitting different temperature segments to Eq. (8-4), of which estimated values are listed in Table 8-2. The obtained ΔH at 733 to 923 K was 0.8 eV, which is consistent with that of the previous results of Fe- and (Fe,Al)-bearing bridgmanite with the dominant charge transportation mechanisms of small polaron conduction (Katsura et al., 1998; Ohta et al., 2008; Sinmyo et al., 2014; Xu et al., 1998a). We could not observe a significantly higher ΔH reported on $(Mg_{0.9}Fe_{0.1})SiO_3$ Pv at *P*-*T* conditions of >100 GPa and 2500 K attributed to the ionic conduction (Ohta et al., 2008), which should be due to the limited temperature achieved in the present EHDAC study. In contrast, the derived ΔH at 288 to 723 K showed a significantly lower value of 0.1 eV. Such a low ΔH has reported in Li and Jeanloz (1990) for $Mg_{0.88}Fe_{0.12}SiO_3$ bridgmanite, but this was probably due to the difficulties in controlling the temperature in a laser-heated DAC below 1000 K. We attributed this extremely low ΔH to the proton conduction, which is thought to be a dominant conduction mechanism at low temperature (Yoshino, 2010).

Our results indicate that hydration of bridgmanite significantly enhances its pre-exponential factor for both proton and small polaron conductions. By assuming no change in the conduction mechanism at a higher temperature, we can calculate the electrical conductivity of ~500 ppm wt. water-bearing bridgmanite by extrapolating the present results at 30 GPa and 733−923 K to a higher temperature using Eq. (8-4) with the obtained pre-exponential factor and activation enthalpy. Note that neglecting the possible change in transport mechanism may underestimate the temperature extrapolated conductivity. The electrical conductivity of bridgmanite with ~500 ppm wt. water shows at least two orders of magnitude higher values than that of anhydrous bridgmanite up to T=2000 K ($10^4/T$=5) (Katsura et al., 1998; Sinmyo et al., 2014; Xu et al., 1998a; Yoshino et al., 2008b) (Fig. 8-6). The observed hydration effect on the high P,T electrical conductivity of bridgmanite is similar to that of the other major mantle minerals such as olivine, which conductivity differs by two to three orders of magnitude by changing the water content from 10 to 1000 ppm (Wang et al., 2006; Yoshino et al., 2008a), and that of wadsleyite and ringwoodite reported to increase by two orders of magnitude by increasing the water content from 100 to 10000 ppm (Huang et al., 2005; Xu et al., 1998b; Yoshino et al., 2008a).

The one-dimensional electrical conductivity depth profile of ~500 ppm wt. H_2O-bearing bridgmanite was calculated using a typical geotherm (Brown and Shankland, 1981) (Fig. 8-7). It is important to emphasize that neglecting the positive pressure dependence and the possible change in transport mechanism underestimates the calculated conductivity. Bridgmanite with ~500 ppm wt. H_2O shows around two orders of magnitude higher electrical conductivity than that inferred by electromagnetic observation in Olsen (1999) and Velímský (2010) throughout the lower mantle, which

of those are thought to be the global average conductivity profiles. The conductivity difference between the other observation, which may be expressing a regional enhanced conductivity profile (Ohta et al., 2010a) and our estimation for hydrous bridgmanite also differs around two orders of magnitude in the mid-lower mantle depth (<1700 km depth), which gets closer at further depth and corresponds at the lowermost mantle. The enhanced electrical conductivity of the deep lower mantle is often explained by the bridgmanite to post-perovskite transition (Ohta et al., 2008) and/or the presence of the subducted MORB (Ohta et al., 2010a), but regional water heterogeneity may also make a contribution.

The water concentration dependence of the pre-exponential factor of proton conduction shows a linear relation when following the Nernst-Einstein equation (Yoshino, 2010). Karato (2011) estimated the water concentration in the upper mantle and the mantle transition zones by adopting a conductivity model showing a linear dependence by increasing water content. To estimate the water content of lower mantle bridgmanite, we assumed a linear conductivity dependence with water content (Karato, 2011). Although previous electrical conductivity measurements on bridgmanite lacked labeling the water content of their sample, the amount of water in (Fe,Al)-bearing bridgmanite synthesized in a MA without adding water resources is generally below the detection limit in FTIR measurement (Bolfan-Casanova et al., 2000; Ohtani, 2015). The water concentration of bridgmanite used in previous laboratory measurements was assumed to be 0.5 ppm wt. H_2O, which is a typical detection limit of H_2O in FTIR measurement (Peslier et al., 2017). The calculated electrical conductivity with 0.5 ppm wt. H_2O at 30 GPa was fixed to the conductivity of pyrolite at equivalent pressure (Ohta et al., 2010a). As a result, the water concentration of lower mantle bridgmanite was

found to be 0.2 to 9.6 ppm wt. H_2O to explain the global average electromagnetic observations (Olsen, 1999; Velímský, 2010) (Fig. 8-8). Note that water content can be even lower since again this is an underestimation, so we conclude that the water concentration of lower mantle bridgmanite is less than 10 ppm wt. H_2O. This corresponds to 0.02 times the ocean mass, indicating a significantly dry lower mantle compared to the previous estimates of up to 4.3 times the ocean mass (Peslier et al., 2017).

Conductivity comparison between our results and that from the regional Occam inversion analysis in Ohta et al. (2010a) deeper than 1800 km indicates a possible strong conductivity heterogeneity produced by the regional water concentration variation. In the surrounding mantle, the total hydrogen content is constant with depth when mantle convection occurs without any large chemical fractionation, so such regional water concentration variation in the lower mantle could be mainly caused by subduction processes (Sobolev et al., 2019) which was also suggested by Ohta et al. (2010a). The enhanced conductivity profile in Ohta et al. (2010a) may also be explained by the effect of pressure, the change of conduction mechanism to ionic conduction (Xu and McCammon, 2002). Further conductivity measurements at a higher temperature of ~2500 K is required to fully explain the regional conductivity profile differences (Ohta et al., 2010a; Olsen, 1999; Velímský, 2010).

8.4. Implications

8.4.1. Water abundance in the Earth's silicate mantle

We gave a constraint on the water concentration in the lower mantle of no more than ~10 ppm wt. H_2O. With the reported average water content in the upper mantle and transition zone, we can calculate the total water content contained in the silicate Earth. Table 8-3 summarizes the water concentrations in the Earth's mantle estimated based on the geophysical approach. The amount of water in the lower mantle is significantly depleted than those in the other silicate layers, and the total water corresponds to 1.3－1.9 times the ocean mass.

The isotopic similarity between the bulk silicate Earth and the enstatite meteorites suggests that a large fraction of the Earth's building blocks consist of enstatite chondrites (EC) (Dauphas, 2017; Javoy et al., 2010; Warren, 2011). To explain the excess of the highly siderophile elements, i.e., the rare earth elements (REE), the additional ~1−4% primitive meteorite has been thought to be brought after the core formation, which is called the "late-veneer" hypothesis (Albarède, 2009; Chou, 1978; Fischer-Gödde et al., 2020; Wang and Becker, 2013). Carbonaceous chondrite (CC) is the strong candidate for the late-veneer meteoritic material (Fischer-Gödde et al., 2020), having an extensive water content of ~10 wt.% H_2O (King et al., 2015), which corresponds to ~4.5 times the ocean mass (Table 8-3). ECs has thought to be volatile-poor than the other chondrites (Robert et al., 1987), but the latest study has shown that those are moderately hydrous by comparing meteorites with different thermal metamorphism degrees (Piani et al., 2020). From the reported water contents in the EC (Piani et al., 2020; Robert et al., 1987), CC (Robert et al., 1987), and ordinary chondrites (OC) (Alexander et al., 2012), we calculated the potential water abundance

provided to the early Earth with three different suggested chondritic models (Dauphas, 2017; Javoy et al., 2010; Warren, 2011) (Table 8-3). Even with the extreme case using conventional volatile-poor water content in EC of <500 wt. ppm H_2O (Robert et al., 1987) and with 100% EC accretion model (Javoy et al., 2010) brings explainable water in the mantle and the hydrosphere. The relatively hydrous EC (Piani et al., 2020) enhances to ~24 times the ocean mass delivery without the contribution of CC, and at most ~166 times the ocean mass with the model suggested in Warren (2011). This indicates that the chondrite accretion models would not contradict the bulk-silicate water content. It is important to note that the calculated water contents by chondritic models are upper limits since volatiles can escape via the degassing processes during the Earth's accretion (Hamano et al., 2013). Still, most of the calculated models involve a significant amount of water exceeding the estimated bulk mantle water content, which implies an extensive amount of hydrogen in the core (Sakamaki et al., 2016; Umemoto and Hirose, 2015) and necessitates an explanation why only the lower mantle is devoid of water compared to other layers.

8.4.2. The origin of the dry lower mantle

The estimated water concentration of bridgmanite with less than 10 ppm H_2O is significantly small when taking into account that ringwoodite in the lower mantle contains 3000−6000 ppm H_2O (Karato, 2013) and the partition coefficient of H_2O between ringwoodite and bridgmanite is about 15:1 (Inoue et al., 2010), and was also much less than the reported water solubility of (Fe,Al)-bearing bridgmanite (Litasov et al., 2003; Murakami et al., 2002). Comparison of seismic tomography and EM studies

show evidence of the fluid between the mantle transition zone (Fukao et al., 2004). This is suggested to be formed by the dehydration of wadsleyite and ringwoodite due to olivine transition (Bercovici and Karato, 2003) and decomposition to bridgmanite and ferropericlase (Schmandt et al., 2014), respectively, which of those having much lower water solubilities than mantle transition zone minerals. This transition water filter model (Bercovici and Karato, 2003) with continuous whole mantle convection indicates that the water in the mantle would be concentrated to the transition zone, which may explain the dry lower mantle to some extent. However, it is not sufficient when considering the recently preferred large primordial bridgmanite domain-preserving scenario against the efficient whole mantle convection mixing (Ballmer et al., 2017; Gülcher et al., 2020) (see *Chapter 4*).

After the metal-silicate fractionation and the core formation, ~1 wt.% metallic iron is suggested to form in the lower mantle due to the disproportionation of ferrous iron by bridgmanite formation (Frost et al., 2004). This iron is considered to be trapped in grain boundaries in lower mantle minerals forming isolated pockets, hence the contribution to the lower mantle electrical conductivity is thought to be minimal (Frost et al., 2004). This metallic iron may perform as a water absorber; hydrogen is thought to be highly siderophile at high-*P,T* conditions (Hirose et al., 2019; Okuchi, 1997), note that there is a study claimed that it is rather lithophile, but it must be due to the hydrogen escape before the analysis due to the recovering of the sample at ambient pressure (Clesi et al., 2018). For instance, it has recently been found that H_2O strongly prefers metallic iron over olivine, wadsleyite, and ringwoodite (Shibazaki et al., 2009; Zhu et al., 2019). Although there is no experimental report that quantified the H_2O partitioning between metallic iron and bridgmanite, it is likely that a large number of

hydrogen partitions from bridgmanite to a co-existing metallic iron in the lower mantle (Zhu et al., 2019). The amount of metallic iron formed in the other layers are thought to be much less than in the lower mantle, which is at most ~0.1 wt.% in the upper mantle (Rohrbach et al., 2007), so this model can explain the dry (<10 ppm wt. H_2O) lower mantle bridgmanite and the wet mantle transition zones simultaneously.

Bridgmanite crystallized from the magma ocean may contain up to 4000 ppm wt. H_2O (Murakami et al., 2002). Here, if most hydrogen partitions to the co-existing 1 wt.% metallic iron, ~1600 ppm wt. H_2O in bridgmanite would sufficiently form an iron hydride with 50 atm.% hydrogen (FeH). Stoichiometric face-center cubic (fcc) FeH is reported to have a significantly low melting temperature of 2380 K at the core-mantle boundary (CMB) *P-T* conditions (Hirose et al., 2019). If the initial bridgmanite contains >1600 ppm H_2O, the subsequently formed co-existing metallic iron hydride can be fully molten at the early-stage hot solid lower mantle. Percolation of the iron melt is feasible to occur at lower mantle pressures (Shannon and Agee, 1998; Shi et al., 2013), hence metallic iron formed after the core formation may have additionally fallen to the core. This involves an extensive amount of REE in the lower mantle extracting to the core, so a late veneer accretion model may be necessary to explain the geochemical abundance of the siderophile trace elements (Kimura et al., 1974; O'Neill, 1991). On the other hand, if bridgmanite crystallized from the magma ocean does not contain sufficient water for co-existing metallic iron to form an fcc FeH, those can be present in the lower mantle due to the relatively higher melting temperature of $FeH_{x\leq1}$ of ~3000 K at CMB conditions (Tagawa, 2019). In this case, water brought down to the lower mantle by plate subduction can be stored in this metallic iron. Since around 50 times ocean mass can be stored to form a stoichiometric FeH, the water from the hydrosphere may be

continuously be stored in the lower mantle up to the present. Moreover, since the reaction between iron and water is thought to oxidize the surrounding mantle (Okuchi, 1997), the presence of metallic iron and the plate circulation may have contributed to secular oxidation of the Earth's mantle (Nicklas et al., 2019). Either which model takes place should strongly be dependent on the water distribution coefficient between bridgmanite and metallic iron, the water solubility of bridgmanite, and water concentration in the deep ancient magma ocean, so detailed investigation on these topics should be focused in the future study.

8.5. References

Akahama, Y., Kawamura, H., 2004. High-pressure Raman spectroscopy of diamond anvils to 250 GPa: Method for pressure determination in the multimegabar pressure range. J. Appl. Phys. 96, 3748−3751. https://doi.org/10.1063/1.1778482

Albarède, F., 2009. Volatile accretion history of the terrestrial planets and dynamic implications. Nature 461, 1227−1233. https://doi.org/10.1038/nature08477

Alexander, C.M.O.D., Bowden, R., Fogel, M.L., Howard, K.T., Herd, C.D.K., Nittler, L.R., 2012. The provenances of asteroids, and their contributions to the volatile inventories of the terrestrial planets. Science 337, 721−723. https://doi.org/10.1126/science.1223474

Ballmer, M.D., Houser, C., Hernlund, J.W., Wentzcovitch, R.M., Hirose, K., 2017. Persistence of strong silica-enriched domains in the Earth's lower mantle. Nat. Geosci. 10, 236−240. https://doi.org/10.1038/ngeo2898

Bauerle, J.E., 1969. Study of solid electrolyte polarization by a complex admittance method. Solid State Commun. 7, ii. https://doi.org/10.1016/0038-1098(69)90484-0

Bell, D.R., Rossman, G.R., 1992. Water in Earth's Mantle: The Role of Nominally Anhydrous Minerals. Science 255, 1391−1397. https://doi.org/10.1126/science.255.5050.1391

Bell, D.R., Rossman, G.R., Maldener, J., Endisch, D., Rauch, F., 2003. Hydroxide in olivine: A quantitative determination of the absolute amount and calibration of the IR spectrum. J. Geophys. Res. Solid Earth 108, 1−9. https://doi.org/10.1029/2001jb000679

Bercovici, D., Karato, S.I., 2003. Whole-mantle convection and the transition-zone water filter. Nature 425, 39−44. https://doi.org/10.1038/nature01918

Bolfan-Casanova, N., Keppler, H., Rubie, D.C., 2000. Water partitioning between nominally anhydrous minerals in the $MgO-SiO_2-H_2O$ system up to 24 GPa: implications for the distribution of water in the Earth's mantle. Earth Planet. Sci. Lett. 182, 209−221. https://doi.org/10.1016/S0012-821X(00)00244-2

Brown, J.M., Shankland, T.J., 1981. Thermodynamic parameters in the Earth as determined from seismic profiles. Geophys. J. R. Astron. Soc. 66, 579−596. https://doi.org/10.1111/j.1365-246X.1981.tb04891.x

Chang, Y.Y., Hsieh, W.P., Tan, E., Chen, J., 2017. Hydration-reduced lattice thermal conductivity of olivine in Earth's upper mantle. Proc. Natl. Acad. Sci. U. S. A. 114, 4078−4081. https://doi.org/10.1073/pnas.1616216114

Chen, J., Inoue, T., Weidner, D.J., Wu, Y., Vaughan, M.T., 1998. Strength and water weakening of mantle minerals, olivine, wadsleyite and ringwoodite. Geophys. Res. Lett. 25, 575−578. https://doi.org/10.1029/98GL00043

Chou, C.L., 1978. Fractionation of siderophile elements in the Earth's upper mantle. Proc. Lunar Planet. Sci. Conf. 9, 219−230.

Clesi, V., Bouhifd, M.A., Bolfan-Casanova, N., Manthilake, G., Schiavi, F., Raepsaet, C., Bureau, H., Khodja, H., Andrault, D., 2018. Low hydrogen contents in the cores of terrestrial planets. Sci. Adv. 4, 4−10. https://doi.org/10.1126/sciadv.1701876

Dai, L., Karato, S. ichiro, 2009a. Electrical conductivity of pyrope-rich garnet at high temperature and high pressure. Phys. Earth Planet. Inter. 176, 83−88. https://doi.org/10.1016/j.pepi.2009.04.002

Dai, L., Karato, S. ichiro, 2009b. Electrical conductivity of orthopyroxene: Implications for the water content of the asthenosphere. Proc. Japan Acad. Ser. B Phys. Biol. Sci. 85, 466−475. https://doi.org/10.2183/pjab.85.466

Dauphas, N., 2017. The isotopic nature of the Earth's accreting material through time. Nature 541, 521−524. https://doi.org/10.1038/nature20830

Dobson, D., 2003. Oxygen ionic conduction in $MgSiO_3$ perovskite. Phys. Earth Planet. Inter. 139, 55−64. https://doi.org/10.1016/S0031-9201(03)00144-4

Duffy, T.S., Ahrens, T.J., Lange, M.A., 1991. The shock wave equation of state of brucite $Mg(OH)_2$. J. Geophys. Res. 96, 319−330. https://doi.org/10.1029/91jb00987

Fiquet, G., 2018. Melting in the earth's deep interior, Magmas Under Pressure: Advances in High-Pressure Experiments on Structure and Properties of Melts. Elsevier Inc. https://doi.org/10.1016/B978-0-12-811301-1.00004-6

Fischer-Gödde, M., Elfers, B.M., Münker, C., Szilas, K., Maier, W.D., Messling, N., Morishita, T., Van Kranendonk, M., Smithies, H., 2020. Ruthenium isotope vestige of Earth's pre-late-veneer mantle preserved in Archaean rocks. Nature 579, 240−244. https://doi.org/10.1038/s41586-020-2069-3

Frost, D.J., Liebske, C., Langenhorst, F., McCammon, C.A., Trønnes, R.G., Rubie, D.C., 2004. Experimental evidence for the existence of iron-rich metal in the Earth's lower mantle. Nature 428, 409−412. https://doi.org/10.1038/nature02413

Fuji-Ta, K., Katsura, T., Matsuzaki, T., Ichiki, M., 2007. Electrical conductivity measurements of brucite under crustal pressure and temperature conditions. Earth, Planets Sp. 59, 645−648. https://doi.org/10.1186/BF03352725

Fukao, Y., Koyama, T., Obayashi, M., Utada, H., 2004. Trans-Pacific temperature field in the mantle transition region derived from seismic and electromagnetic tomography. Earth Planet. Sci. Lett. 217, 425−434. https://doi.org/10.1016/S0012-821X(03)00610-1

Funamori, N., Sato, T., 2008. A cubic boron nitride gasket for diamond-anvil experiments. Rev. Sci. Instrum. 79, 053903. https://doi.org/10.1063/1.2917409

Ghosh, S., Ohtani, E., Litasov, K.D., Suzuki, A., Dobson, D., Funakoshi, K., 2013. Effect of water in depleted mantle on post-spinel transition and implication for 660km seismic discontinuity. Earth Planet. Sci. Lett. 371−372, 103−111. https://doi.org/10.1016/j.epsl.2013.04.011

Gülcher, A.J.P., Gebhardt, D.J., Ballmer, M.D., Tackley, P.J., 2020. Variable dynamic styles of primordial heterogeneity preservation in the Earth's lower mantle. Earth Planet. Sci. Lett. 536, 116160. https://doi.org/10.1016/j.epsl.2020.116160

Hamano, K., Abe, Y., Genda, H., 2013. Emergence of two types of terrestrial planet on solidification of magma ocean. Nature 497, 607−610. https://doi.org/10.1038/nature12163

Hirose, K., 2002. Phase transitions in pyrolitic mantle around 670-km depth: Implications for upwelling of plumes from the lower mantle. J. Geophys. Res. Solid Earth 107, ECV 3-1-ECV 3-13. https://doi.org/10.1029/2001jb000597

Hirose, K., Tagawa, S., Kuwayama, Y., Sinmyo, R., Morard, G., Ohishi, Y., Genda, H., 2019. Hydrogen Limits Carbon in Liquid Iron. Geophys. Res. Lett. 46, 5190−5197. https://doi.org/10.1029/2019GL082591

Huang, X., Xu, Y., Karato, S., 2005. Water content in the transition zone from electrical conductivity of wadsleyite and ringwoodite. Nature 434, 746−749. https://doi.org/10.1038/nature03457.1.

Inoue, H., Suehiro, S., Ohta, K., Hirose, K., Ohishi, Y., 2020. Resistivity saturation of hcp Fe-Si alloys in an internally heated diamond anvil cell: A key to assessing the Earth's core conductivity. Earth Planet. Sci. Lett. 543, 116357. https://doi.org/10.1016/j.epsl.2020.116357

Inoue, T., Wada, T., Sasaki, R., Yurimoto, H., 2010. Water partitioning in the Earth's mantle. Phys. Earth Planet. Inter. 183, 245−251. https://doi.org/10.1016/j.pepi.2010.08.003

Javoy, M., Kaminski, E., Guyot, F., Andrault, D., Sanloup, C., Moreira, M., Labrosse, S., Jambon, A., Agrinier, P., Davaille, A., Jaupart, C., 2010. The chemical composition of the Earth: Enstatite chondrite models. Earth Planet. Sci. Lett. 293, 259−268. https://doi.org/10.1016/j.epsl.2010.02.033

Karato, S., 1990. The role of hydrogen in the electrical conductivity of the upper mantle. Nature 347, 272−273. https://doi.org/10.1038/347272a0

Karato, S., 2013. Physics and Chemistry of the Deep Earth. Phys. Chem. Deep Earth. https://doi.org/10.1002/9781118529492

Karato, S., 2011. Water distribution across the mantle transition zone and its implications for global material circulation. Earth Planet. Sci. Lett. 301, 413−423. https://doi.org/10.1016/j.epsl.2010.11.038

Katsura, T., Sato, K., Ito, E., 1998. Electrical conductivity of silicate perovskite at lower-mantle conditions. Nature 395, 493−495. https://doi.org/10.1038/26736

Khan, A., Shankland, T.J., 2012. A geophysical perspective on mantle water content and melting: Inverting electromagnetic sounding data using laboratory-based electrical conductivity profiles. Earth Planet. Sci. Lett. 317−318, 27−43. https://doi.org/10.1016/j.epsl.2011.11.031

Kimura, K., Lewis, R.S., Anders, E., 1974. Distribution of gold and rhenium between nickel-iron and silicate melts: implications for the abundance of siderophile elements on the Earth and Moon. Geochim. Cosmochim. Acta 38, 683−701. https://doi.org/10.1016/0016-7037(74)90144-6

King, A.J., Solomon, J.R., Schofield, P.F., Russell, S.S., 2015. Characterising the CI and CI-like carbonaceous chondrites using thermogravimetric analysis and infrared spectroscopy Planetary science. Earth, Planets Sp. 67. https://doi.org/10.1186/s40623-015-0370-4

Li, X., Jeanloz, R., 1990. Laboratory studies of the electrical conductivity of silicate perovskites at high pressures and temperatures. J. Geophys. Res. 95, 5067−5078. https://doi.org/10.1029/jb095ib04p05067

Libowitzky, E., Rossman, G.R., 1996. Principles of quantitative absorbance measurements in anisotropic crystals. Phys. Chem. Miner. 23, 319−327. https://doi.org/10.1007/BF00199497

Litasov, K., Ohtani, E., Langenhorst, F., Yurimoto, H., Kubo, T., Kondo, T., 2003. Water solubility in Mg-perovskites and water storage capacity in the lower mantle. Earth Planet. Sci. Lett. 211, 189−203. https://doi.org/10.1016/S0012-821X(03)00200-0

Liu, J., Dorfman, S.M., Zhu, F., Li, J., Wang, Y., Zhang, D., Xiao, Y., Bi, W., Ercan Alp, E., 2018. Valence and spin states of iron are invisible in Earth's lower mantle. Nat. Commun. 9. https://doi.org/10.1038/s41467-018-03671-5

Morbidelli, A., Chambers, J., Lunine, J.I., Petit, J.M., Robert, F., Valsecchi, G.B., Cyr, K.E., 2000. Source regions and timescales for the delivery of water to the Earth. Meteorit. Planet. Sci. 35, 1309−1320. https://doi.org/10.1111/j.1945-5100.2000.tb01518.x

Murakami, M., Hirose, K., Yurimoto, H., Nakashima, S., Takafuji, N., 2002. Water in Earth' s Lower Mantle. Science 295, 1885−1888.

Nestola, F., Smyth, J.R., 2015. Diamonds and water in the deep Earth: a new scenario. Int. Geol. Rev. 58, 263−276. https://doi.org/10.1080/00206814.2015.1056758

Nicklas, R.W., Puchtel, I.S., Ash, R.D., Piccoli, P.M., Hanski, E., Nisbet, E.G., Waterton, P., Pearson, D.G., Anbar, A.D., 2019. Secular mantle oxidation across

the Archean-Proterozoic boundary: Evidence from V partitioning in komatiites and picrites. Geochim. Cosmochim. Acta 250, 49−75. https://doi.org/10.1016/j.gca.2019.01.037

Nomura, R., Hirose, K., Uesugi, K., Ohishi, Y., Tsuchiyama, A., Miyake, A., Ueno, Y., 2014. Low Core-Mantle Boundary Temperature Inferred from the Solidus of Pyrolite. Science 343, 522−525. https://doi.org/10.1126/science.1248186

O'Neill, H.S.C., 1991. The origin of the moon and the early history of the earth-A chemical model. Part 1: The moon. Geochim. Cosmochim. Acta 55, 1135−1157. https://doi.org/10.1016/0016-7037(91)90168-5

Ohta, K., Hirose, K., Ichiki, M., Shimizu, K., Sata, N., Ohishi, Y., 2010a. Electrical conductivities of pyrolitic mantle and MORB materials up to the lowermost mantle conditions. Earth Planet. Sci. Lett. 289, 497−502. https://doi.org/10.1016/j.epsl.2009.11.042

Ohta, K., Hirose, K., Shimizu, K., Sata, N., Ohishi, Y., 2010b. The electrical resistance measurements of $(Mg,Fe)SiO_3$ perovskite at high pressures and implications for electronic spin transition of iron. Phys. Earth Planet. Inter. 180, 154−158. https://doi.org/10.1016/j.pepi.2009.11.002

Ohta, K., Onoda, S., Hirose, K., Sinmyo, R., Shimizu, K., Sata, N., Ohishi, Y., Yasuhara, A., 2008. The Electrical Conductivity of Post-Perovskite in Earth's D'' Layer. Science 320, 89−91. https://doi.org/10.1126/science.1155148

Ohtani, E., 2015. Hydrous minerals and the storage of water in the deep mantle. Chem. Geol. 418, 6−15. https://doi.org/10.1016/j.chemgeo.2015.05.005

Okuchi, T., 1997. Hydrogen partitioning into molten iron at high pressure: Implications for earth's core. Science 278, 1781−1784. https://doi.org/10.1126/science.278.5344.1781

Okuchi, T., Purevjav, N., Tomioka, N., Lin, J.-F., Kuribayashi, T., Schoneveld, L., Hwang, H., Sakamoto, N., Kawasaki, N., Yurimoto, H., 2015. Synthesis of large and homogeneous single crystals of water-bearing minerals by slow cooling at deep-mantle pressures. Am. Mineral. 100, 1483−1492. https://doi.org/10.2138/am-2015-5237

Olsen, N., 1999. Induction studies with satellite data. Surv. Geophys. 20, 309−340. https://doi.org/10.1023/a:1006611303582

Paterson, M.S., 1982. The determination of hydroxyl by infrared absorption in quartz, silicate glasses and similar materials. Bull. Minéralogie 105, 20−29. https://doi.org/10.3406/bulmi.1982.7582

Pearson, D.G., Brenker, F.E., Nestola, F., McNeill, J., Nasdala, L., Hutchison, M.T., Matveev, S., Mather, K., Silversmit, G., Schmitz, S., Vekemans, B., Vincze, L., 2014. Hydrous mantle transition zone indicated by ringwoodite included within diamond. Nature 507, 221−224. https://doi.org/10.1038/nature13080

Peslier, A.H., Schönbächler, M., Busemann, H., Karato, S.I., 2017. Water in the Earth's Interior: Distribution and Origin. Space Sci. Rev. 212, 1−68. https://doi.org/10.1007/s11214-017-0387-z

Peyronneau, J., Poirier, J.P., 1989. Electrical conductivity of the Earth's lower mantle. Nature 342, 537−539. https://doi.org/10.1038/342537a0

Piani, L., Marrocchi, Y., Rigaudier, T., Vacher, L.G., Thomassin, D., Marty, B., 2020. Earth's water may have been inherited from material similar to enstatite chondrite meteorites. Science 369, 1110−1113. https://doi.org/10.1126/science.aba1948

Potapkin, V., McCammon, C., Glazyrin, K., Kantor, A., Kupenko, I., Prescher, C., Sinmyo, R., Smirnov, G. V., Chumakov, A.I., Rüffer, R., Dubrovinsky, L., 2013. Effect of iron oxidation state on the electrical conductivity of the Earth's lower mantle. Nat. Commun. 4, 4−9. https://doi.org/10.1038/ncomms2436

Raymond, S.N., Quinn, T., Lunine, J.I., 2004. Making other earths: Dynamical simulations of terrestrial planet formation and water delivery. Icarus 168, 1−17. https://doi.org/10.1016/j.icarus.2003.11.019

Robert, F., Javoy, M., Halbout, J., Dimon, B., Merlivat, L., 1987. Hydrogen isotope abundances in the solar system. Part II: Meteorites with terrestrial-like ratio. Geochim. Cosmochim. Acta 51, 1807−1822. https://doi.org/10.1016/0016-7037(87)90171-2

Roberts, J.J., Tyburczy, J.A., 1991. Frequency dependent electrical properties of polycrystalline olivine compacts. J. Geophys. Res. 96. https://doi.org/10.1029/91jb01574

Rohrbach, A., Ballhaus, C., Golla-Schindler, U., Ulmer, P., Kamenetsky, V.S., Kuzmin, D. V., 2007. Metal saturation in the upper mantle. Nature 449, 456−458. https://doi.org/10.1038/nature06183

Sakamaki, T., Ohtani, E., Fukui, H., Kamada, S., Takahashi, S., Sakairi, T., Takahata, A., Sakai, T., Tsutsui, S., Ishikawa, D., Shiraishi, R., Seto, Y., Tsuchiya, T., Baron, A.Q.R., 2016. Constraints on Earth's inner core composition inferred from measurements of the sound velocity of hcp-iron in extreme conditions. Sci. Adv. 2, e1500802. https://doi.org/10.1126/sciadv.1500802

Schmandt, B., Jacobsen, S.D., Becker, T.W., Liu, Z., Dueker, K.G., 2014. Dehydration melting at the top of the lower mantle. Science 344, 1265−1268. https://doi.org/10.1126/science.1253358

Shankland, T.J., Peyronneau, J., Poirier, J.P., 1993. Electrical conductivity of the Earth's lower mantle. Nature 366, 453−455. https://doi.org/10.1038/366453a0

Shannon, M.C., Agee, C.B., 1998. Percolation of core melts at lower mantle conditions. Science 280, 1059−1061. https://doi.org/10.1126/science.280.5366.1059

Shi, C.Y., Zhang, L., Yang, W., Liu, Y., Wang, J., Meng, Y., Andrews, J.C., Mao, W.L., 2013. Formation of an interconnected network of iron melt at Earth's lower mantle conditions. Nat. Geosci. 6, 971−975. https://doi.org/10.1038/ngeo1956

Shibazaki, Y., Ohtani, E., Terasaki, H., Suzuki, A., Funakoshi, K. ichi, 2009. Hydrogen partitioning between iron and ringwoodite: Implications for water transport into the Martian core. Earth Planet. Sci. Lett. 287, 463−470. https://doi.org/10.1016/j.epsl.2009.08.034

Sinmyo, R., Pesce, G., Greenberg, E., McCammon, C., Dubrovinsky, L., 2014. Lower mantle electrical conductivity based on measurements of Al, Fe-bearing perovskite under lower mantle conditions. Earth Planet. Sci. Lett. 393, 165−172. https://doi.org/10.1016/j.epsl.2014.02.049

Sobolev, A. V., Asafov, E. V., Gurenko, A.A., Arndt, N.T., Batanova, V.G., Portnyagin, M. V., Garbe-Schönberg, D., Wilson, A.H., Byerly, G.R., 2019. Deep hydrous

mantle reservoir provides evidence for crustal recycling before 3.3 billion years ago. Nature 571, 555−559. https://doi.org/10.1038/s41586-019-1399-5

Suehiro, S., Wakamatsu, T., Ohta, K., Hirose, K., Ohishi, Y., 2019. High-temperature electrical resistivity measurements of hcp iron to Mbar pressure in an internally resistive heated diamond anvil cell. High Press. Res. 39, 579−587. https://doi.org/10.1080/08957959.2019.1692008

Sun, N., Wei, W., Han, S., Song, J., Li, X., Duan, Y., Prakapenka, V.B., Mao, Z., 2018. Phase transition and thermal equations of state of (Fe,Al)-bridgmanite and post-perovskite: Implication for the chemical heterogeneity at the lowermost mantle. Earth Planet. Sci. Lett. 490, 161−169. https://doi.org/10.1016/j.epsl.2018.03.004

Tagawa, S., 2019. Hydrogen in the core. Doctoral thesis.

Umemoto, K., Hirose, K., 2015. Liquid iron-hydrogen alloys at outer core conditions by first-principles calculations. Geophys. Res. Lett. 42, 7513−7520. https://doi.org/10.1002/2015GL065899

Velímský, J., 2010. Electrical conductivity in the lower mantle: Constraints from CHAMP satellite data by time-domain EM induction modelling. Phys. Earth Planet. Inter. 180, 111−117. https://doi.org/10.1016/j.pepi.2010.02.007

Wang, D., Mookherjee, M., Xu, Y., Karato, S., 2006. The effect of water on the electrical conductivity of olivine. Nature 443, 977−980. https://doi.org/10.1038/nature05256

Wang, Z., Becker, H., 2013. Ratios of S, Se and Te in the silicate Earth require a volatile-rich late veneer. Nature 499, 328−331. https://doi.org/10.1038/nature12285

Warren, P.H., 2011. Stable-isotopic anomalies and the accretionary assemblage of the Earth and Mars: A subordinate role for carbonaceous chondrites. Earth Planet. Sci. Lett. 311, 93−100. https://doi.org/10.1016/j.epsl.2011.08.047

Wirth, R., Vollmer, C., Brenker, F., Matsyuk, S., Kaminsky, F., 2007. Inclusions of nanocrystalline hydrous aluminium silicate “Phase Egg” in superdeep diamonds from Juina (Mato Grosso State, Brazil). Earth Planet. Sci. Lett. 259, 384−399. https://doi.org/10.1016/j.epsl.2007.04.041

Withers, A.C., 2013. On the use of unpolarized infrared spectroscopy for quantitative analysis of absorbing species in birefringent crystals. Am. Mineral. 98, 689−697. https://doi.org/10.2138/am.2013.4316

Xu, Y., McCammon, C., 2002. Evidence for ionic conductivity in lower mantle (Mg,Fe)(Si,Al)O_3 perovskite . J. Geophys. Res. Solid Earth 107, ECV 11-1-ECV 11-7. https://doi.org/10.1029/2001jb000677

Xu, Y., McCammon, C., Poe, B.T., 1998a. The effect of alumina on the electrical conductivity of silicate perovskite. Science 282, 922−924. https://doi.org/10.1126/science.282.5390.922

Xu, Y., Poe, B.T., Shankland, T.J., Rubie, D.C., 1998b. Electrical Conductivity of Olivine, Wadsleyite, and Ringwoodite Under Upper-Mantle Conditions. Science 280, 1415−1418. https://doi.org/10.1126/science.280.5368.1415

Yang, X., Keppler, H., McCammon, C., Ni, H., 2012. Electrical conductivity of orthopyroxene and plagioclase in the lower crust. Contrib. to Mineral. Petrol. 163, 33−48. https://doi.org/10.1007/s00410-011-0657-9

Yang, X., Keppler, H., McCammon, C., Ni, H., Xia, Q., Fan, Q., 2011. Effect of water on the electrical conductivity of lower crustal clinopyroxene. J. Geophys. Res. Solid Earth 116. https://doi.org/10.1029/2010JB008010

Yoshino, T., 2010. Laboratory Electrical Conductivity Measurement of Mantle Minerals. Surv. Geophys. 31, 163−206. https://doi.org/10.1007/s10712-009-9084-0

Yoshino, T., Kamada, S., Zhao, C., Ohtani, E., Hirao, N., 2016. Electrical conductivity model of Al-bearing bridgmanite with implications for the electrical structure of the Earth's lower mantle. Earth Planet. Sci. Lett. 434, 208−219. https://doi.org/10.1016/j.epsl.2015.11.032

Yoshino, T., Katsura, T., 2012. Re-evaluation of electrical conductivity of anhydrous and hydrous wadsleyite. Earth Planet. Sci. Lett. 337−338, 56−67. https://doi.org/10.1016/j.epsl.2012.05.023

Yoshino, T., Manthilake, G., Matsuzaki, T., Katsura, T., 2008a. Dry mantle transition zone inferred from the conductivity of wadsleyite and ringwoodite. Nature 451, 326−329. https://doi.org/10.1038/nature06427

Yoshino, T., Matsuzaki, T., Yamashita, S., Katsura, T., 2006. Hydrous olivine unable to account for conductivity anomaly at the top of the asthenosphere. Nature 443, 973−976. https://doi.org/10.1038/nature05223

Yoshino, T., Yamazaki, D., Ito, E., Katsura, T., 2008b. No interconnection of ferro-periclase in post-spinel phase inferred from conductivity measurement. Geophys. Res. Lett. 35, 1−5. https://doi.org/10.1029/2008GL035932

Zedgenizov, D., Kagi, H., Ohtani, E., Tsujimori, T., Komatsu, K., 2020. Retrograde phases of former bridgmanite inclusions in superdeep diamonds. Lithos 370−371, 105659. https://doi.org/10.1016/j.lithos.2020.105659

Zhan, Z., 2020. Mechanisms and Implications of Deep Earthquakes. Annu. Rev. Earth Planet. Sci. 48:147–74. https://doi.org/10.1146/annurev-earth-053018-060314

Zhu, F., Li, J., Liu, J., Dong, J., Liu, Z., 2019. Metallic iron limits silicate hydration in Earth's transition zone. Proc. Natl. Acad. Sci. U. S. A. 116, 22526−22530. https://doi.org/10.1073/pnas.1908716116

8.6. Tables and Figures

Table 8-1. Electrical conductivity of hydrous bridgmanite at high *P-T*.

Run	Pressure (GPa)	Temperature (K)	Resistance (kΩ)	Conductivity σ ($\times 10^3$ S/m)	Log(σ) (S/m)
05	30	288	6510	6.1(10)	-2.214
		290	4590	8.7(14)	-2.063
		311	4000	9.9(16)	-2.003
		409	1727	23.0(37)	-1.638
		504	962	41.3(66)	-1.384
		594	581	68.4(109)	-1.165
		618	487	81.5(129)	-1.089
		644	589	67.5(107)	-1.171
		699	539	73.7(117)	-1.132
		723	439	90.6(144)	-1.043
		733	561	70.9(113)	-1.149
		780	241	164.9(262)	-0.783
		782	257	154.7(246)	-0.810
		788	198	200.5(318)	-0.698
		791	201	197.4(313)	-0.705
		853	92	431.3(685)	-0.365
		883	65	611.5(971)	-0.214
		923	38	1040.6(1652)	0.017

Table 8-2. The obtained activation enthalpies and preexponential factors.

Sample	Run	Temperature range (K)	$\log(\sigma_0)$	ΔH (eV)
Hydrous bdg	05	288-723	-0.32(5)	0.10(1)
	05	733-923	4.38(14)	0.80(2)

Table 8-3. Water concentrations in the silicate Earth.

	Concentration ppm wt. H_2O	x Mass Oceans	Volume ratio (%)	Model
Crust[1]	-	0.3−0.4	1.2	-
Upper mantle[1]	200	0.1	18.2	-
Transition zone[1]	3140−5100	0.9−1.4	12.1	-
Lower mantle	<10	<0.02	68.5	-
Total silicate Earth	~600−800	1.3−1.9	100	-
Silicate Earth+Hydrosphere	-	2.3−2.9	-	-
1% late-veneer CI[2]	~100000	~4.5	-	a
100% EC[3]	<500	<2.4	-	b
100% EC[4]	~5000	~23.5	-	b
68%EC[3]+32%CC[3]	<32300	<151	-	c
68%EC[4]+32%CC[3]	~35400	~166	-	c
71%EC[3]+5%CC[3]+24%OC[5]	<7500	<35	-	d
71%EC[4]+5%CC[3]+24%OC[5]	~10700	~50	-	d

EC, enstatite chondrite; CC, carbonaceous chondrite; OC, ordinary chondrite.

[1,2,3,4,5]: Water content provided in Peslier et al. (2017), King et al. (2015), Robert et al. (1987), Piani et al. (2020), and Alexander et al. (2012), respectively.

[a,b,c,d]:Chondritic models suggested in King et al. (2015), Javoy et al. (2010), Warren (2011), and Dauphas (2017), respectively.

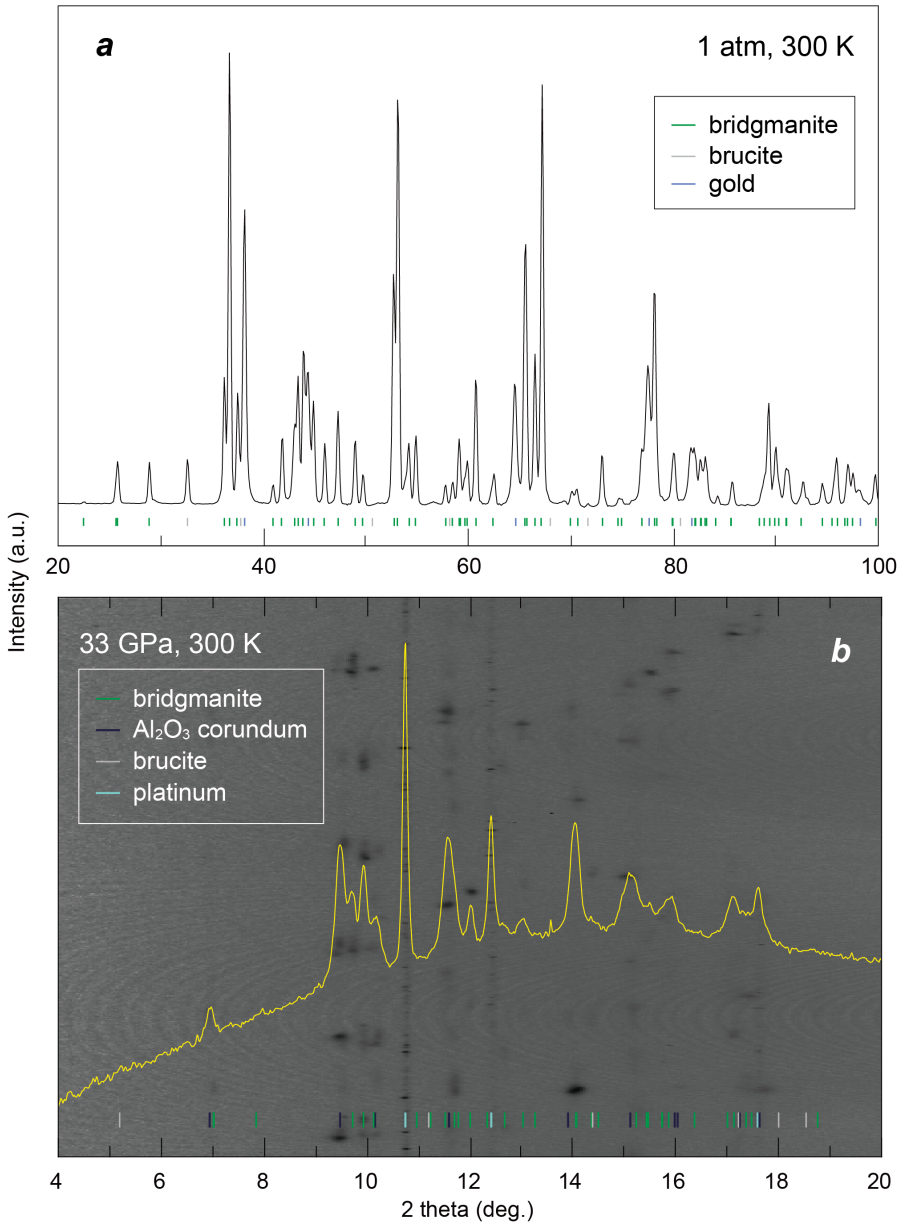

Fig. 8-1. XRD pattern of the bridgmanite sample OT2463 (a) at ambient and (b) at high pressure in a DAC. Green, gray, and blue lines in Fig. 8-1a show the peaks of bridgmanite, brucite, and gold, respectively. The XRD pattern shown in Fig. 8-1b was obtained in BL10XU, Spring-8. Note the spotty bridgmanite peaks indicating a single crystal sample, and the minimal amount of brucite peaks.

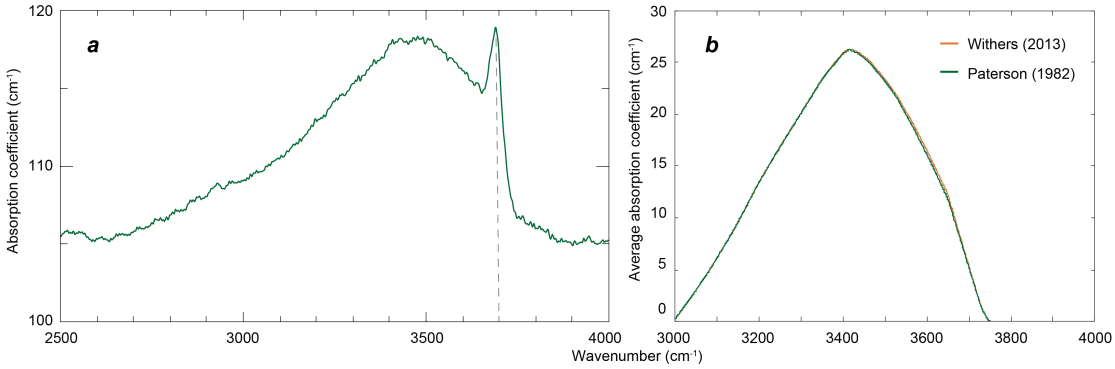

Fig. 8-2. (a) example of the obtained unpolarized FTIR spectrum of bridgmanite sample OT2463, and (b) total average absorption coefficient as a function of wavenumber after subtracting baseline and the peak from brucite. Gray broken line in Fig. 8-2a indicates the brucite peak at 3690 cm^{-1} (Bolfan-Casanova et al., 2000). Green and orange curves in Fig. 8-2b show the absorption coefficient calculated in the manner described in Paterson (1987) and Withers (2013), respectively.

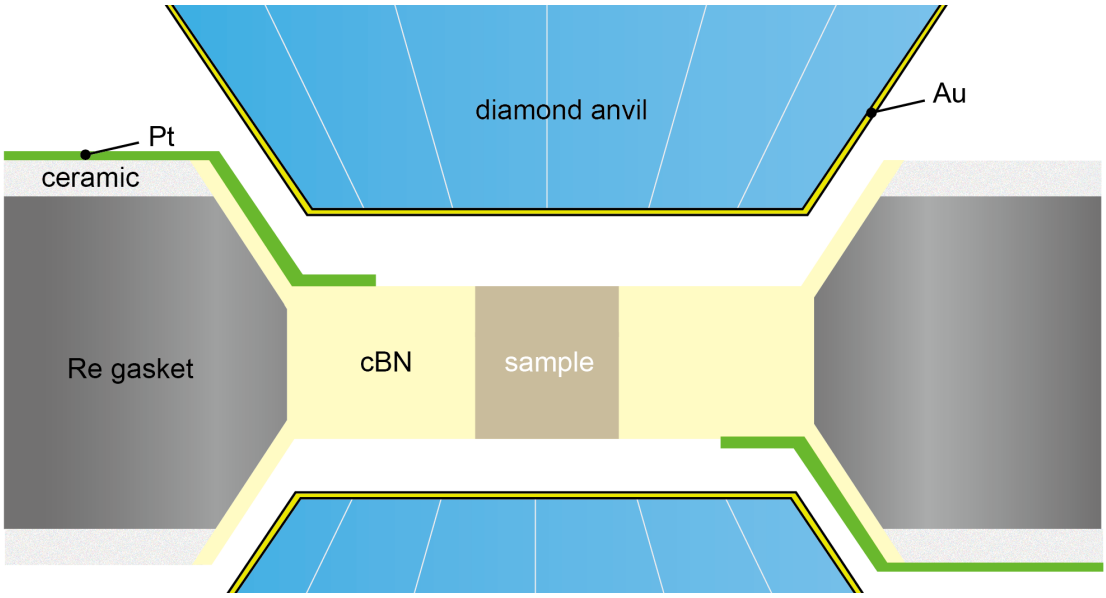

Fig. 8-3. Schematic DAC configuration for the electrical conductivity measurement.

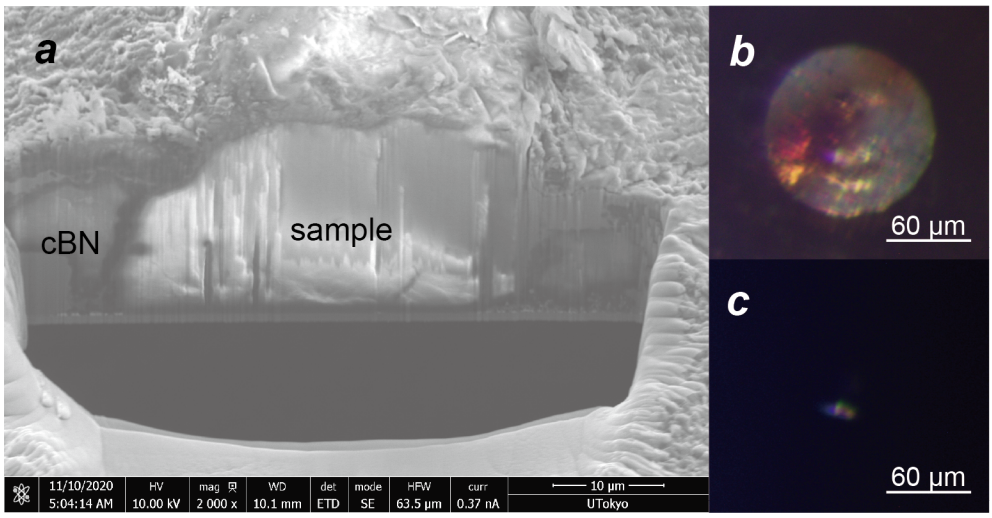

Fig. 8-4. (a) SEM image of the cross-section of the recovered sample, and (b)(c) photomicrographs of the recovered sample gasket with and without the top light, respectively. The bright portion in Fig. 8-4c is from the bottom light through the sample.

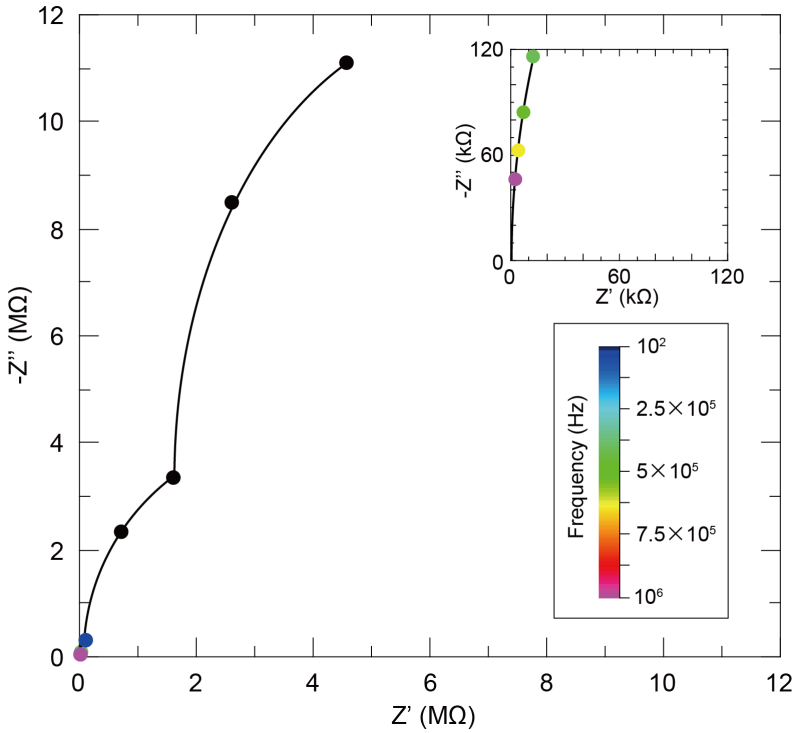

Fig. 8-5. Typical obtained impedance spectrum. The color scale indicates the frequency applied to the sample. Insert figure shows the impedance spectrum collected at relatively higher frequencies of $>10^5$ Hz.

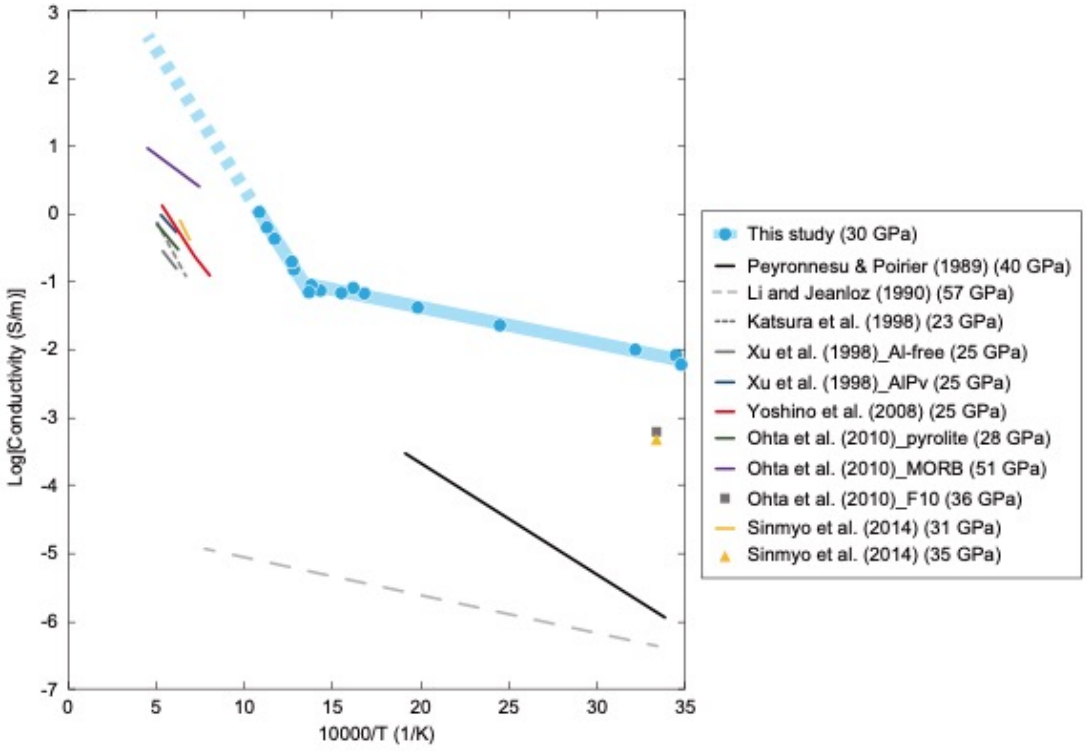

Fig. 8-6. The logarithm of the electrical conductivity of bridgmanite as a function of reciprocal temperature. Light blue circles and line indicate the $Mg_{0.88}Fe_{0.14}Al_{0.11}Si_{0.91}O_3$ bridgmanite with ~500 ppm wt. H_2O (this study), and light broken line shows its temperature extrapolation (i.e., reciprocal temperature interpolation). Light gray and gray broken lines, gray and black lines, and gray square indicate previous results for Al-free and Fe-bearing bridgmanite with composition of $(Mg_{0.88}Fe_{0.12})SiO_3$ (Li and Jeanloz, 1990), $(Mg_{0.93}Fe_{0.07})SiO_3$ (Katsura et al., 1998), $(Mg_{0.915}Fe_{0.085})SiO_3$ (Xu et al., 1998a), $(Mg_{0.92}Fe_{0.08})SiO_3$ (Peyronneau and Poirier, 1989), and $(Mg_{0.9}Fe_{0.1})SiO_3$ (Ohta et al., 2010b), respectively. Dark blue and yellow lines, and yellow triangle indicate previous results for (Fe,Al)-bearing bridgmanite containing Fe 8.8 atm.% and Al 2.5 wt.% (Xu et al., 1998a), and composition of $Mg_{0.83}Fe_{0.21}Al_{0.06}Si_{0.91}O_3$ (Sinmyo et al., 2014),

respectively. Green and purple lines indicate the reported electrical conductivity of pyrolite and MORB, respectively (Ohta et al., 2010a).

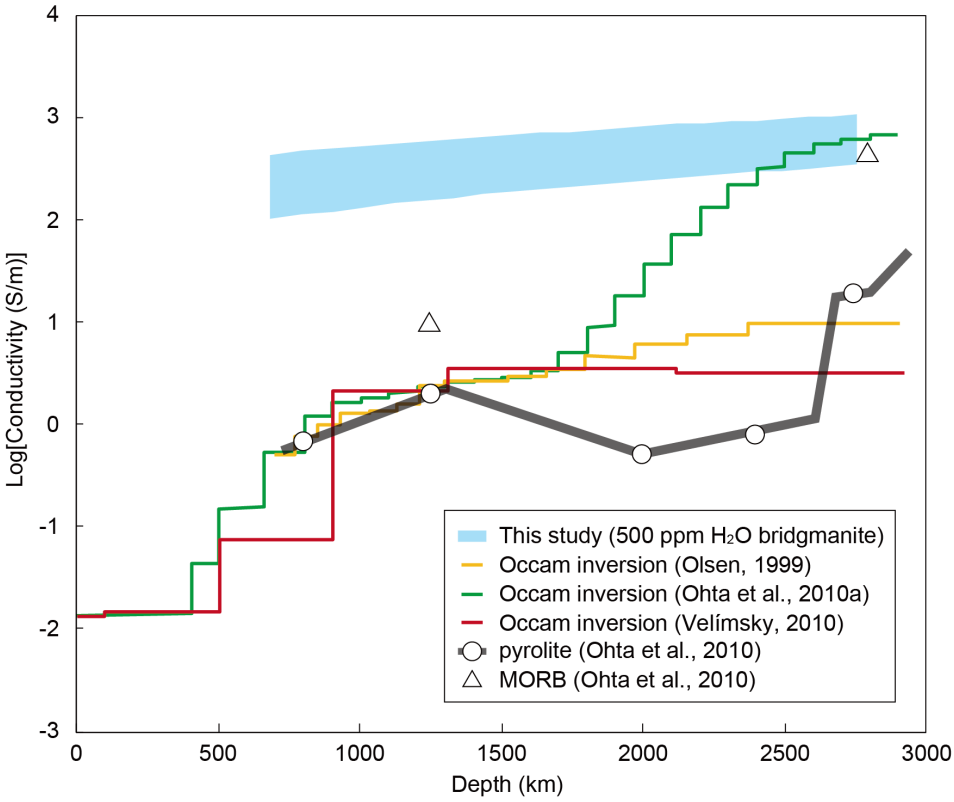

Fig. 8-7. One-dimensional depth profiles of the electrical conductivity of the lower mantle. Light blue band indicates the profile of ~500 ppm wt. H_2O-bearing bridgmanite from this study. Open circles and triangles indicate the laboratory measurements of pyrolite and MORB, respectively (Ohta et al., 2010a). Yellow, red and green lines indicate the profiles obtained by the Occam inversion from the observed C-response data from Olsen (1999), Velímský (2010), and Ohta et al. (2010a), respectively.

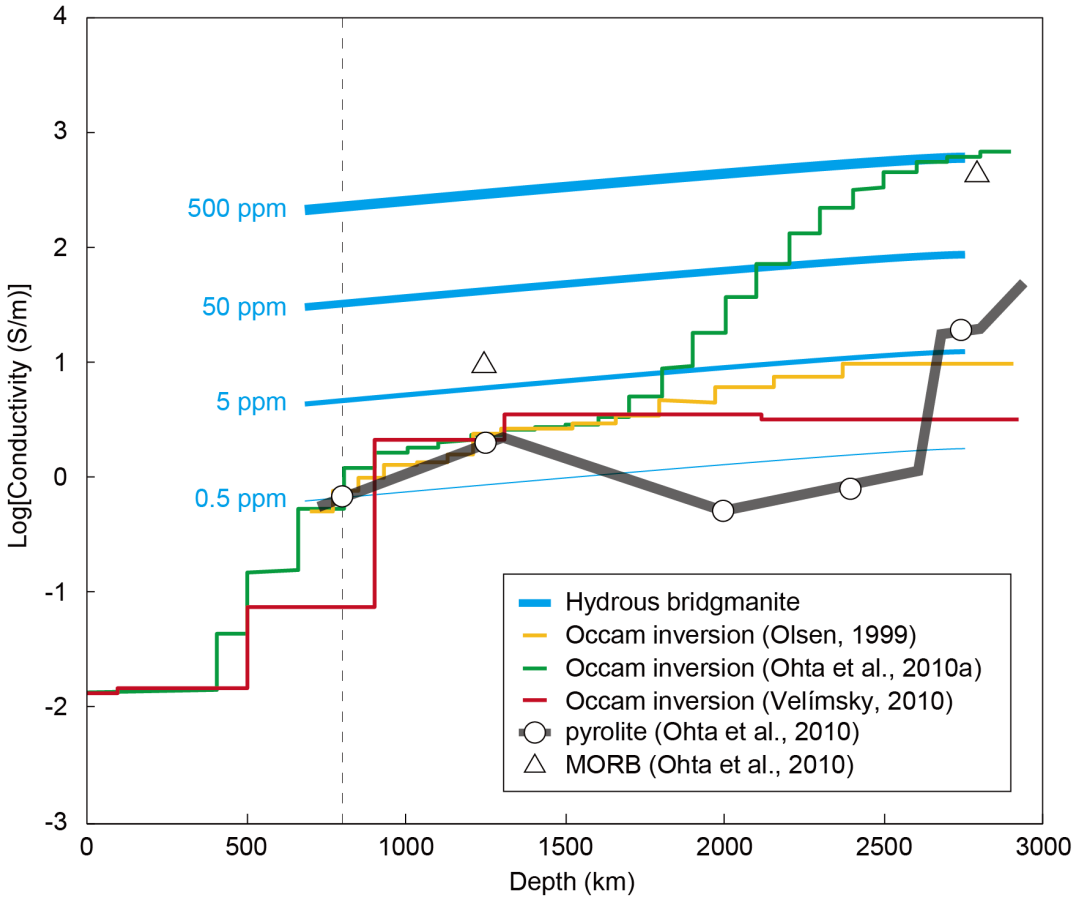

Fig. 8-8. One-dimensional depth profiles of the electrical conductivity of the lower mantle with different water concentration. Gray broken line indicates the depth corresponding to 30 GPa, which is the pressure conducted in the present study.

Chapter 9. Synthesis

9.1. Review of the previous chapters

Here we summarize the present results showed in each chapter as follows.

- **Chapter 2**

We reported the first experimental data providing the effect of both Fe and Al incorporations on the thermal conductivity of bridgmanite. The obtained results showed a minor reduction compared to the reported values with Mg-pure compositions.

- **Chapters 3−5**

From the systematic studies on X-ray diffraction measurements (Chapter 3) and *in-situ* Mössbauer spectroscopy measurements (Chapter 4), we found that bridgmanite synthesis at high-*P,T* conditions where Fe in B-site stabilizes as the low-spin state is the key for accommodating the low-spin Fe, and clarified that bridgmanite in the Earth's lower mantle undergoes the spin transition. We also found that the thermal conductivity of bridgmanite reduces at the pressure range where Fe is in the mixed-spin state, while the conductivity at the high- and the low-spin state has a minor effect (Chapter 5). This indicates that the spin transition is unlikely to affect the thermal conductivity of bridgmanite at the lowermost mantle. The impurity effect of Fe and Al on thermal conductivity of bridgmanite was formulated, which enables us to calculate the conductivity with pyrolitic and mid-ocean ridge basalt (MORB) composition.

- **Chapter 6**

We showed the first thermal conductivity measurement of Fe-bearing post-perovskite at high-*P,T* conditions. The conductivity values were moderately lower

than that of the Mg-pure ones. Also, the grain boundary effect on the thermal conductivity of post-perovskite was found to be small at the Earth's lower mantle *P,T* conditions.

- **Chapter 7**

  We developed a new externally heated diamond anvil cell (EHDAC) technique capable of performing temperature-accurate and stable high-*P,T* experiments up to 1,500 K. The heater assembly was applicable for conducting high-*P,T* electrical conductivity measurements, which was used in that reported in Chapter 8.

- **Chapter 8**

  The long-standing unknown amount of water in the lower mantle was cleared by the electrical conductivity measurements on hydrous bridgmanite, which was estimated as <10 ppm wt. H_2O. A significantly dry lower mantle indicates that the effect of hydration on the thermal conductivity of bridgmanite should be negligible.

The collected thermal conductivity data of bridgmanite and post-perovskite allow us to estimate the thermal conductivity of the lowermost mantle and calculating the temperature profile above the core-mantle boundary (CMB). In the next section, we calculate the CMB temperature profile from our lower mantle thermal conductivity data, and in the end, estimate the CMB heat flow.

9.2. Core-mantle boundary temperature profile

9.2.1. Calculation of the lowermost mantle temperature profile: 1. Upper bound of the core-mantle boundary temperature in the dry lower mantle

Calculation of the lowermost mantle temperature profile by heat conduction equation requires the information and the thermal conductivity and the temperature at the CMB (see Chapter 1). The upper and the lower bound of the CMB temperature can be derived from the mantle solidus and the melting temperature of the core, respectively, based on the observation of the solid lowermost mantle (Yu and Garnero, 2018) and the molten outer core. The solidus temperature of pyrolite was first experimentally determined by Fiquet et al. (2010) by observing the in situ diffuse X-ray scattering, which was estimated as 4180 ± 150 K at the CMB. The later report showed a significantly lower pyrolite solidus temperature of 3570 ± 200 K at the CMB from X-ray computed tomography (CT) image of the recovered sample (Nomura et al., 2014). The starting material used in Fiquet et al. (2010) was a glass which is generally anhydrous, while Nomura et al. (2014) used the gel starting material with ~400 ppm wt. H_2O. Their conflicting results are often explained by the reduced solidus temperature of wet pyrolite. However, a very recent study by Kim et al. showed a low anhydrous pyrolite solidus temperature of 3430 ± 130 K at the CMB using the same melting criteria in Fiquet et al. (2010) but with using their developed multichannel collimator, which allows them observing the diffuse signal from a relatively small amount of melt (Kim et al., 2020). They argued that the high anhydrous pyrolite solidus temperature reported in Fiquet et al. (2010) is due to the difficulty in detecting the diffuse scattering from a small volume of

melts at the solidus by conventional instruments. They also concerned the method in Nomura et al. (2014) that the observation of the melt in their sample is conducted after decompression to an ambient condition, which may involve textural change yielding the confusion in identifying the melting temperature in their laser heating experiments. Thereby, anhydrous pyrolite solidus temperature of 3430 ± 130 K at the CMB (Kim et al., 2020) can be even lowered by additional hydration but has yet to been investigated by their improved method.

Based on the dry lower mantle inferred from our electrical conductivity measurement (see Chapter 8), we adopted the upper bound of the CMB temperature of 3430 ± 130 K (Kim et al., 2020) for temperature profile calculation at the CMB. Such a low CMB temperature of ~3400 K is close or can be even lower than the reported melting temperature of pure iron (Anzellini et al., 2013; Boehler, 1993; Sinmyo et al., 2019). The requirement that the CMB temperature is higher than the core melting temperature can be satisfied when alloying volatiles that lowers the melting temperature such as hydrogen (Hirose et al., 2019), sulfur (Mori et al., 2017), carbon (Mashino et al., 2019), and/or oxygen (Morard et al., 2017).

9.2.2. Calculation of the lowermost mantle temperature profile:2. Lower mantle thermal conductivity model

We calculated the temperature profile above the CMB in a similar manner estimated in Dekura et al. (2019), using the following heat conduction equation:

$$\frac{\partial T(z(P),t)}{\partial t} = \frac{1}{C_{\mathrm{p}}(z(P,T))\rho(z(P,T))}\frac{\partial}{\partial z}\left[\kappa(z(P),T)\frac{\partial T(z(P),t)}{\partial z}\right], \quad (9\text{-}1)$$

where C_p, ρ, and κ are the heat capacity, density, and the thermal conductivity of the lower mantle as a function of depth z, respectively. C_p was set as a constant value of 1300 J/Kg/K. Density as a function of depth z of $0.51z$+4094 kg/m^3 was applied for the ρ, which was yielded by a linear fitting of the one-dimensional density-depth profile in the Earth's lower mantle (Dziewonski and Anderson, 1981). We used the commercial software package COMSOL Multiphysics 5.3a for the calculation. Mantle geometry was set as a two-dimensional rectangle with a height of 1200 km (corresponding to 1700−2900 km in depth) and a width of 1000 km. Dekura et al. (2019) chose the CMB temperature (T_{CMB}) fixed to be 3800 K (Kawai and Tsuchiya, 2009), whereas we fixed it to 3400 K based on the most recently provided upper bound (Kim et al., 2020). The temperature at 1200 km above the CMB was fixed to 2353 K (T_0), which was referred from the adiabatic temperature ($T_{adiabat}$) provided in Brown and Shankland (1981). The initial temperature was set to T_0 for all depths except for the CMB temperature fixed to T_{CMB}. Triangle meshes were applied as grids, which resolution in depth was set as 0.75 km. Time integration was divided into 100 steps in t= 10^7−10^9 yrs. We used the thermal conductivity of (Fe,Al)-bearing bridgmanite modeled in *Chapter 5*, and Fe-bearing post-perovskite modeled in *Chapter 6*, respectively; the thermal conductivity model introduced in *section S.5-6* in *Chapter 5* was used for that of bridgmanite as follows:

$$\kappa_{\mathrm{bdg}}(P,T) = \kappa_{\mathrm{bdg},x}(P, 300\ \mathrm{K})\left(\frac{300\ \mathrm{K}}{T}\right)^{a}, \tag{9-2}$$

$$\kappa_{\mathrm{bdg},x}(P, 300\ \mathrm{K}) = \mathrm{A}(P)x + \mathrm{B}(P), \tag{9-3}$$

where x is the summation of Fe and Al content in per formula unit, $\kappa_{bdg,x}$ is the thermal conductivity of bdg with Fe+Al=x (pfu), and a is the temperature coefficient, respectively. We used the coefficients in Eq. (9-3) of A(P)=-(7.0e-4)P^2-(6.4e-2)P-2.6 and B(P)=(4e-

4)P^2-0.13P+6.3, which was provided in *section S.5-6* in *Chapter 5*. We used the temperature dependence coefficient a of 0.37−0.43 (Chapter 2). For the thermal conductivity of post-perovskite, we applied the following thermal conductivity model:

$$\kappa = \kappa_{\mathrm{ref}} \left(\frac{\rho}{\rho_{\mathrm{ref}}}\right)^{g} \left(\frac{T_{\mathrm{ref}}}{T}\right)^{a}, \qquad (9\text{-}4)$$

where κ_{ref} and ρ_{ref} are thermal conductivity and density at reference pressure and temperature (T_{ref}), g and a are pressure and temperature dependence coefficients, respectively. The parameters of a=0.65, g=6.0, κ_{ref} =59.8 W/m/K, T_{ref}=300 K, and ρ_{ref} =5.47 g/cm^3 were used, which were given in *Chapter 6*. The thermal conductivity of ferropericlase (Ohta et al., 2017) was combined in addition to the $MgSiO_3$ polymorph to calculate the pyrolite conductivity using the Hashin-Shtrikman averaging (Hashin and Shtrikman, 1963) (see *Chapter 6*). Since recent laboratory seismic wave velocity measurements (Mashino et al., 2020; Murakami et al., 2012; Wakamatsu, *D thesis*) prefer perovskitic lower mantle rather than the traditional pyrolitic composition (Ringwood, 1962), we calculated the CMB temperature profile with and without the contribution of ferropericlase, respectively. We neglected the contribution of Ca-perovskite due to the small volume fraction in the lower mantle and the lack of its thermal conductivity data at high-P,T conditions.

Seismic observations have shown that two relatively hot regions compared to the surrounding beneath the Central Pacific and Africa verge the CMB, known as the Large Low Shear wave Velocity Provinces (LLSVPs, Garnero and McNamara, 2008). We determined the “hot geotherm” by attributing the D” discontinuity observed by seismic observation at the top of the CMB under Central Pacific, to the bridgmanite to post-perovskite phase transition, and the “average geotherm” by assuming that the

discontinuous change in the PREM profile is due to the onset of the thermal boundary layer (TBL) above the CMB, respectively. The Clapeyron slope of 8 MPa/K was used, which was robustly constrained from both mineral-physically and theoretically (Ohta et al., 2008; Tsuchiya et al., 2004). The temperature gradient in the TBL was obtained by calculating the average temperature gradient from the CMB to the point where $(T-T_{adiabat})/(T_{CMB}-T_{adiabat})$ is 0.01 (Kawai and Tsuchiya, 2009).

9.2.3. Temperature profile at the base of the mantle and the absence of double-crossing of $MgSiO_3$ polymorph

The calculated average geotherm of the lowermost mantle with pyrolitic and perovskite compositional models show only a slight difference (Fig. 9-1). The estimated temperature gradient in the average geotherm was ~5.0 ± 0.4 K/km, which is smaller than the previous estimation from the seismic studies of 10 ± 3.8 K/km (van der Hilst et al., 2007). This may because they investigated beneath the subduction zone at Central America, which is thought to be relatively a cold region. The calculated average geotherm with the suggested Clapeyron slope of bridgmanite to post-perovskite transition (Ohta et al., 2008; Tsuchiya et al., 2004) well explains the D" discontinuity beneath central Asia, Arctic, and the Caribbean (Fig. 9-1).

The estimated hot geotherm of the pyrolitic model shows a weaker depth dependence than that of the perovskite model. This should be due to the larger thermal conductivity of bdg+fp aggregate (pyrolitic model) than that of bdg (perovskite model). The temperature gradient in the pyrolitic model and perovskite model were estimated as 0.6 ± 0.1 K/km and 1.1 ± 0.1 K/km, respectively, which is fairly consistent with those

estimated in Dekura et al. (2019) of 1.4 K/km. However, the geotherm inferred from the seismic study at the LLSVP beneath the Central Pacific, which is thought to be the representative of hot geotherm, was reported to be 8.5 ± 2.5 K/km (Lay et al., 2006). The seismic study by Lay et al. (2006) obtained a shear wave velocity depth profile in the LLSVP beneath the Central Pacific, and observed a discontinuous increase and a subsequent sharp decrease. They have attributed the increase of s-wave to the bridgmanite to post-perovskite transition, and the decrease to the back transformation of post-perovskite to bridgmanite. However, in our geotherm calculation, we could not get a solution that shows a double-crossing by changing the T_{CMB} ranging from 3400−3800 K with the Clapeyron slope of 8 MPa/K (Ohta et al., 2008; Tsuchiya et al., 2004). The double-crossing requires an unrealistically large Clapeyron slope of ~16 MPa/K and/or a high T_{CMB} of 4200 K (Kawai and Tsuchiya, 2009). Together with the recently preferred low T_{CMB} of ~3400 K (Kim et al., 2020; see *section 9.2.1*), we suggest that the bridgmanite to post-perovskite to bridgmanite transition is unlikely to occur in the Earth's lowermost mantle. Numerical simulation infers a huge temperature gradient in the LLSVP (Nakagawa and Tackley, 2005), indicating a strong lateral dependence of the seismic velocity profile there. Indeed, the depth of the reflection where s-wave velocity increase was observed, attributed to the bridgmanite to post-perovskite transition, shows a strong local dependence (Lay et al., 2006) varying by ~200 km. On the other hand, those where discontinuous s-wave velocity reduction was observed, attributed to the back transformation of post-perovskite in Lay et al. (2006), showed only a slight difference at most of ~15 km. This supports that the s-wave velocity reduction observed in Lay et al. (2006) is not due to the back transformation of post-perovskite in the LLSVP.

Then, what causes the observed discontinuous s-wave velocity reduction in the LLSVP at ~2800 km depth (Thomas et al., 2004; Lay et al., 2006)? The anticorrelation between s-wave and bulk sound velocity implies in the LLSVP implies a thermochemically distinct structure (Masters et al., 2000), which can be accumulated dense oceanic plates piled throughout the Earth's subduction history (e.g., McNamara and Zhong, 2005; Ohta et al., 2008). SiO_2 phase is thought to account for ~20% in the mid-ocean ridge basalt, and its phase transition from $CaCl_2$-type to α-PbO_2-type is thought to show a negative s-wave velocity jump of about -0.5% (Karki et al., 1997). This transition was thought to take place about 70 km shallower than the bridgmanite to post-perovskite transition in pyrolite (Murakami et al., 2003; Ohta et al., 2008). Still, the SiO_2 phase has been reported to contain volatiles such as water (e.g., Litasov et al., 2007) and nitrogen (Fukuyama et al., 2020), which incorporation may affect its phase transition *P-T* conditions. If the origin of a negative reflection of s-wave velocity at the base of the LLSVP is due to the $CaCl_2$-type to the α-PbO_2-type transition of the SiO_2 phase, the Clapeyron slope of this transition should be very small (<8 MPa/K) to explain the negligible location dependence of the reflection depth of the discontinuous s-wave velocity reduction (Thomas et al., 2004; Lay et al., 2006), but is not well constrained (Murakami et al., 2003). Detailed studies on the SiO_2 phase transition with volatiles may clear the origin of the negative s-wave velocity reduction observed at the base of the LLSVP.

9.3. CMB heat flow

We calculated the CMB heat flow Q_{CMB} by the Fourier's law with the estimated temperature gradient at the CMB in the previous section and the thermal conductivity of lowermost mantle estimated in Chapters 5 and 6:

$$Q_{\mathrm{CMB},i} = -\kappa_i \left(\frac{\partial T}{\partial z}\right)_i A, \qquad (9\text{-}5)$$

where κ_i is the thermal conductivity of the lowermost mantle, $\left(\frac{\partial T}{\partial z}\right)_i$ is the temperature gradient, i is the difference in the assumed lower mantle compositional model, and A is the CMB surface area, respectively. The applied thermal conductivity of the lowermost mantle with pyrolitic ppv+fp and perovskite model (all ppv) were 12.8± 1.3 and 14.0± 1.3 W/m/K, respectively. The Q_{CMB} with the estimated average geotherm was calculated to be 9.8 ± 1.9 TW for pyrolitic lower mantle and 10.8 ± 2.0 TW for perovskite model (Fig. 9-2), indicating a minimal dependence of the Q_{CMB} with the compositional model of the lower mantle. For hot geotherm, Q_{CMB} was 1.2 ± 0.2 TW for the pyrolitic model and 2.3 ± 0.4 TW for the perovskite model. We also calculated the Q_{CMB} with seismically inferred temperature gradient in the cold region of 10 ± 3.8 K/km (van der Hilst et al., 2007), which shows a high heat flow of 19.7 ± 8.9 TW for pyrolite and 21.6 ± 9.5 TW for perovskite model. The average heat flows calculated with the hot and cold geotherms were 10.4 ± 4.9 TW for pyrolite and 11.9 ± 5.3 TW for perovskite, which is consistent with the average heat flow calculated from the estimated average temperature profile. The perovskite model is an extreme case without the contribution of ferropericlase. The suggested perovskitic model indicates the bridgmanite accounting for 88−92 vol.% (Mashino et al., 2020; Murakami et al., 2012; Wakamatsu, *D thesis*). Therefore, the

estimated Q_{CMB} of our perovskite model (all ppv) would be the upper bound of the actual one. From the minimum and maximum Q_{CMB} values of both compositional models, we conclude that the net Q_{CMB} is 10.4 ± 2.5 TW. The estimated average Q_{CMB} was within the old prediction of 5−13 TW (e.g., Stacey, 1992), and is consistent with those from seismic observations with using the typically used thermal conductivity value of 10 W/m/K, of 13 ± 4 TW (Lay et al., 2006; van der Hilst et al., 2007).

The unknown contribution of mantle cooling can be calculated from the terrestrial heat-flow balance. By neglecting the minor heat sources such as tidal heating (<0.4 TW) (Lay et al., 2008), the estimated total Q_{CMB} of 10.4 ± 2.5 TW with the global radiogenic heat of 20 ± 3 TW (Araki et al., 2005; Jaupart et al., 2015), and the total surface heat flow of 46 ± 3 TW (Lay et al., 2008) gives the secular mantle cooling of ~16 TW in average, but with wide uncertainty of ~9 TW due to the uncertainties in each component (Fig. 9-3). Mantle cooling consists of the contribution from the upwelling hot plumes and downwelling cold slabs. Generally, estimation of the energy propagation by upwelling is much difficult than that by subduction due to a low resolution of deep plume heads via tomographic images (Montelli et al., 2004) and possible small undetectable plumes (Malamud and Turcotte, 1999). The contribution of cold subduction was estimated to be 13−14 TW from finite frequency tomography and the Stokes' flow model (Nolet et al., 2006). With the mantle cooling of ~16 TW, the hot plumes carry only ~2 TW from the mantle to the surface, indicating that a large portion of mantle cooling is performed by subduction of cold slab rather than the hot plumes. This is consistent with the view that not all the hot plumes are buoyant enough to bring energy to the surface due to the interaction between other plumes, the negative Clapeyron slope at the 660 km depth, and heavier materials upwelling from the chemically distinct dense LLSVPs (Labrosse, 2002).

Because of the large uncertainty, we cannot exclude the possible larger contribution of the upwelling plumes up to ~11 TW but would not be larger than the contribution of subducting oceanic plates (Fig. 9-3), which strengthens that plate tectonics control the Earth's mantle cooling.

The estimated Q_{CMB} with hot and cold geotherm showed a huge difference by more than ten times of ~1−22 TW, in other words, an extreme peak-to-peak lateral variation of CMB heat flow as suggested from numerical simulation (Nakagawa and Tackley, 2008). The thermal conductivity difference of lowermost mantle due to temperature and compositional variation is at most ~50% (see *Chapters 5, 6*), whereas the $\left(\frac{\partial T}{\partial z}\right)$ difference between hot and cold geotherm was ~1000%, so the cause of the lateral heat flow variation is mainly due to the difference in regional temperature variation. The estimated Q_{CMB} variation is consistent with that derived from the temperature variation inferred from seismology assuming that seismic wave velocity variations merely thermal origin, and a constant thermal conductivity, as 0−22 TW (Stackhouse et al., 2015). This supports the huge temperature variation creating CMB heat flux diversity than thermal conductivity difference.

The parameter $q^*=(q_{max}-q_{min})/2q_{mean}$ indicates the strength of the lateral heat flux variation at the CMB. From the hot and cold geotherms, the q^* values for pyrolite and perovskite model were calculated as $1.1^{+0.8}_{-0.5}$ and $1.2^{+0.9}_{-0.6}$, respectively. A smaller value of ~0.2 has been preferred, which was inferred from seismological studies investigated beneath relatively hot Central Pacific (Lay et al., 2006) and cold Central America (van der Hilst et al., 2007). Again, we suggest that the assumption of the double-crossing with non-realistic Clapeyron slope led to a relatively strong temperature gradient at hot regions

corresponding to a small q^* value. Numerical dynamo simulations showed that the structure and strength of the magnetic field can strongly be dependent on the q^* at the CMB. Gubbins et al. (2011) showed that increasing the q^* from 0.15 to 0.45 generates strongly concentrated downwellings flow in the outer core beneath the cold regions at the CMB. They expected that such narrow downwellings would increase the heat flux at the inner core boundary (ICB), which may be enough to cause localized melting of the inner core. Our estimated large q^* value of ~1 is much higher than 0.45, and thus supports the localized melting of the inner core (Gubbins et al., 2011). Since a solid inner core is suggested to contain less volatiles than the surrounding outer core (Birch, 1952), the melting of the inner core should form a stable dense volatile-poor layer above the ICB (Gubbins et al., 2011), which may explain the origin of p-wave anomalies observed right above this boundary so-called F-layer (Song and Helmberger, 1995; Souriau and Poupinet, 1991). Also, laboratory experiment has shown that such heterogeneous heat flow at the ICB causes a temperature difference in the core and induces an anisotropic inner core crystallization (Sumita and Olson, 1999), which is likely to explain the seismically observed west-eastern hemispherical P-wave velocity and attenuation anomalies in the inner core (e.g., Tanaka and Hamaguchi, 1997).

Moreover, an increase of q^* is found to enhance the localization of the outer core convection and the geodynamo activity, which generates a stronger magnetic field (Takahashi et al., 2008). They observed a broad outer core downwelling shifted from the cold region at the CMB when applying q^* =0.5, and by increasing q^* to ~1 the downwelling flow was strongly concentrated under the high heat flow region (i.e., relatively cold area) creating a stronger magnetic field, indicating that geodynamo structure is dependent on the strength of CMB thermal heterogeneity. As an important

example, they suggested that the symmetrical thermally heterogeneous lowermost mantle with regard to the equator can generate a stable and extremely strong magnetic field, which might be the origin of the Superchron such as the Cretaceous Normal Superchron. A large q^* of ~1 found in this study have profound implications for the outer core convection, geodynamo, and inner core structure. We expect further geodynamo and mantle dynamics simulations with parameterizing a higher q^* value for a better understanding of core and lower mantle dynamics.

9.4. Future perspectives and Conclusions

In the final section, I will summarize the expected further studies related to this dissertation.

(I). Thermal conductivity of pyrolitic ppv+fp aggregate

A series of thermal conductivity measurements on lower mantle minerals have quantified the effects of impurity and Fe spin transition, which allows us to evaluate the thermal conductivity of pyrolite and MORB. So far, the thermal conductivity of pyrolitic bdg+fp aggregate has reported (Geballe et al., 2020), but that of ppv+fp has never been measured. Direct thermal conductivity measurements on pyrolite and MORB at CMB-*P,T* conditions can infer that of the lowermost mantle without relying on thermal conductivity models.

(II). Thermal conductivity of (Fe,Al)-bearing bridgmanite and ferropericlase at high-*P,T* conditions

To our knowledge, so far three thermal conductivity measurements have reported on (Fe,Al)-bearing bridgmanite (Okuda et al., 2017, Chapter 2; Hsieh et al., 2017; Okuda et al., 2019, Chapter 5), and two measurements on ferropericlase (Ohta et al., 2017; Hsieh et al., 2018) at high pressure using a DAC. However, all of these studies remain in room-*T* measurements. Direct thermal conductivity measurements at lower mantle high-*P,T* conditions is required since spin state of Fe would be affected by temperature (also stated in future study III).

(III). Spin state of Fe in bridgmanite at high-*P,T* conditions

Theoretical study (Tsuchiya and Wang, 2013) showed that the Fe spin transition pressure enhances by increasing temperature, but we lack experimental confirmations. The onset depth of the spin transition of Fe in bdg occurs have profound implications including reduction of the thermal conductivity of the lower mantle found in *Chapter 5*.

(IV). Development of seismic observation, and investigation of the temperature dependence of seismic wave velocity of lower mantle minerals

Development of a new analysis such as wave inversion technique have provided high-definition seismic depth profiles at the lowermost mantle. The increase of seismological events and/or further developments on the seismic observations would give a seismic data from the base of the mantle with higher resolution. The temperature dependence of seismic wave velocity of lower mantle minerals currently relies on

theoretical calculations (Wentzcovitch et al., 2006, 2009), which calls for experimental verifications.

(V). The water content in the Earth's lower mantle

Due to the relatively lower temperature and pressure achieved in the present study (Chapter 8), we could only estimate the upper limit of the lower mantle water abundance. Electrical conductivity measurements at high-*P,T* covering the entire lower mantle conditions provide more detailed information of the water content in the lower mantle and hence that of the bulk Earth.

In conclusion, I hope this thesis has supplied an important insight to the CMB heat flow and the thermal evolution of this planet. Further detailed thermal conductivity measurements and the development in seismology techniques give better understanding of the variety of dynamical phenomena driven from immense thermal conduction at the CMB.

9.5. References

Anzellini, S., Dewaele, A., Mezouar, M., Loubeyre, P., Morard, G., 2013. Melting of Iron at Earth's Inner Core Boundary Based on Fast X-ray Diffraction. Science 340, 464−466. https://doi.org/10.1126/science.1233514

Araki, T., Enomoto, S., Furuno, K., Gando, Y., Ichimura, K., Ikeda, H., Inoue, K., Kishimoto, Y., Koga, M., Koseki, Y., Maeda, T., Mitsui, T., Motoki, M., Nakajima, K., Ogawa, H., Ogawa, M., Owada, K., Ricol, J.S., Shimizu, I., Shirai, J., Suekane, F., Suzuki, A., Tada, K., Takeuchi, S., Tamae, K., Tsuda, Y., Watanabe, H., Busenitz, J., Classen, T., Djurcic, Z., Keefer, G., Leonard, D., Piepke, A., Yakushev, E., Berger, B.E., Chan, Y.D., Decowski, M.P., Dwyer, D.A., Freedman, S.J., Fujikawa, B.K., Goldman, J., Gray, F., Heeger, K.M., Hsu, L., Lesko, K.T., Luk, K.B., Murayama, H., O'Donnell, T., Poon, A.W.P., Steiner, H.M., Winslow, L.A., Mauger, C., McKeown, R.D., Vogel, P., Lane, C.E., Miletic, T., Guillian, G., Learned, J.G., Maricic, J., Matsuno, S., Pakvasa, S., Horton-Smith, G.A., Dazeley, S., Hatakeyama, S., Rojas, A., Svoboda, R., Dieterle, B.D., Detwiler, J., Gratta, G., Ishii, K., Tolich, N., Uchida, Y., Batygov, M., Bugg, W., Efremenko, Y., Kamyshkov, Y., Kozlov, A., Nakamura, Y., Karwowski, H.J., Markoff, D.M., Nakamura, K., Rohm, R.M., Tornow, W., Wendell, R., Chen, M.J., Wang, Y.F., Piquemal, F., 2005. Experimental investigation of geologically produced antineutrinos with KamLAND. Nature 436, 499−503. https://doi.org/10.1038/nature03980

Birch, F., 1952. Elasticity and constitution of the Earth's interior. J. Geophys. Res. 57, 227−286. https://doi.org/10.1029/JZ057i002p00227

Boehler, R., 1993. Temperatures in the Earth's core from melting-point measurements of iron at high static pressures. Nature 363, 534−536. https://doi.org/10.1038/363534a0

Brown, J.M., Shankland, T.J., 1981. Thermodynamic parameters in the Earth as determined from seismic profiles. Geophys. J. R. Astron. Soc. 66, 579–596. https://doi.org/10.1111/j.1365-246X.1981.tb04891.x

Dekura, H., Tsuchiya, T., 2019. Lattice Thermal Conductivity of $MgSiO_3$ Postperovskite Under the Lowermost Mantle Conditions From Ab Initio Anharmonic Lattice Dynamics. Geophys. Res. Lett. 1−8. https://doi.org/10.1029/2019GL085273

Dziewonski, A.M., and Anderson, D.L., 1981. Preliminary reference Earth model. Physics of the Earth and Planetary Interiors 25: 297–356. https://doi.org/10.1016/0031-9201(81)90046-7

Fiquet, G., Auzende, A.L., Siebert, J., Corgne, A., Bureau, H., Ozawa, H., Garbarino, G., 2010. Melting of peridotite to 140 gigapascals. Science 329, 1516–1518. https://doi.org/10.1126/science.1192448

Fukuyama, K., Kagi, H., Inoue, T., Kakizawa, S., Shinmei, T., Hishita, S., Takahata, N., Sano, Y., 2020. High nitrogen solubility in stishovite (SiO_2) under lower mantle conditions. Sci. Rep. 10, 1–8. https://doi.org/10.1038/s41598-020-67621-2

Garnero, E.J., McNamara, A.K., 2008. Structure and dynamics of earth's lower mantle. Science 320, 626–628. https://doi.org/10.1126/science.1148028

Geballe, Z.M., Sime, N., Badro, J., van Keken, P.E., Goncharov, A.F., 2020. Thermal conductivity near the bottom of the Earth's lower mantle: Measurements of pyrolite up to 120 GPa and 2500 K. Earth Planet. Sci. Lett. 536, 116161. https://doi.org/10.1016/j.epsl.2020.116161

Gubbins, D., Sreenivasan, B., Mound, J., Rost, S., 2011. Melting of the Earths inner core. Nature 473, 361−364. https://doi.org/10.1038/nature10068

Hashin, Z., Shtrikman, S., 1963. A variational approach to the theory of the elastic behaviour of multiphase materials. J. Mech. Phys. Solids 11, 127−140. https://doi.org/10.1016/0022-5096(63)90060-7

Hirose, K., Tagawa, S., Kuwayama, Y., Sinmyo, R., Morard, G., Ohishi, Y., Genda, H., 2019. Hydrogen Limits Carbon in Liquid Iron. Geophys. Res. Lett. 46, 5190−5197. https://doi.org/10.1029/2019GL082591

Hsieh, W.P., Deschamps, F., Okuchi, T., Lin, J.F., 2018. Effects of iron on the lattice thermal conductivity of Earth's deep mantle and implications for mantle dynamics. Proc. Natl. Acad. Sci. U. S. A. 115, 4099–4104. https://doi.org/10.1073/pnas.1718557115

Hsieh, W.P., Deschamps, F., Okuchi, T., Lin, J.F., 2017. Reduced lattice thermal conductivity of Fe-bearing bridgmanite in Earth's deep mantle. J. Geophys. Res. Solid Earth 122, 4900–4917. https://doi.org/10.1002/2017JB014339

Jaupart, C., Labrosse, S., Lucazeau, F., Mareschal, J.C., 2015. Temperatures, Heat, and Energy in the Mantle of the Earth, Treatise on Geophysics: Second Edition. Elsevier B.V. https://doi.org/10.1016/B978-0-444-53802-4.00126-3

Karki, B.B., Stixrude, L., Crain, J., 1997. Ab initio elasticity of three high-pressure polymorphs of silica. Geophys. Res. Lett. 24, 3269–3272. https://doi.org/10.1029/97GL53196

Kawai, K., Tsuchiya, T., 2009. Temperature profile in the lowermost mantle from seismological and mineral physics joint modeling. Proc. Natl. Acad. Sci. U. S. A. 106, 22119−22123. https://doi.org/10.1073/pnas.0905920106

Kim, T., Ko, B., Greenberg, E., Prakapenka, V., Shim, S.H., Lee, Y., 2020. Low Melting Temperature of Anhydrous Mantle Materials at the Core-Mantle Boundary. Geophys. Res. Lett. 47, 1−10. https://doi.org/10.1029/2020GL089345

Konôpková, Z., McWilliams, R.S., Gómez-Pérez, N., Goncharov, A.F., 2016. Direct measurement of thermal conductivity in solid iron at planetary core conditions. Nature 534, 99−101. https://doi.org/10.1038/nature18009

Labrosse, S., 2002. Hotspots, mantle plumes and core heat loss. Earth Planet. Sci. Lett. 199, 147−156. https://doi.org/10.1016/S0012-821X(02)00537-X

Lay, T., Hernlund, J., Buffett, B.A., 2008. Core-mantle boundary heat flow. Nat. Geosci. 1, 25−32. https://doi.org/10.1038/ngeo.2007.44

Lay, T., Hernlund, J., Garnero, E.J., Thorne, M.S., 2006. A post-perovskite lens and D″ heat flux beneath the central Pacific. Science 314, 1272−1276. https://doi.org/10.1126/science.1133280

Litasov, K.D., Kagi, H., Shatskiy, A., Ohtani, E., Lakshtanov, D.L., Bass, J.D., Ito, E., 2007. High hydrogen solubility in Al-rich stishovite and water transport in the lower mantle. Earth Planet. Sci. Lett. 262, 620–634. https://doi.org/10.1016/j.epsl.2007.08.015

Malamud, B.D., Turcotte, D.L., 1999. How many plumes are there? Earth Planet. Sci. Lett. 174, 113−124. https://doi.org/10.1016/S0012-821X(99)00257-5

Mashino, I., Miozzi, F., Hirose, K., Morard, G., Sinmyo, R., 2019. Melting experiments on the Fe−C binary system up to 255 GPa: Constraints on the carbon content in the Earth's core. Earth Planet. Sci. Lett. 515, 135−144. https://doi.org/10.1016/j.epsl.2019.03.020

Mashino, I., Murakami, M., Miyajima, N., Petitgirard, S., 2020. Experimental evidence for silica-enriched Earth's lower mantle with ferrous iron dominant bridgmanite 1−7. https://doi.org/10.1073/pnas.1917096117

Masters, G., Laske, G., Bolton, H., Dziewonski, A., 2000. The relative behavior of shear velocity, bulk sound speed, and compressional velocity in the mantle: Implications for chemical and thermal structure, in: Earth's Deep Interior; Mineral Physics and Tomography from the Atomic. pp. 63–87. https://doi.org/10.1029/GM117p0063

McNamara, A.K., Zhong, S., 2005. Thermochemical structures beneath Africa and the Pacific Ocean. Nature 437, 1136–1139. https://doi.org/10.1038/nature04066

Montelli, R., Nolet, G., Dahlen, F.A., Masters, G., Engdahl, E.R., Hung, S.H., 2004. Finite-Frequency Tomography Reveals a Variety of Plumes in the Mantle. Science 303, 338−343. https://doi.org/10.1126/science.1092485

Morard, G., Andrault, D., Antonangeli, D., Nakajima, Y., Auzende, A.L., Boulard, E., Cervera, S., Clark, A., Lord, O.T., Siebert, J., Svitlyk, V., Garbarino, G., Mezouar, M., 2017. Fe−FeO and Fe−Fe_3C melting relations at Earth's core−mantle boundary conditions: Implications for a volatile-rich or oxygen-rich core. Earth Planet. Sci. Lett. 473, 94−103. https://doi.org/10.1016/j.epsl.2017.05.024

Mori, Y., Ozawa, H., Hirose, K., Sinmyo, R., Tateno, S., Morard, G., Ohishi, Y., 2017. Melting experiments on Fe−Fe_3S system to 254 GPa. Earth Planet. Sci. Lett. 464, 135−141. https://doi.org/10.1016/j.epsl.2017.02.021

Murakami, M., Hirose, K., Ono, S., Ohishi, Y., 2003. Stability of $CaCl_2$-type and α-PbO_2-type SiO_2 at high pressure and temperature determined by in-situ X-ray measurements. Geophys. Res. Lett. 30, 1999–2002. https://doi.org/10.1029/2002gl016722

Murakami, M., Ohishi, Y., Hirao, N., Hirose, K., 2012. A perovskitic lower mantle inferred from high-pressure, high-temperature sound velocity data. Nature 485, 90−94. https://doi.org/10.1038/nature11004

Nakagawa, T., Tackley, P.J., 2005. The interaction between the post-perovskite phase change and a thermo-chemical boundary layer near the core-mantle boundary. Earth Planet. Sci. Lett. 238, 204–216. https://doi.org/10.1016/j.epsl.2005.06.048

Nakagawa, T., Tackley, P.J., 2008. Lateral variations in CMB heat flux and deep mantle seismic velocity caused by a thermal-chemical-phase boundary layer in 3D spherical convection. Earth Planet. Sci. Lett. 271, 348−358. https://doi.org/10.1016/j.epsl.2008.04.013

Nolet, G., Karato, S.I., Montelli, R., 2006. Plume fluxes from seismic tomography. Earth Planet. Sci. Lett. 248, 685−699. https://doi.org/10.1016/j.epsl.2006.06.011

Nomura, R., Hirose, K., Uesugi, K., Ohishi, Y., Tsuchiyama, A., Miyake, A., Ueno, Y., 2014. Low Core-Mantle Boundary Temperature Inferred from the Solidus of Pyrolite. Science 343, 522−525. https://doi.org/10.1126/science.1248186

Ohta, K., Hirose, K., Lay, T., Sata, N., Ohishi, Y., 2008. Phase transitions in pyrolite and MORB at lowermost mantle conditions: Implications for a MORB-rich pile above the core-mantle boundary. Earth Planet. Sci. Lett. 267, 107−117. https://doi.org/10.1016/j.epsl.2007.11.037

Ohta, K., Kuwayama, Y., Hirose, K., Shimizu, K., Ohishi, Y., 2016. Experimental determination of the electrical resistivity of iron at Earth's core conditions. Nature 534, 95−98. https://doi.org/10.1038/nature17957

Ohta, K., Yagi, T., Hirose, K., Ohishi, Y., 2017. Thermal conductivity of ferropericlase in the Earth's lower mantle. Earth Planet. Sci. Lett. 465, 29−37. https://doi.org/10.1016/j.epsl.2017.02.030

Okuda, Y., Ohta, K., Sinmyo, R., Hirose, K., Yagi, T., Ohishi, Y., 2019. Effect of spin transition of iron on the thermal conductivity of (Fe, Al)-bearing bridgmanite. Earth Planet. Sci. Lett. 520, 188–198. https://doi.org/10.1016/j.epsl.2019.05.042

Okuda, Y., Ohta, K., Yagi, T., Sinmyo, R., Wakamatsu, T., Hirose, K., Ohishi, Y., 2017. The effect of iron and aluminum incorporation on lattice thermal conductivity

of bridgmanite at the Earth's lower mantle. Earth Planet. Sci. Lett. 474, 25–31. https://doi.org/10.1016/j.epsl.2017.06.022

Ringwood, A.E., 1962. A model for the upper mantle. J. Geophys. Res. 67, 857−867. https://doi.org/10.1029/JZ067i002p00857

Sinmyo, R., Hirose, K., Ohishi, Y., 2019. Melting curve of iron to 290 GPa determined in a resistance-heated diamond-anvil cell. Earth Planet. Sci. Lett. 510, 45−52. https://doi.org/10.1016/j.epsl.2019.01.006

Song, X., Helmberger, D. V., 1995. Depth dependence of anisotropy of Earth's inner core. J. Geophys. Res. 100, 9805−9816. https://doi.org/10.1029/95JB00244

Souriau, A., Poupinet, G., 1991. The velocity profile at the base of the liquid core from PKP(BC+Cdiff) data: An argument in favour of radial inhomogeneity. Geophys. Res. Lett. 18, 2023−2026. https://doi.org/10.1029/91GL02417

Stacey, F., 1992. Physics of the Earth. Brookfield, Brisbane, Australia, ed. 1.

Stackhouse, S., Stixrude, L., Karki, B.B., 2015. First-principles calculations of the lattice thermal conductivity of the lower mantle. Earth Planet. Sci. Lett. 427, 11−17. https://doi.org/10.1016/j.epsl.2015.06.050

Sumita, I., Olson, P., 1999. A laboratory model for convection in Earth's core driven by a thermally heterogeneous mantle. Science 286, 1547−1549. https://doi.org/10.1126/science.286.5444.1547

Takahashi, F., Tsunakawa, H., Matsushima, M., Mochizuki, N., Honkura, Y., 2008. Effects of thermally heterogeneous structure in the lowermost mantle on the geomagnetic field strength. Earth Planet. Sci. Lett. 272, 738−746. https://doi.org/10.1016/j.epsl.2008.06.017

Tanaka, S., Hamaguchi, H., 1997. Degree one heterogeneity and hemispherical variation of anisotropy in the inner core from PKP (BC)- PKP (DF) times. J. Geophys. Res. Solid Earth 102, 2925−2938. https://doi.org/10.1029/96JB03187

Thomas, C., Kendall, J.M., Lowman, J., 2004. Lower-mantle seismic discontinuities and the thermal morphology of subducted slabs. Earth Planet. Sci. Lett. 225, 105–113. https://doi.org/10.1016/j.epsl.2004.05.038

Tsuchiya, T., Tsuchiya, J., Umemoto, K., Wentzcovitch, R.M., 2004. Phase transition in $MgSiO_3$ perovskite in the earth's lower mantle. Earth Planet. Sci. Lett. 224, 241−248. https://doi.org/10.1016/j.epsl.2004.05.017

Tsuchiya, T., Wang, X., 2013. Ab initio investigation on the high-temperature thermodynamic properties of Fe^{3+}-bearing $MgSiO_3$ perovskite. J. Geophys. Res. Solid Earth 118, 83−91. https://doi.org/10.1029/2012JB009696

van der Hilst, R.D., de Hoop, M. V., Wang, P., Shim, S.-H., Ma, P., Tenorio, L., 2007. Seismostratigraphy and Thermal Structure of Earth's Core-Mantle Boundary Region. Science 315, 1813−1817. https://doi.org/10.1126/science.1137867

Wakamatsu, T., 2020. Constraints on the composition of the deep Earth based on high-pressure ultrasonic measurements. Doctoral thesis.

Wentzcovitch, R.M., Justo, J.F., Wu, Z., da Silva, C.R.S., Yuen, D.A., Kohlstedt, D., 2009. Anomalous compressibility of ferropericlase throughout the iron spin cross-over. Proc. Natl. Acad. Sci. 106, 8447−8452. https://doi.org/10.1073/pnas.0812150106

Wentzcovitch, R.M., Tsuchiya, T., Tsuchiya, J., 2006. $MgSiO_3$ postperovskite at D″ conditions. Proc. Natl. Acad. Sci. U. S. A. 103, 543−546. https://doi.org/10.1073/pnas.0506879103

Yu, S., Garnero, E.J., 2018. Ultralow Velocity Zone Locations: A Global Assessment. Geochemistry, Geophys. Geosystems 19, 396−414. https://doi.org/10.1002/2017GC007281

9.6. Figures

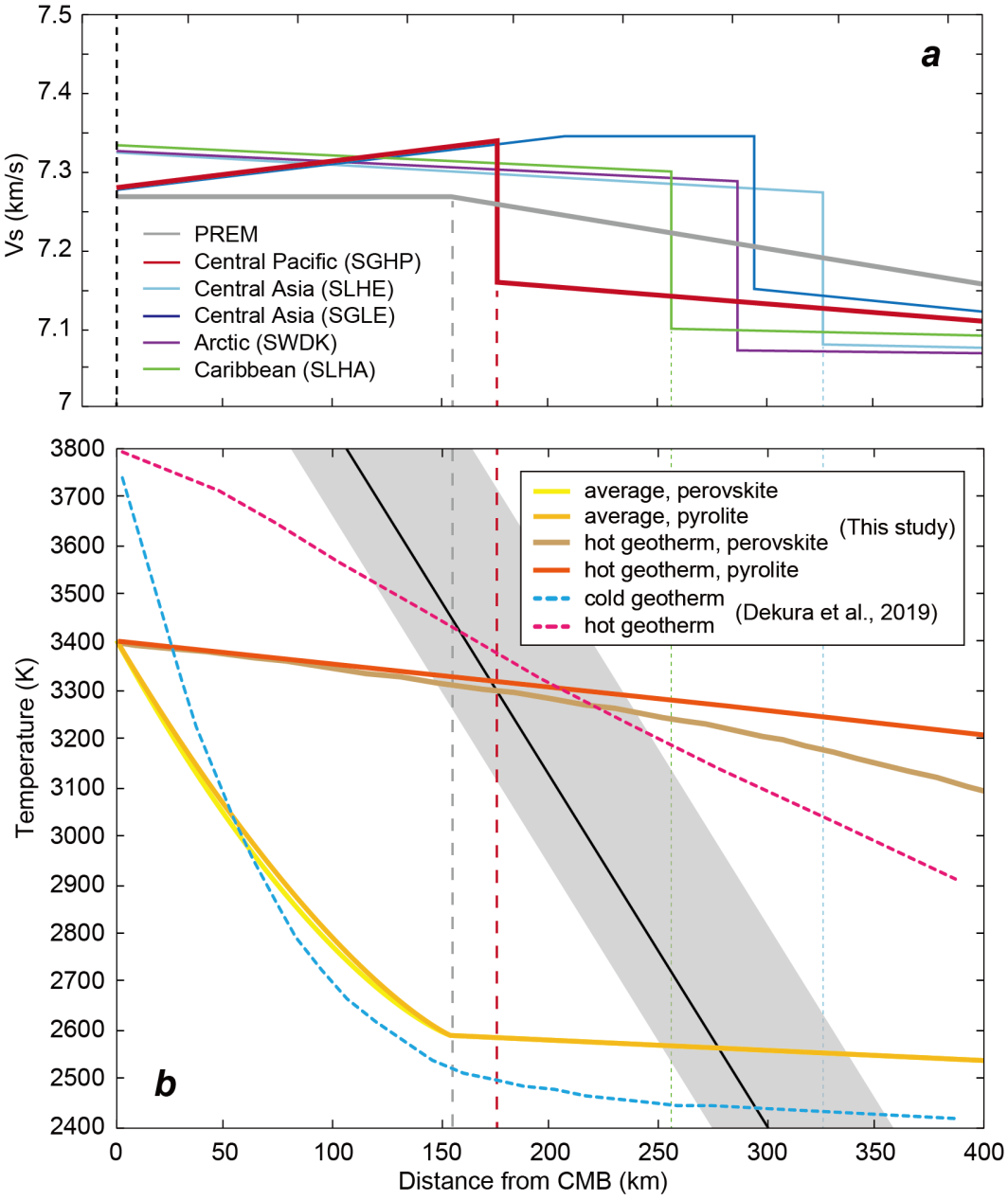

Fig. 9-1. (a) Shear velocity models at the CMB in several different regions inferred from double-array stack studies (modified after Kawai and Tsuchiya, 2019), and (b) the estimated temperature profile above the CMB. Yellow and dark yellow lines indicate the calculated average geotherm with perovskite and pyrolitic model, respectively, and

brown and orange lines indicate the calculated hot geotherm with perovskite and pyrolitic model, respectively. Pink and blue broken lines indicate the estimated hot and cold geotherm in Dekura et al. (2019), respectively. Black line and gray band indicate the Clapeyron slope of bridgmanite to post-perovskite transition with $MgSiO_3$-pure (Tsuchiya et al., 2004) and pyrolitic composition (Ohta et al., 2008), respectively.

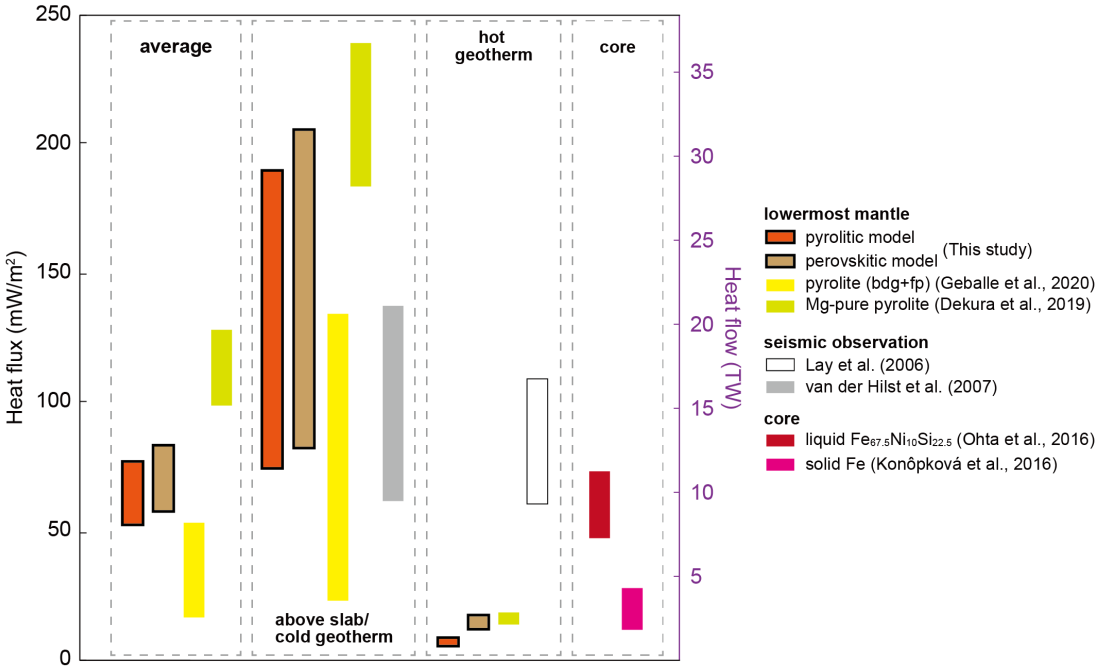

Fig. 9-2. The complied CMB heat flux and surface flow. Orange and brown bars indicate the estimated CMB heat flow of pyrolitic and perovskite composition, respectively, and yellow and green bars indicate those with the reported thermal conductivity of pyrolitic rock (Geballe et al., 2020) and $MgSiO_3$ PPv + MgO aggregate (Dekura and Tsuchiya, 2019), respectively. Gray and open bars indicate the CMB heat flow estimated from the seismically inferred temperature gradient above the CMB beneath Central Pacific (Lay et al., 2006) and Central America (van der Hilst et al., 2007), respectively, and with the typically used lowermost mantle thermal conductivity of 10 W/m/K (Stacey, 1992). Red and pink bars indicate the CMB heat flow estimated from the core thermal conductivity and its adiabat estimated in Ohta et al. (2016) and Konôpková et al. (2016), respectively.

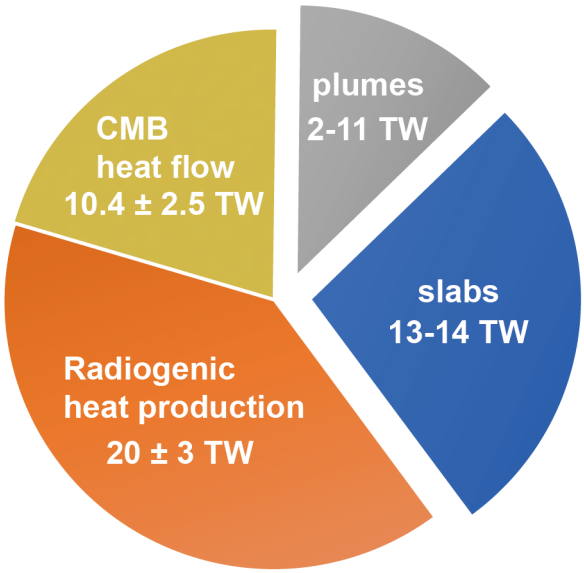

Fig. 9-3. Global heat-flow balance of the Earth. Tidal heating contribution is not considered here. Cooling rate via slab subduction was referred from Nolet et al. (2006).

Acknowledgments

I would like to show my greatest appreciation to my supervisor Assoc. Prof. K. Ohta, for all his guidance and encouragement. There would be no end to enumerate his constructive comments and invaluable suggestions. I have learned tens of hundreds of things from him, about Earth science, procedure and attitude toward research, and about life. The time I have been free to study with him for the last six years is my irreplaceable property. Especially in the last year, I learned a lot from his research attitude “Never stop learning” under the coronavirus crisis. The gratitude is undoubtedly comparable to that of the universe.

I owe a very important debt to Prof. K. Hirose. At first, I was interested in space science, but I stepped into the geoscience world with his words, which was certainly an “introduction to deep Earth science (DES)”. All his support, insightful comments and suggestions were indispensable for my life in Ph.D.

I would like to express my gratitude and respect to Dr. S. Tateno and Dr. H. Tateno for their pioneering geoscience outreaching activities, which have strongly stimulated my ambition. I would like to thank Dr. S. Yamazaki and Dr. T. Hamura for providing me valuable outreaching opportunities. I would like to thank everyone involved in our outreaching activities.

I am grateful to A. Kobayashi, my bosom friend making a strenuous effort in a completely different field from mine. We improved ourselves through friendly rivalry. Let’s continue camping out.

I would like to offer my special thanks to T. Wakamatsu and Y. Park, my best colleagues. They are indispensable in carrying out my experiments. I also thank Dr. S. Azuma, Dr. S. Suehiro, A. Hasegawa, Dr. H. Gomi, Dr. Y. Kuwayama, S. Kimura, H. Inoue, T. Yamamoto, K. Oka, and all members of Ohta and Hirose laboratory, and ELSI. I am very happy to be belonging to such a unique lab. I also would like to particularly thank S. Tagawa in U-Tokyo. His sophisticated ideas are always great to learn. Starting materials were provided from Assoc. Prof. R. Sinmyo and Prof. Y. Nishihara. Dr. T. Yagi, Dr. N. Hirao, and Dr. S. I. Kawaguchi gave me helpful comments about experimental techniques.

My heartfelt appreciation goes to the mates of the fruit club, T. Wakamatsu, A. Nakajima, H. Sakuraba, and H. Yagi. Thanks to them, my Ph.D. life was very fulfilling. I would like to thank everyone who played football with me. I often eat boxed lunch of Mikawa-ya, yakiniku at Gyu-kaku and Futaba, and ramen at Musashi-ya. These were my energy source.

I would like to offer my special thanks to Dr. B. Chen, an instructor at the UHM for accepting me as a visiting international student. I have learned a lot from his up-and-coming and aggressiveness.

I was supported by the Japan Society for the Promotion of Science (JSPS) Research Fellowship for Young Scientists (DC2) and was supported by the JSPS Overseas Challenge Program for Young Researchers. I would like to gratefully acknowledge Assoc. Prof. H. Genda, Assoc. Prof. A. Ishikawa, Prof. T. Nakamoto, and Assoc. Prof. W. Kanda for reviewing my Ph. D. dissertation. Their comments and suggestions further improved the manuscript.

Finally, my father, my mother, and my identical twin brother have been extraordinarily supportive. Without their persistent help, this dissertation would not have been possible. Thank you.

Paper list

1. Okuda, Y., Ohta, K., Yagi, T., Sinmyo, R., Wakamatsu, T., Hirose, K., Ohishi, Y., 2017. The effect of iron and aluminum incorporation on lattice thermal conductivity of bridgmanite at the Earth's lower mantle. Earth Planet. Sci. Lett. **474**, 25–31. https://doi.org/10.1016/j.epsl.2017.06.022
   Chapter 2 is based on this paper.
2. Okuda, Y., Ohta, K., Sinmyo, R., Hirose, K., Yagi, T., Ohishi, Y., 2019. Effect of spin transition of iron on the thermal conductivity of (Fe, Al)-bearing bridgmanite. Earth Planet. Sci. Lett. **520**, 188–198. https://doi.org/10.1016/j.epsl.2019.05.042
   Chapter 5 is based on this paper.
3. Hasegawa, A., Ohta, K., Yagi, T., Hirose, K., Okuda, Y., Kondo, T., 2019. Composition and pressure dependence of lattice thermal conductivity of (Mg,Fe)O solid solutions. Comptes Rendus Geosci. **351**, 229–235. https://doi.org/10.1016/j.crte.2018.10.005
4. Okuda, Y., Ohta, K., Hasegawa, A., Yagi, T., Hirose, K., Kawaguchi, S.I., Ohishi, Y., 2020a. Thermal conductivity of Fe-bearing post-perovskite in the Earth's lowermost mantle. Earth Planet. Sci. Lett. **547**, 116466. https://doi.org/10.1016/j.epsl.2020.116466
   Chapter 6 is based on this paper.
5. Okuda, Y., Ohta, K., Sinmyo, R., Hirose, K., Ohishi, Y., 2020b. Anomalous compressibility in (Fe,Al)-bearing bridgmanite: implications for the spin state of iron. Phys. Chem. Miner. **47**, 40. https://doi.org/10.1007/s00269-020-01109-3
   Chapter 3 is based on this paper.
6. Okuda, Y., Kimura, S., Ohta, K., Park, Y., Wakamatsu, T., Mashino, I., Hirose, K., 2021. A cylindrical SiC heater for an externally heated diamond anvil cell to 1500 K. Rev. Sci. Instrument. accepted.
   Chapter 7 is based on this paper.